Title
Computing the Seismic Attenuation in Complex Porous Materials

Author
Masson, Yder Jean

Publication Date
2010

Peer reviewed|Thesis/dissertation

Computing the Seismic Attenuation in Complex Porous Materials

by

Yder Jean Masson

A dissertation submitted in partial satisfaction

of the requirements for the degree of

Doctor of Philosophy

in

Earth and Planetary science

in the

Graduate Division

of the

University of California, Berkeley

Committee in charge:

Professor Michael Manga, Chair
Professor Steven D. Glaser
Professor Steven R. Pride
Professor James W. Rector
Professor Barbara A. Romanowicz

Fall 2010

Abstract

Computing the Seismic Attenuation in Complex Porous Materials

by

Yder Jean Masson

Doctor of Philosophy in Earth and Planetary science

University of California, Berkeley

Professor Michael Manga, Chair

The present work analyzes seismic attenuation due to wave-induced flow in complex poroelastic materials containing an arbitrary amount of heterogeneity and fully or partially saturated with a mixture of fluids.

In the first part, two distinct finite-difference (FDTD) numerical schemes for solving Biot's poroelastic set of equations are introduced. The first algorithm is designed to be used in the seismic band of frequencies; i.e., when the permeability of the medium doesn't depend on frequency. The second algorithm accounts for viscous boundary layers that appear in the pores at high frequencies (in this case, the permeability depends on frequency) and can be used across the entire band of frequencies.

An innovative numerical method is presented in the second part allowing computation of seismic attenuation due to wave-induced flow for any poroelastic material. This method is applied to study the attenuation associated with different classes of materials saturated with a single fluid (water). For a material having a self-affine (fractal) distribution of elastic properties, it is demonstrated that frequency dependence in the attenuation is controlled by a single parameter that is directly related to the fractal dimension of the material. For anisotropic materials, a relation is established between the attenuation levels associated with waves propagating in different directions and the geometrical aspect ratio of the heterogeneities present within the material.

The third part concerns the study of attenuation associated with materials having a homogeneous solid skeleton saturated with a mixture of immiscible fluids. The special case where the distribution of fluids is the result of an invasion-percolation process is treated in detail.

Finally, the last part presents a novel experimental setup designed to measure fluctuations of the elastic properties in real rock samples. This device performs automated micro-indentation tests at the surface of rock samples and produces maps of the spatial distribution of Young's modulus. These maps are then used in combination with the aforementioned numerical methods to compute accurately the attenuation as a function of frequency associated with real rock samples.

To my Grandfather Charles who, I am sure, would have been very proud of this achievement.

Contents

List of Figures

List of Tables

Acknowledgements

First, not to forget anyone... I would like to thank all the people who helped and inspired me during my doctoral study.

I especially want to thank my advisor, Professor Steve Pride, for his trust in me, and for the freedom I had throughout these years of research. I am sure not all advisors can wait months with no news without questioning the abilities of their students. There is no need to state that he is a great scientist, and it's always a pleasure to discuss science and other things with him. I am also grateful for the time he spent reading and correcting my papers.

I would also like to thank my committee members for reading this manuscript and for their very interesting comments.

I am happy to thank Kurt Nihei for sharing his numerical code, which was very helpful when I started working on this project.

Thank you to all the teachers from whom I have learned so much through the years the good ones who are inspiring and make you want to learn more, and the bad ones who are so obscure that you really want to learn more... both helped me a great deal! To the medium ones, I say thank you too! We always learn something when sitting in the classroom, even if it is not the topic of the day. I especially want to thank Catherine Goasdoue, Dominique Gibert, Martine Kerzero, Gerard Antier, Philippe Boulvais, Annick Chauvin, Florence Nicollin, Frederic Conil, and Steve Pride.

Thank you to Barbara Romanowicz for associating with me in projects, for sharing data, and for the very inspiring discussion we had. I wish I could take more time to develop the ideas we discussed, and I am sure I will get back to them.

Thank you to the French connection: the Houlie family, Lolo, Paul, Marie, Catherine, and all the others. You guys made my stay a lot more fun.

Thank you very much to Liviu Tomutsa, for opening his laboratory to me and sharing his experience. Thank you to Seiji Nakagawa for his helpful advice. Thank you to Michael Manga, who found a place in his lab for me to set up my experiments. Thank you to Paul Cook and Phil Rizzo who engineered some parts of the micro indentation scanner.

I am very grateful to my good friends and colleagues Benoit Chauveau, Guillaume Daniel, Guitch, Olivier Pourret and Charles Poitou for the good times we have spent together.

Last, I would not have finished this project without the support of my wife Anne, my son Felix, and all my family, who have always been there for me. Whenever I need them, the encouragement they give to keep going and their love to empower me never fails. Thank you.

Chapter 1

Introduction

1.1 General context

An important part of the research effort in geophysics consists of understanding the different geological processes occurring within the upper part of the earth's crust, which contains most of the natural resources that are vital to modern society. Apart from a limited number of boreholes, we have no direct access to this region, and most information is collected via indirect geophysical methods. Seismic methods, such as reflection seismology, seismic refraction, and seismic tomography, are very powerful and are used extensively to image the Earth's interior. Reflection seismology, for example, can produce high-resolution 3D images of the earth's interior. Such images are obtained by migrating the seismic data, and provide accurate geometrical information on the location of interfaces in the propagating medium. Seismic tomography is more powerful in that it determines the seismic velocities of the rocks through which the waves are propagating. As most of the geomaterials encountered at the earth's surface consist of porous rocks saturated with one or more fluids, the problem of how to invert seismic data to deduce the hydro-physical properties of the propagating medium has attracted considerable interest. However, despite more than 50 years of effort since Biot first derived the poroelastic laws describing wave propagation in porous materials, this problem remains unsolved. In the present work, the question of how the spatial distribution of hydro-physical properties in heterogeneous porous rocks influences the dispersion and attenuation of seismic waves is addressed. This is one more step in the long-standing quest to invert for the hydro-physical properties of rocks from seismic data.

1.2 Definition of seismic attenuation

Seismic attenuation is a measure of the energy lost by a seismic wave as it propagates through the earth. There are two types of mechanisms that dissipate seismic-wave energy with distance. The first is scattering, which is due to wave interaction with heterogeneities at the scale of the wavelength (or smaller) that moves seismic energy out of the coherent first-arrival pulse. The second is called intrinsic attenuation, and refers to seismic energy lost as heat. When identifying these two mechanisms, the total attenuation Q_{Total}^{-1} inferred from the amplitude of the coherent pulses on the seismograms can be decomposed as

$$Q_{Total}^{-1} = Q_{Scat}^{-1} + Q^{-1} \tag{1.1}$$

where Q_{Scat}^{-1} denotes scattering attenuation and Q^{-1} is intrinsic attenuation. In Equation 1.1, Q^{-1} is the inverse "quality factor" that is physically defined as

$$\frac{1}{Q(\omega)} = \frac{\text{loss of energy in one wave period}}{4\pi \text{ average elastic energy reversibly stored in one period}} \tag{1.2}$$

and thus is a convenient dimensionless way to quantify intrinsic attenuation. Whether Q is an appropriate measure of scattering attenuation is a matter of debate (see Morozov, 2009.). The present work focuses on intrinsic attenuation due to wave-induced fluid flow, and the inverse quality factor is used as our measure of attenuation.

In the case of linear elasticity, the response of the propagating medium to seismic wave stimulation can be expressed in general terms as

$$\text{Response}(\omega) = \text{Modulus}(\omega) \times \text{Stimulation}(\omega). \tag{1.3}$$

For materials in which loss processes operate, there is a phase lag between stimulation and response and the elastic moduli are complex and frequency-dependent

$$\text{Modulus}(\omega) = M_R(\omega) + iM_I(\omega). \tag{1.4}$$

Due to causality (i.e., the response cannot occur prior to the stimulation), an analyticity condition must be satisfied that results in the real and imaginary parts of the moduli being related by the the Kramers-Kronig relations

$$M_R(\omega) = \frac{1}{\pi} P \int_{\infty}^{\infty} \frac{M_I(\omega_0)}{\omega - \omega_0} d\omega_0 \tag{1.5}$$

$$M_I(\omega) = \frac{1}{\pi} P \int_{\infty}^{\infty} \frac{M_R(\omega_0)}{\omega - \omega_0} d\omega_0 \tag{1.6}$$

where P denotes the Cauchy principal value. These relations imply that if there is loss related to the presence of M_I, there will always be a frequency dependence in the real part of the modulus. Such frequency-dependence in the elastic moduli is called "dispersion". It can be demonstrated (O'Connell and Budiansky, 1978) that Equation 1.2 is exactly equivalent to

$$\frac{1}{Q(\omega)} = \frac{M_I(\omega)}{M_R(\omega)}. \tag{1.7}$$

All the curves of attenuation as a function of frequency presented in this work have been obtained using Equation 1.7.

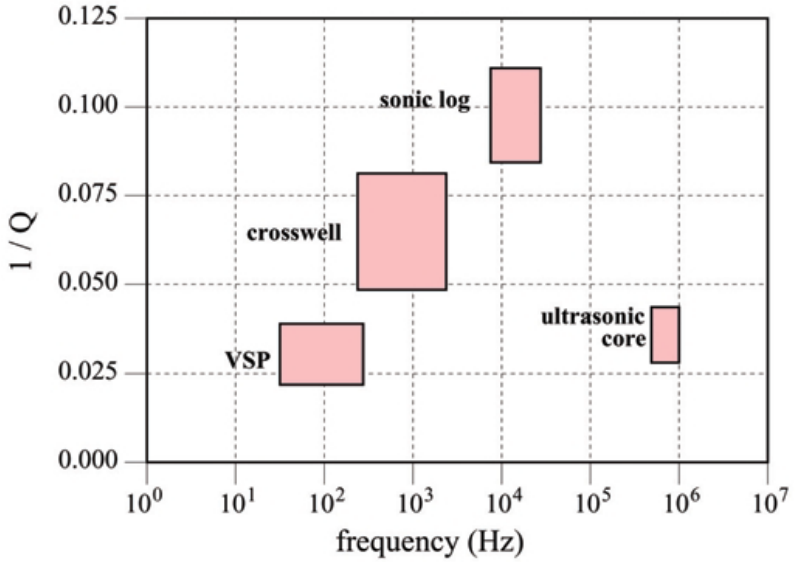

Figure 1.1. Intrinsic P-wave attenuation 1/Q as determined by Sams et al. (1997) on rocks from the same geologic sequence. The number of Q estimates coming from different depth ranges that fall within each rectangle above are as follows: 40 VSP, 69 crosswell, 854 sonic log, and 46 ultrasonic core measurements.

1.3 Field data

Proper estimation of intrinsic attenuation from field measurements is difficult because it requires subtracting attenuation due to scattering from the total measured attenuation. Although this operation is theoretically possible and has been the subject of ongoing research for more than twenty years (see Wu and Aki 1988, 1989, 1990), it is not yet feasible in all situations. For example, most analysis of scattering loss is based on loss occuring during transmission and there is not yet an agreed upon protocol for determining scattering loss from reflection data. Fortunately, in many situations, attenuation due to scattering is either negligible (e.g., horizontal well-to-well transmission through plane-layered strata), or it can be reliably estimated using transmission-based methods (e.g., for regional seismic data or for vertical-seismic profiling VSP data in which a source is placed on the surface and the receivers are down a well or for well-to-well transmission data). A detailed review of successful estimates of intrinsic attenuation from field measurements is provided by Pride et al. (2003). An important series of experiments has been conducted by Sams et al. (1997) at the Imperial College borehole test site in northeastern England; they used different experimental and inversion methods to obtain the intrinsic attenuation over a wide frequency band (30 Hz – 24 kHz) for a layered sequence of limestones, sandstones, siltstones, and mudstones in the first few hundred meters of the subsurface. Their estimates of intrinsic attenuation versus frequency are reproduced in Figure 1.1 and are representative of loss levels ($10^{-2} < Q^{-1} < 10^{-1}$) observed in shallow sedimentary rocks. However, the Q^{-1} associated with stiffer rocks

deeper in a basin can be one or two orders of magnitude smaller than this range (see Pride et al., 2003 for some specific field examples).

1.4 Laboratory data

In addition to field measurements, considerable effort is put into measuring attenuation and dispersion in the laboratory for real rock samples. To propagate seismic waves and analyze loss in transmission through lab samples typically requires a wavelength of a few centimeters or less. This corresponds to waves in the ultrasonic band of frequencies (say, 200 kHz to 1 MHz). Most laboratory measurements of attenuation have therefore focused on this band of frequencies. However, other non-propagative methods can be used to study attenuation in the seismic frequency band.

The resonant-bar technique (Birch and Bancroft , 1938; Winkler and Nur, 1982; Murphy, 1982; Lucet et al., 1991; Cadoret, 1998) is a popular method that consists of vibrating a rod of material at variable frequency to generate standing waves within rock samples. The attenuation is then obtained by measuring the wave's damping. The resonant-bar method is typically able to measure acoustic properties of rocks in the sonic (kilohertz) frequency range. One of the major drawbacks of the resonant-bar technique is that due to the modal analysis of wave damping, it gives estimates of attenuation at only a few distinct frequencies. Also, the low-frequency range (say, below 100 Hz) is hard to investigate with this method due to the large sample sizes ($\gg 1$ m) required.

To study seismic attenuation in the low-frequency range, quasi-static methods have been introduced. In these methods, a sinusoidal, axial force is applied to a rock sample while transducers measure the applied force and resulting sample displacement. The attenuation is then computed by taking the spectral ratio of the stress and strain responses. This approach is very similar to the numerical method employed in this thesis work. Spencer (1981) developed a unique laboratory apparatus that measures the complex Young's modulus of rock samples at arbitrary frequencies between 4 and 400 Hz. Batzle et al. (2006) used a similar device but measured the sample strain in a different manner; attenuation estimates at a strain amplitude of 10^{-7} from 5 Hz to 800 KHz are presented. It is generally observed (e.g., Winkler and Nur, 1982) that attenuation is independent of strain for strains less than roughly 10^{-6}. Recently, Adam et al. (2009) used the Batzle device to study seismic attenuation in carbonates.

Over the years, some important conclusions have been obtained from laboratory experiments. For dry rock samples, the measured attenuations are small ($Q^{-1} \ll 10^{-2}$) compared to typical field values of Q^{-1} measured in the upper crust. The observed attenuations are larger when the samples are saturated with fluids ($10^{-2} < Q^{-1} < 10^{-1}$). The highest attenuation levels ($Q^{-1} \approx 10^{-1}$) are observed for partially-saturated samples. Finally, attenuation depends greatly on frequency in fully or partially saturated rocks, but this is not the case in dry rocks.

1.5 Analytical models of seismic attenuation

The theory for acoustic propagation in a porous and elastic medium is generally credited to Biot (1956a,b, 1962), although Frenkel (1944) derived a similar set of equations. Many authors, including Levy (1979), Burridge and Keller (1981), Pride at al. (1992), and Pride and Berryman (1998), have used different approaches to demonstrate that Biot's theory is correct. The Biot theory predicts that when a porous rock is saturated with a single fluid, seismic energy is converted to heat and wave attenuation occurs due to wave-driven fluid flow between the peaks and troughs of the waves. It is implicitly assumed that at this scale of the wavelength, the porous medium is homogenous. Such equilibration of the fluid pressure differences between compressions and rarefactions is known as the Biot mechanism. However, the frequency at which the predicted attenuation is maximum is too high (typically by a few orders of magnitude) to explain attenuation levels in the seismic band of frequencies.

The squirt-flow model accounts for fluid flow due to micro-cracks present in the grains. When a seismic wave locally compresses the medium, these micro-cracks are squeezed and respond with a higher fluid-pressure increase than the rest of the pore space. Thus, fluid flow occurs to equilibrate this pressure gradient, and produces attenuation. These ideas were first introduced by Mavko and Nur (1975, 1979), followed by Budianski and O'Connell (1976), O'Connell and Budiansky (1977), and Dvorkin et al. (1995). Similar to the Biot mechanism, squirt flow tends to produce peak attenuation at ultrasonic frequencies and thus fails to explain attenuation levels in the seismic band.

In the patchy-saturation model introduced by White (1975) and White et al. (1975), wave-induced fluid flow is created by fluid patches of special geometry (spheres or layers) present at the mesoscopic scale. Mesoscopic length scales are those larger than the grain size but smaller than the wavelength. In a manner similar to the squirt-flow model, when a wave locally compresses the medium, fluid patches that are more or less compressible than the surrounding material respond with a different pressure increase. This mechanism can produce high levels of attenuation in the seismic band of frequencies. Dutta and Ode (1979) and Dutta and Seriff (1979) later improved the original White model for patchy saturation. Recently, Johnson (2001) proposed a new patchy-saturation model with no restriction on the patch geometries.

More recently, Pride and Berryman (2003a,b) introduced a double-porosity model in which wave-induced flow results from the presence of lithological heterogeneities at the mesoscopic scale. Similarly to the patchy-saturation model, this model allows patches having different incompressibilities to react with different fluid pressures when the medium is locally compressed by a seismic wave. This model is also able to predict the attenuation levels observed in the seismic frequency band.

1.6 Numerical methods

Numerical solutions to the Biot set of equations trace back to the seventies. To our knowledge, Garg et al. (1974) were the first to use them. They computed 1-D Green's functions (artificially damped) with a finite-differences method. Direct methods, where the geological model is approximated by a numerical mesh, were introduced later for poroelasticity and are now the main concentration of research efforts. These methods include finite-difference (FD), pseudo-spectral (PS), finite-element (FEM), and spectral-element (SEM) methods. Various implementations of the finite-differences and pseudo-spectral methods can be found in Zhu and McMechan (1991); Carcione and Goode (1995); Özdenvar and McMechan (1997); Carcione and Helle (1999); and Zhang (1999). An extensive presentation of the spectral generalization of the finite-element method can be found in Morency and Tromp (2008). Even though the formulation of the problem differs in these methods, most of the difference between them lies in the way the spatial derivatives are computed. Both the finite-difference and pseudo-spectral methods apply to regular meshes. The finite-difference method uses low-order operators to compute spatial derivatives, while the pseudo-spectral method uses high (virtually infinite) order operators to evaluate spatial derivatives. The spectral-element method is to the finite-element method what the pseudo-spectral method is to the finite-difference method, in the sense that it uses higher-order interpolating functions to compute spatial derivatives. Both the finite-element method and the spectral-element method can be used with irregular meshes.

1.7 Difficulties encountered

The ideas introduced for the development of analytical models predicting attenuation due to wave-induced flow have greatly improved our understanding of possible mechanisms explaining attenuation levels observed in the seismic band of frequencies. However, while able to accurately predict the observed attenuation, these analytical models apply only to materials having simple geometries, and suggest that the way attenuation varies versus frequency greatly depends on the geometry of the heterogeneities present at the mesoscopic scale in complex materials.

Numerical methods can be used to compute seismic attenuation in media with arbitrary complex distribution of mesoscopic heterogeneities, but are inefficient due to the different scales involved in the problem. Indeed, on the one hand, the numerical mesh must be fine enough to account for any mesoscopic heterogeneities present in the medium (typically we have $\Delta x \approx 1\text{mm}$); on the other, the size of the computational domain in which the seismic waves propagate must be at least a few wavelengths. The difference between the small grid spacing imposed to account for the heterogeneities and the wavelength often exceeds three orders of magnitude. In addition, using a small grid spacing requires the use of a small time increment in order to obtain a stable response. Consequently, using numerical methods to propagate waves and estimate attenuation in a medium containing heterogeneities at the mesoscopic scale is highly inefficient.

Experimental methods such as the resonant-bar method offer a way to measure attenuation and dispersion in samples of natural rocks. However, interpretation of the data is delicate, and it is not easy to estimate and separate the amount of attenuation due to the wave-induced flow mechanism, nor to obtain attenuation and dispersion predictions over a wide range of frequencies.

1.8 Proposed method

In order to address these difficulties, we propose a numerical method allowing numerical computation of attenuation and dispersion in artificial samples that contain an arbitrary amount of mesoscopic heterogeneity. To significantly reduce the computational cost associated with wave propagation, we propose to perform quasi-static relaxation experiments. These numerical experiments consist of applying a step change in stress to computer-generated rock samples containing mesoscopic-scale heterogeneity, and measuring the poroelastic response using a finite-difference algorithm. During the experiments, the average strain throughout the sample is computed, along with the effective complex and frequency-dependent elastic moduli of the sample. The ratio of the imaginary and real parts of these moduli determines the attenuation as a function of frequency associated with the modes of applied stress. The method can be used to validate analytical models and help the interpretation of experimental measurements. Another advantage of this method is that it allows the complete separation of intrinsic attenuation (due to the wave-induced flow) from scattering loss, which is not easily achieved when computing full wave propagation.

In order to produce realistic estimates of the attenuation, the hydro-physical properties of the numerical samples used for the modeling should be as close as possible to the properties of real rocks. Most important is to quantify fluctuations in the mechanical properties of the propagating medium at the mesoscale, since they control the fluid-pressure response and attenuation levels. To achieve this goal, we have developed an experimental device that performs automated indentation tests and is able to produce maps of the Young's modulus for actual rock samples. Using these experimental measurements as an input to the proposed numerical method will help to produce accurate predictions of the expected attenuation associated with real rocks.

1.9 Organization of the dissertation

The present work consists of a series of papers organized in four parts. The first part deals with the numerical solution to the Biot set of equations, and consists of two papers. In the first paper, we present a new finite-differences algorithm that solves the Biot equations in the seismic frequency band. A key point of this paper is the derivation of an exact stability condition for the numerical scheme. In the second paper, the finite-differences algorithm is

extended to account for frequency dependence in the permeability due to viscous boundary layers that appear in the pores at high frequencies.

The second part consists of three papers about attenuation due to wave-induced flow associated with lithological heterogeneities present at the mesoscopic scale. The quasi-static modeling method is presented in a first paper; we show that the results obtained for attenuation versus frequency are in agreement with the double porosity model for simple materials. The method is then used to study attenuation in materials having a more complex distribution of mesoscopic heterogeneities. In a second paper, we show that for fractal materials where heterogeneities of all sizes are present, attenuation scales differently and can be related to frequency by a power law. In the final paper of the second section, we show that the quasi-static method can be used to study anisotropy in the attenuation due to wave-induced flow.

The third part is dedicated to the study of attenuation due to partial saturation. This part consists of a single paper where attenuation associated with complex fluid distributions is investigated. The special case of fluid distributions generated via an invasion percolation process is discussed in detail.

Finally, in the last part we present preliminary experimental results showing the spatial distribution of the elastic moduli within real rock samples. These results have been obtained using a novel micro-indentation scanner that is still under development. We provide examples showing how these results can be used in combination with numerical methods to compute highly-accurate estimations of attenuation versus frequency.

Chapter 2

Numerical solution of Biot's poroelastic set of equations

2.1 Finite difference solution of the Biot set of equations at seismic frequencies

(Published in the JOURNAL OF GEOPHYSICAL RESEARCH,
Y. J. Masson, S. R. Pride, and K. T. Nihei, J. Geophys. Res., Volume 111, B10305, 2006.)

2.1.1 Introduction

Many authors, including Levy (1979), Burridge and Keller (1981), Pride et al. (1992) and Pride and Berryman (1998), have used various analytical coarse-graining procedures to demonstrate that Biot's (1956a,b and 1962) theory is the correct general model governing poroelastic response. Poroelastic response allows for the coupled interactions between the elastic deformation of a porous solid and the fluid flow and fluid accumulation in the same material. In the earth sciences, poroelastic theory finds application in the consolidation of soils and rocks under applied loads, the fluid redistribution in the crust following an earthquake, the flow induced by seismic waves, and hydrological fluid-pressure diffusion and fluid flow in rocks and soils. In applications involving a heterogeneous earth model or complicated stressing patterns due to slip on a fault, numerical solutions are required, and we have become interested in optimal ways to solve the laws of poroelasticity using finite-difference approximations.

There have been several finite-difference algorithms presented in the literature for the solution of Biot's equations (e.g., Zhu and McMechan, 1991; Carcione and Goode, 1995; Özdenvar and McMechan, 1997; Carcione and Helle, 1999; and Zhang, 1999). However, none of these algorithms use both a standard velocity-stress staggered grid and direct explicit time differencing for the updates. For example, Carcione and Goode (1995) and Carcione and Helle (199) use a velocity-stress staggered grid but perform the time updates in an approximate two step integration process, while Özdenvar and McMechan (1997) use a staggered grid in a displacement formulation that requires derivatives of the elastic moduli to be computed. Carcione and Goode (1995) state that the presence of the diffusive fluid-pressure response renders the equations stiff (i.e., possessing response on widely different time scales) and thus "precludes the use of standard explicit time-integration techniques since they require a very small time step to satisfy the stability condition."

In the present work, we present a standard explicit time-integration technique for Biot's equations that is analagous to the algorithm of Levander (1988) for the purely elastic case. We perform a rigorous time stability analysis of the scheme and demonstrate that under all normal conditions, the usual Courant stability condition holds as if the problem involved purely elastic waves. The presence of fluid-pressure diffusion does not render the algorithm unstable so long as there is an inertial acceleration term present in Darcy's law. The required time steps are no different than in usual elastodynamic response. To be sure, if the goal is to model the creation of Biot slow waves at interfaces (fluid pressure diffusion generated at a material property contrast), one must use a fine spatial sampling in order to accurately sample the slow wave. However, we demonstrate that explicit time-differencing can be efficiently and accurately applied to Biot's equations and we feel this point has not been understood in the literature.

In this paper, we: (1) carefully present the low-frequency poroelastic equations that are to be solved; (2) introduce our explicit finite-differencing scheme; (3) derive the rigorous stability conditions; and (4) demonstrate the accuracy and stability of the algorithm by comparing numerical simulations to exact analytical results.

2.1.2 Poroelastic response at low frequencies

The fluid flow induced by a seismic wave propagating through a porous material is well modeled using a generalized Darcy's law that allows for both the flow due to the induced pressure gradient and the flow created by the acceleration of the framework of grains which is the frame of reference for the relative fluid motion. Assuming an $e^{-i\omega t}$ time dependence, the generalized Darcy law is written in the frequency domain as

$$\mathbf{q} = \frac{k(\omega)}{\eta} \left[-\nabla p + i\omega \rho_f \mathbf{v} \right]. \tag{2.1}$$

Here, p is the fluid pressure, $\mathbf{q}$ the Darcy filtration velocity, $\mathbf{v}$ the velocity of the solid framework of grains, η the fluid viscosity, ρ_f the fluid density, and $k(\omega)$ the complex (or "dynamic") permeability.

The frequency dependence in $k(\omega)$ results from the appearance of viscous boundary layers in the pores at sufficiently high frequencies. At low frequencies, the flow profile in each pore is controlled by viscous shearing and is locally "parabolic" (laminar). At high frequencies, inertial effects begin to dominate the shear forces, resulting in an ideal-flow "plug" profile except in a thin viscous boundary layer near the fluid/solid interface where shear forces again must dominate because the relative motion must decrease to zero on the grain surfaces. The thickness of the viscous boundary layers decreases with increasing frequency as $1/\sqrt{\omega}$.

Johnson et al. (1987) connect these two frequency limits using a complex permeability function that obeys causality constraints. Their model for the frequency dependence of $k(\omega)$ is

$$\frac{k(\omega)}{k_0} = \left[\sqrt{1 - i\frac{4}{n_J}\frac{\omega}{\omega_J}} - i\frac{\omega}{\omega_J}\right]^{-1} \tag{2.2}$$

where the relaxation frequency ω_J at which viscous boundary layers first develop is

$$\omega_J = \frac{\eta}{\rho_f F k_0}. \tag{2.3}$$

Here, k_0 is the dc limit of the permeability (the usual hydrological permeability), F is the electrical formation factor, and n_J is a dimensionless parameter given by $n_J = \Lambda^2/(Fk_0)$ where the length Λ is a weighted pore-volume to grain-surface ratio with the weight emphasizing constricted portions of the porespace [see Johnson et al. (1987) for the precise mathematical definition of Λ]. For clean sands, $n_J = 8$ is consistent with both numerical and laboratory experiments. For shaly sands, one can have $n_J \ll 8$.

Using typical values appropriate for water-saturated clastic rocks (e.g., $k_0 < 10^{-13}$ m^2, $\eta = 10^{-3}$ Pa s, $\rho_f = 10^3$ kg/m^3, and $F < 100$), one has that $\omega_J/(2\pi) \gg 10$ kHz. Thus, over the seismic band of frequencies loosely defined as $\omega/(2\pi) < 10$ kHz, the relative flow is well characterized as being in the low-frequency limit where $\omega/\omega_J \ll 1$. In this limit, equation (2.2) becomes

$$\frac{1}{k(\omega)} = \frac{1}{k_0}\left[1 - i(1+\Phi)\frac{\omega}{\omega_J} + O\left(\frac{\omega^2}{{\omega_J}^2}\right)\right] \tag{2.4}$$

where we have introduced a real dimensionless parameter Φ that is given by

$$\Phi = 2/n_J \tag{2.5}$$

in the Johnson et al. (1987) model. This Φ is bounded as $\Phi \geq 1/4$ for all porous materials. Although the term $(1+\Phi)\omega/\omega_J$ is, for rocks and soils, negligible compared to one over the seismic band of frequencies, we will demonstrate later that it can never be set to zero in our explicit time-stepping finite-difference scheme since it is entirely responsible for the stability of the algorithm.

Transforming to the time domain, the low-frequency form of the generalized Darcy's law to be employed, that properly models the physics whenever seismic frequencies satisfy $\omega/\omega_J \ll 1$, is

$$\rho_f(1+\Phi)F\frac{\partial \mathbf{q}}{\partial t} + \frac{\eta}{k_0}\mathbf{q} = -\nabla p - \rho_f\frac{\partial \mathbf{v}}{\partial t}. \tag{2.6}$$

Using this equation, as opposed to the more general equation 2.1, is what is meant by the "low-frequency" or "seismic" limit of Biot theory. Once again, the physics not modeled by equation2.6 is the creation of viscous boundary layers in the pores at frequencies $\omega > \omega_J$.

The remaining equations of Biot's theory include the total conservation of linear momentum

$$\rho \frac{\partial \mathbf{v}}{\partial t} = \nabla \cdot \tau - \rho_f \frac{\partial \mathbf{q}}{\partial t} \tag{2.7}$$

where ρ is the bulk density of the porous material and $\tau = \tau_{ij} \hat{\mathbf{i}}\hat{\mathbf{j}}$ is the total stress tensor, as well as the stress-strain constitutive laws for an isotropic porous material

$$\frac{\partial \tau}{\partial t} = (\lambda_u \nabla \cdot \mathbf{v} + \alpha M \nabla \cdot \mathbf{q})\, \mathbf{I} + \mu \left[\nabla \mathbf{v} + (\nabla \mathbf{v})^{\mathbf{T}}\right] \tag{2.8}$$

$$-\frac{\partial p}{\partial t} = M\left(\alpha \nabla \cdot \mathbf{v} + \nabla \cdot \mathbf{q}\right). \tag{2.9}$$

The poroelastic constants used here are the undrained Lamé modulus λ_u, the shear modulus μ (the same for both drained and undrained conditions), the so-called Biot-Willis (1957) constant α, and the fluid-storage coefficient M. For any porous material, these constants are related to the undrained bulk modulus K_u, the drained bulk modulus K_d, and Skempton's (1954) undrained fluid-pressure to confining-pressure ratio B as

$$\lambda_u = K_u - 2\mu/3 = K_d + \alpha^2 M - 2\mu/3 \tag{2.10}$$

$$\alpha = (1 - K_d/K_u)/B \tag{2.11}$$

$$M = BK_u/\alpha. \tag{2.12}$$

In the special case considered by Gassmann (1951), in which the solid frame is composed of a single isotropic mineral characterized by a bulk modulus K_s, we have as well the so-called "fluid-substitution" relations given by

$$B = \frac{1/K_d - 1/K_s}{1/K_d - 1/K_s + \phi(1/K_f - 1/K_s)} \tag{2.13}$$

$$K_u = \frac{K_d}{1 - B(1 - K_d/K_s)} \tag{2.14}$$

where K_f is the fluid bulk modulus and ϕ is the porosity. From these, one further obtains $\alpha = 1 - K_d/K_s$.

2.1.3 Finite-differencing scheme

The two-dimensional (2D) fourth-order staggered-grid method given by Levander (1988) to solve the elastic set of equations using second-order time differences for the updating is widely used in seismology. As such, we propose to adopt here a similar approach to the low-frequency Biot equations. Being based on a Yee (1966) staggered grid, this method offers a good compromise between numerical accuracy and computational efficiency. In seismology,

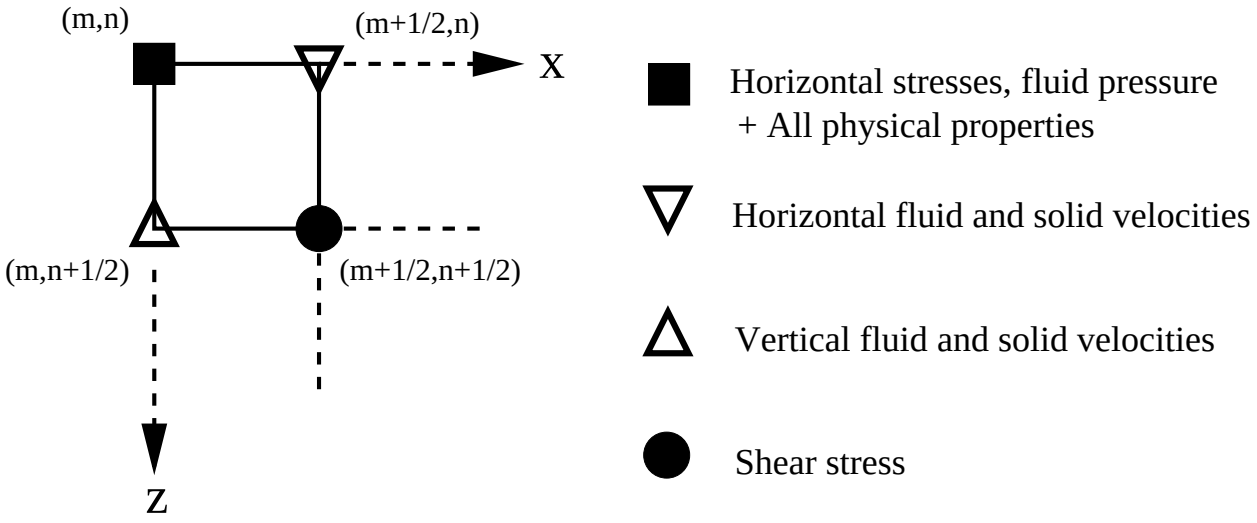

Figure 2.1. Convention adopted in the present paper for the spatial position of the stresses, pressure, and fluid/solid velocities field on the staggered grid

the staggered grid was pioneered by Madariaga (1976), Aki and Richards (1980), and Virieux (1986).

The finite-difference equations to be solved in 2D are obtained by discretizing the space variables into a square grid, and assigning the field variables and material properties to the grid points as defined in Figure 2.1. All the material properties and the stress components τ_{xx}, τ_{zz}, and p are assigned to the grid points $x = m\Delta_x, z = n\Delta_z$ where m and n are integers; the horizontal velocities v_x and q_x to the points $x = (m + 1/2)\Delta_x, z = n\Delta_z$; the vertical velocities v_z and q_z to the points $x = m\Delta_x, z = (n + 1/2)\Delta_z$; and the shear stress τ_{xz} to the points $x = (m + 1/2)\Delta_x, z = (n + 1/2)\Delta_z$. Further, all the velocities are temporally discretized at the time points $t = l\Delta_t$, while all the stresses are discretized at the time points $t = (l + 1/2)\Delta_t$.

Knowing q_i, v_i at time $t = l\Delta_t$ and τ_{ij}, p at time $t = (l - 1/2)\Delta_t$, the discrete form of

the constitutive laws (2.8) and (2.9) are used to update τ_{ij} and p at time $t = (l + 1/2)\Delta_t$

$$\begin{aligned} D_t\tau_{xx} &= (\lambda_u + 2\mu)\, D_x v_x + \lambda_u D_z v_z \\ &\quad +\alpha M\, (D_x q_x + D_z q_z) \Big|_{m,n,l} \end{aligned} \tag{2.15}$$

$$\begin{aligned} D_t\tau_{zz} &= \lambda_u D_x v_x + (\lambda_u + 2\mu)\, D_z v_z \\ &\quad +\alpha M\, (D_x q_x + D_z q_z) \Big|_{m,n,l} \end{aligned} \tag{2.16}$$

$$D_t\tau_{xz} = \mu_{\text{av}}\, (D_x v_z + D_z v_x) \Big|_{m+\frac{1}{2},n+\frac{1}{2},l} \tag{2.17}$$

$$\begin{aligned} D_t p &= -\alpha M\, (D_x v_x + D_z v_z) \\ &\quad +M\, (D_x q_x + D_z q_z) \Big|_{m,n,l} \end{aligned} \tag{2.18}$$

where μ_{av} is a locally-averaged shear modulus with the averaging symmetrically distributed around the shear stress position $(m + 1/2, n + 1/2)$

$$\begin{aligned} \frac{1}{\mu_{\text{av}}} &= \frac{1}{4}\left[\frac{1}{\mu(m,n)} + \frac{1}{\mu(m+1,n)}\right. \\ &\quad \left. +\frac{1}{\mu(m,n+1)} + \frac{1}{\mu(m+1,n+1)}\right]. \end{aligned} \tag{2.19}$$

A geometric (rather than arithmetic) average has been taken to enhance local stress continuity at a local discontinuity in μ. The vertical line at the right of each finite-difference equation denotes the space and time position at which the terms in the equations are all centered.

Inserting equation (2.7) into equation (2.6) leads to the discrete expression used to update q_i at time $t = (l + 1)\Delta_t$ knowing τ_{ij} and p at time $t = (l + 1/2)\Delta_t$, and q_i and v_i at time $t = l\Delta_t$

$$\begin{aligned} &\psi_m \langle \rho_f \rangle_m D_t q_x + \left\langle \frac{\eta}{k_0} \right\rangle_m \langle q_x \rangle_l = \\ &\quad -D_x p - \frac{\langle \rho_f \rangle_m}{\langle \rho \rangle_m}(D_x \tau_{xx} + D_z \tau_{xz}) \Big|_{m+\frac{1}{2},n,l+\frac{1}{2}} \end{aligned} \tag{2.20}$$

$$\begin{aligned} &\psi_n \langle \rho_f \rangle_n D_t q_z + \left\langle \frac{\eta}{k_0} \right\rangle_n \langle q_z \rangle_l = \\ &\quad -D_z p - \frac{\langle \rho_f \rangle_n}{\langle \rho \rangle_n}\, (D_z \tau_{zz} + D_x \tau_{xz}) \Big|_{m,n+\frac{1}{2},l+\frac{1}{2}} \end{aligned} \tag{2.21}$$

where the dimensionless property ψ_m is defined as

$$\psi_m = \langle (1 + \Phi) F \rangle_m - \frac{\langle \rho_f \rangle_m}{\langle \rho \rangle_m}. \tag{2.22}$$

The brackets denote both time averaging $\langle\ \rangle_l$ and space averaging $\langle\ \rangle_m$ or $\langle\ \rangle_n$, and are defined as follows

$$\langle q_x \rangle_l \Big|_{l+\frac{1}{2}} = \frac{q_x(l+1) + q_x(l)}{2} \tag{2.23}$$

$$\langle \rho \rangle_m \Big|_{m+\frac{1}{2},n} = \frac{\rho(m+1,n) + \rho(m,n)}{2} \tag{2.24}$$

$$\langle \rho \rangle_n \Big|_{m,n+\frac{1}{2}} = \frac{\rho(m,n+1) + \rho(m,n)}{2}. \tag{2.25}$$

Similar definitions hold for the averages of q_z, ρ_f, and so forth.

Finally, knowing τ_{ij}, p, $D_t q_i$ at time $t = (l+1/2)\Delta_t$ and v_i at time $t = l\Delta_t$, v_i is updated at time $t = (l+1)\Delta_t$ by inserting equation (2.6) into equation (2.7) to obtain

$$\begin{aligned} \langle \rho \rangle_m D_t v_x &= \left(1 + \frac{1}{\psi_m} \frac{\langle \rho_f \rangle_m}{\langle \rho \rangle_m}\right) (D_x \tau_{xx} + D_z \tau_{xz}) \\ &+ \frac{1}{\psi_m} \left(D_x p + \left\langle \frac{\eta}{k_0} \right\rangle_m \langle q_x \rangle_l\right)\Big|_{m+\frac{1}{2},n,l+\frac{1}{2}} \end{aligned} \tag{2.26}$$

$$\begin{aligned} \langle \rho \rangle_n D_t v_z &= \left(1 + \frac{1}{\psi_n} \frac{\langle \rho_f \rangle_n}{\langle \rho \rangle_n}\right) (D_x \tau_{xz} + D_z \tau_{zz}) \\ &+ \frac{1}{\psi_n} \left(D_z p + \left\langle \frac{\eta}{k_0} \right\rangle_n \langle q_z \rangle_l\right)\Big|_{m,n+\frac{1}{2},l+\frac{1}{2}}. \end{aligned} \tag{2.27}$$

Equations (2.15)–(2.27) provide our finite-difference modeling algorithm.

Last, any order of differencing approximation may be employed for the first-space derivative operators D_x and D_z and the first-time derivative D_t. However the stability analysis and numerical implementation of the present paper uses the fourth-order space operator given by

$$\begin{aligned} D_x v_x \Big|_{m,n} &= \frac{1}{\Delta_x} \{c_1 [v_x(m+1/2,n) - v_x(m-1/2,n)] \\ &- c_2 [v_x(m+3/2,n) - v_x(m-3/2,n)]\}, \end{aligned} \tag{2.28}$$

with $c_1 = 9/8$ and $c_2 = 1/24$ the fourth-order differencing weights, and the second-order time operator given by

$$D_t v_x \Big|_{m,n,l+1/2} = \frac{1}{\Delta_t} [v_x(m,n,l+1) - v_x(m,n,l)]. \tag{2.29}$$

2.1.4 Stability and dispersion

The stability of the numerical scheme with fourth-order spatial and second-order temporal differencing is now investigated using a von Neumann stability analysis. In order to simplify

the problem and make it analytically tractable, we consider a plane longitudinal disturbance advancing in the x direction through a homogeneous material (i.e., q_z, v_z, τ_{zz}, and τ_{xz} are all set to zero along with all spatial derivatives with respect to z). Displacements u_x and w_x are also introduced through the defining relations

$$v_x = D_t u_x \tag{2.30}$$

$$q_x = D_t w_x. \tag{2.31}$$

In this case, the set of difference equations (2.15)–(2.27) can be combined into the matrix system

$$Qu = 0 \tag{2.32}$$

where the 2×2 matrix operator Q is given by

$$Q = \left[\begin{array}{c|c} (\lambda_u + 2\mu)D_{xx} & (\alpha M)D_{xx} - \rho_f D_{tt} \\ -\rho D_{tt} & \\ \hline (\alpha M)D_{xx} - \rho_f D_{tt} & M D_{xx} - \frac{\eta}{k_0} D_t \langle\,\rangle_l \\ & -\rho_f(1+\Phi)F D_{tt} \end{array}\right] \tag{2.33}$$

and

$$u = [u_x, w_x]^T. \tag{2.34}$$

Here, D_{xx} and D_{tt} are the finite second-derivative operators in space (fourth order) and time (second order) respectively.

The von Neumann stability analysis assumes that the independent solutions of equation (2.32) are of the form

$$\left[\begin{array}{c} u_x(m,l) \\ w_x(m,l) \end{array}\right] = G^l e^{ikm\Delta_x} \left[\begin{array}{c} u_o \\ w_o \end{array}\right] \tag{2.35}$$

where k is a real spatial wave number and $G = G(k)$ is the complex amplification factor. In this context, testing the stability of the numerical scheme is equivalent to testing the hypothesis

$$\|G\| \leq 1 \;\; \forall \;\; k. \tag{2.36}$$

If equation (2.36) is true, then the scheme is stable. Note that one may equivalently identify $G = e^{-i\omega\Delta_t}$ and require that $\mathrm{Im}\{\omega\} \leq 0 \; \forall \; k$.

An expression for $G(k)$ is obtained by requiring the determinant of the linear system to vanish; i.e., $\det|Q| = 0$ after allowing the finite-difference operators to act on the common factor $G^l e^{ikm\Delta_x}$. The second-order finite-difference time derivatives give

$$D_t\langle G^l\rangle_l = \left(\frac{G - G^{-1}}{2\Delta_t}\right) G^l \tag{2.37}$$

$$D_{tt} G^l = \left(\frac{G - 2 + G^{-1}}{\Delta_t^2}\right) G^l \tag{2.38}$$

while the fourth-order finite-difference space derivatives give

$$D_{xx} e^{ikm\Delta_x} = -\frac{4\phi_k}{\Delta_x^2} e^{ikm\Delta_x} \tag{2.39}$$

with the periodic function ϕ_k given by

$$\begin{aligned}\phi_k &= \left\{c_1^2 + 2c_1c_2\left[1 - 4\cos^2\left(\frac{k\Delta_x}{2}\right)\right]\right\}\sin^2\left(\frac{k\Delta_x}{2}\right) \\ &\quad + c_2^2\sin^2\left(\frac{3k\Delta_x}{2}\right). \end{aligned} \tag{2.40}$$

Again, $c_1 = 9/8$ and $c_2 = 1/24$ are the fourth-order differencing weights. The determinant then yields the quartic

$$\det|Q| = a_5G^4 + a_4G^3 + a_3G^2 + a_2G + a_1 = 0 \tag{2.41}$$

where the a_i coefficients are real functions of the physical properties of the material, the spatial and temporal sampling intervals, and the wave number k, and are defined as

$$a_5 = \pi_1 + \Delta_t\pi_4 \tag{2.42}$$

$$a_4 = -4\pi_1 + 4\frac{(\Delta_t)^2}{(\Delta_x)^2}\phi_k\pi_2 - 2\Delta_t\pi_4 + 4\frac{(\Delta_t)^3}{(\Delta_x)^2}\phi_k\pi_5 \tag{2.43}$$

$$a_3 = 6\pi_1 - 8\frac{(\Delta_t)^2}{(\Delta_x)^2}\phi_k\pi_2 + 16\frac{(\Delta_t)^4}{(\Delta_x)^4}\phi_k^2\pi_3 \tag{2.44}$$

$$a_2 = -4\pi_1 + 4\frac{(\Delta_t)^2}{(\Delta_x)^2}\phi_k\pi_2 + 2\Delta_t\pi_4 - 4\frac{(\Delta_t)^3}{(\Delta_x)^2}\phi_k\pi_5 \tag{2.45}$$

$$a_1 = \pi_1 - \Delta_t\pi_4. \tag{2.46}$$

The π_i coefficients are defined as

$$\pi_1 = \rho_f\rho[(1+\Phi)F - \rho_f/\rho] \tag{2.47}$$

$$\pi_2 = \rho_f(1+\Phi)F(\lambda_u + 2\mu) + \rho M - 2\alpha M\rho_f \tag{2.48}$$

$$\pi_3 = M(\lambda_u + 2\mu - \alpha^2 M) \tag{2.49}$$

$$\pi_4 = \frac{\eta\rho}{2k_0} \tag{2.50}$$

$$\pi_5 = \frac{\eta}{2k_0}(\lambda_u + 2\mu) \tag{2.51}$$

and depend only on the physical properties of the material.

The quartic $P(G) = 0$ of equation (2.41) can be solved using a numerical evaluation of the analytical expressions given by Abramowitz and Stegun (1965). As an example, Figure 2.2 plots the four complex roots $G = \{r1, r2, r3, r4\}$ of $P(G) = 0$. In each plot, the roots vary with wave number. The only difference between the three panels labeled (A), (B) and (C) is the value of Δ_t. The material properties and Δ_x are held constant for all three plots. The roots $\{r1, r2\}$ are associated with the advanced and retarded fast-P (or normal compressional wave) response, while the roots $\{r3, r4\}$ are associated with the advanced and retarded slow-P (or fluid-pressure diffusion) response. The stability requirement can now be

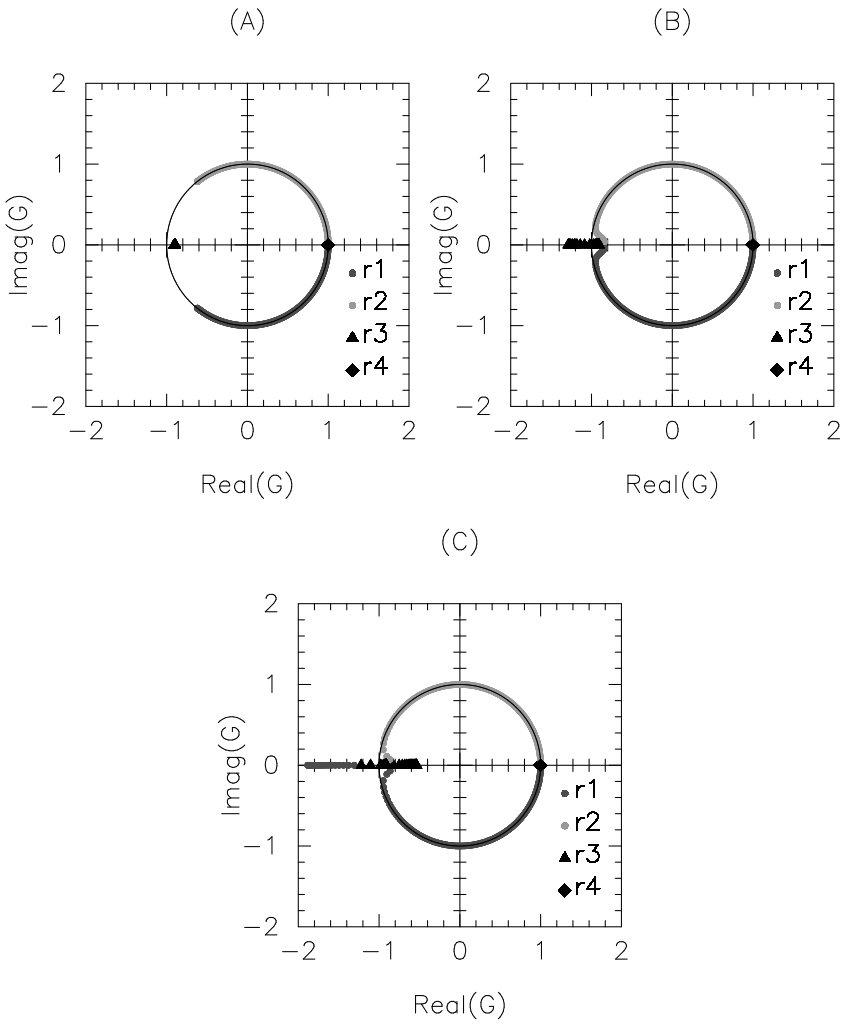

Figure 2.2. The four complex roots of the polynomial $P(G)$ are displayed as Δ_t is varied. Panel (A): Δ_t is relatively small and the numerical scheme is stable (i.e., all the roots are within the unit circle). Panels (B) and (C): Δ_t is made progressively larger and the numerical scheme becomes unstable as roots move outside the unit circle. In Panel (B), only the slow-wave root r_3 has moved out of the unit circle, while in Panel (C) this root is joined outside the circle by the fast-wave root r_1.

Table 2.1. Material properties of a lightly-consolidated sand.

Solid grain material	
Bulk modulus (K_s)	36.0 GPa
Density (ρ)	2650 kg/m^3
Skeletal framework of grains	
Bulk modulus (K_d)	621 MPa
Shear modulus (μ)	455 MPa
Porosity (ϕ)	0.3
Permeability (k)	10^{-12} m^2
Fluid	
Bulk modulus (K_f)	2.25 GPa
Density (ρ_f)	1000 kg/m^3
Viscosity (η)	10^{-3} N s m^{-2}

stated

$$\left\{ \begin{array}{c} \|r_1\| \leq 1 \\ \text{and} \\ \|r_2\| \leq 1 \\ \text{and} \\ \|r_3\| \leq 1 \\ \text{and} \\ \|r_4\| \leq 1 \end{array} \right\} \quad \forall \;\; k. \tag{2.52}$$

In the example of Figure 2.2A (Δ_t relatively small), all roots are within the unit circle and the algorithm is stable. However, as Δ_t is increased (Figures 2.2B and then 2.2C), one or more roots leave the unit circle, and the algorithm becomes unstable. We next investigate the specific conditions required for all four roots to lie within the unit circle.

Figure 2.3 shows the numerical estimation of the separation surface between the stable domain [i.e., where equation (2.52) is satisfied] and the unstable domain as a function of the spatial sampling interval Δ_x, the temporal sampling interval Δ_t, and the low-frequency form-drag parameter $(1 + \Phi)F$ that is associated with the acceleration of the Darcy flow in equation (2.6). One important aspect of this surface is that the relation between Δ_x and Δ_t is linear for any value of $(1 + \Phi)F$. As a consequence, if the code is stable for a given pair of values (Δ_x,Δ_t), it will be stable for any pair of values ($C\Delta_x$,$C\Delta_t$) where C is an arbitrary multiplicative factor. Another interesting point is that for values of $(1 + \Phi)F$ less than a critical value to be analytically determined below, the numerical scheme is unconditionally unstable. Finally, and this is the most important result here, when the parameter $(1 + \Phi)F$ becomes large enough (as will be defined below), the linear relation between Δ_x and Δ_t asymptotes to the classic Courant condition that, in one dimension, is given by

$$\Delta_t \leq \frac{\Delta_x}{(c_1 + c_2)V_p} \tag{2.53}$$

This condition was also determined by Levander (1988) in the purely elastic case. In the

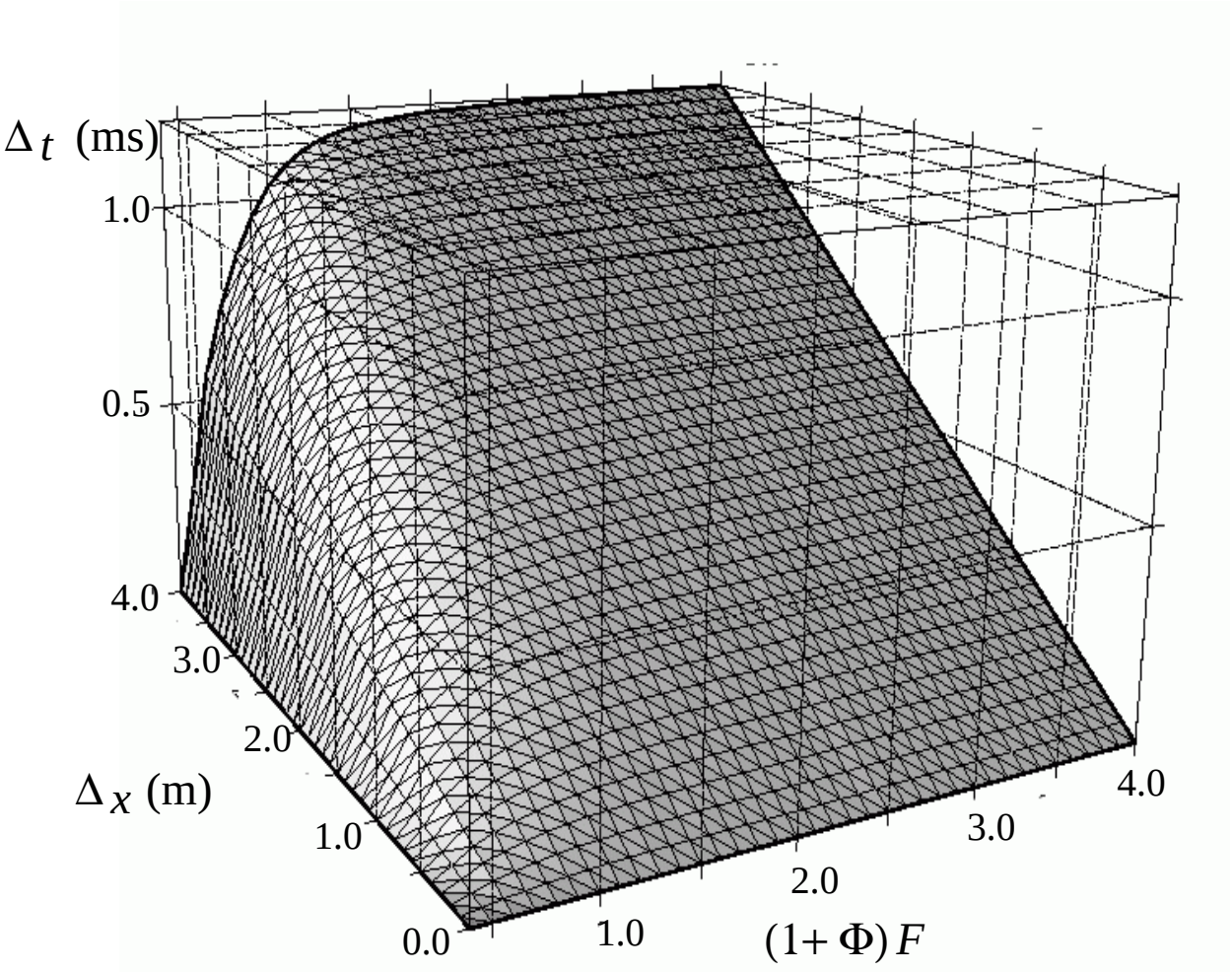

Figure 2.3. Separation surface between the stable domain (under the surface of this plot) and the unstable domain (above the surface) as a function of Δ_x, Δ_t and $(1 + \Phi)F$. The surface has been computed using the physical properties given in Table 2.1. Some interesting properties of the surface are: the relation between Δ_x and Δ_t is linear for any $(1 + \Phi)F$; under the critical value of $(1 + \Phi)F = \rho_f/\rho$, the numerical scheme becomes unconditionally unstable; when $(1+\Phi)F$ becomes large, the stability criterion tends to the Courant condition that holds in the case of elastic waves.

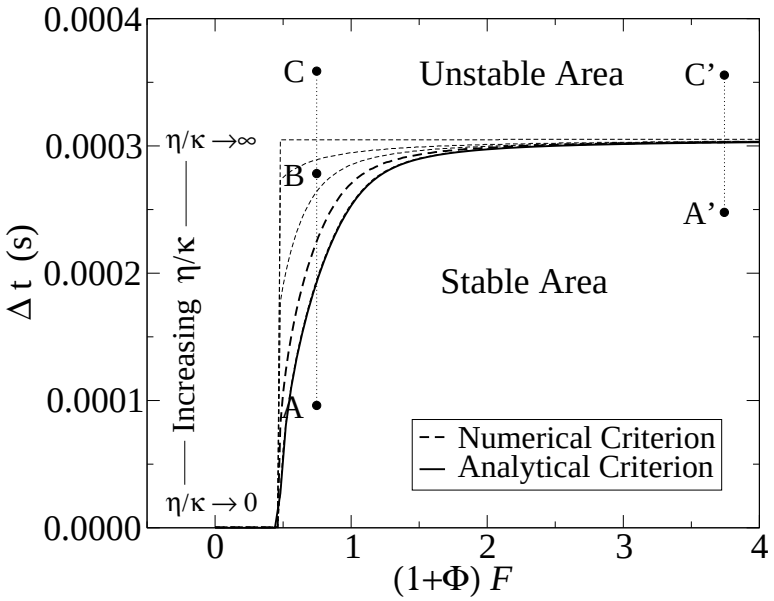

Figure 2.4. Boundary separating the stable and unstable domains plotted as a function of Δ_t and $(1+\Phi)F$ for a constant Δ_x. All the curves are obtained from the properties given in Table 2.1. The solid black line is the curve given by equation (2.57) which corresponds to $\eta/k_o = 0$. The different dashed lines show the boundary between the stable and unstable domains at different values of η/k_0. The points **A** and **A'** are always in the stable domain (i.e for any η/k_0), the points **C** and **C'** are always in the unstable domain, and the point **B** can be either in the stable or in the unstable domain depending on η/k_0.

context of the Biot theory, V_p is the velocity associated with the undrained fast P-wave (see Pride, 2005, for a demonstration that the low-frequency P-wave response is undrained) and is equal to

$$V_p = \sqrt{\frac{\lambda_u + 2\mu}{\rho}}. \tag{2.54}$$

It will be seen below that for typical values of $(1+\Phi)F$ in rocks, the stability requirement of equation (2.53) always applies. Another physical parameter that controls the shape of the stability surface is the hydraulic resistivity η/k_0. Figure 2.4 is a slice through the surface given in Figure 2.3 taken at $\Delta_x = \text{const}$. It shows that when η/k_0 goes to infinity, the stability criterion tends to that of equation (2.53) for any value of $(1+\Phi)F$ greater than the critical value. In the other limit, when η/k_0 goes to zero, the separation surface converges to a particular surface (the solid curve in Figure 2.4) under which the numerical scheme is always stable.

A simple way to obtain an analytical expression for this most restrictive stability surface (i.e., when $\eta/k_0 = 0$), is to note that the roots of the quartic $P(G) = 0$ that go outside the unit circle when $\eta/k_0 = 0$ are both real and negative. Thus, by putting $G = -1$ in equation (2.41), we obtain a quadratic equation for Δ_t/Δ_x whose solution directly gives the

solid line in Figure 2.4

$$\left[\left(\frac{\Delta_t}{\Delta_x}\right)^2 \phi^k\right]^2 \pi_3 - \left[\left(\frac{\Delta_t}{\Delta_x}\right)^2 \phi^k\right] \pi_2 + \pi_1 = 0. \tag{2.55}$$

The two solutions of equation (2.55) are

$$\left(\frac{\Delta_t}{\Delta_x}\right)^2 \phi^k = \frac{\pi_2 \pm \sqrt{\pi_2^2 - 4\pi_3\pi_1}}{2\pi_3}. \tag{2.56}$$

Taking the more restrictive solution that is associated with the minus sign, and maximizing the function ϕ_k with respect to k [i.e., $\max\{\phi_k\} = (c_1 + c_2)^2$] so that the restriction on Δ_t given Δ_x is as strong as possible, defines the domain where the numerical scheme is always stable (for any η/k_0)

$$\Delta_t \leq \Delta_x \sqrt{\frac{\pi_2 - \sqrt{\pi_2^2 - 4\pi_3\pi_1}}{2(c_1 + c_2)^2 \pi_3}}. \tag{2.57}$$

An asymptotic analysis of the right-hand side, as $(1 + \Phi)F$ goes to infinity, leads to equation (2.53). We also obtain that when $\pi_1 = 0$, the right-hand side is zero, and there is no finite value of Δ_t that results in stability. From equation (2.47), the critical value of $(1+\Phi)F$ at which $\pi_1 = 0$ is given by

$$(1 + \Phi)F_c = \rho_f/\rho. \tag{2.58}$$

For all values of $(1 + \Phi)F \leq \rho_f/\rho$, the algorithm is unconditionally unstable. Another way to see (and say) the same thing is to note that the coefficient $\psi = (1 + \Phi)F - \rho_f/\rho$ present in equations (2.20) and (2.21) must be positive in order for the response to be stable.

Another practical approach to defining the stability is to ask what value of $(1 + \Phi)F$ is required so that the stability criterion is given by

$$\Delta_t \leq \frac{\Delta_x}{(c_1 + c_2)V_p}(1 - \epsilon) \tag{2.59}$$

where $(1 - \epsilon)$ ranges between 0 and 1 and represents the fraction of the Courant stability criterion that one wants to work at. An algebraic manipulation of the right-hand side of equation (2.57) then yields the result

$$\begin{aligned}(1 + \Phi)F_{(1-\epsilon)} &= \frac{1}{1 - (1 - \epsilon)^2} \\ &\times \left(\frac{\rho_f}{\rho} - \frac{M(2\alpha\rho_f - \rho)}{\rho_f(\lambda_u + 2\mu)}(1 - \epsilon)^2 \right. \\ &\left. - \frac{\rho M(\lambda_u + 2\mu - \alpha^2 M)}{\rho_f(\lambda_u + 2\mu)^2}(1 - \epsilon)^4\right).\end{aligned} \tag{2.60}$$

It is again seen that the numerical scheme is never stable (i.e., $\epsilon = 1$) when $(1 + \Phi)F = \rho_f/\rho$. Since typically $\rho_f/\rho \leq 1/2$ for water-saturated materials, and since for all porous materials $(1+\Phi)F \gg 1$ (e.g., the lightly-consolidated clean sand properties in Table 2.1 give

$(1 + \Phi)F \approx 6$), one can conclude that using the physically appropriate value for $(1 + \Phi)F$ guarantees that $(1 + \Phi)F \gg (1 + \Phi)F_c$ so that the classic Courant condition of equation (2.53) applies.

The stability of the scheme in higher dimension (2D and 3D) has not been formally derived. However, from numerical experiments in both 2D and 3D and from analogy with the elastic case, we have numerically verified that dividing the right-hand side of equations (2.53), (2.57), and (2.59) by $\sqrt{d}$, where d is the Euclidean dimension of the modeling, gives the appropriate expressions. The numerical dispersion of the finite-difference scheme associated with the fast P-wave can be investigated by a numerical evaluation of the root r_1 for different wave numbers k. Figure 2.5 shows that the dispersion in our poroelastic algorithm is slightly greater than in the purely elastic scheme of Levander (1988). From numerical experiments, it seems that twenty grid points per wavelength is required to provide great accuracy (much less than 1% of dispersion) in the poroelastic modeling.

2.1.5 Numerical examples

In order to show that the numerical algorithm acts stably and produces the qualitatively expected response, we first give (section 5.1) some numerical snapshots corresponding to the longtitudinal response generated from an isotropic confining-pressure source acting at a point. The material corresponds to a lightly-consolidated clean sand with properties given in Table 2.1. In order to quantify the accuracy of the modeled response, we then numerically compute (section 5.2) the plane-wave attenuation and dispersion for both fast compressional waves and slow waves and compare to the exact analytical results.

2.1.5.1 Some snapshots

Figure 2.6 shows the isotropic point-source response when the center frequency of the source is sufficiently small (10 kHz) that the inertial "form drag" acceleration term in equation (2.6) is much smaller than the usual "viscous drag" Darcy term; i.e., when $\omega \ll \eta/[\rho_f k_o(1 + \Phi)F]$. The upper panel is the bulk (or confining) pressure and the lower panel is the fluid pressure. The wave seen in the snapshot is the Biot fast-P wave and only differs from the usual elastic P wave in that it is attenuated due to viscous flow from the compressed regions to the dilated regions. There is no noticable Biot slow wave seen in the snapshot. At these frequencies, the slow wave is purely diffusive and simply does not show up on the grey-scale used. In contrast, Figure 2.8 shows the response when the center frequency of the same source in the same material is sufficiently high (100 kHz) that the acceleration term in Darcy's law begins to dominate the viscous-drag term. In this case, the slow wave is propagative and is clearly visible in the snapshot along with the usual fast-compressional wave. In a real porous material at these frequencies, the creation of viscous boundary layers would begin to also be important. However, as stated, we have not allowed for the creation of viscous boundary layers in our modeling since the focus is on the seismic band of frequencies.

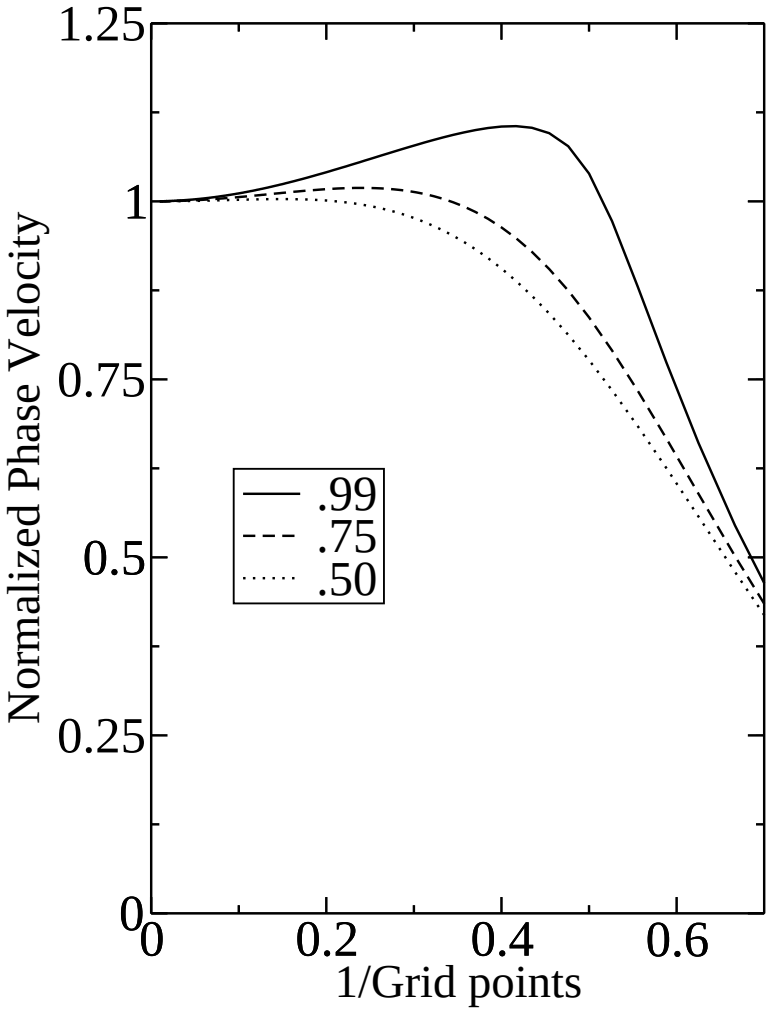

Figure 2.5. Numerical dispersion of the fast P-wave. The horizontal axis is the wavelength divided by the spatial sampling interval (1 over the number of grid points per wavelength). Each curve is obtained for a different time sampling interval, which correspond respectively, to 99%, 75% and 50% of the stability limit.

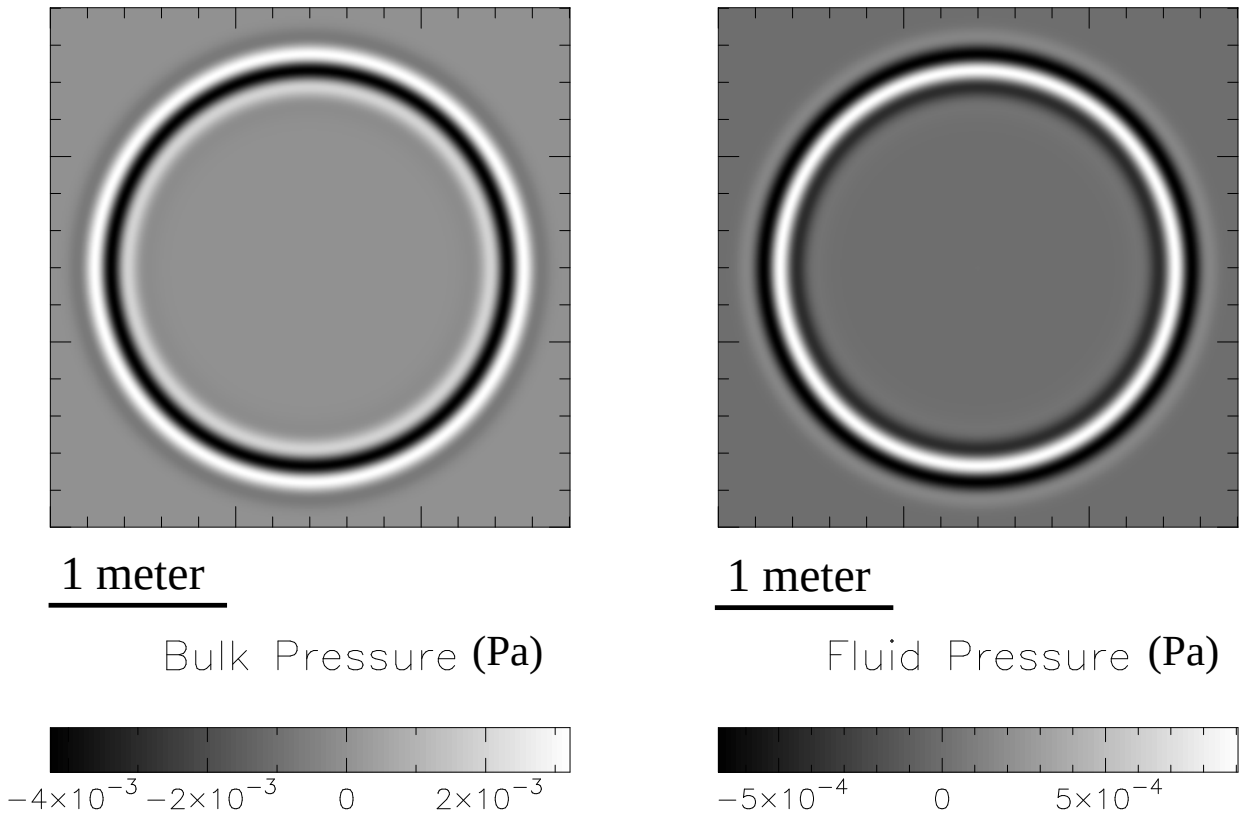

Figure 2.6. Snapshot of the bulk "confining" pressure ($= -(\tau_{xx} + \tau_{zz})/2$) and the fluid pressure for the case of a low-frequency wave (as discussed in the text) propagating in a sandstone. The material properties are given in Table 2.1. Here the central frequency of the source is $f_c = 10$ kHz (see Figure (2.7) to compare this frequency to the Biot relaxation frequency). Here, $\Delta_x = \Delta_z = 7 \times 10^{-3}$m, $\Delta_t = 1.25 \times 10^{-6}$s and the travel time is about 6×10^{-4} s. Only the Biot fast-P wave is seen at this frequency.

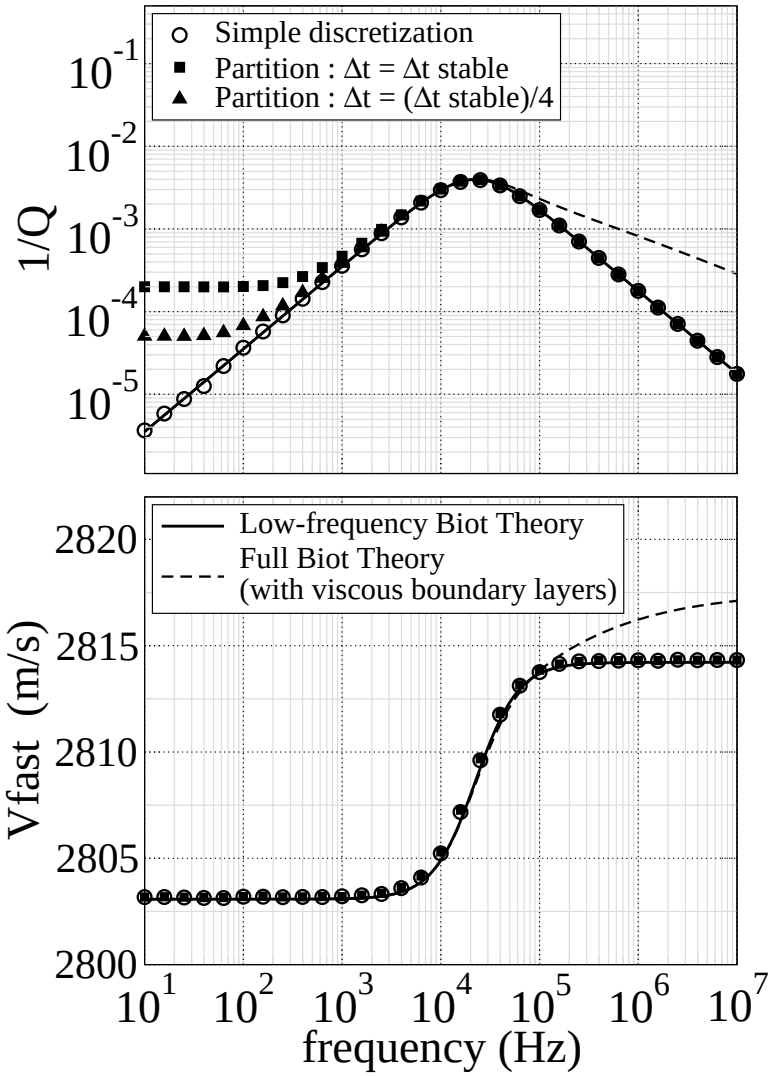

Figure 2.7. Fast wave example: comparison between the numerically measured levels of attenuation and dispersion and the Biot theory for the material given in Table 2.1. The upper panel is the inverse quality factor and the lower panel is the fast-P wave velocity. The solid lines represent the exact analytical attenuation and dispersion when $k(\omega)$ is given by equation (4) [no viscous boundary layers allowed for which is the focus of this study]. The dashed lines are obtained using the $k(\omega)$ of equation (2.2) which accounts for viscous boundary layers. The filled and open squares are the numerical measurements obtained with the partition algorithm for two different time sampling interval (the first one equal to the stability requirement, and the second four times smaller). The circles represent the measurements made with our algorithm presented in Section 3 and sampled at the stability requirement.

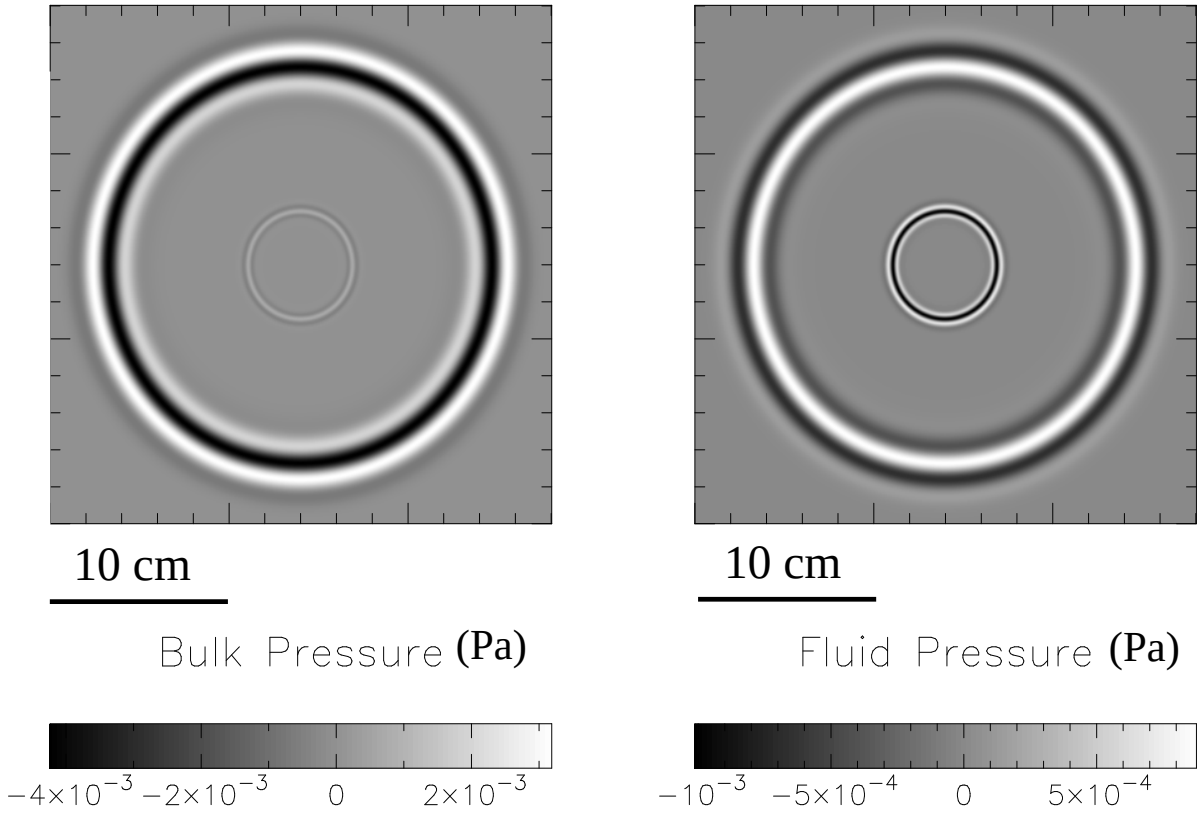

Figure 2.8. Everything is the same as in Figure 2.6 except the central frequency of the source is 10 times higher $f_c = 100$ kHz. The larger circle (fast wave) is the fast P-wave and the smaller one is the Biot slow wave which is no longer a pure diffusion at these frequencies.

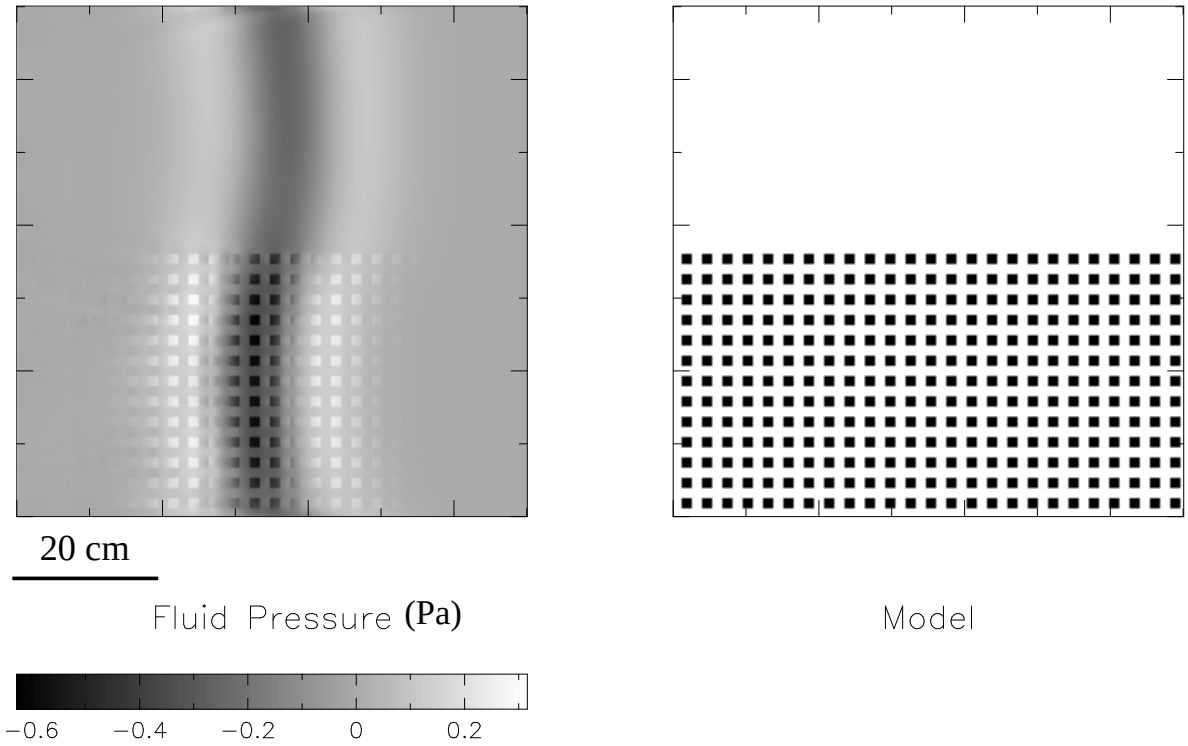

Figure 2.9. Snapshot of the fluid-pressure response for the case of low-frequency (f_c = 10 kHz) plane wave propagating to the right in an heterogeneous material. The upper half space is kept homogeneous as a reference. The bottom half space has small squares of more compliant material embedded within the matrix material of the upper half space. The material properties of the matrix are the ones of Table 2.1 while the square patches have a drained bulk modulus that is 10 times smaller and a permeability that is 1000 times smaller. The upper and lower boundaries maintain periodic boundary conditions which is responsible for the peculiar S-shaped nature of the wavefront.

The amount of attenuation due to the wavelength-scale fluid-pressure equilibration within a fast-P wave propagating through a uniform material (so-called "Biot loss") is well known to be insufficient to explain the amount of attenuation measured both in the field and the laboratory. Recent theory (e.g., Pride and Berryman, 2003 a,b, and Pride et al., 2004), has shown that heterogeneity in the elastic compliance of the framework of grains over scales larger than the grains but smaller than the wavelengths (the so-called "mesoscopic" length scales) generates fluid-pressure gradients over these scales that generate a significant amount of seismic attenuation even at seismic frequencies.

To demonstrate these issues, Figure 2.9 is the snapshot of a 10 kHz "plane wave" generated by a uniform excitation of a plane far to the left of the panel and propagating to the right through a material in which the upper half-space is uniform, and the lower half-space has small heterogeneities of more compliant material embedded within the same material comprising the upper half space. The small squares patches of embedded material are roughly 1/20 the central wavelength. The local pressure gradients created by this heterogeneity are

much stronger and therefore attenuate more wave energy than the wavelength-scale pressure gradient in the upper half-space. The numerical quantification of such attenuation due to wave-induced flow in mesoscopic-scale heterogeneity is the sole focus of a follow-up article.

2.1.5.2 Dispersion and attenuation in a homogeneous material

In order to quantify the accuracy of the finite-difference scheme presented in this paper, we use it to calculate both the speed and amplitude decay (attenuation) of fast and slow compressional plane waves in a homogeneous material having the properties given in Table 2.1. Further, we also calculate the numerical response using a scheme presented by Carcione and Goode (1995) (see also Carcione et al., 2000) that they call the "partition method". We then compare these numerically determined estimates of attenuation and dispersion to the exact analytical results and draw some conclusions.

We first present the Carcione and Goode (1995) partition method. To begin with, equations (2.6) and (2.7) are substituted into each other and written in one dimension (say x) as

$$\frac{\partial q}{\partial t} = \frac{-1}{\rho_f \psi}\left[\frac{\eta}{k_o} q + D_x p + \frac{\rho_f}{\rho} D_x \tau_{xx}\right] \tag{2.61}$$

$$\frac{\partial v}{\partial t} = \frac{1}{\rho \psi}\left[\frac{\eta}{k_o} q + (1+\Phi) F D_x \tau_{xx} + D_x p\right] \tag{2.62}$$

where $\psi = (1+\Phi)F - \rho_f/\rho$ and must be positive as shown earlier. These are simply our equations (2.20) and (2.26). In the partition method, these equations are approximately solved in two steps. First, the stress-gradient terms are dropped relative to the Darcy term, and the resulting equations are solved analytically by time integrating from t to $t + \Delta_t$. In discrete form, given the total response q_l and v_l at time-step l, an intermediate solution q^*_{l+1} and v^*_{l+1} at time-step $l+1$ is obtained as

$$q^*_{l+1} = e^{-\eta \Delta_t/(k_o \rho_f \psi)} q_l \tag{2.63}$$

$$v^*_{l+1} = v_l + \frac{\rho_f}{\rho}\left\{1 - e^{-\eta \Delta_t/(k_o \rho_f \psi)}\right\} q_l. \tag{2.64}$$

The exponentials in equations (2.63) and (2.64) again show explicitly why ψ must be positive to achieve stable response. The full solution is then obtained by adding to this intermediate solution the time integral of the remaining stress-gradient terms

$$q_{l+1} = q^*_{l+1} - \frac{\Delta_t}{\rho_f \psi}\left[(\rho_f/\rho) D_x \tau_{xx} + D_x p\right] \Big|_{m,l+1/2} \tag{2.65}$$

$$v_{l+1} = v^*_{l+1} + \frac{\Delta_t}{\rho \psi}\left[(1+\Phi) F D_x \tau_{xx} + D_x p\right] \Big|_{m,l+1/2}. \tag{2.66}$$

where fourth-order finite-difference approximations are used for the space derivatives. Finally, the stresses and pressure field are updated using equations (2.15)–(2.18) in one dimension. The attenuation and dispersion results presented in Figures 2.7 (fast compres-

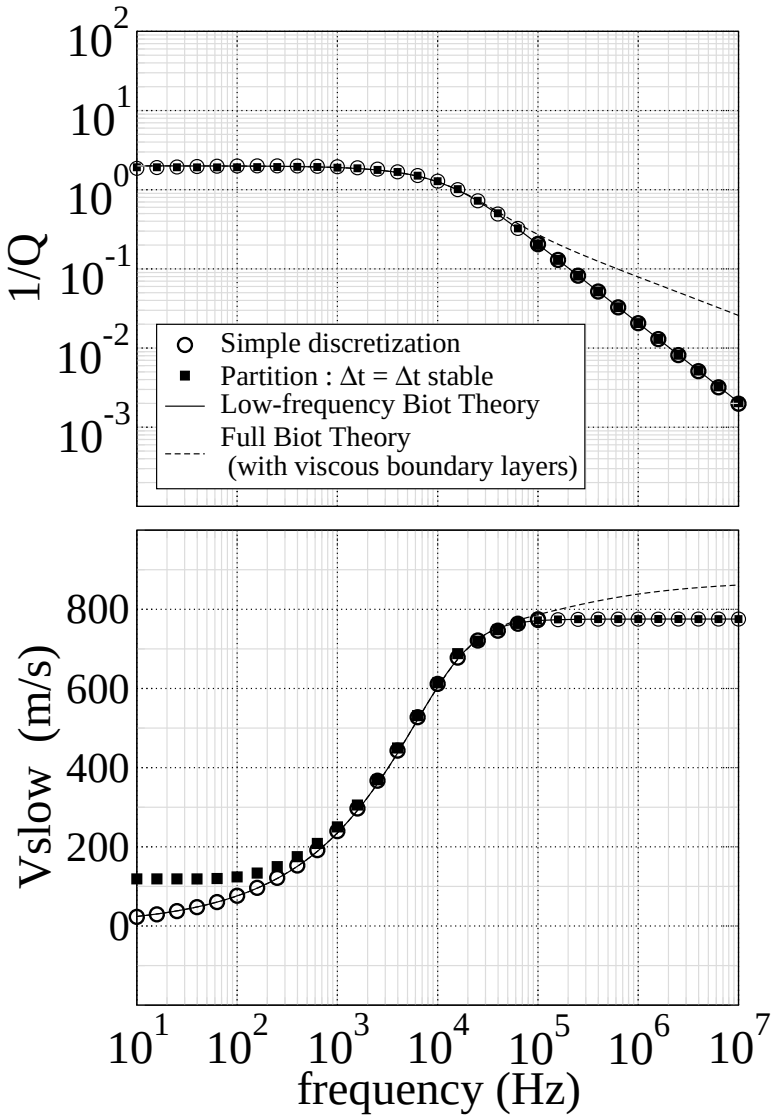

Figure 2.10. Slow wave example: comparison between the numerically measured levels of attenuation and dispersion and the Biot theory for the material given in Table 2.1. The upper panel is the inverse quality factor and the lower panel is the slow-P wave velocity. The solid lines represent the exact analytical attenuation and dispersion when $k(\omega)$ is given by equation (4) [no viscous boundary layers allowed for which is the focus of this study]. The dashed lines are obtained using the $k(\omega)$ of equation (2.2) which accounts for viscous boundary layers. The filled squares are the numerical measurements obtained with the partition algorithm when the time sampling interval is at the stability requirement. The circles represent the measurements made with our algorithm presented in Section 3 and also time sampled at the stability requirement.

sional wave) and 2.10 (slow compressional wave) are obtained using both our explicit finite-difference scheme presented in Section 3 (called "simple discretization" in the figures), and the partition method. For the numerical measurements of the fast wave, we use a solid particle-velocity source and a source time function that is the real part of a Morlet wavelet which has support over a narrow frequency band surrounding the central frequency. For the slow wave generation, we use a Darcy velocity source. Each point (i.e., symbol/marker) in Figures 2.7 and 2.10 corresponds to one numerical experiment and is plotted at the center frequency of the source wavelet spectrum (the frequency having the peak amplitude). The attenuation and velocity measurements have been obtained by time integrating the solid velocity field and measuring the maximum amplitude of the wavelet, and its associated travel time, at different distances form the source. The temporal discretization interval Δ_t was determined, for both of the numerical methods, using the Courant condition of equation (2.53).

The numerical results are compared to the exact analytical solutions for the inverse quality factor Q^{-1} and velocities of the Biot equations (e.g., Pride, 2005). In Figure 2.7, the solid line is the analytical attenuation and dispersion of a fast compressional wave when viscous-boundary layers are neglected (the focus of the present paper), while the dashed line is when viscous-boundary layers are allowed for. Even in the absence of viscous-boundary layer relaxation, there is a relaxation when the fluid pressure between the peaks and troughs of the fast compressional wave just has time to equilibrate in a single wave period. Pride (2005) has shown that the onset of viscous boundary layers and wavelength-scale equilibration occur at roughly the same relaxation frequency. In Figure 2.10, equivalent results are given for the Biot slow compressional wave. In this slow wave example, our simple discretization and the partition method both used the same temporal and spatial discretization interval.

The simple discretization of the present paper does an excellent job of fitting the exact analytical results for both the fast and slow waves. The partition method is less accurate at low frequencies. This error can be reduced by reducing the temporal sampling interval as shown in Figure 2.7; however, at a significant increase in computational cost. Even when the partition method and our explicit-updating scheme use the same Δ_t, there are significantly less floating point operations involved per time step in our scheme.

2.1.6 Conclusion

In summary, we have presented an explicit time-stepping finite-differencing scheme for the low-frequency Biot equations and obtained precise conditions for the scheme to be stable. This is the first time, to our knowledge, that rigorous stability conditions have been derived for the Biot equations. The stability of the scheme is entirely due to the inertial acceleration term in the low-frequency Darcy law. Across the seismic band, this term has a negligible amplitude relative to the usual Darcy frictional resistance; however, its presence is required for the finite-difference updating to be stable. The method is both computationally efficient and accurate. Modeling Biot's equations using explicit time updating presents no inherent stability problems due to the presence of the diffusive fluid-pressure response. It is true that if

the generation of a Biot slow wave at a material-property contrast is to be *accurately* modeled, one must spatially discretize to scales Δ_x smaller than the diffusive skindepth associated with the slow wave. However, the stability condition of the finite-difference updating is still the standard Courant condition given by $\Delta_t \leq \Delta_x/[(c_1 + c_2)V_p]$ for a wide range of material properties that are typical of those in the earth. In future work, we will apply the code to the problem of modeling seismic attenuation and dispersion in media possessing mescoscopic-scale heterogeneity.

2.2 Finite-difference modeling of Biot's poroelastic equations across all frequencies

(Published in GEOPHYSICS,
Y. J. Masson and S. R. Pride, Geophysics, Volume 75, Issue 2, N33, 2010.)

2.2.1 Introduction

In a recent work, Masson et al. (2006) present a simple time-stepping staggered-grid finite-difference scheme for solving Biot's (1956) equations of wave propagation in porous materials. They restrict their analysis to low enough seismic frequencies that the generation of viscous boundary layers in the pores of the rocks can be neglected. For consolidated earth materials such as sandstones, the transition frequency at which viscous-boundary layers first develop is typically greater than 100 kHz so schemes that neglect this physics are valid for most seismic applications. Accordingly, most papers that have presented finite-difference approaches for solving Biot's equations (e.g., Zhu and McMechan, 1991; Carcione and Quiroga-Goode, 1995; Özdenvar and McMechan, 1997; Carcione and Helle, 1999; and Zhang, 1999) have focused on the low-frequency form of the equations.

However, in unconsolidated sediments, the transition frequency at which viscous boundary layers must be accounted for can be as small as 1 kHz (even less). Therefore, for many seismological applications to unconsolidated (or high-permeability) sediments, it is useful to have a finite-difference scheme for solving Biot's equations across the entire band of frequencies. Furthermore, many laboratory experiments on porous materials are conducted at ultrasonic frequencies in which case it is always necessary to account for the development of viscous boundary layers. In poroelastic theory, such pore-scale dynamics is allowed for in the time domain by using a "dynamic permeability" convolution operator in a generalized Darcy law. In the frequency domain, the dynamic permeability corresponds to a complex frequency-dependent permeability coefficient.

Carcione (1996) presents a finite-differencing approach that allows for the dynamic permeability by approximating it as a sum of Zener relaxation functions. It is of interest to

more directly treat the explicit time-domain form of the dynamic-permeability convolution operator using finite differences. To this end, Hanyga and Lu (2005) first convert the convolution integral to an integral over an infinite time domain and then implement a somewhat complicated application of the Gauss-Jacobi and Laguerre quadrature formulae. The present article presents a more direct evaluation of the dynamic-permeability convolution and requires no more memory terms to perform the convolution than it takes to cover the waveform with discretization points in time. Its advantage is thus being both efficient and relatively simple to implement.

Using the classic work of Levander (1988) on the elastodynamic equations as our guide, we present our poroelastic finite-differencing scheme in 2D instead of 3D for reasons of compactness and clarity. Taking the algorithm to 3D involves adding an additional spatial loop within the time loop and writing down the update equations for all of the tensorial components. If readers are interested in a 3D version or our code written in Fortran77, they may contact Yder Masson by email.

2.2.2 Poroelastic response

Poroelasticity not only accounts for the displacements and stresses acting on each voxel of a porous body, but allows for the fluid-pressure changes and fluid flow as well. Implicit in the theory is that the wavelength of a mechanical disturbance moving through a porous material is far greater than the size of the grains making up the material so that a porous-continuum description is justified.

The fluid flow is well modeled using a generalized Darcy's law that allows both for flow due to induced pressure gradients and for flow created by the acceleration of the framework of grains which is the frame of reference for the relative fluid motion. Assuming an $e^{-i\omega t}$ time dependence, the generalized Darcy law is written in the frequency domain as

$$\mathbf{q} = \frac{k(\omega)}{\eta} \left[-\nabla p + i\omega \rho_f \mathbf{v} \right]. \tag{2.67}$$

Here, p is the fluid pressure, $\mathbf{q}$ the Darcy filtration velocity, $\mathbf{v}$ the velocity of the solid framework of grains, η the fluid viscosity, ρ_f the fluid density, and $k(\omega)$ the complex (or "dynamic") permeability.

The frequency dependence in $k(\omega)$ results from the appearance of viscous boundary layers in the pores at sufficiently high frequencies. At low frequencies, the flow in each pore is controlled by viscous shearing and is entirely laminar. At high frequencies, inertial effects begin to dominate the shear forces, resulting in an ideal "plug flow" in each pore except near the fluid/solid interface where shear forces again must dominate since the relative motion is zero on the grain surfaces. There are thus created viscous boundary layers near the grain surfaces whose thickness decrease with increasing frequency as $1/\sqrt{\omega}$.

Johnson et al. (1987) derive a complex permeability function that connects these two frequency limits while obeying causality constraints. Their model for the frequency dependence

of $k(\omega)$ is

$$\frac{k(\omega)}{k_0} = \left[\sqrt{1 - i\frac{\omega}{\Omega}} - i\frac{\omega}{\omega_J}\right]^{-1} \tag{2.68}$$

where the two relaxation frequencies ω_J and Ω are defined

$$\omega_J = \frac{\eta}{\rho_f F k_0} \tag{2.69}$$

$$\Omega = \frac{n_J \omega_J}{4} \tag{2.70}$$

with n_J a dimensionless parameter given by

$$n_J = \frac{\Lambda^2}{F k_o}. \tag{2.71}$$

Here, k_0 is the steady-flow (zero frequency) limit of the permeability, F is the electrical formation factor, and Λ is a weighted pore-volume to grain-surface ratio with the weight emphasizing constricted portions of the porespace [see Johnson et al. (1987) for the precise mathematical definition of Λ] that is also an important length parameter in modeling the surface electrical conductivity in rocks (Pride, 1994). For clean sands, $n_J = 8$ is consistent with both numerical and laboratory experiments. For shaly sands, one can have $n_J \ll 8$. Physically, Ω is the circular frequency at which viscous boundary layers first develop.

We perform the finite-difference modeling in the time domain. Plyushchenkov and Turchaninov (2000) analytically obtain the inverse Fourier transfom of the $k(\omega)$ given by equation 2.68. Using this result, the time-domain version of the generalized Darcy law in equation 2.67 is exactly equivalent to

$$-\nabla p - \rho_f \frac{\partial \mathbf{v}}{\partial t} = \rho_f F \frac{\partial \mathbf{q}}{\partial t} + \frac{\eta}{k_0} \int_0^t \frac{e^{-\Omega(t-s)}}{\sqrt{\pi \Omega (t-s)}} \left[\frac{\partial \mathbf{q}(s)}{\partial s} + \Omega \mathbf{q}(s)\right] ds \tag{2.72}$$

where s is the past time variable. This result is easily confirmed by taking the Fourier transform of equation 2.72 and using the convolution theorem, to obtain equations 1 and 2 (going the other direction is more involved). Upon taking the leading order in $-i\omega$ low-frequency limit in equation 2 and then returning to the time domain, one obtains the low-frequency variant of equation 2.72

$$-\nabla p - \rho_f \frac{\partial \mathbf{v}}{\partial t} = \left(1 + \frac{2}{n_J}\right) \rho_f F \frac{\partial \mathbf{q}}{\partial t} + \frac{\eta}{k_0} \mathbf{q}. \tag{2.73}$$

Our earlier work on how to perform finite-difference modeling of the Biot equations (Masson et al., 2006), was based on the low-frequency law of equation 2.73. The present work deals with the entire frequency range and specifically addresses how to introduce the convolution of equation 2.72 into the scheme.

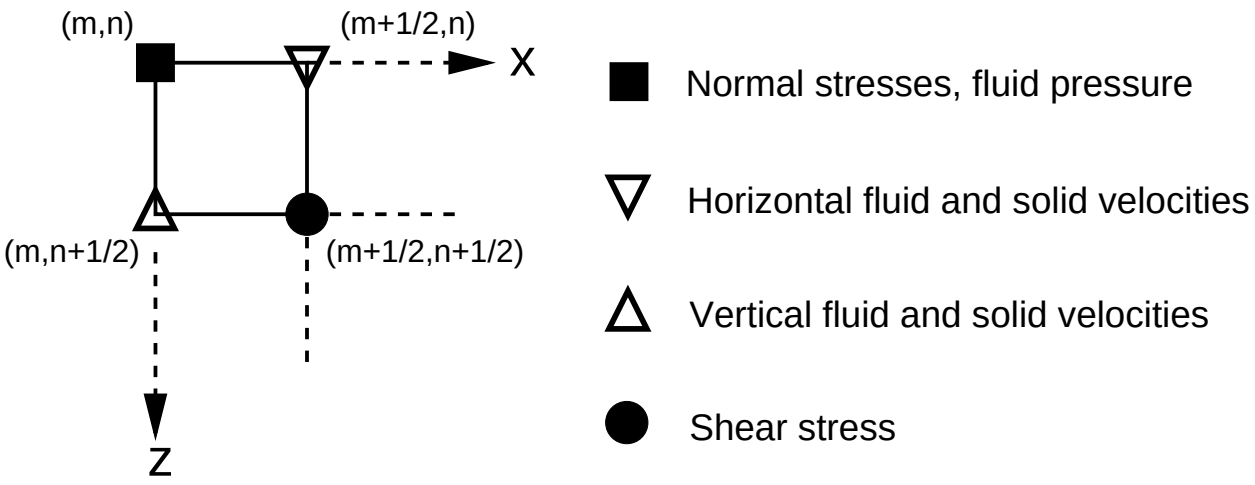

Figure 2.11. Convention used for the spatial position of the stresses, pressure, and fluid and solid velocities on the staggered grid.

The remaining equations of Biot's theory include the total conservation of linear momentum

$$\rho \frac{\partial \mathbf{v}}{\partial t} = \nabla \cdot \tau - \rho_f \frac{\partial \mathbf{q}}{\partial t} \tag{2.74}$$

where ρ is the bulk density of the porous material and $\tau = \tau_{ij} \hat{\mathbf{i}}\hat{\mathbf{j}}$ is the total stress tensor, as well as the stress-strain constitutive laws for an isotropic porous material

$$\frac{\partial \tau}{\partial t} = (\lambda_u \nabla \cdot \mathbf{v} + \alpha M \nabla \cdot \mathbf{q})\, \mathbf{I} + \mu \left[\nabla \mathbf{v} + (\nabla \mathbf{v})^{\mathbf{T}}\right] \tag{2.75}$$

$$-\frac{\partial p}{\partial t} = M\,(\alpha \nabla \cdot \mathbf{v} + \nabla \cdot \mathbf{q}) \tag{2.76}$$

with $\mathbf{I} = \delta_{ij} \hat{\mathbf{i}}\hat{\mathbf{j}}$ the identity tensor. The poroelastic constants used here are the undrained Lamé modulus λ_u, the shear modulus μ (the same for both drained and undrained conditions), the so-called Biot-Willis (1957) constant α, and the fluid-storage coefficient M. Modeling suggestions and further discussion of these poroelastic constants are given in many places including Masson et al. (2006) and Pride (2005).

2.2.3 Finite-differencing scheme

The time-stepping finite-difference scheme of Masson et al. (2006) for solving the low-frequency Biot (1956) equations is quite similar to Levander's (1988) two-dimensional (2D) fourth-order velocity-stress staggered-grid method for the elastodynamic equations. Levander's (1988) scheme built on the velocity-stress staggered-grid modeling of Madariaga (1976) and Virieux (1986). The present work adopts the 2D velocity-stress staggered grid defined in Figure 2.11. The stress components τ_{xx}, τ_{zz}, and p are assigned to the grid points

$x = m\Delta_x, z = n\Delta_z$ where m and n are integers; the horizontal velocities v_x and q_x to the points $x = (m+1/2)\Delta_x, z = n\Delta_z$; the vertical velocities v_z and q_z to the points $x = m\Delta_x, z = (n+1/2)\Delta_z$; and the shear stress τ_{xz} to the points $x = (m+1/2)\Delta_x, z = (n+1/2)\Delta_z$. Further, all the velocities are temporally discretized at the time points $t = l\Delta_t$, while all the stresses are discretized at the time points $t = (l+1/2)\Delta_t$.

Any order of differencing approximation may be employed for the first-space derivative operators D_x and D_z and the first-time derivative D_t in what follows. However the stability analysis and numerical implementation of the present paper uses the second-order time derivative and fourth-order space operator given by

$$\begin{aligned} D_x v_x \Big|_{m,n} &= \frac{1}{\Delta_x} \{c_1 [v_x(m+1/2,n) - v_x(m-1/2,n)] \\ &- c_2 [v_x(m+3/2,n) - v_x(m-3/2,n)]\}, \end{aligned} \tag{2.77}$$

with $c_1 = 9/8$ and $c_2 = 1/24$ the fourth-order differencing weights.

2.2.3.1 Update equations for stresses and pressure

Knowing q_i, v_i at time $t = l\Delta_t$ and τ_{ij}, p at time $t = (l-1/2)\Delta_t$, the discrete form of the constitutive laws 2.75 and 2.76 are used to update τ_{ij} and p at time $t = (l+1/2)\Delta_t$

$$\begin{aligned} D_t \tau_{xx} &= (\lambda_u + 2\mu) D_x v_x + \lambda_u D_z v_z \\ &\quad + \alpha M (D_x q_x + D_z q_z) \Big|_{m,n,l} \end{aligned} \tag{2.78}$$

$$\begin{aligned} D_t \tau_{zz} &= \lambda_u D_x v_x + (\lambda_u + 2\mu) D_z v_z \\ &\quad + \alpha M (D_x q_x + D_z q_z) \Big|_{m,n,l} \end{aligned} \tag{2.79}$$

$$D_t \tau_{xz} = \mu (D_x v_z + D_z v_x) \Big|_{m+\frac{1}{2},n+\frac{1}{2},l} \tag{2.80}$$

$$\begin{aligned} D_t p &= -\alpha M (D_x v_x + D_z v_z) \\ &\quad + M (D_x q_x + D_z q_z) \Big|_{m,n,l} \end{aligned} \tag{2.81}$$

where D_t, D_x, and D_z denote finite-difference derivatives and where the vertical line at the right of each equation denotes the space and time position at which the terms in the equations are all centered.

2.2.3.2 Update equations for the Darcy velocity

To treat the convolution in equation 2.72, the integration domain is broken into a finite number $N+1$ of past time intervals. The number N can be chosen so that $e^{-\Omega N \Delta_t} < \epsilon$ or

$$N = -\frac{\ln \epsilon}{\Omega \Delta_t} \tag{2.82}$$

where ϵ is a small number like 10^{-3} that determines the accuracy. To perform the integrations, we assume that within each of the past finite-difference time intervals Δ_t, the Darcy velocity is continuously varying as a linear function. As Figure 2.12 indicates, the first time interval is half of Δ_t, while the remaining $j = 1, N$ intervals are each of duration Δ_t. We have

$$\begin{aligned} I(t) &= \int_0^t ds \, \frac{e^{-\Omega(t-s)}}{\sqrt{\pi \Omega (t-s)}} \left[\frac{\partial q(s)}{\partial s} + \Omega q(s) \right] \qquad (2.83) \\ &\approx \int_{t-\Delta_t/2}^t ds \, \frac{e^{-\Omega(t-s)}}{\sqrt{\pi \Omega (t-s)}} \\ &\quad \times \left\{ \frac{\partial q}{\partial t} + \Omega \left[q(t) + (s-t) \frac{\partial q}{\partial t} \right] \right\} \\ &\quad + \sum_{j=1}^{N} \int_{t-j\Delta_t-\Delta_t/2}^{t-j\Delta_t+\Delta_t/2} ds \, \frac{e^{-\Omega(t-s)}}{\sqrt{\pi \Omega (t-s)}} \\ &\quad \times \left\{ \left. \frac{\partial q}{\partial s} \right|_{t-j\Delta_t} + \Omega \left[\left. q \right|_{t-j\Delta_t} + (s-t+j\Delta_t) \left. \frac{\partial q}{\partial s} \right|_{t-j\Delta_t} \right] \right\} \qquad (2.84) \end{aligned}$$

In the final line of equation 2.84, both $q(s)$ and its time derivative $\partial q(s)/\partial s$ are being evaluated at the time $s = t - j\Delta_t$ in the center of each interval j and are therefore constants in each interval that can be taken outside the integrals. For N sufficiently large, the only approximation in passing from equation 2.83 to 2.84 is taking the Darcy velocity as linearly varying in each time interval Δ_t.

If the current finite-difference time index for the Darcy velocity is l, the current time in the convolution integral of equation 2.84 is $t = (l + 1/2)\Delta_t$. Upon making the substitution of variables $u = \Omega(t-s)$ in the above integrals, the discrete form of equation 2.84 can be written

$$\begin{aligned} I(l+\frac{1}{2}) &= \frac{(G_o - H_o)}{\Omega} D_t q + G_o \langle q \rangle \\ &\quad + \sum_{j=1}^{N} \left\{ \frac{[(1+j\Omega\Delta_t)G_j - H_j]}{\Omega} D_t q + G_j \langle q \rangle \right\} \Bigg|_{l+\frac{1}{2}-j} \qquad (2.85) \end{aligned}$$

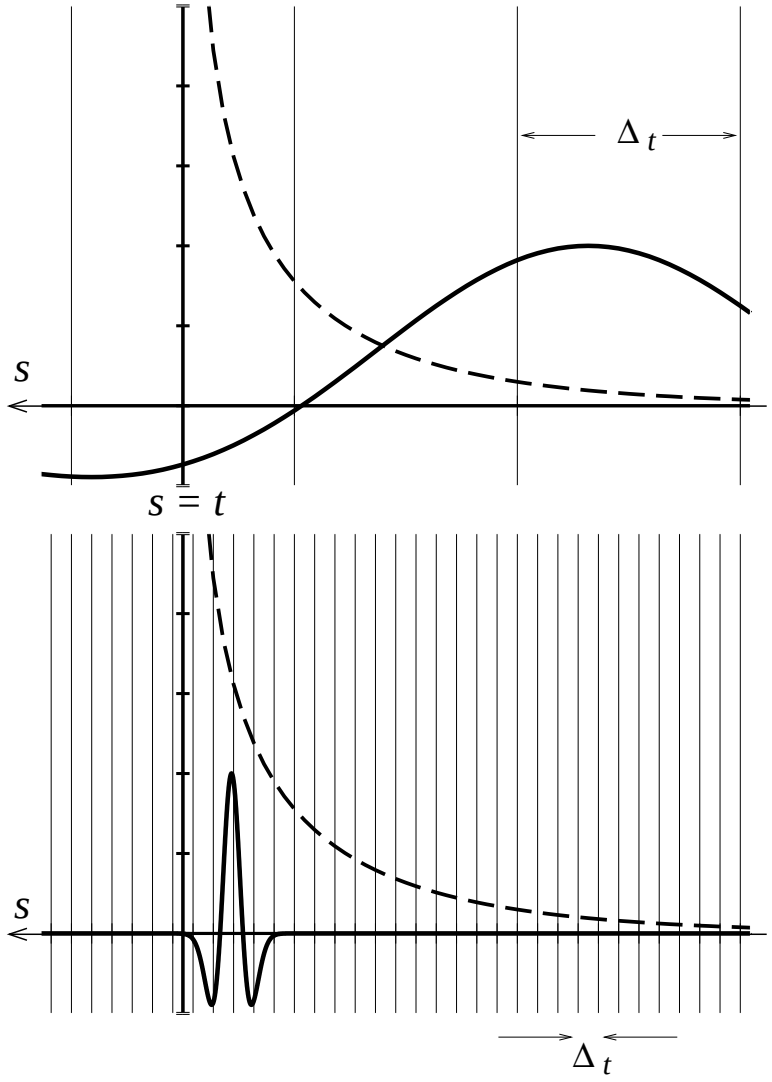

Figure 2.12. Schematic of the kernel of the convolution integral (dashed-line curves, normalized to be unitless) and Darcy flow (solid curves, normalized to be unitless) as a function of the convolution time variable s. The upper panel corresponds to seismic frequencies that are smaller than the viscous-boundary-layer transition ($\Omega\Delta_t > 1$). The lower panel corresponds to a seismic frequencies that are larger than the viscous-boundary-layer transition ($\Omega\Delta_t < 1$). Present time corresponds to $s = t$ where the kernel has an integrable singularity.

where the coefficients G_o, H_o, G_j, and H_j are defined

$$G_o = \int_0^{\Omega\Delta_t/2} \frac{e^{-u}}{\sqrt{\pi u}}\, du \tag{2.86}$$

$$G_j = \int_{(j-1/2)\Omega\Delta_t}^{(j+1/2)\Omega\Delta_t} \frac{e^{-u}}{\sqrt{\pi u}}\, du \tag{2.87}$$

$$H_o = \int_0^{\Omega\Delta_t/2} e^{-u}\sqrt{\frac{u}{\pi}}\, du \tag{2.88}$$

$$H_j = \int_{(j-1/2)\Omega\Delta_t}^{(j+1/2)\Omega\Delta_t} e^{-u}\sqrt{\frac{u}{\pi}}\, du \tag{2.89}$$

and where the 2nd order discrete time derivative $D_t q$ and the average $\langle q \rangle$ when centered at $l + 1/2$ are defined

$$D_t q = \frac{q(l+1) - q(l)}{\Delta_t} \tag{2.90}$$

$$\langle q \rangle = \frac{q(l+1) + q(l)}{2}. \tag{2.91}$$

The coefficients G_o, H_o, G_j, and H_j in equations 2.86–2.89 only depend on the material property Ω and the time interval Δ_t. They can be computed ahead of time using any favorite integral solver. For finite limits on the integrals, they cannot be computed analytically. However, in the limit that $\Omega\Delta_t \gg 1$, which would correspond to the low-frequency seismic limit for wave propagation applications, we have the analytical results that $G_o = 1$, $H_o = 1/2$, and $G_j = H_j = 0$.

Using these results for the convolution, and inserting the discrete form of equation 2.74 into the discrete form of equation 2.72 gives the update equations for determining $q_i(l+1)$

$$\left[\psi + \frac{\eta}{k_0}\frac{(G_o - H_o)}{\Omega}\right] D_t q_x + \frac{\eta}{k_0} G_o \langle q_x \rangle = \\ -\frac{\eta}{k_0} S_x - D_x p - \frac{\rho_f}{\rho}(D_x \tau_{xx} + D_z \tau_{xz}) \Big|_{m+\frac{1}{2},n,l+\frac{1}{2}} \tag{2.92}$$

$$\left[\psi + \frac{\eta}{k_0}\frac{(G_o - H_o)}{\Omega}\right] D_t q_z + \frac{\eta}{k_0} G_o \langle q_z \rangle = \\ -\frac{\eta}{k_0} S_z - D_z p - \frac{\rho_f}{\rho}(D_z \tau_{zz} + D_x \tau_{xz}) \Big|_{m,n+\frac{1}{2},l+\frac{1}{2}}. \tag{2.93}$$

Here, the parameter ψ is defined

$$\psi = \rho_f F - \frac{\rho_f^2}{\rho}, \tag{2.94}$$

while S_x and S_z are defined

$$S_x = \sum_{j=1}^{N} \left\{ \frac{[(1+j\Delta_t\Omega)G_j - H_j]}{\Omega} D_t q_x + G_j \langle q_x \rangle \right\} \Big|_{m+\frac{1}{2},n,l+\frac{1}{2}-j} \quad (2.95)$$

$$S_z = \sum_{j=1}^{N} \left\{ \frac{[(1+j\Delta_t\Omega)G_j - H_j]}{\Omega} D_t q_z + G_j \langle q_z \rangle \right\} \Big|_{m+\frac{1}{2},n,l+\frac{1}{2}-j} \quad (2.96)$$

and are the contributions to the convolution that come from the N time steps that precede the first half time step. The dominant contribution to the convolution comes from the first half time step and is allowed for on the left hand side of equations 2.92 and 2.93 by the terms involving G_o and H_o.

In the limit of low seismic frequencies, or, more specifically, when $\Omega\Delta_t/2 \gg 1$, we have $S_x = S_z = 0$, $G_o = 1$, and $H_o = 1/2$ and it is easily verfied that equations 2.92 and 2.93 exactly reduce to the low-frequency form of equation 2.73. In this limit, the kernel of the convolution is concentrated in the first half time interval of past time and effectively acts as a Dirac delta function so that no memory terms need be kept (i.e., $N = 0$).

As seismic frequencies increase, $\Omega\Delta_t$ decreases and more memory terms must be stored in order to accurately compute the convolution as the simple rule $N = -\ln\epsilon/(\Omega\Delta_t)$ suggests. However, once $\Omega\Delta_t < 1$, it is not necessary to keep increasing the number of memory terms indefinitely. In such a high-frequency limit, the lower panel of Figure 2.12 illustrates how the seismic wavelet becomes more concentrated in time relative to the extent of the kernel. The convolution is important in this limit only when the wavelet is close to the present time so one need only keep enough memory terms to cover the temporal extent of the wavelet. Accordingly, for central wave frequencies ω that satisfy $\omega > \Omega$ (the "high frequency" domain), one need only keep $N = -\ln\epsilon/(\omega\Delta_t)$ past time points to obtain accurate results for the convolution. In practice, we never need to keep more than roughly 20 terms in memory.

2.2.3.3 Update equations for the particle velocity

Finally, knowing τ_{ij}, p, and $D_t q_i$ at time $t = (l+1/2)\Delta_t$ and v_i at time $t = l\Delta_t$, v_i is updated at time $t = (l+1)\Delta_t$ by inserting equation 2.72 into equation 2.74 to obtain

$$\rho D_t v_x = D_x\tau_{xx} + D_z\tau_{xz} - \rho_f D_t q_x \,|_{m+\frac{1}{2},n,l+\frac{1}{2}} \quad (2.97)$$

$$\rho D_t v_z = D_x\tau_{xz} + D_z\tau_{zz} - \rho_f D_t q_z \,|_{m,n+\frac{1}{2},l+\frac{1}{2}} \,. \quad (2.98)$$

Equations 2.78–2.98 provide our finite-difference modeling algorithm.

2.2.4 Stability

In order to investigate the stability of the numerical scheme, we first perform a von Neumann stability analysis in the case where the convolution product in equations 2.92–2.93

is entirely neglected; i.e., an analysis assuming $\eta/k_0 = 0$. Then the effects of the remaining parameters on the stability ($\eta/k_0 \neq 0$ and $N \neq 0$) are tested numerically. It is demonstrated that stability is always achieved using the criterion in which η/k_0 is neglected. In passing, we note that in our earlier paper (Masson et al., 2006), we performed a more complicated version of the analysis assuming that $\eta/k_o \neq 0$.

To keep the analytical treatment tractable, we consider a plane longitudinal disturbance advancing in the x direction through a homogeneous material (i.e., q_z, v_z, τ_{zz}, and τ_{xz} are all set to zero along with all spatial derivatives with respect to z). To investigate stability in higher dimensions, we perform purely numerical tests to establish a criterion (see the discussion at the end of this discussion). Displacements u_x and w_x are introduced through the defining relations

$$v_x = D_t u_x \tag{2.99}$$

$$q_x = D_t w_x. \tag{2.100}$$

In this case, the set of difference equations 2.78–2.98 can be combined into the matrix system

$$Qu = 0 \tag{2.101}$$

where the 2×2 matrix operator Q is given by

$$Q = \left[\begin{array}{c|c} (\lambda_u + 2\mu)D_{xx} - \rho D_{tt} & \alpha M D_{xx} - \rho_f D_{tt} \\ \hline \alpha M D_{xx} - \rho_f D_{tt} & M D_{xx} - \rho_f F D_{tt} \end{array} \right] \tag{2.102}$$

and

$$u = [u_x, w_x]^T. \tag{2.103}$$

Here, D_{xx} and D_{tt} are the finite second-derivative operators in space (fourth order) and time (second order) respectively.

The von Neumann stability analysis assumes that the independent solutions of equation 2.101 are of the form

$$\left[\begin{array}{c} u_x(m,l) \\ w_x(m,l) \end{array} \right] = e^{ikm\Delta_x - i\omega\Delta_t} \left[\begin{array}{c} u_o \\ w_o \end{array} \right] \tag{2.104}$$

where k is a real spatial wave number. In this context, testing the stability of the numerical scheme is equivalent to testing the hypothesis

$$\mathrm{Im}\{\omega\} \leq 0 \ \forall \ k. \tag{2.105}$$

If equation 2.105 is true, then the scheme is stable.

An expression for the stability criterion is obtained by requiring the determinant of the linear system to vanish; i.e.,

$$\det|Qe^{ikm\Delta_x - i\omega\Delta_t}| = 0. \tag{2.106}$$

The two roots of equation 2.106 are

$$D_{xx}e^{ikm\Delta_x - i\omega\Delta_t} = \frac{\pi_2 \pm \sqrt{\pi_2^2 - 4\pi_3\pi_1}}{2\pi_3} D_{tt}e^{ikm\Delta_x - i\omega\Delta_t} \tag{2.107}$$

where the π_i coefficients are defined as

$$\begin{aligned}
\pi_1 &= \rho_f \rho (F - \rho_f/\rho) && (2.108)\\
\pi_2 &= \rho_f F(\lambda_u + 2\mu) + \rho M - 2\alpha M \rho_f && (2.109)\\
\pi_3 &= M(\lambda_u + 2\mu - \alpha^2 M). && (2.110)
\end{aligned}$$

It is easily established that the second-order finite-difference time derivatives yield

$$D_{tt} e^{ikm\Delta_x - i\omega\Delta_t} = -\frac{4}{\Delta_t^2} \sin^2\left(\frac{\omega\Delta t}{2}\right) e^{ikm\Delta_x - i\omega\Delta_t} \tag{2.111}$$

while the fourth-order finite-difference space derivatives give

$$D_{xx} e^{ikm\Delta_x - i\omega\Delta_t} = -\frac{4\phi_k}{\Delta_x^2} e^{ikm\Delta_x - i\omega\Delta_t} \tag{2.112}$$

with the periodic function ϕ_k given by

$$\begin{aligned}
\phi_k &= \left\{ c_1^2 + 2c_1c_2 \left[1 - 4\cos^2\left(\frac{k\Delta_x}{2}\right)\right]\right\} \sin^2\left(\frac{k\Delta_x}{2}\right)\\
&\quad + c_2^2 \sin^2\left(\frac{3k\Delta_x}{2}\right). && (2.113)
\end{aligned}$$

Again, $c_1 = 9/8$ and $c_2 = 1/24$ are the fourth-order differencing weights.

The stability criterion is established by inserting equations 2.111–2.112 into equation 2.107, and requiring that ω be real (i.e., $\mathrm{Im}\{\omega\} = 0$). Taking the more restrictive solution that is associated with the minus sign in equation 2.107, and using the maximum of the function ϕ_k with respect to k [i.e., $\max\{\phi_k\} = (c_1 + c_2)^2$] so that the restriction on Δ_t given Δ_x is as strong as possible, defines the domain where the numerical scheme is stable when $\eta/k_0 = 0$

$$\Delta_t \le \Delta_x \sqrt{\frac{\pi_2 - \sqrt{\pi_2^2 - 4\pi_3\pi_1}}{2(c_1 + c_2)^2 \pi_3}}. \tag{2.114}$$

For all values of $F \le \rho_f/\rho$, the algorithm is unconditionally unstable. Another way to see (and say) the same thing is to note that the coefficient $\psi = F - \rho_f/\rho$ present in equations 2.92 and 2.93 must be positive in order for the response to be stable.

Finally, an asymptotic analysis of the right-hand side of equation 2.114 as the parameter F becomes large results in the linear relation between Δ_x and Δ_t asymptoting to the classic Courant condition that, in one dimension, is given by

$$\Delta_t \le \frac{\Delta_x}{(c_1 + c_2) V_p}. \tag{2.115}$$

Here, V_p is the velocity associated with the undrained fast P-wave

$$V_p = \sqrt{\frac{\lambda_u + 2\mu}{\rho}}. \tag{2.116}$$

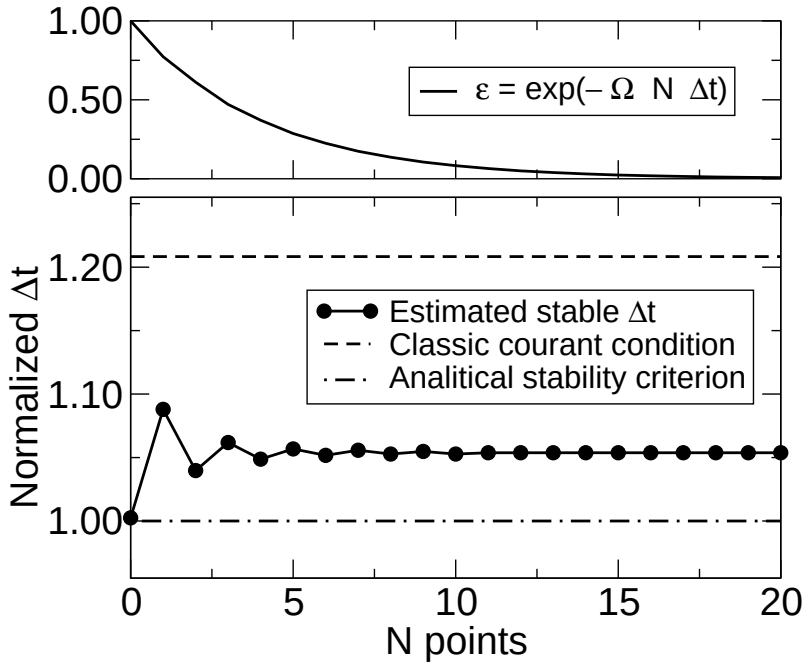

Figure 2.13. Evolution of the numerical stability of the scheme as a function of the number N of memory variables used in equations 2.92–2.93. Top panel: percentage of the integral in equation 2.85 contained in the first N terms of the sum. Bottom panel: stability criterion plotted as a function of the number of memory variables N with $\eta/k_0 = \text{const}$. When N equals zero, the stability criterion is equal to the analytical criterion in equation 2.114. When adding more memory variables, the stability criterion converges toward a plateau somwhere between the analytical criterion and the classic Courant value. Note that using an odd number of memory variable tends to stabilize the numerical scheme.

For typical values of F in rocks, the stability requirement of equation 2.115 always applies. We now test the effect of having a non-zero value for η/k_0 and account for any number N of memory terms in equations 2.92–2.93. This true stability criterion is obtained by numerically implementing the full scheme for different values of Δt and verifying stability for each Δ_t. In Figure 2.13, we show the effect of adding more memory terms to equations 2.92–2.93 for a given value of η/k_0. When no memory terms are used, the stability citerion is the one in equation 2.114. Adding more memory terms tends to improve the stability until it reaches a plateau value somewhere between the analytical criterion in equation 2.114 and the classic Courant condition in equation 2.115. Note that the plateau is reached when N is given by equation 2.82 and the convolution is being properly computed.

To see why allowing for the convolution makes the scheme even more stable (i.e., allows a larger time step to be used) compared to the most restrictive condition of equation 2.114, one need only consider the coefficient multiplying the time derivative of the Darcy velocity in equations 2.92–2.93 that we may call the "effective fluid inertia" and given by $\psi + (G_o - H_o)\eta/k_o$. The convolution coefficients G_o and H_o (note that $G_o > H_o$) are adding to ψ to make the effective inertia even larger than when the convolution and η/k_o were neglected. Indeed, the more general condition for the scheme to be stable is that

$$\psi > -\frac{\eta}{k_o}\frac{(G_o - H_o)}{\Omega} \tag{2.117}$$

which is more strongly satisfied than the condition $\psi > 0$ associated with equation 2.114. Earth materials always have $\psi > 0$ so this condition is always met. In Figure 2.14, we present the behavior of the stability criterion as a function of η/k_0. The most important result is that the stability criterion is strictly increasing with η/k_0 (for the same reason that the effective fluid inertia is increasing with increasing η/k_o), which means that the criterion of equation 2.114 holds true for any value of η/k_0. The true stability limit for Δ_t is seen to lie somewhere between the criteria given by equations 2.114 and 2.115.

Last, we have performed numerical tests of stability in both 2D and 3D versions of the scheme and have emperically determined that dividing the right-hand side of equation 2.114 by $\sqrt{d}$ where d is the Eucledian dimension of the modeling domain, gives an appropriate criterion. This is also the result for staggered-grid implementation of the elastodynamic equations (Virieux and Madariaga, 1982).

2.2.5 Numerical examples

In this section, we first present some numerical snapshots of the fields to demonstrate that the scheme produces qualitatively reasonable (expected) results. We then go on to demonstrate the accuracy of the scheme by comparing numerical results for the velocity dispersion and attenuation to exact analytical results.

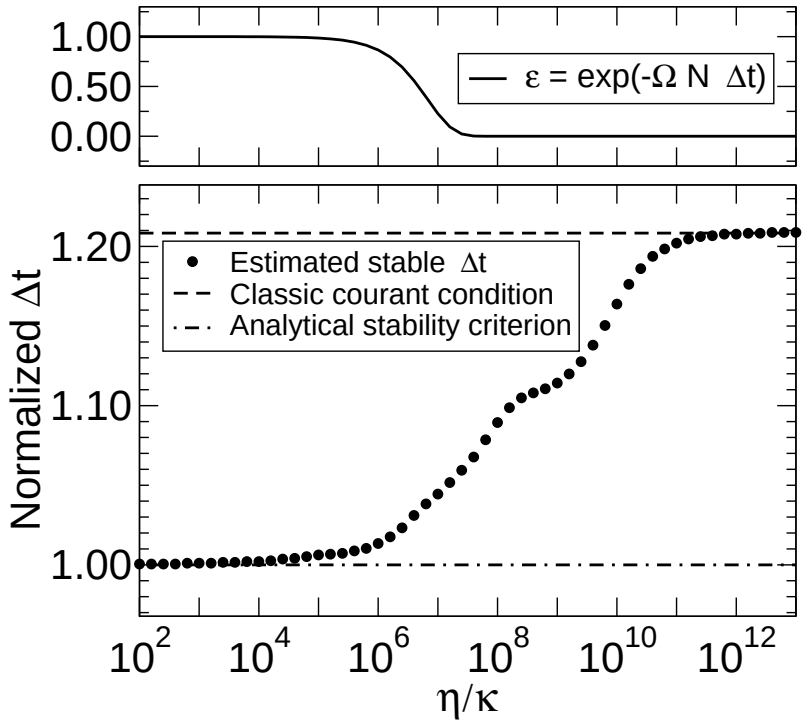

Figure 2.14. Numerical determination of the stability criterion ploted as a function of η/k_0. The estimate is made by varying Δt for a given value of η/k_0 and keeping the others parameters fixed. Below the black dots, the scheme is stable, while above the black dots, it is unstable. The key result is that the stability criterion is bounded between the classic Courant condition of equation 2.115 as $\eta/k_0 \to 0$ and the analytical criterion of equation (2.114) as $\eta/k_0 \to \infty$. The specific shape of the black dotted curve can vary somewhat depending on the values of the other parameters; however, it always stays between the upper and lower limits just mentioned.

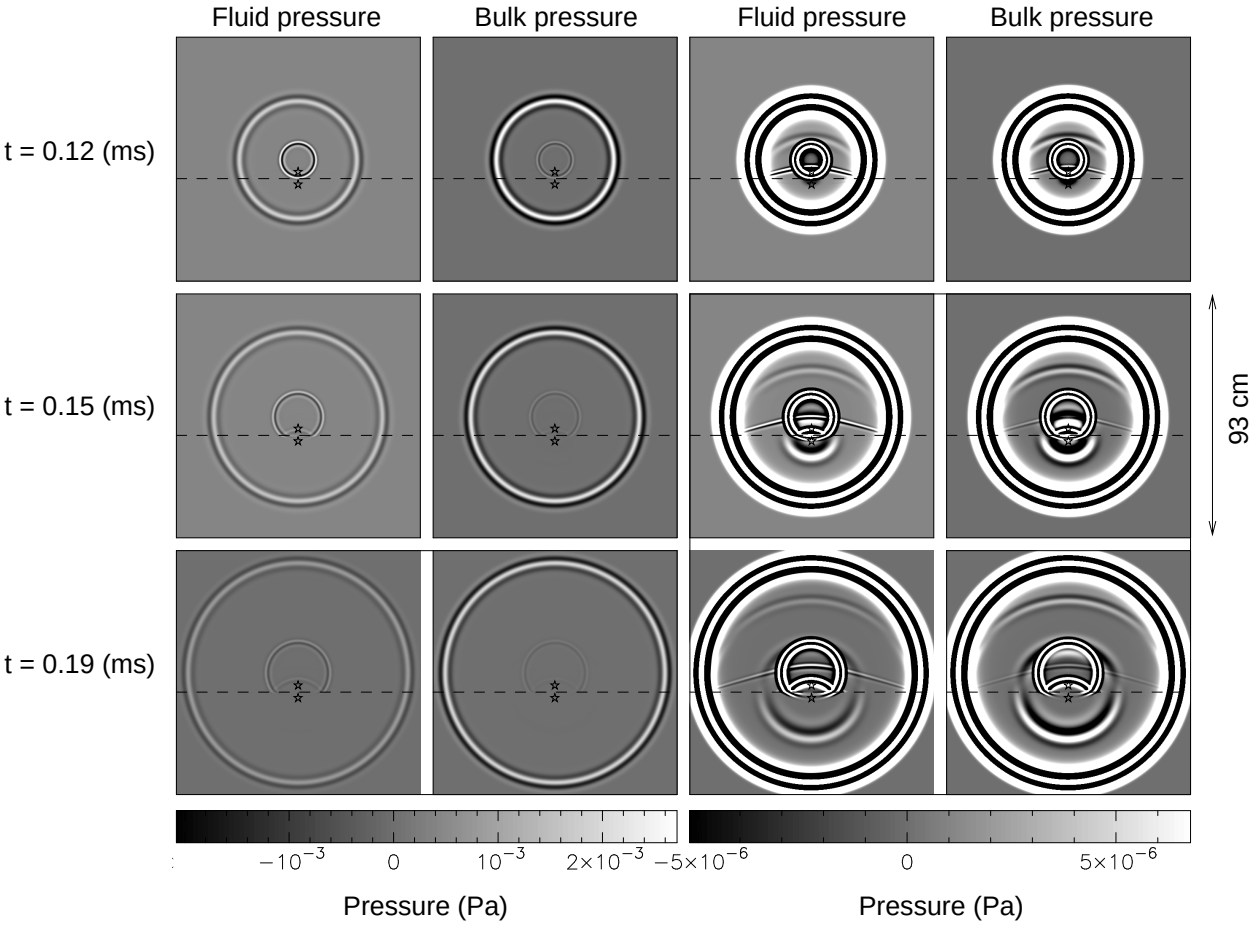

Figure 2.15. Snapshots of the fluid pressure (first and third columns) and bulk pressure (second and fourth columns) for a point source at the center generating a 50 kHz central frequency compressional pulse. The two columns on the left are plotted at full scale, while the columns on the right are plotted with a saturated scale that allows the fine details of the slow waves to be observed. In this example, all material properties except permeability are uniform throughout. Above the dashed line, $k_0 = 2 \times 10^{-11}$ m^2 (20 Darcy), the relaxation frequency is 1.1 kHz, and the wave propagation is thus in the high-frequency regime where the slow wave is propagatory. Below the dashed line, $k_0 = 2{\times}10^{-13}$ m^2 (0.2 Darcy), the relaxation frequency is 110 kHz, and the wave propagation is in the low-frequency regime where the slow wave is purely diffusive. The various waves are the primary or reflected/transmitted fast and slow waves. The stars indicate the positions where waveforms are recorded (see Figure 2.16).

2.2.5.1 Snapshots

We now consider a modeling example that requires the complete convolution form of the dynamic-permeability operator.

Consider the situation depicted in Figure 2.15 involving a compressional point source that sends out both fast and slow compressional waves. The center frequency of the compressional pulse is 50 kHz. The dimensions of the numerical modeling domain (roughly 1 m to each side) and the frequency of the source are typical of some laboratory experiments on ocean sediments performed by Hefner and Williams (2006) and of the underwater field experiments on ocean sediments performed by Williams et al. (2002). To obtain non-trivial results involving the reflection and transmission of both fast and slow waves, we introduce a permeability interface below the source point (denoted with a horizontal dashed line in the figure) while keeping all other material properties uniform throughout the modeled region. Above the interface, the permeability is $k_0 = 20$ Darcy while below it is 0.2 Darcy. This results in the Biot relaxation frequency being 1.1 kHz above the interface and 110 kHz below. Thus, for waves above the interface, the 50 kHz pulse is in the high-frequency domain where the slow wave is propagatory, while below the interface, the pulse is in the low-frequency domain where the slow wave is purely diffusive. Columns (a) and (b) in the figure are plotted using the full scale of the pressure pulses, while columns (c) and (d) are plotted using a saturated scale that allows the smaller amplitude details of the slow waves to be observed.

When the direct fast P wave arrives at the permeability interface, most of its energy is transmitted downward; however, there is observed as well a very weak reflected P wave and a somewhat stronger reflected slow wave. When the direct slow wave arrives at the interface, there are generated weakly transmitted and reflected fast P waves as well as a strongly reflected slow wave. The slow wave that is transmitted is a pure diffusion. There are no shear waves generated at the source. The shear waves generated by compressional pulses at a contrast in permeability are much smaller in energetic amplitude than the various compressional pulses and are not observed in the present plots because a shear wave propagates with no change in either fluid or bulk pressure.

Since the interface separates wave propagation in the low- and high-frequency regimes, proper modeling of the slow wave amplitudes in this example requires the inclusion of the convolution integral involving the Darcy flow. If only the low-frequency form of the generalized Darcy law (equation 2.73) is used as opposed to the complete convolution of the present example, the amplitudes of the slow waves are far too large as is seen in the traces of Figure 2.16. In this figure, the column to the left corresponds to a receiver located just above the interface (denoted with a star in Figure 2.15), while the column to the right corresponds to a receiver just below the interface. The reason the low-frequency equations predict a slow wave recorded at the lower receiver with such a large amplitude is because as the slow wave passed from the source to the interface, the attenuation was being greatly underestimated. This example demonstrates the importance of using the complete theory involving the dynamic-permeability convoltion.

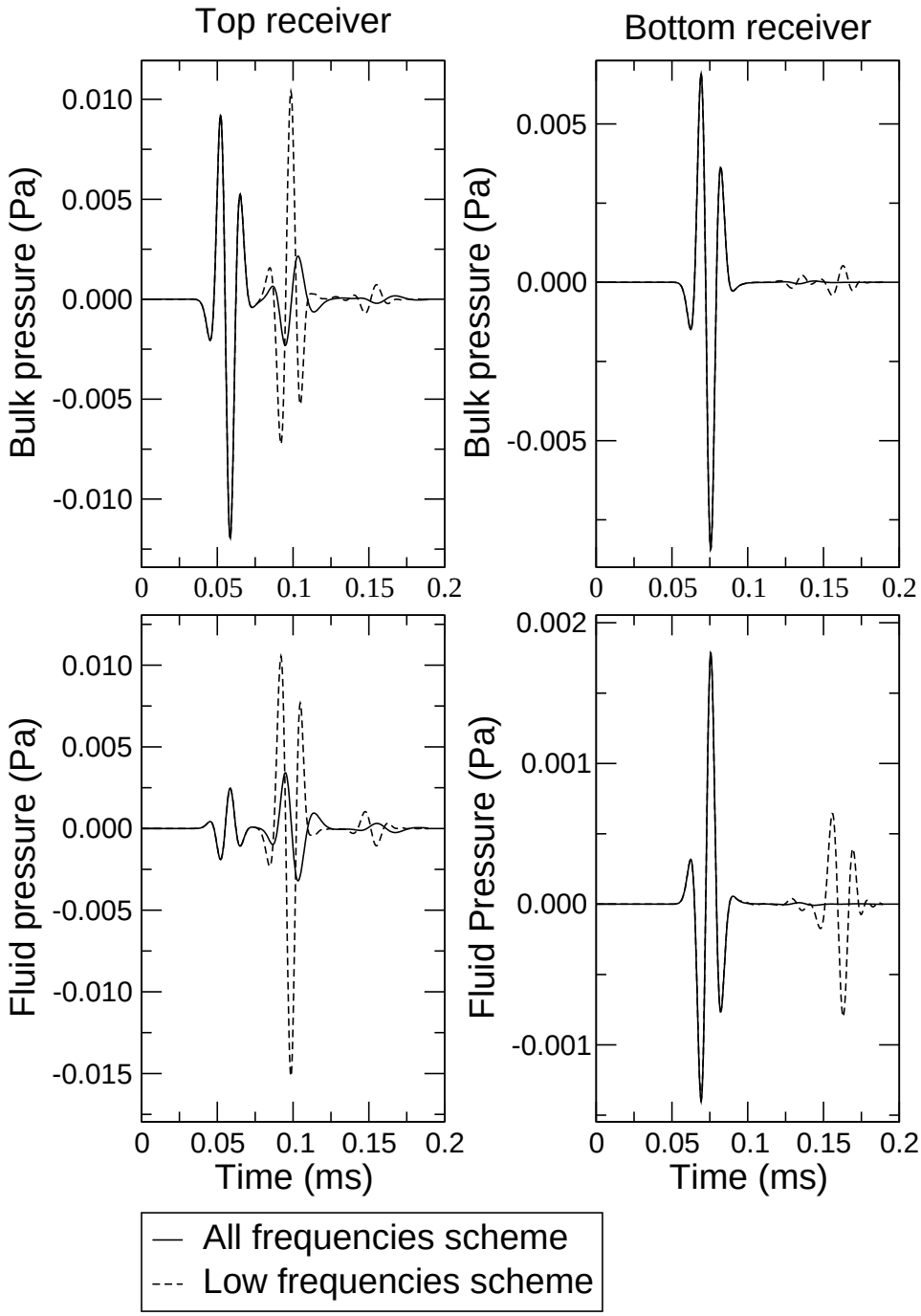

Figure 2.16. Waveforms recorded at the starred positions in Figure 2.15. The solid lines are the result of the present paper's modeling that includes the dynamic-permeability convolution while the dashed lines are the result of the low-frequency modeling in which the permeability coefficient is taken as a simple multiplicative constant. The main difference is that the low-frequency equations grossly underestimate the attenuation and dispersion of the slow waves.

Table 2.2. Material properties of a lightly-consolidated sand.

Solid grain material	
Bulk modulus (K_s)	36.0 GPa
Density (ρ)	2650 kg/m^3
Skeletal framework of grains	
Bulk modulus (K_d)	621 MPa
Shear modulus (μ)	455 MPa
Porosity (ϕ)	0.3
Permeability (k)	10^{-12} m^2
Fluid	
Bulk modulus (K_f)	2.25 GPa
Density (ρ_f)	1000 kg/m^3
Viscosity (η)	10^{-3} N s m^{-2}

2.2.5.2 Dispersion and attenuation in a homogeneous material

In order to quantify the accuracy of the present finite-difference modeling, the velocity dispersion and attenuation of both fast and slow waves is determined as a function of frequency and compared to the exact analytical results in both Figures 2.18 and 2.17. The numerical experiments are performed by sending a plane wave across a uniform region (properties given in the table). Each data point given in Figures 2.18 and 2.17 corresponds to a different experiment involving a pulse with a different center frequency. A Morlet wavelet is used having a narrow-band of support around a center frequency. By recording the solid particle velocity at two different points in the direction of propagation, and time integrating the recording to obtain the maximum displacement amplitude and associated travel time for each recording, both the velocity and attenuation are determined at each frequency. Upon comparing the crosses (finite-difference results) to the solid line (analytical results) in Figures 2.18 and 2.17, the scheme is seen to produce accurate results. If only the low-frequency form of the generalized Darcy law (equation 2.73) is used, the attenuation falls off far too rapidly as ω^{-1} instead of as $\omega^{-1/2}$ as seen in the figure.

2.2.6 Conclusion

A time-domain finite-difference scheme was presented for solving Biot's equations across all frequencies while allowing for the possible development of viscous boundary layers in the pores at sufficiently high frequencies. In this case, the generalized Darcy law controlling the movement of fluid relative to solid contains a time convolution between a kernel that exponentially decays into the past and the past time values of the Darcy flow. It was shown how to model this convolution in an efficient and accurate manner that typically does not require more than 20 past time values to be stored (and often considerably less). Snapshots

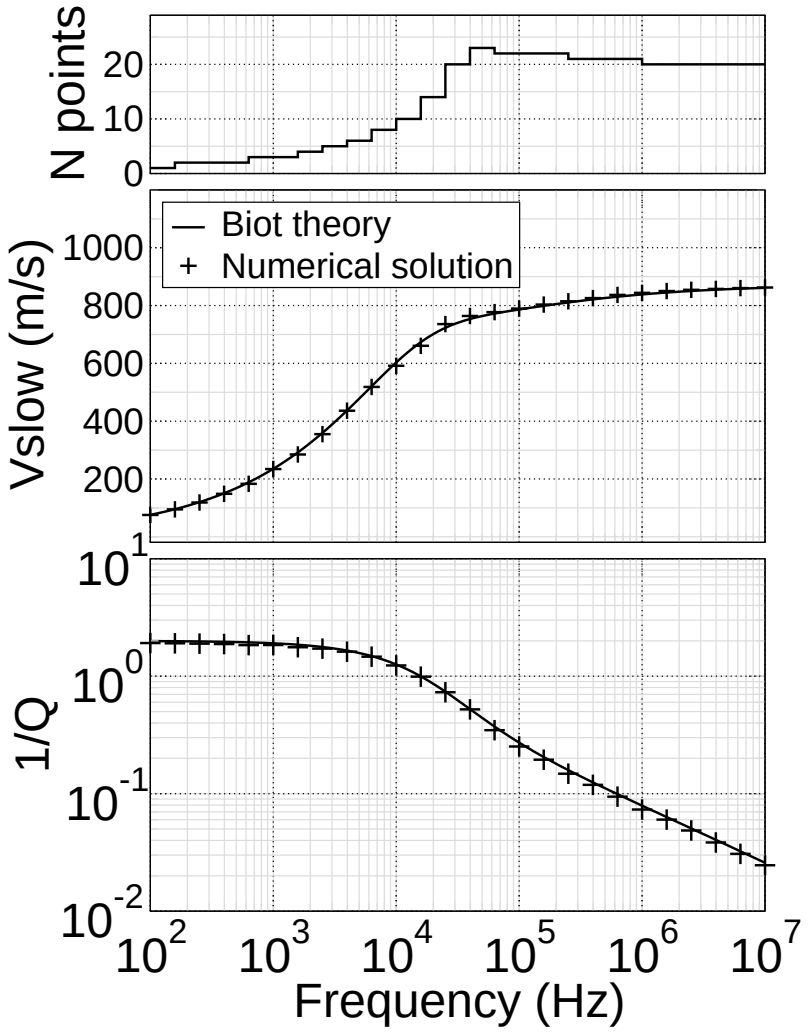

Figure 2.17. Demonstration of the accuracy of the scheme for Biot slow waves. The slow wave velocity and attenuation is determined by performing a transmission experiment at the various center frequencies as denoted with crosses. The number of memory points used in the convolution is given in the top panel. The solid lines in the two lower panels are the analytically exact results.

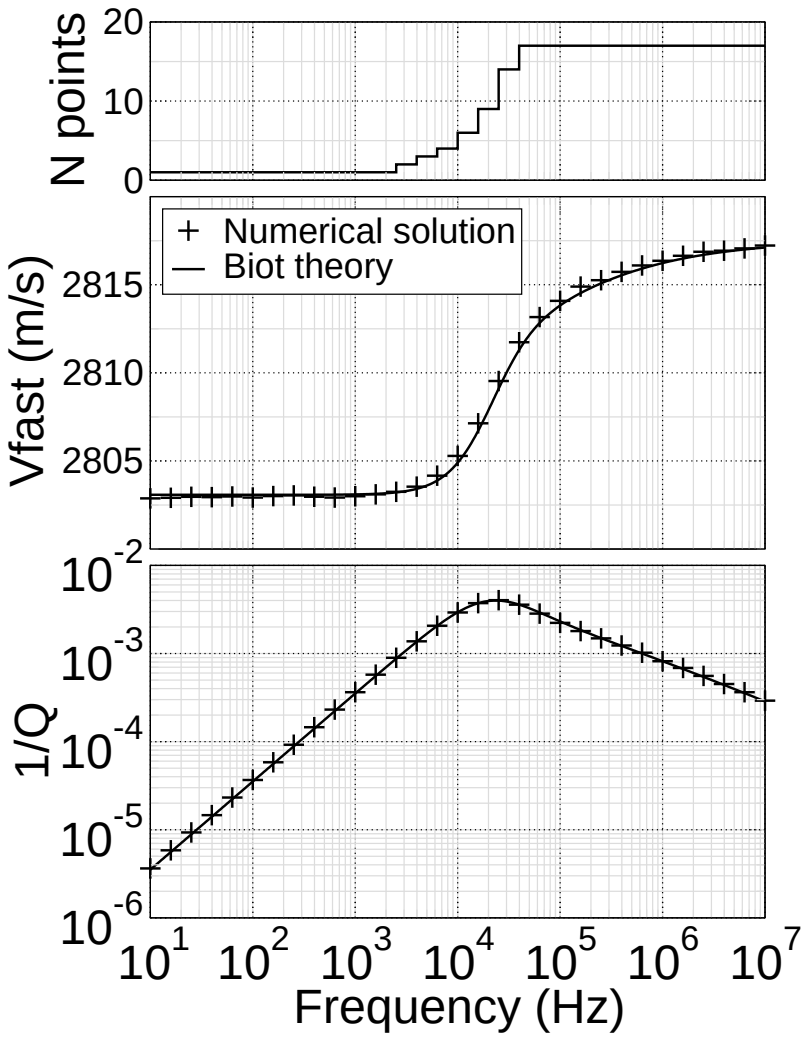

Figure 2.18. Demonstration of the accuracy of the scheme for Biot fast waves. The fast wave velocity and attenuation is determined by performing a transmission experiment at the various center frequencies as denoted with crosses. The number of memory points used in the convolution is given in the top panel. The solid lines in the two lower panels are the analytically exact results.

generated by the scheme show how slow waves above the viscous-boundary-layer transition frequency have a propagatory nature to them while slow waves below the transition frequency are pure diffusions. Getting the amplitudes of these slow waves correct requires the use of the complete theory involving the dynamic-permeability convolution. The accuracy of the scheme was determined by comparing the attenuation and velocity of numerically modeled plane waves at different frequencies to the analytical results. The accuracy was excellent over a broad range of frequencies that included the transition frequency.

Chapter 3

Seismic attenuation due to lithological heterogeneities

3.1 Poroelastic finite-difference modeling of seismic attenuation and dispersion due to mesoscopic-scale heterogeneity

(Published in the JOURNAL OF GEOPHYSICAL RESEARCH,
Y. J. Masson and S. R. Pride, J. Geophys. Res., Volume 112, B03204, 2007.)

3.1.1 Introduction

A long-standing challenge in seismology is to both measure and interpret seismic attenuation in the earth. Identifying the attenuation/dispersion mechanisms at work as seismic waves propagate through the porous materials of the earth's crust remains the subject of ongoing research. Part of the problem in isolating seismic-band (1 Hz to 10^4 Hz) mechanisms is that performing laboratory experiments on rocks over these frequencies is itself a difficult endeavor (c.f., Batzle et al., 2006). The present paper is devoted to numerically simulating one loss mechanism that can be important across the seismic band of frequencies when heterogeneity is present within fluid-saturated porous samples.

Most samples of the earth's crust contain heterogeneity across the mesoscopic scales that

range from a few grain diameters to say a tenth of the seismic wavelength. In particular, if the incompressibility of the framework of grains has heterogeneity across such mesoscales, a wave compressing the material will induce a heterogeneous fluid-pressure response that correlates with the incompressibility structure present. Such wave-induced fluid-pressure gradients equilibrate via pore-pressure diffusion which results in viscous loss. Attenuation, as measured by $1/Q$, is at a maximum when the fluid pressure has just enough time in a wave period to diffuse across the heterogeneous patches present. Peak attenuation thus occurs at a frequency that scales as k/L^2 where k is the local permeability and L a characteristic patch size of the meso-scale heterogeneity. As such, depending on the values of k and L within a sample, it is quite possible to have peak attenuation within the seismic band of frequencies.

In the present paper, the flow induced within a heterogeneous sample by a time-varying stress applied to the sample's surface is numerically determined using the Biot theory of poroelasticity (Biot, 1956 and Biot, 1962) as the local model controlling the physics. The finite-difference algorithm we use is described by Masson et al. (2006). By numerically measuring the strain of the sample, it is possible to determine the complex frequency-dependent elastic moduli of the sample. The imaginary parts of these moduli are due to phase differences between the stress and strain created by the mesoscale viscous flow.

Pride and Berryman (2003a,b) and Pride et al. (2004) have obtained analytical models for the seismic attenuation and dispersion in the special case where the heterogeneity is due to a mixture of two distinct porous phases and when the heterogeneity has a single dominant length scale. In more general media, involving the mixing of many porous materials or the gradual transition from one material type to another or the presence of many length scales of heterogeneity, no analytical theory presently exists. Numerical solution of the Biot equations with arbitrary heterogeneity in the coefficients is one way to study the seismic response of such materials.

Other analytical models of mesoscopic-scale induced flow are those of White (1975) and Johnson (2001) in the case of patchy saturation, and White et al. (1975), Norris (1993), and Gurevich and Lopatnikov (1995) in the case of layered porous media. The squirt-flow models of Mavko and Nur (1979) and Dvorkin et al. (1995) are similar in that the fluid within relatively compressible cracks in the grains is allowed to equilibrate with the stiffer main porespace between the grains. However, due to the size of grain-scale cracks, it is more normal for squirt models to produce peak attenuation at frequencies closer to 1 MHz which is well above the seismic band of interest here. The attenuation allowed for in the standard Biot (1956) theory is that due to flow at the scale of the wavelength, from the compressions to the dilations. Such macro flow is well known to produce negligible attenuation in the seismic band. Numerical tests of the White (1975) model based on finite-difference modeling of the Biot equations have been performed by Carcione et al. (2003).

3.1.2 Elastic moduli and attenuation

Our goal is to numerically compute the complex elastic moduli of numerically created porous samples that contain mesoscale heterogeneity. Over the seismic band of frequencies

(1 to 10^4 Hz) that is the focus here, it can be shown (e.g., Pride, 2005) that the elastic response is effectively "undrained" which means that the fluid flow into and out of each sample of the porous material can be neglected. However, significant fluid flow may occur within each sample due to the presence of mesoscale heterogeneity.

The porous samples are required to be large enough to contain a statistically significant representation of any mesoscale structure in the porous continuum, but much smaller than the wavelengths. They can be considered to be the finite-difference voxels used in the macroscopic forward modeling of a seismic experiment. Saying that the wave response is undrained means that the wave properties would be unaffected if each porous sample were bounded by a vanishingly thin impermeable jacket having comparable elastic moduli and density to that of the surrounding material.

For an isotropic sample, we aim to determine the complex undrained bulk modulus $K_u(\omega)$ and shear modulus $G_u(\omega)$ as defined by Hooke's law

$$\left[\dot{\tau}_{ik} = 2G_u(\omega)\left(\dot{\epsilon}_{ik} - \frac{1}{3}\delta_{ik}\dot{\epsilon}_{ll}\right) + K_u(\omega)\delta_{ik}\dot{\epsilon}_{ll}\right]_{\zeta=0} \tag{3.1}$$

where δ_{ik} is the Kroneker delta function. Here, ζ denotes the fractional changes of fluid mass within the sample, and the condition $\zeta = 0$ therefore denotes undrained conditions. The bulk stress tensor τ_{ik} represents the average total stress tensor throughout the sample under consideration and we use the notation $\dot{\tau}_{ik}(\omega) = -i\omega\tau_{ik}(\omega)$ to denote the stress-rate tensor in the frequency domain. The strain-rate tensor of the sample is defined as

$$\dot{\epsilon}_{ik}(\omega) = \frac{1}{2}\left(\frac{\partial v_i(\omega)}{\partial x_k} + \frac{\partial v_k(\omega)}{\partial x_i}\right) \tag{3.2}$$

where v_i is the average velocity of the solid material within the sample [c.f., Pride and Berryman (1998) for a rigorous demonstration of this definition].

For sake of both simplicity and computation time, the present paper only considers 2D modeling of the local mesoscopic response within each sample. This is equivalent to assuming a 3D response in which no strain out of the modeling plane is allowed to develop (plane strain). Using cartesian coordinates, we take $x_1 = x$ and $x_3 = z$ to be the modeling plane, and $x_2 = y$ to be the direction in which no displacements or displacement gradients can occur. Adding the $\dot{\tau}_{xx}$ and $\dot{\tau}_{zz}$ components of Equation 3.1 and using the plane-strain condition $\dot{\epsilon}_{yy} = 0$ leads to the relation

$$K_u^{3D}(\omega) = K_u^{2D}(\omega) - \frac{G^{3D}(\omega)}{3} \tag{3.3}$$

for the 3D elastic modulus of interest, where K_u^{2D} is given by the definition

$$K_u^{2D}(\omega) = \frac{1}{2}\left(\frac{\dot{\tau}_{xx} + \dot{\tau}_{zz}}{\dot{\epsilon}_{xx} + \dot{\epsilon}_{zz}}\right)_{\zeta=0}. \tag{3.4}$$

The 3D shear modulus will be obtained by applying different amounts of normal stress to the x and z faces. As such, it can be derived by taking $\dot{\epsilon}_{yy} = 0$ and subtracting $\dot{\tau}_{xx}$ from $\dot{\tau}_{zz}$

in Equation 3.1 to obtain

$$G_u^{3D}(\omega) = \frac{1}{2}\left(\frac{\dot{\tau}_{zz} - \dot{\tau}_{xx}}{\dot{\epsilon}_{zz} - \dot{\epsilon}_{xx}}\right)_{\zeta=0}. \tag{3.5}$$

The only way there can be a net change in the fluid content of an unjacketed sample during a pure shear is if the sample were anisotropic. We nonetheless focus on the "undrained" shear response of Equation (3.5) because not all of the modeling examples to be considered are isotropic. Note that even when a sample is anisotropic, we only will be measuring the one shear stiffness defined by Eq. (3.5) and not the entire suite of shear stiffnesses. Berryman and Wang (2001) have shown that this shear stiffness, G_u^{3D}, is the one that has potential dependence on the fluid's bulk modulus within a porous sample. Further, Equations (3.3)–(3.5) provide a valid definition of K_u^{3D} even for anisotropic samples.

The viscous relaxation (fluid equilibration) that results in changes of the bulk and shear moduli with frequency is also responsible for wave attenuation. The inverse quality factor Q^{-1} will be used as our measure of attenuation. The physical definition of Q^{-1} that we employ is

$$\frac{1}{Q} = \frac{\text{total energy lost per stress period}}{4\pi(\text{average energy reversibly stored per period})}. \tag{3.6}$$

O'Connell and Budiansky (1978) show that this definition requires Q^{-1} to be the ratio of the imaginary and real parts of the elastic modulus involved in the response. We note in passing that this definition, which is the standard one that most seismologists employ, places no upper bound on $1/Q$ since the average energy reversibly stored over one period can fall toward zero for an extremely efficient loss mechanism.

Thus, we define Q_{Ku}^{-1} to be the attenuation associated with a pure undrained compression and given by

$$Q_{Ku}^{-1}(\omega) = \frac{\text{Im}\left\{K_u^{3D}\right\}}{\text{Re}\left\{K_u^{3D}\right\}]}. \tag{3.7}$$

Similarly, Q_G^{-1} is the attenuation of a pure shear and is given by

$$Q_G^{-1}(\omega) = \frac{\text{Im}\left\{G_u^{3D}\right\}}{\text{Re}\left\{G_u^{3D}\right\}}. \tag{3.8}$$

For the remainder of the article, the 3D moduli of a sample will simply referred to as K_u and G_u.

3.1.3 Quasi-static modeling

The low-frequency Biot (1962) equations, in which viscous-boundary layers do not develop in the pores, are solved numerically using a finite-difference algorithm that we have recently developed (Masson et al., 2006). For most earth materials, viscous boundary layers may be neglected over the seismic band ($< 10^4$ Hz). We emphasize that the Biot equations are being used to model the local response within a sample. Upon averaging such local poroelastic response, macroscopic viscoelastic moduli are obtained for the sample as a whole

that could be used, for example, in the viscoelastic modeling of a seismic experiment. In Appendix A, the local poroelastic equations are given along with all the necessary local input parameters.

The finite-differencing algorithm involves explicit time stepping on a staggered grid, and requires the local porous-medium properties to be discretized onto a finite grid. The spatial sampling interval of the grid is determined by the size of the smallest heterogeneous patch of porous continuum within the sample; we require a minimum of four fourth-order spatial differencing points to be present in the smallest patch in order to avoid numerical artifacts. The time-sampling interval is determined using the stability criteria derived by Masson et al. (2006) which, for all ranges of the material properties considered here, amounts to the usual Courant condition.

The mesoscale heterogeneities being allowed for are typically several orders of magnitude smaller than seismic wavelengths. As such, using a a full-waveform modeling to study the attenuation and dispersion of P and S waves would require several thousand grid points per wavelength, and would be computationally inefficient. Instead, we study the attenuation and dispersion by applying stress quasi-statically to a sample; i.e., the wavelengths over the seismic band in such modeling are always much larger than the sample size.

All the numerical results presented in this study have been obtained using the following three steps:

1. On a 2D rectangular mesh, generate a synthetic sample of the material to be studied.
2. Apply a normal stress in the time domain to each external face of the sample and record both the average stress and average strain throughout the sample. Figure 3.1 gives a representation of such an experiment.
3. Take a temporal Fourier transform of the average stress and strain and compute the complex macroscopic elastic moduli $K_u(\omega)$ and $G_u(\omega)$ using Equations (3.3)–(3.5).

Figure 3.2 shows the spatial position where the stresses, fluid pressure, particle velocities, and local physical properties are computed within the discretized sample. During step 2, the following sealed boundary conditions are imposed on the external faces of the sample

$$\begin{aligned} \tau_{xx} &= \begin{cases} S_x(t) & \text{on the left and right faces,} \\ 0 & \text{elsewhere;} \end{cases} \\ \tau_{zz} &= \begin{cases} S_z(t) & \text{on the top and bottom faces,} \\ 0 & \text{elsewhere;} \end{cases} \\ \tau_{xz} &= p_f = v_x = v_z = q_x = q_z = 0. \end{aligned} \tag{3.9}$$

Here, $S_i(t)$ denotes the stress function applied in the ith direction. To properly allow for these boundary conditions, second-order spatial differencing operators are used in the first three layers of grid points around the computational domain, while fourth-order spatial operators are used throughout the remainder of the grid points. This is depicted in Figure 3.2.

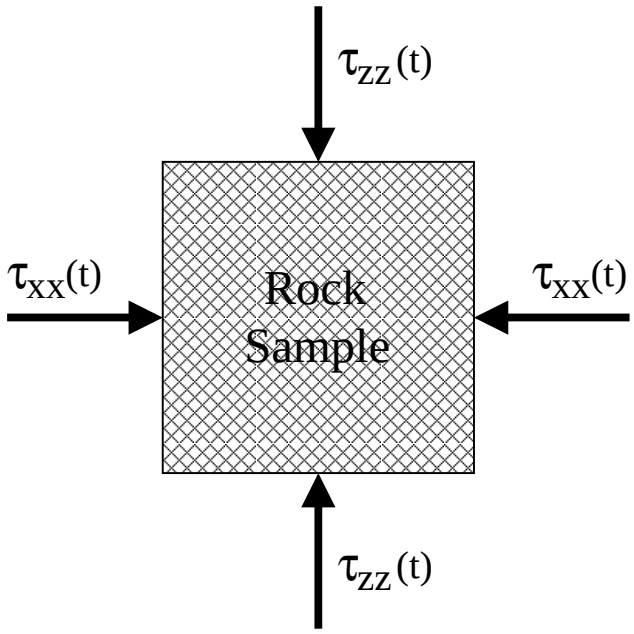

Figure 3.1. Setup for the numerical experiments: The elastic moduli of the porous sample are obtained by applying a stress on the bounding faces of a sealed sample and measuring the strain response.

The stress function $S(t)$ has been choosen to offer a wide band of frequency content within a small time duration. For all examples, it is taken to be

$$S(t) = \frac{S_o}{2} \left\{1 + \tanh\left[r\left(t - t_0\right)\right]\right\}. \tag{3.10}$$

The constant amplitude S_o fixes the stress level, while the time dependence becomes a simple step function when the stretching parameter r goes to infinity. For the experiments, the parameter t_0 is set sufficiently large that $rt_0 \gg 1$ so that $S(t=0) \simeq 0$. The lowest frequency present in the function $S(t)$ is controlled by the duration of the signal, while the largest frequency is related to the parameter r. To avoid undesirable high-frequency resonance, the stretching parameter r is adjusted in order to obtain the largest frequency content without appreciably exciting wavelengths comparable to sample dimensions.

During the numerical experiments, the following average fields are recorded at each time step

$$\langle D_i v_i \rangle(l) = \frac{1}{N-2}\frac{1}{M-2}\sum_{m=2}^{M-1}\sum_{n=2}^{N-1}\left[D_i v_i\right]_{l,m,n} \tag{3.11}$$

$$\langle D_t \tau_{ii} \rangle(l) = \frac{1}{N-2}\frac{1}{M-2}\sum_{m+2}^{M-1}\sum_{n=2}^{N-1}\left[D_t \tau_{ii}\right]_{l,m,n}. \tag{3.12}$$

Once the modeling is finished, the stress rate and strain rate are computed in the frequency

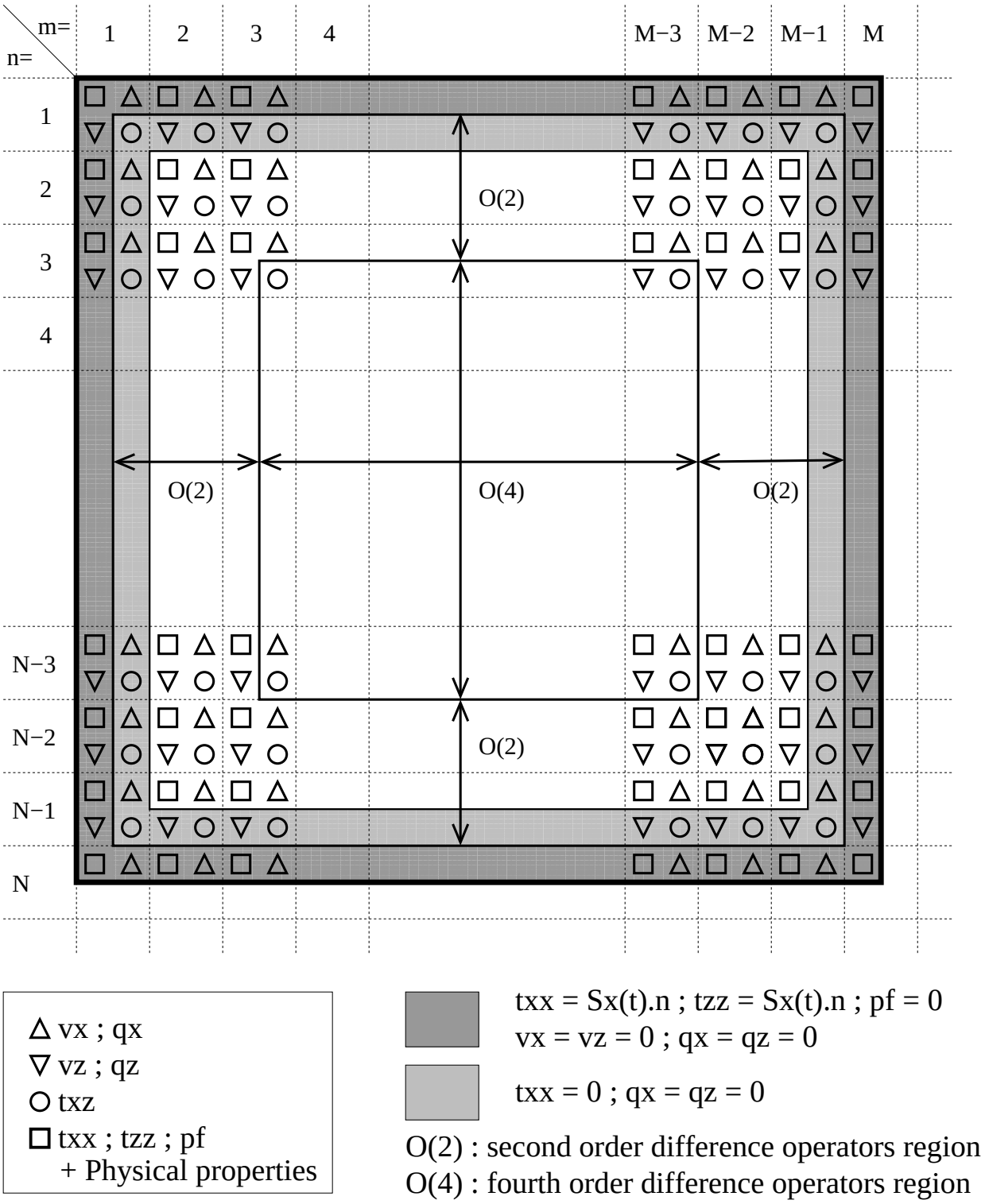

Figure 3.2. Relative position of the field components on the staggered grids. The stress function is applied in the external dark-gray layer of grid points. To simulate undrained experiments, the fluid parcticle velocity field $\mathbf{q}$ is kept to zero in the light gray area. The boundary conditions are better allowed for by using $O(2)$ spatial finite operators in the external region and $O(4)$ throughout the remaining interior region.

Table 3.1. Material properties of the samples shown in Figure 3.3. Phase 1 is more compressible than phase 2 and has a higher permeability.

Property	**Phase 1**	**Phase 2**
Grain		
Bulk modulus (K_s)	36.0 GPa	36.0 GPa
Density (ρ_s)	2650 kg/m^3	2650 kg/m^3
Frame		
Bulk modulus (K_d)	621 MPa	6.21 GPa
Shear modulus (μ)	455 MPa	455 MPa
Porosity (ϕ)	0.33	0.33
Permeability (k)	10^{-12} m^2	10^{-15}m^2
Fluid		
Bulk modulus (K_f)	2.25 GPa	2.25 GPa
Density (ρ_f)	10^3 kg/m^3	10^3 kg/m^3
Viscosity (η)	10^{-3} N s m^{-2}	10^{-3} N s m^{-2}

domain using a Fourier transform (FT)

$$\dot{\epsilon}_{ii}(\omega) = \mathrm{FT}\left\{\langle D_i v_i \rangle\right\} \tag{3.13}$$

$$\dot{\tau}_{ii}(\omega) = \mathrm{FT}\left\{\langle D_t \tau_{ii} \rangle\right\}. \tag{3.14}$$

Finally, the undrained bulk and shear moduli, as well as the respective attenuation, are computed using Equations (3.3)–(3.8). In order to obtain $K_u(\omega)$ and $G_u(\omega)$, two kinds of experiments are performed: (1) pure compression experiments in which $S_x(t) = S_z(t) = S(t)$; and (2) pure shear experiments in which $S_x(t) = S(t)$ and $S_z(t) = -S(t)$. Performing a single mixed experiment with $|S_x| \neq |S_z|$ to give both K_u and G_u simultaneously gives noisier results.

3.1.4 Attenuation and dispersion due to pure compression

3.1.4.1 Double porosity and simple geometrical effects

In order to compare the numerical method to the double-porosity theory (e.g., Pride et al., 2004), two series of four numerical experiments have been realized. In all eight experiments, the samples consist of square-shaped porous inclusions embedded within a homogeneous porous matrix. The physical properties of the two porous phases are given in Table 3.1 and the spatial positions of the inclusions are shown in Figure 3.3 (a), (b), (c) and (d). The number of inclusions in each material has been adjusted to have the same partial volumes of each phase present in all samples; specifically, 1/4 inclusion and 3/4 matrix.

In the first series of experiments, the inclusions are stiffer and less permeable than the

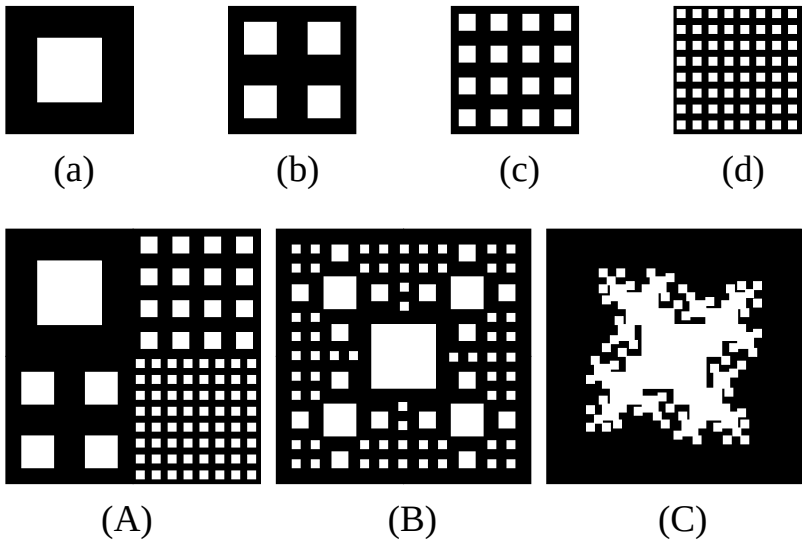

Figure 3.3. Geometries of the samples used for testing the double-porosity theory. The sizes of the small and the large samples are 64 mm and 128 mm respectively. The sizes of the white squares in (a), (b),(c) and (d) are 32, 16, 8 and 4 millimeters respectively. Each material is made of 1/4 white phase and 3/4 black phase. The three composites (A), (B) and (C) are obtained by mixing together (a), (b), (c) and (d) in different ways.

surrounding matrix. In this case, the diffusive fluid flow in response to the step change in applied stress advances into the inclusions, with fluid pressure remaining almost spatially uniform throughout the softer and more permeable matrix (the fluid pressure gradually decreases through time in the more permeable phase, but remains effectively uniform in space). The undrained bulk modulus K_u and the associated attenuation Q_{Ku}^{-1} numerically measured for the samples (a), (b), (c) and (d) are plotted as symbols in Figure 3.4. The theoretical results, obtained using the analytical double-porosity theory of Pride et al. (2004), are plotted as the solid lines. The analytical expressions, along with additional discussion of the double-porosity theory, are given in Appendix B. As seen there, all parameters required by the double-porosity theory are either known or calculated using their theoretical definition. There are no free parameters that are adjusted to achieve a good fit to the numerical data.

The finite-difference results show a good agreement with the double-porosity theory. The spatial-sampling interval for the finite differencing was taken to be 0.5 mm while the smallest patch of heterogeneity was 4 mm (c.f., Figure 3.3), which corresponds to 8 grid points within the smallest patch. The time-sampling interval was given by the stability criterion of Masson et al. (2006). Fluctuations in the numerical response above 10^4 Hz are due to sample resonance.

At low enough frequencies, the attenuation increases linearly with increasing frequency. This is a consequence of the finite size of the sample (as will be discussed in the next section). At peak attenuation, the fluid has just enough time in each period to diffusively penetrate each inclusion. The fluid-pressure diffusivity D of a porous material goes as (c.f., Pride, 2005, for a demonstration and Appendix A for definitions of α, B, K, and K_U; however, this

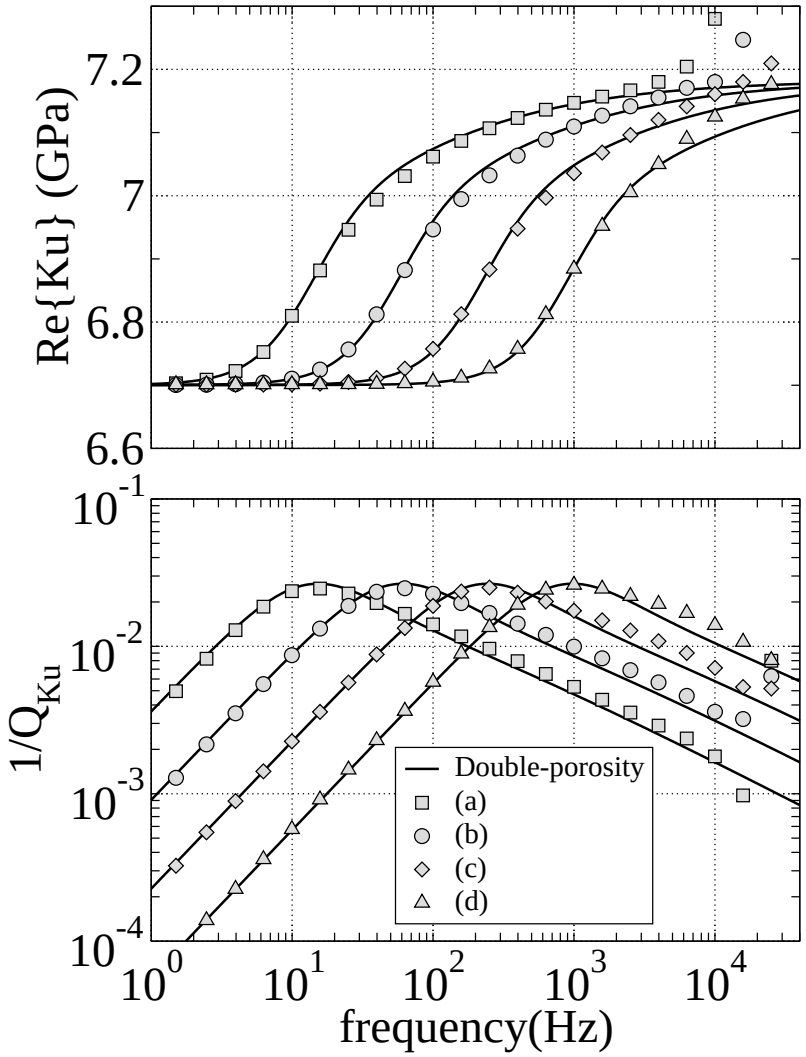

Figure 3.4. Real part of the bulk modulus and the respective attenuation obtained from the geometries (a),(b), (c) and (d) in Figure 3.3. In this example, the black regions in Figure 3.3 are filled with the softer/more-permeable phase 1 and the white regions with the stiffer/less-permeable phase 2. The properties of phases 1 and 2 are given in Table 3.1.

result for D can be found in many places)

$$D = \frac{kBK_U}{\eta\alpha}\left(\frac{K + 4G/3}{K_U + 4G/3}\right) \approx \frac{kK_f}{\eta\phi} \tag{3.15}$$

where K_f is the fluid's bulk modulus, ϕ is porosity, and η is the fluid viscosity. Peak attenuation occurs at the relaxation frequency ω_p given by $\omega_p = D/L^2 \propto k/L^2$ where L is a characteristic patch size defined explicitly in Appendix B. Finally, at high frequencies, the attenuation decreases as the square root of the frequency. This is a consequence of the diffusive penetration depth of the fluid pressure into the less-permeable inclusion decreasing with increasing frequency as $\omega^{-1/2}$. The permeability is the same in all samples so the relaxation frequency ω_p only varies due to L. Figure 3.5 gives snapshots of the fluid pressure during an experiment with a sample containing different sizes of inclusions. Looking at the times needed by each size of inclusion to equilibrate gives a visual idea of how the relaxation frequency depends on L.

For the second series of numerical experiments, the two porous phases in (a), (b), (c) and (d) have simply been swapped so that what was inclusion material is now matrix and vice versa (see figure 3.3). In this case, the fluid-pressure equilibration takes place mainly within the low-permeability matrix. Figure 3.6 shows the measured values for K_u and Q_{Ku}^{-1} versus frequency. Here again, the finite-difference results are consistent with the double-porosity theory.

To begin investigating more complex materials, we construct three composites (A), (B) and (C) as depicted in Figure 3.3. Each of these three materials has exactly the same numbers of each size of square inclusions. The only difference is where these square inclusions are placed inside the sample. Further, the volume fractions of the inclusion and matrix phases in composites (A), (B), (C) and (a), (b), (c) are all identical. Again, we test the two scenarios in which the inclusions and matrix are either made of material one or two from Table 3.1.

Figure 3.7 shows the results obtained when the matrix is softer and more permeable than the inclusions. Interestingly, in this case, the K_u and Q_{Ku}^{-1} curves are very similar for the three composites. The results for (A) and (B) are almost equal, while for (C), the curves are slightly shifted at lower frequencies. This shifting is due to the fact that the fluid pressure takes more time to equilibrate within the relatively large aggregate in (C). The similarity in the results suggests the different inclusions are not strongly interacting so that a theoretical estimate can be made by simply averaging together the double-porosity theory estimates corresponding to examples (a), (b), (c), and (d) in Figure 3.3. Figure 3.7 shows that such a theoretical estimate (solid line) is very consistent with the numerical data.

The results obtained after swapping the roles of the two phases in (A), (B) and (C) are presented in Figure 3.8. The numerical results for material (A) in this case are again well fit by a simple mean of the Figure 3.6 results. However, materials (B) and (C) show more significant discrepancies between the numerical results and the simple mean curve. This is because the black regions in Figures 3.3(B) and 3.3(C) have a distinctly different geometry than the black region of Figure 3.3(A). In particular, material (B) has a black area with a narrow range of length scales between the white inclusions which results in the enhanced

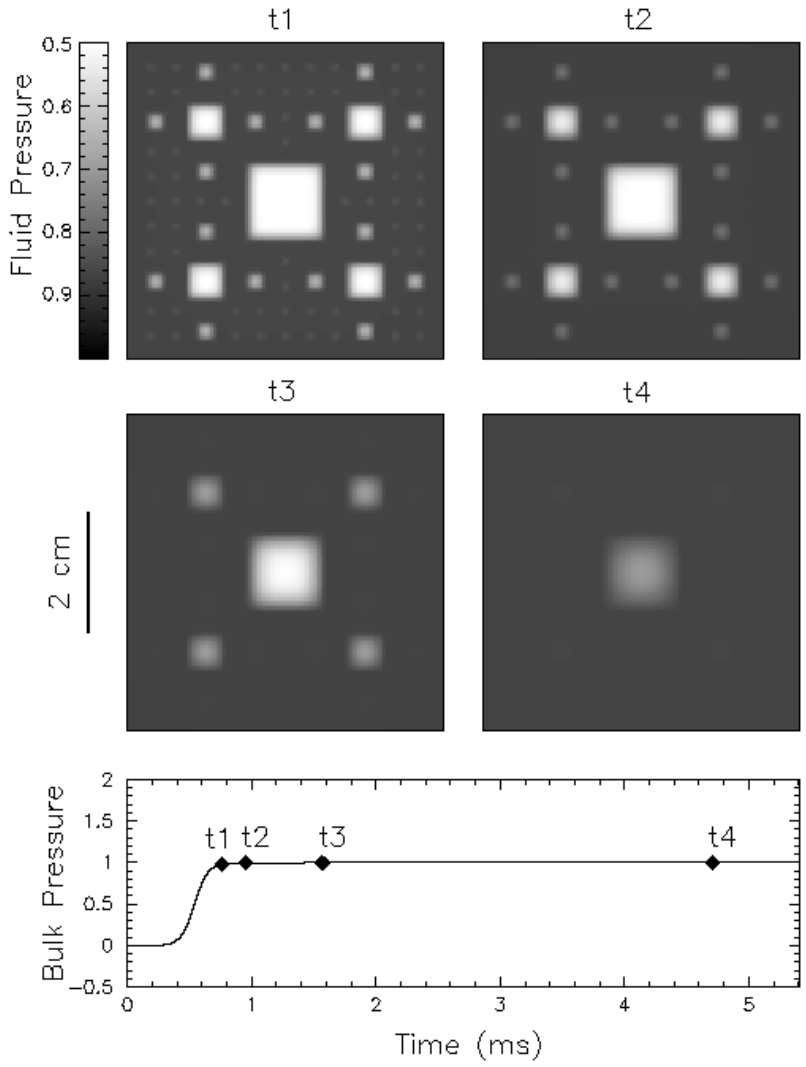

Figure 3.5. Snapshots showing the fluid pressure at different times during a purely compressional experiment. The applied stress is shown as a function of time in the bottom plot.

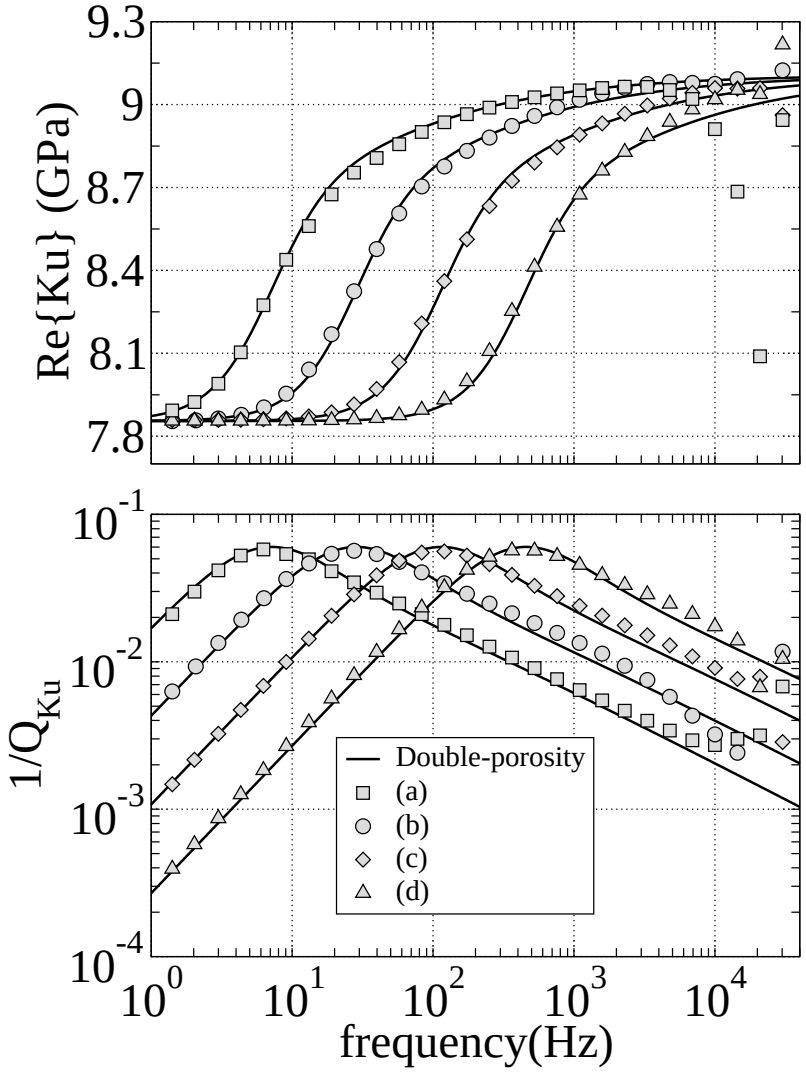

Figure 3.6. Real part of the bulk modulus and the associated attenuation obtained from the geometries (a),(b), (c) and (d) in Figure 3.3. In this example, the black regions in Figure 3.3 are filled with phase 2 and the white regions with phase 1 from Table 3.1. Just the opposite from the results of Figure 3.4.

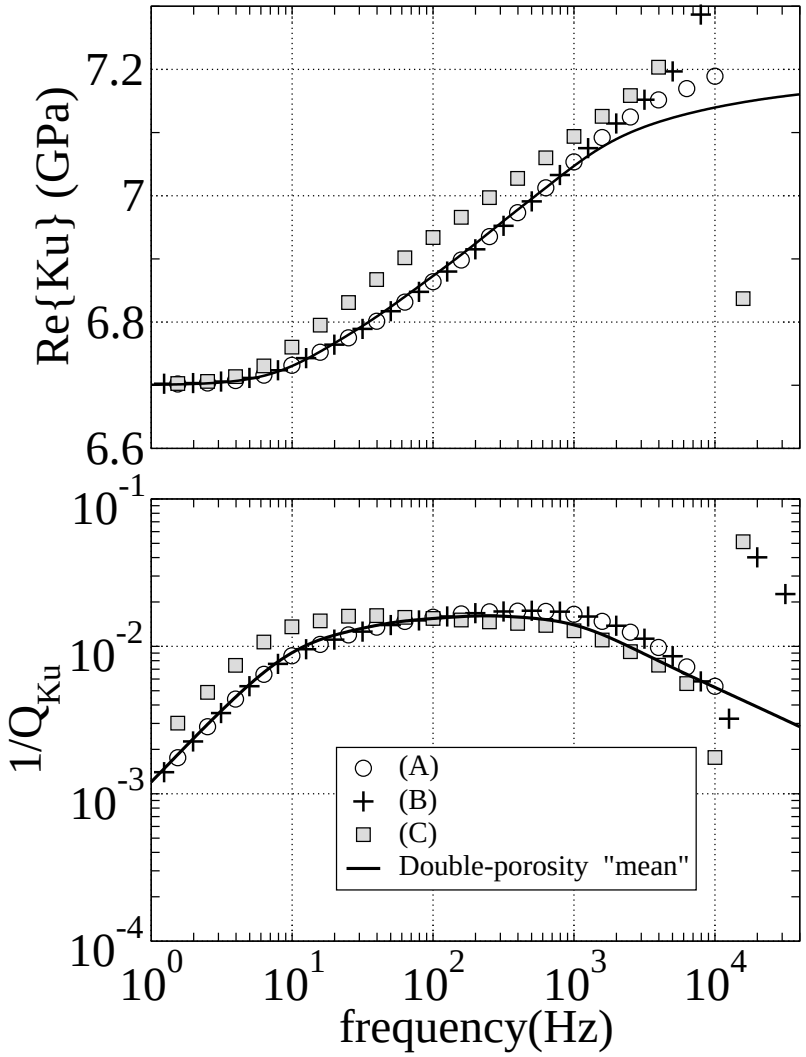

Figure 3.7. Real part of the bulk modulus and the associated attenuation obtained from the geometries (A), (B) and (C) in Figure 3.3. The black and white areas in Figure 3.3 where filled with materials 1 and 2, respectively, from Table 3.1. The solid line is a simple mean of the four theoretical curves associated with the samples (a), (b), (c) and (d) presented in Figure 3.4.

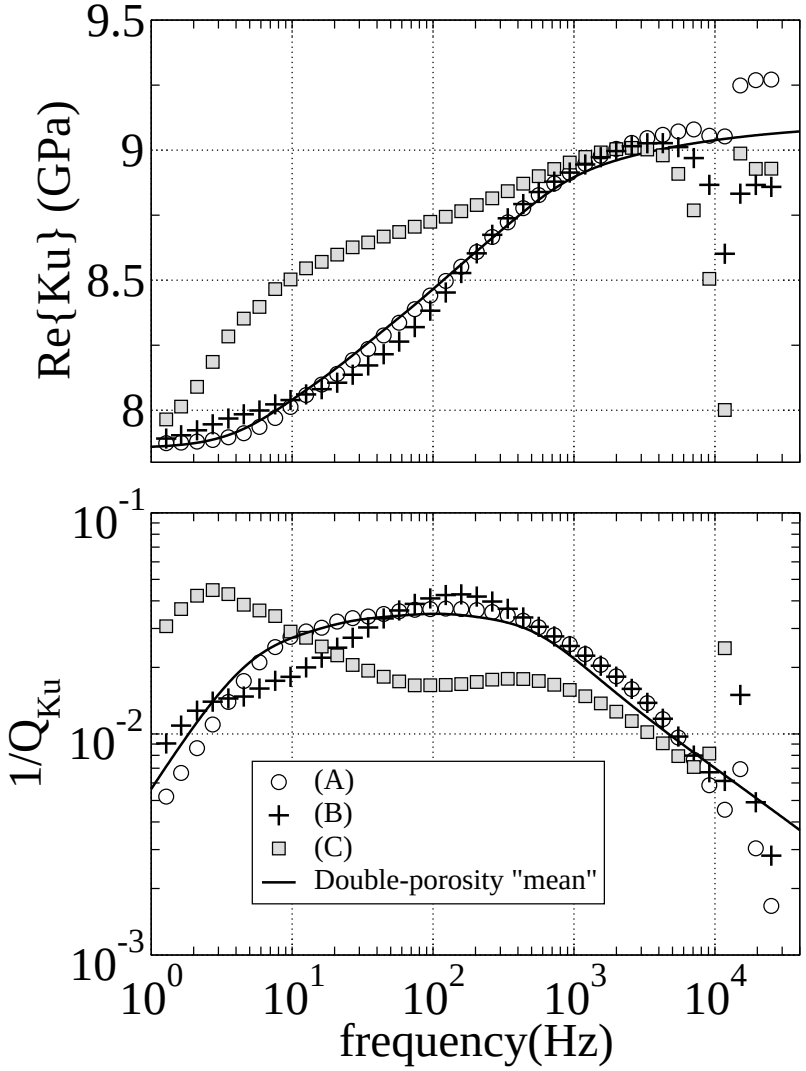

Figure 3.8. Real part of the bulk modulus and the respectives attenuations obtained from the geometries (A), (B) and (C) in Figure 3.3. The black and white areas in Figure 3.3 where filled with phase 2 and phase 1, respectively, from Table 3.1. The solid line is a simple mean of the four theoretical curves associated with the samples (a), (b), (c) and (d) presented in Figure 3.6.

peak of Figure 3.8. Similarly, material (C) has a dominant length scale that is much larger than in any of the other examples which results in the low-frequency peak seen in Figure 3.8.

The conclusion is that when the diffusion is controlled by the inclusions (i.e., the inclusion material has the smaller fluid-pressure diffusivity), then it does not matter where the inclusions are placed within the sample. However, when the diffusion is controlled by the matrix, the fact that the geometry of the matrix changes greatly depending on where the inclusions are placed means that the shape of the attenuation curves will be more sensitive to where the inclusions are placed.

3.1.4.2 Gradual transitions in the local properties

We next investigate what is the consequence on the frequency dependence of $K_u(\omega)$ if there is a gradual transition in the local moduli from one patch of material to the next as opposed to the abrupt step changes so far considered.

Consider first the simple situation depicted in Figure 3.10, in which there is a linear transition in the local drained (frame) moduli from one porous material to another. The transition occurs across a layer that has a thickness h. Figure 3.9 shows how the frequency dependence of Q_{Ku}^{-1} is affected by changing the transition layer's thickness h. The effect is to make the high-frequency limit of Q_{Ku}^{-1} change from $\omega^{-1/2}$ in the case where no transition layer is present (a step change in local properties) to ω^{-1} when the transition layer is present. So long as the diffusive penetration distance $\delta = \sqrt{D/\omega}$ is larger than the transition thickness h, but smaller than the size L of the main low-permeability patch that is being diffusively penetrated, one has that Q_{Ku}^{-1} will decrease with increasing frequency as $\omega^{-1/2}$. However, at frequencies where $\delta < h$, a transition to a linear decrease with frequency occurs because the fluid-pressure gradient is no longer controlled by diffusion into a uniform material, but by the simple gradient in material properties present in the transition layer. A more detailed explanation of this frequency dependence will be provided in the following subsection. The frequency $\omega_{\rm sw}$ at which the transition from $\omega^{-1/2}$ to ω^{-1} attenuation fall-off occurs can thus be estimated as

$$\omega_{\rm sw} = D/h^2. \tag{3.16}$$

As shown in Figure 3.11, this estimate (the solid line) is consistent with the numerical experiments.

In Figure 3.12, the transition inside the sample takes place with various smooth profiles as shown (not just linear transitions) and the permeability is allowed to vary as well. All conclusions so far obtained about the high-frequency dependence being ω^{-1} in the presence of gradual transitions (instead of $\omega^{-1/2}$ in the presence of step transitions), continue to hold. The explanation for this is now provided.

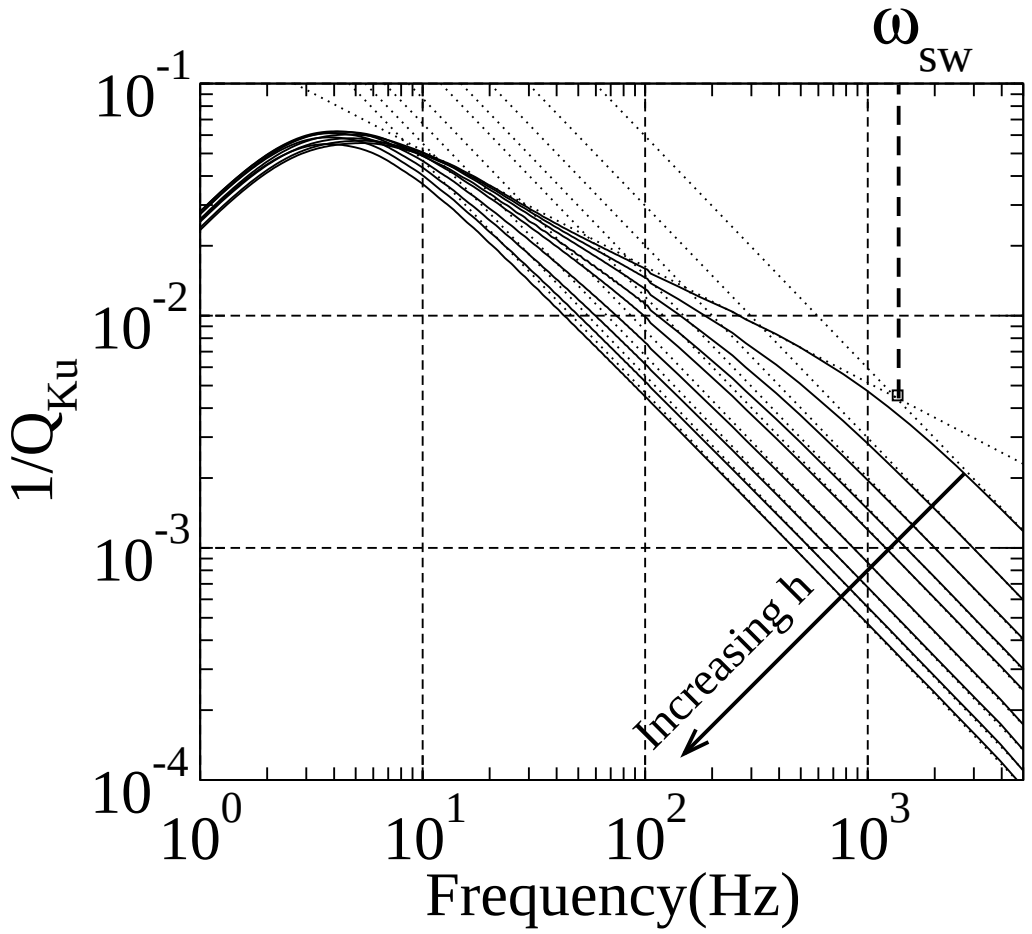

Figure 3.9. Attenuation curves $Q^{-1}(\omega)$ obtained by varying the thickness of the transition layer h (see Figure 3.10). The thin dotted lines are obtained by fitting the data in the high frequency range with a function of the form $Q^{-1}(\omega) = A\omega^{-1}$. For each experiment, the transition frequency ω_{sw} is measured at the intersection between the high-frequency asympote (thin dotted line) at a given h, and the high-frequency asymptote when $h = 0$.

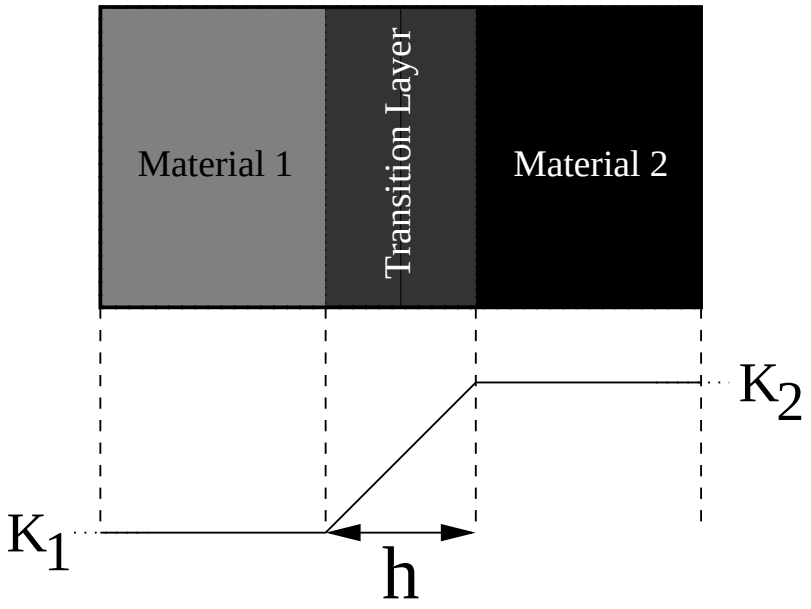

Figure 3.10. Geometry of the sample used to study the effect of smooth transitions from one material to another. The physical properties of materials 1 and 2 are given in Table 3.1 as Phase 1 and Phase 2 respectively with the exception that the permeability is constant everywhere ($k = 5 \times 10^{-16} m^2$). Inside the transition zone, the physical properties are linearly interpolated between the two materials.

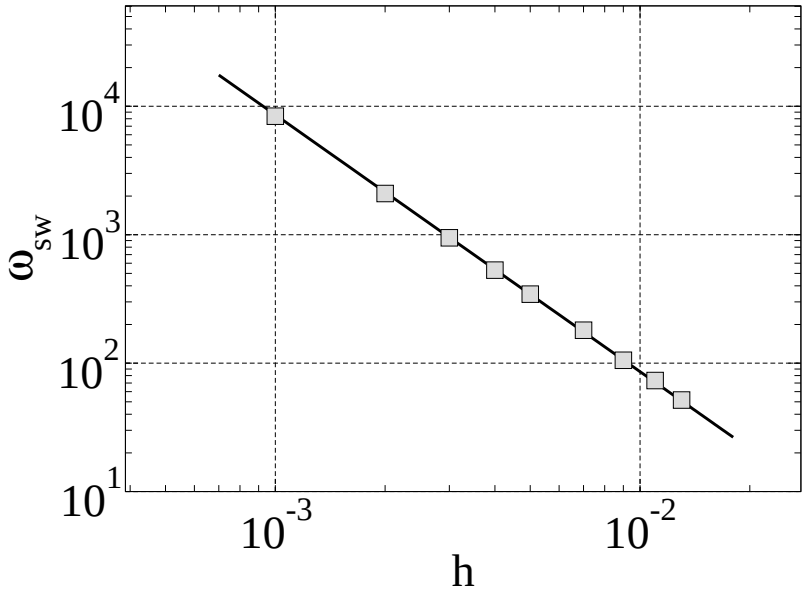

Figure 3.11. Measured relaxation frequency ω_{sw} as defined in Figure 3.9 plotted as a function of the thickness of the transition layer (see Figure 3.10). The solid line is Equation (3.16).

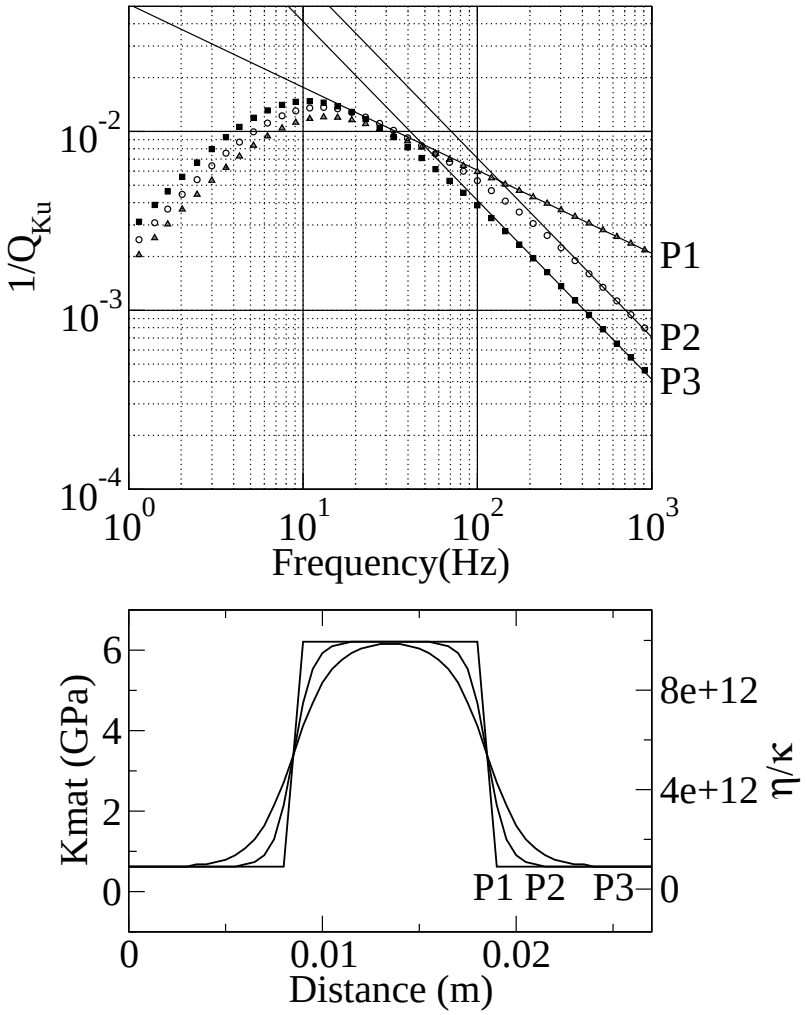

Figure 3.12. Similar experiment as in Figure 3.9 but with permeability variations and different profiles for the transition layer. Here the sample consists of a single circular inclusion embedded within a homogeneous matrix. The three curves have been obtained using three differents profiles (P1, P2, P3) for the transition layer. The solid lines are obtained by fitting the data in the high frequencies range. The slopes of the lines associated with P2 and P3 are very close to 1, while the one associated with P1 is very close to 1/2. The local drained modulus and permeability profiles along the diameter of the circular inclusion is shown in the bottom plot. The other physical properties correspond to the values shown in Table 3.1

3.1.4.3 Explanation for the nature of $Q_{Ku}^{-1}(\omega)$

We now provide a simple "back-of-the-envelope" analysis of $Q_{Ku}^{-1}(\omega)$ in order to better explain the observed frequency dependence in the limits of low and high frequencies and to define how the maximum value of Q_{Ku}^{-1} depends on the material properties. The goal is to obtain a simple understanding of Q_{Ku}^{-1} that is nonethless useful and robust. This is done at the expense of mathematical rigor.

To do so, we exploit the physical definition of Q provided earlier as Equation (3.6). For ease of explanation, we assume the composite is predominantly a mixture of two porous phases (a double-porosity model) and designate using a 1 the porous phase having the smaller fluid-pressure diffusivity D. Phase 1 thus controls the timing of the diffusive penetration of the fluid-pressure and, therefore, contains the strongest fluid-pressure gradients and viscous losses. Despite this double-porosity context, the effect of smooth transitions between the otherwise homogeneous patches will be considered.

The rate at which energy is locally being lost per unit volume of phase 1 is $(k_1/\eta)|\nabla p_f|^2$. Thus, using Equation (3.6) and assuming that the attenuation is small ($Q^{-1} < 1$) so that the average stored energy is equal to half the peak stored energy, we have

$$Q^{-1} = \frac{k_1}{\omega\eta}\frac{\int_{\Omega_1}|\nabla p_f|^2\,dV}{\int_\Omega K_U\epsilon^2\,dV} \approx \frac{k_1}{\omega\eta}\frac{\int_{\Omega_1}|\nabla p_f|^2\,dV}{V\mathrm{Re}\{K_u\}\epsilon^2} \tag{3.17}$$

where $\mathrm{Re}\{K_u\}$ is the macroscopic undrained modulus of the sealed sample, V is the sample volume, ϵ is the applied volumetric strain, and Ω_1 is the domain of phase 1. We now further analyze this expression in the limits of high and low frequencies. In what follows, the fluid-pressure gradients in phase 1 are crudely approximated as $\Delta p_f/\Delta x$ where Δp_f is a characteristic pressure contrast between the two phases that exists over a distance Δ_x within Ω_1.

High frequencies At high frequencies, Δp_f is given by the locally (and globally) undrained response $\Delta p_f = \Delta C\,\epsilon$ where ΔC is the contrast in the local Biot coupling modulus $C = \alpha M$ between two adjacent patches (see Appendix A for definitions of α and M). Further, by definition of "high frequencies", Δx is necessarily smaller than the characteristic size L (defined in Appendix A) of the phase 1 patches. The volume of phase 1 across which the fluid-pressure gradients are non-negligble is roughly $S\Delta x$ where S is the total surface area separating the porous patches. We can thus write

$$Q_\infty^{-1} \approx \frac{k_1}{\omega\eta}\frac{S}{V}\frac{(\Delta C)^2}{K_u(\infty)}\frac{1}{\Delta x} \tag{3.18}$$

where, for a double-porosity material, the high-frequency undrained bulk modulus $K_u(\infty)$ is given by Equation (B.13) of Appendix B.

In the special case where there is an abrupt step change from one patch to the next, one has that $\Delta x = \delta = \sqrt{D_1/\omega}$ is the diffusive penetration depth into phase 1. In this case,

Equation (3.18) gives

$$Q_\infty^{-1} \approx \left[\sqrt{\frac{\phi_1 k_1}{K_f \eta}} \frac{S}{V} \frac{(\Delta C)^2}{K_u(\infty)} \right] \omega^{-1/2} \tag{3.19}$$

as observed in the numerical experiments. In the case where there is a gradual (but otherwise arbitrary) transition over a distance h from one patch to the next and when $\delta < h$, we have that $\Delta x = h$ so that

$$Q_\infty^{-1} \approx \left[\frac{k_1 S}{\eta h V} \frac{(\Delta C)^2}{K_u(\infty)} \right] \omega^{-1} \tag{3.20}$$

also as observed in the numerical experiments.

Peak attenuation Peak attenuation occurs when the diffusive penetration distance δ just equals the size L of the phase 1 patches; i.e., it occurs at the frequency $\omega_p = D_1/L^2$. At peak attenuation, effectively all of phase 1 has a fluid-pressure gradient across it so that

$$Q_{\text{peak}}^{-1} \approx \frac{L^2 k_1}{D_1 \eta} \frac{V_1}{V} \left(\frac{\Delta C}{L} \right)^2 \frac{1}{K_u(\omega_p)} \approx \frac{\phi_1 V_1}{V} \frac{(\Delta C)^2}{K_f K_u(\omega_p)} \tag{3.21}$$

where $K_u(\omega_p)$ is approximated in Appendix B. This useful expression says that the magnitude of peak attenuation is proportional to the square of the contrast in the coupling modulus. If the incompressibility contrast is doubled, the attenuation curves will be shifted upward by a factor of four.

Low frequencies At low frequencies, the distances overwhich the fluid-pressure gradients in phase 1 exist are independent of frequency and are given by $\Delta x = L$. In such a long-time (low-frequency) limit, the diffusional penetration of fluid pressure across the low-permeability phase 1 material has plenty of time to occur within each stress cycle (i.e., $\omega \ll D_1/L^2$). The remaining pressure gradients are decreasing linearly with decreasing frequency because the average fluid-pressure difference between the two phases Δp_f is decreasing. Pride and Berryman (2003b) show that at low frequencies, a double-porosity material will have an average difference of fluid pressure between the two phases given by

$$\Delta p_f = \omega \frac{\eta}{k_1} \left(1 - \frac{B_o}{B_1} \right) \frac{\alpha_1}{K_1} L^2 K_u(0) \epsilon \tag{3.22}$$

where B_o is the static Skempton's coefficient and $K_u(0)$ the static undrained bulk modulus of the double-porosity composite and expressions for each are given in Appendix B. At zero frequency, no fluid pressure gradients in the composite remain. Thus, at low frequencies, the attenuation goes as

$$Q_o^{-1} \approx \left[\frac{V_1}{V} \frac{\eta L^2}{k_1} \left(1 - \frac{B_o}{B_1} \right)^2 \left(\frac{\alpha_1}{K_1} \right)^2 K_u(0) \right] \omega \tag{3.23}$$

as seen in the numerical experiments.

Table 3.2. Material properties of the samples shown in Figure 3.13.

Property	Min	Mean	Max
Grain			
Bulk modulus (K_s)	-	36.0 GPa	-
Density (ρ_s)	-	2650 kg/m^3	-
Frame			
Bulk modulus (K_d)	500 MPa	5 GPa	9.5 GPa
Shear modulus (μ)	333 MPa	3.33 GPa	6.33 GPa
Porosity (ϕ)	0.26	0.33	0.39
Permeability (k)	10^{-16} m^2	10^{-15} m^2	1.9×10^{-15} m^2
Fluid			
Bulk modulus (K_f)	-	2.25 GPa	-
Density (ρ_f)	-	10^3 kg/m^3	-
Viscosity (η)	-	10^{-3} N s m^{-2}	-

3.1.4.4 Random correlated materials

We now consider the attenuation and dispersion in materials having local properties randomly sampled from a probability distribution function (PDF) and for which some specified correlation function of the properties has been imposed. The algorithm used to create such random correlated materials is presented in Appendix D.

Consider the four materials shown in the right column of Figure 3.13 and having either a unimodal Gaussian (G1 and G2) or bimodal Gaussian (B1 and B2) distribution function as shown in the left column. In all four realizations (B1, B2, G1, and G2), a Gaussian correlation function was further imposed having a correlation length of 1 cm. The material properties associated with these distributions are given in Table 3.2.

The dispersion and attenuation associated with the undrained bulk modulus are plotted in Figure 3.15. The greatest attenuation and dispersion are associated with the distribution (B2) which has the largest standard of deviation. As shown above in Section 4.3, the peak value of attenuation is determined by the square of the local contrasts in compressibility present. This is equivalent to saying that the peak attenuation is proportional to the square of the standard of deviation of the PDF used to create the random heterogeneity. Figure 3.14 shows that the numerical experiments are consistent with such a quadratic relation between peak attenuation and a PDF's standard of deviation. Distributions G2 (unimodal) and B1 (bimodal) have identically the same standard of deviation which results in very similar attenuation and dispersion curves in Figure 3.15. The main difference is that the bimodal distribution has a $\omega^{-1/2}$ fall off in the high-frequency attenuation, while the unimodal distribution has a ω^{-1} fall off. The reason has been given above in Sections 4.2 and 4.3: the bimodal distribution has effectively a step contrast in the local properties and, therefore, a $\omega^{-1/2}$ high-frequency attenuation dependence, while the unimodal distribution presents smooth transitions of the local properties and a ω^{-1} dependence.

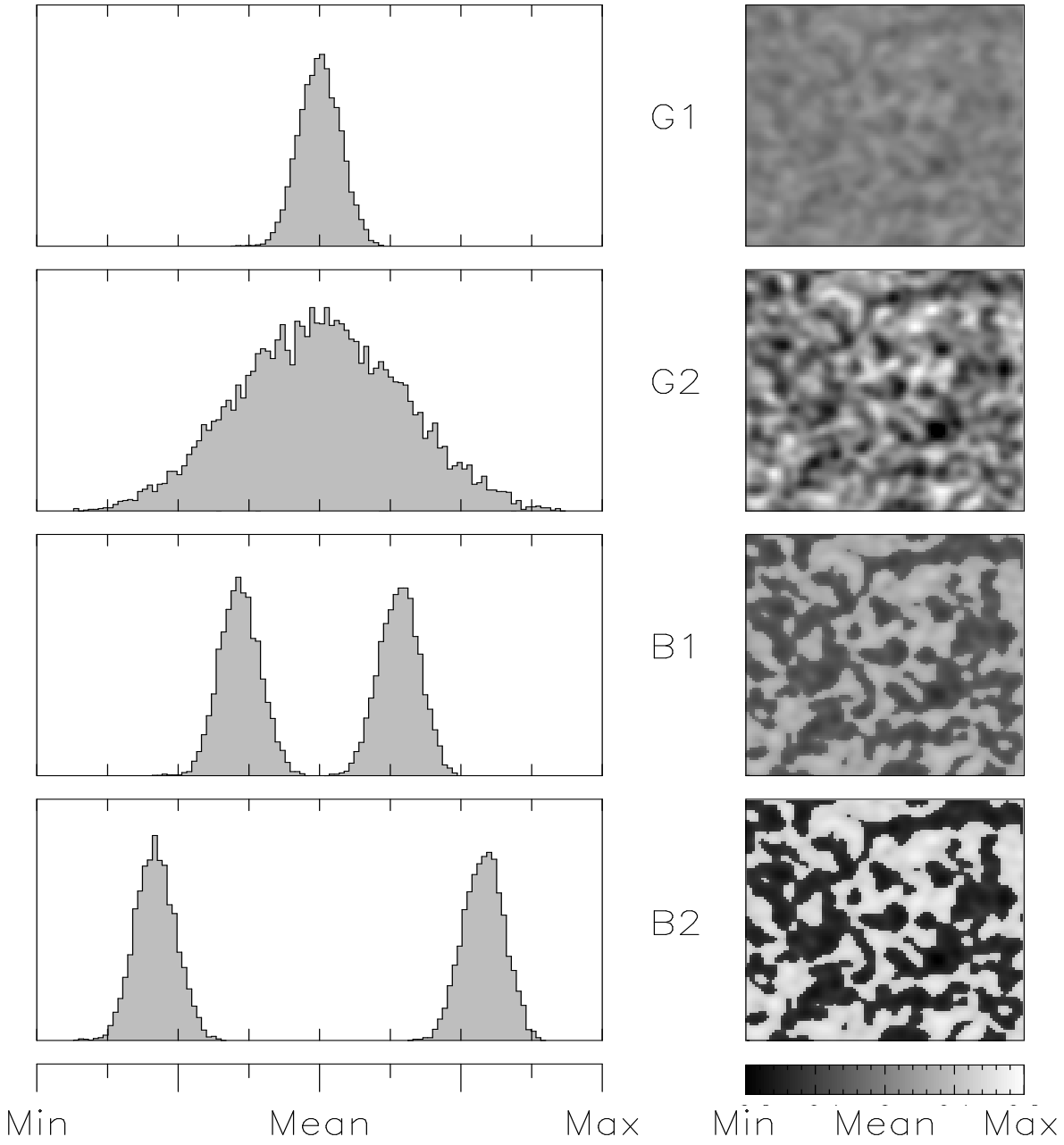

Figure 3.13. Probability density function (PDF) and spatial distribution of the physical properties after a Gaussian correlation function has been applied. Samples G1 and G2 derive from a Gaussian PDF while B1 and B2 from a bimodal PDF. The sample size is 10 centimeters and the imposed correlation length is about 1 centimeter. The physical properties used for the modeling are obtained using a linear mapping (regular binning) between the Min and Max values given in Table 3.2.

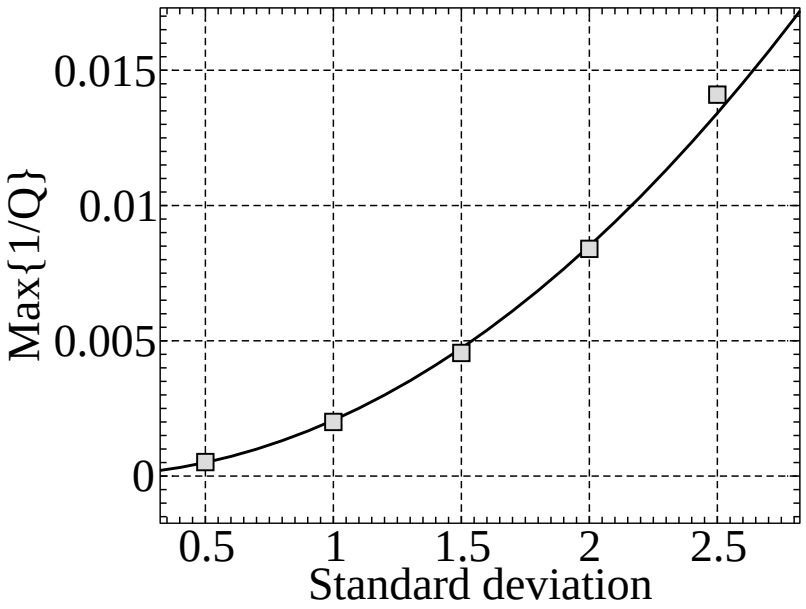

Figure 3.14. Maximum of Q^{-1} plotted as a function of the contrast in the elastic properties for a bimodal material. The samples used are similar to B1 or B2 in Figure 3.13 but with varying standards of deviations. For the mapping, we used the properties given in Table 3.2. The solid line has been obtained by fitting the data as a quadratic function of the standard of deviation.

3.1.5 Attenuation and dispersion due to pure shear

Mesoscale flow can be created even when a pure shear stress is applied to the sample. The condition required for a pure shear to create local fluid-pressure gradients is that the mesoscale geometry have some local anisotropy associated with its shape. A sand lens embedded in shaly sediments or a fracture embedded in a sandstone are natural examples of such geometric anisotropy. Isotropic geometries, such as spherical inclusions, do not permit an applied pure shear to create changes in the fluid pressure of the constituents. Since anisotropic mesoscale geometries are more geologically common than are isotropic geometries, shear-induced mesoflow should be considered the rule rather than the exception in porous rock.

An example of the fluid-pressure response due to a pure shear [having it's maximum (positive) principal stress in the vertical direction and it's minimum (negative) stress in the horizontal direction] is given in Figure 3.16. An ellipse of softer porous material is embedded within a stiffer matrix. The physical properties of the inclusion and matrix are given in Table 3.3. As the orientation of the ellipse is changed relative to the fixed principal-stress directions, there is observed to be a change in the nature of the fluid-pressure response.

When the inclusion is perpendicular (or parallel) to the principal-stress direction (E1), the dilation (or compression) of the ellipse will create a fluid-pressure difference between the inside of the ellipse and the surrounding matrix. A fluid-pressure equilibration then ensues

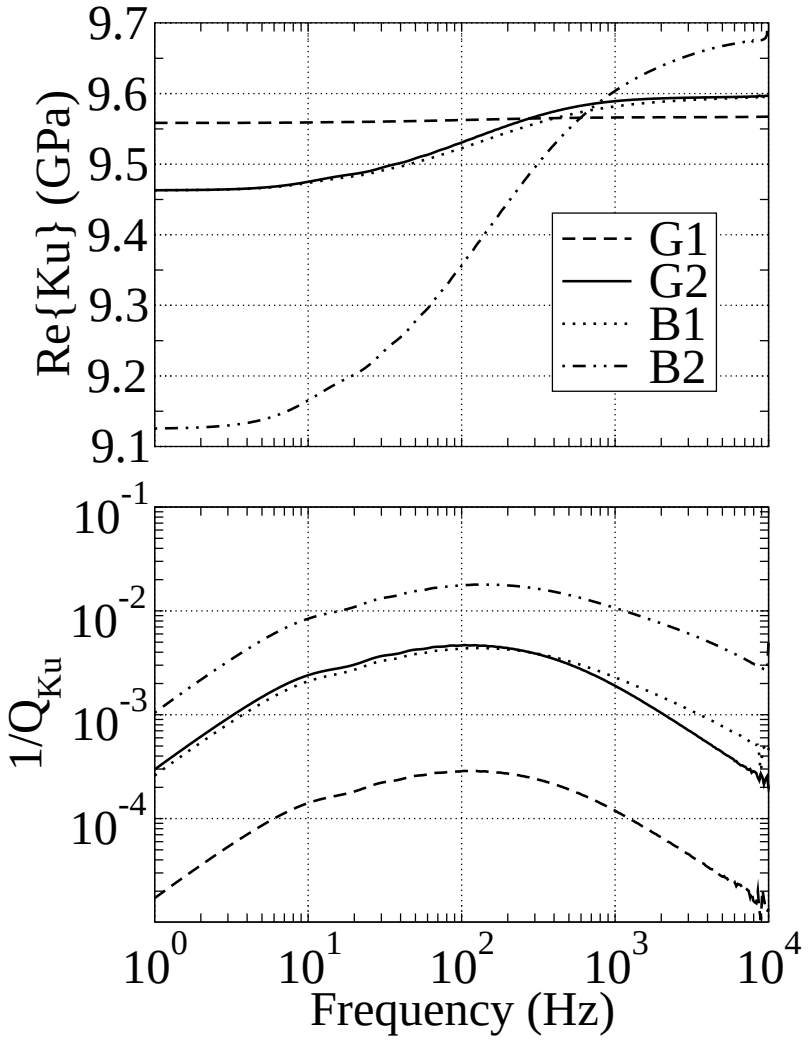

Figure 3.15. Bulk moduli K_u and the respectives attenuations Q^{-1} obtained from the samples shown in Figure 3.13. The samples that have more important local contrasts in their elastic properties (larger standards of deviations) show higher levels of attenuation and dispersion. Salient features of these results are discussed in the text.

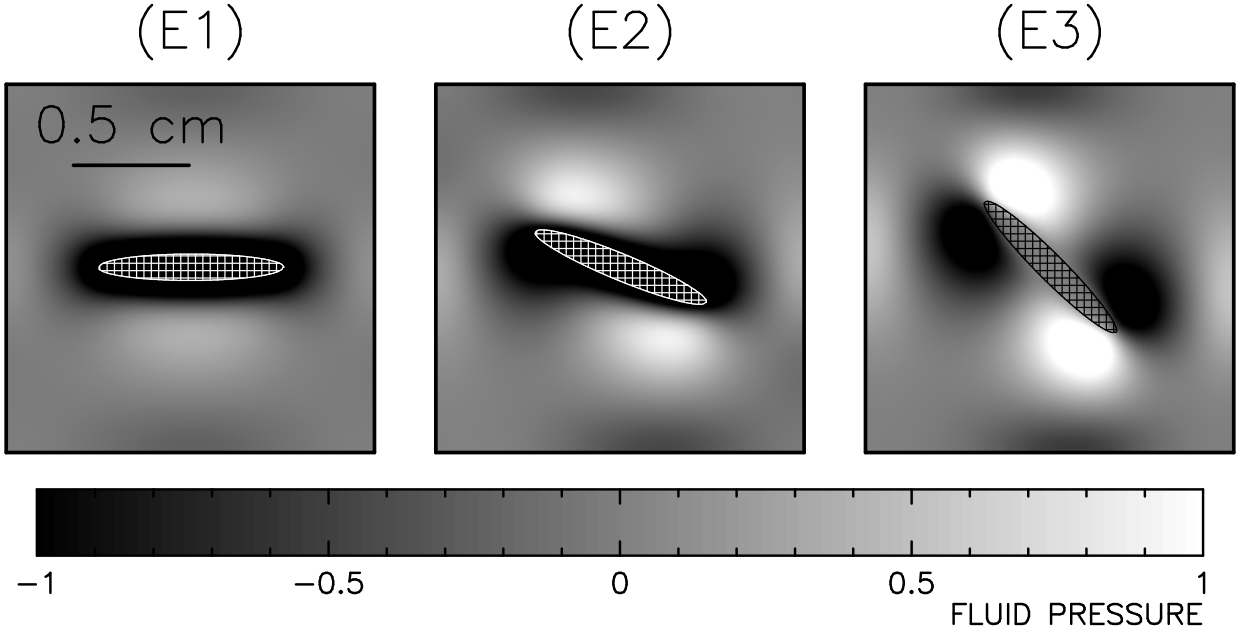

Figure 3.16. Snapshots showing the fluid pressure recorded during three pure shear experiments. Each sample contains a single heterogeneity simulating a crack. In E1, the fluid-pressure equilibration occurs between the inclusion and the matrix. In E3, the fluid pressure equilibrates between the lobes of dilatation and compression in the matrix. Finally, in E2 both kinds of equilibration occur simultaneously.

Table 3.3. Material properties of the samples shown in Figure 3.16.

Property	**Weak Inclusion**	**Matrix**
Grain		
Bulk modulus (K_s)	36.0 GPa	36.0 GPa
Density (ρ_s)	2650 kg/m^3	2650 kg/m^3
Frame		
Bulk modulus (K_d)	62.1 MPa	6.21 GPa
Shear modulus (μ)	45.5 MPa	455 MPa
Porosity (ϕ)	0.33	0.33
Permeability (k)	0 m^2	10^{-15}m^2
Fluid		
Bulk modulus (K_f)	2.25 GPa	2.25 GPa
Density (ρ_f)	10^3 kg/m^3	10^3 kg/m^3
Viscosity (η)	10^{-3} N s m^{-2}	10^{-3} N s m^{-2}

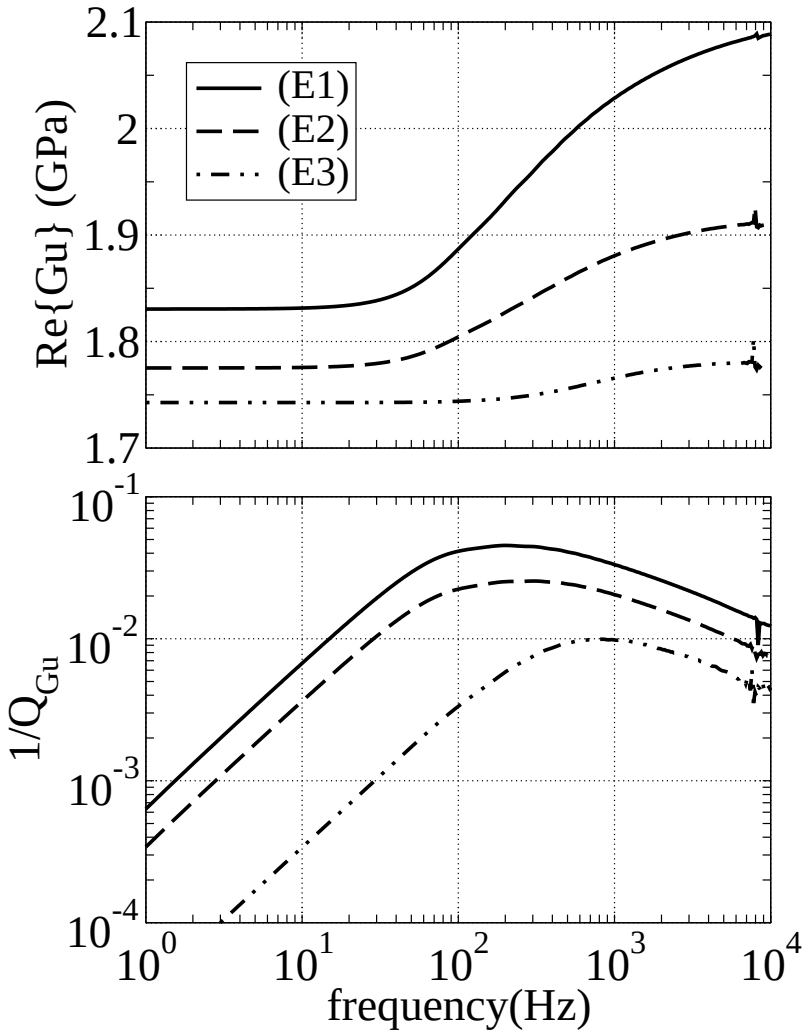

Figure 3.17. Shear modulus G and the associated attenuation Q_G^{-1} obtained from the three samples E1, E2, and E3 shown in Figure 3.16.

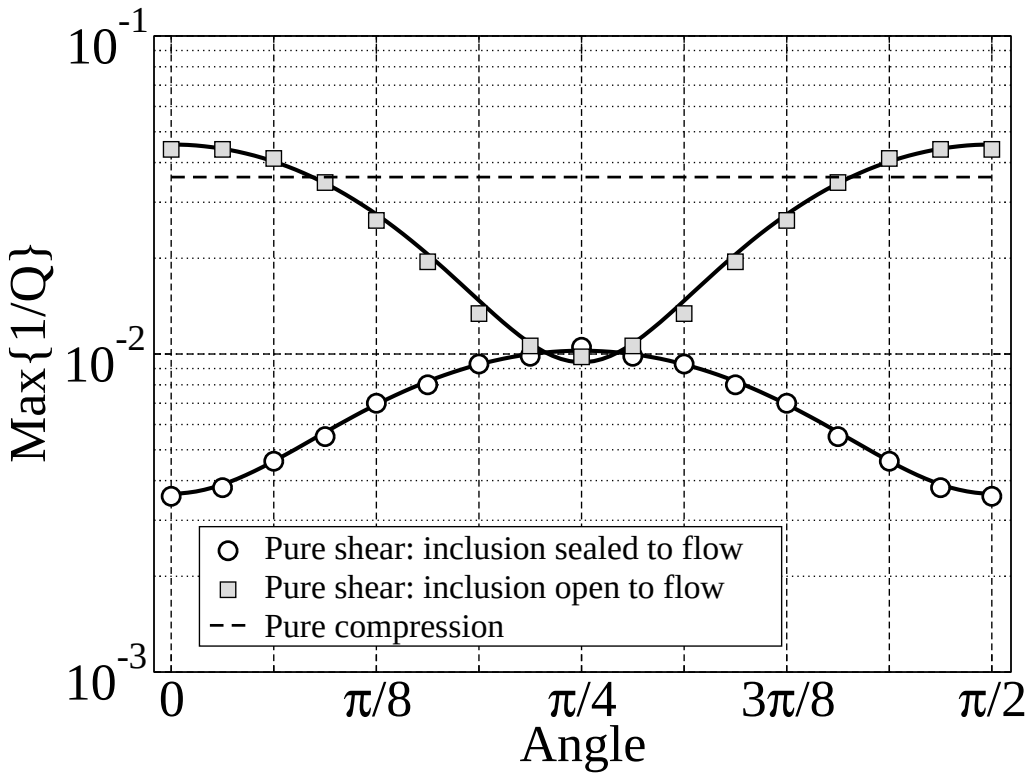

Figure 3.18. Peak attenuation as an open-to-flow ellipse (grey squares) and sealed-to-flow ellipse (white circles) are rotated relative to the principal stress directions of the pure shear. The horizontal dashed line is the measured attenuation due to a pure compression for the same geometries (ellipse orientations).

that both attenuates energy and causes the shear modulus of the composite to relax (see Figure 3.17). In this orientation (E1), the contrast in fluid pressure that is created is due to the contrast in the drained bulk modulus between the inclusion and matrix.

As the ellipse is rotated (E2), there begin to be created lobes of enhanced compression and dilation in the surrounding matrix so long as there is a contrast in the local shear modulus between the inclusion and matrix. This is in addition to the pressure change between the ellipse and matrix caused by the compressibility contrast. When the ellipse is at 45 degrees relative to the principal-stress directions (E3), the ellipse no longer has an average fluid-pressure difference between itself and the surrounding medium; however, the pressure changes in the shear lobes is at a maximum.

As seen in Figure 3.17, the greatest amount of shear-induced attenuation and dispersion is created when there develops a fluid-pressure contrast between the inside and outside of the ellipse. Again, for this to occur, there must exist an incompressibility contrast between the ellipse and matrix and the ellipse cannot be oriented at 45 degrees relative to the principal-stress direction. Another way to quantify these observations is given in Figure 3.18. A single ellipsoid having contrasts in both incompressibility and shear modulus with the surrounding matrix is rotated relative to the principal stress and the peak value of Q_G^{-1} is numerically

measured. Two curves are given in Figure 3.18 corresponding to a sealed inclusion (no fluid exchanges between the ellipse and the matrix) and to an open inclusion. For the sealed inclusion, only the equilibration in the matrix between the shear lobes occurs. For the open inclusion, both mechanisms occur. It is again seen that the attenuation, and, therefore, dispersion, is dominated by the exchanges between inclusion and matrix.

In the mechanism due to fluid exchanges between the inclusion and matrix, the peak attenuation is proportional to the square in the contrast of the incompressibility. While the peak attenuation due to equilibration between the shear lobes is proportional to the square in the contrast of the shear modulus.

3.1.6 Conclusions

In this work, we have seen how mesoscopic-scale geometry in porous samples has an influence on the seismic attenuation and dispersion of the sample. This was done by numerically determining the local poroelastic response inside such samples created by step changes in the stress acting on the sample, and averaging the deformation throughout the sample to obtain the average strain. Taking a Fourier transform of the average stress and strain and dividing, gives the complex frequency-dependent elastic moduli of the sample.

The main results are now summarized. For double-porosity materials characterized by a porous inclusion of given size embedded within a homogeneous matrix, the double-porosity theory of Pride et al. (2004), with no free parameters, fits the numerical results very well. However, for more general media characterized by having continuously variable mesoscopic structures, the assumptions of the double-porosity model breakdown along with the agreement between the analytical model and the numerical results.

In particular, it was shown that when there is a gradual transition between the porous inclusion and the surrounding matrix (as opposed to the step contrast assumed in the double-porosity model), the high-frequency asymptotic behavior of the attenuation is ω^{-1} instead of $\omega^{-1/2}$ in the case of a step contrast. Further, it was shown that having a range of sizes present produces broader curves of attenuation as a function of frequency due to the diffusional relaxation associated with each length scale present.

The peak attenuation in samples containing mesoscale heterogeneity was shown to be proportional to the square of the contrast of the moduli in the case of double-porosity models, and to the square of the standard of deviation in the compressibility distribution for the case of random media.

Last, the attenuation in pure shear was shown to be dominated by fluid exchanges between anisotropically-shaped inclusions and the surrounding matrix. Mesoflow between the shear-induced lobes of compression and dilation in the matrix surrounding the inclusion was shown to be much less important.

3.2 Acoustic attenuation in self-affine porous structures

(Published in the PHYSICAL REVIEW LETTERS,
S. R. Pride and Y. J. Masson ,Phys. Rev. Lett., Volume 97, Issue 18, 184301, 2006.)

Understanding the physics of mechanical wave propagation in porous materials impacts a wide range of applications ranging from the exploration of the earth's crust, to the design of sound absorbing materials, to the non-destructive evaluation of fractured materials. From a fundamental physics perspective, perhaps the greatest challenge is to understand the way that heterogeneity across all length scales smaller than the acoustic wavelength affects the nature of the wave propagation.

In order to define porous-material properties, one needs to consider samples that contain a minimum of roughly 3 grains to the side. Most natural porous materials such as rocks and sediments in the earth have heterogeneity in the porous-continuum properties (e.g., the elastic moduli, density, and fluid-flow permeability of the grain packs) at nearly all scales greater than a few grain sizes ($\geq 10^{-3}$ m). Sound-absorbing porous materials can be manufactured to have heterogeneity over these scales as well. Seismic wavelengths used for exploration of the earth's crust are typically in the range from 1 to 100 m. Further, airborne sound, upon entering sound-absorbing porous materials, typically have wavelengths on the order of 0.1 to 1 m. There are thus a wide range of so-called "mesoscopic" length scales l that are larger than grain sizes d (i.e., can be modeled as a porous-continuum), but smaller than acoustic wavelengths λ. Figure 3.19 graphically depicts the length-scale relation $\lambda > l > d$. For the purpose of modeling an acoustic experiment, it is generally necessary to define the porous-continuum properties at a scale (resolution) of roughly a tenth of a wavelength.

Many studies [1-10] have focused on the effective acoustic properties of fluid-filled porous media in the presence of mesoscopic length-scale heterogeneity. When an acoustic wave compresses a sample of porous material containing mesoscopic heterogeneity, the fluid-pressure response will be relatively large in regions where the compressibility of the framework of grains is large, and small where the framework compressibility is small. A process of fluid-pressure equilibration (i.e., viscous fluid flow) ensues that is capable of attenuating significant amounts of acoustic wave energy.

In the present Letter, we focus on the complex bulk modulus $K_u(\omega)$ of sealed samples of porous media that contain a self-affine fractal structure in the local compressibility of the framework of grains. The subscript u denotes "undrained" which signifies that no fluid exchanges into or out of the sample are allowed to occur. An undrained modulus is of interest because it can be shown (e.g., Ref. [11]) that over the acoustic frequencies ω used in both exploration work and audible-sound absorption (1 Hz $< \omega/2\pi <$ 10 kHz), no significant fluid exchanges occur between the averaging volumes used to define the effective properties and the surrounding material. Any induced flow that needs to be allowed for is occuring within the averaging volume (sample) and is due to the presence of mesoscopic-scale heterogeneity.

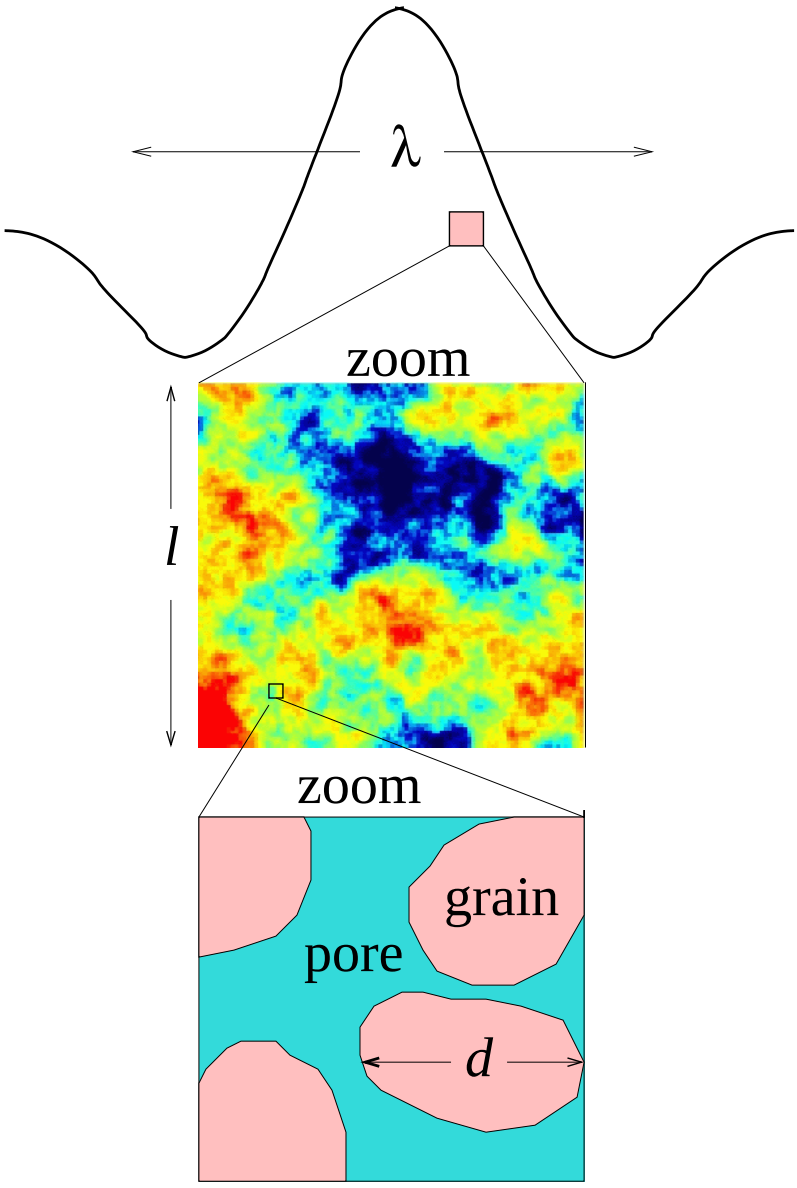

Figure 3.19. Depiction of the length-scale relation $\lambda > l > d$ where λ is the wavelength of the acoustic pulse, l is the linear dimension of a sample containing mesoscopic-scale heterogeneity in the local porous-continuum properties, and d is a characteristic size of a grain.

To obtain the complex undrained bulk modulus, one can first apply a temporal step in the normal stress $-P$ that acts uniformly on the sealed exterior faces of a sample of material. The induced volumetric strain of the sample $\epsilon = \delta V/V$ is then measured through time, and a temporal Fourier transform taken of both the applied stress and measured deformation to yield $K_u(\omega) = -\tilde{P}(\omega)/\tilde{\epsilon}(\omega)$. The compressional attenuation associated with the phase shift between stress and strain is conveniently described using a quality factor Q_{Ku} defined as

$$\frac{4\pi}{Q_{Ku}} = \frac{\text{total energy lost per stress period}}{\text{average energy reversibly stored per period}} \tag{3.24}$$

$$= \frac{\text{Im}\{K_u(\omega)\}}{\text{Re}\{K_u(\omega)\}}. \tag{3.25}$$

It is straightforward to demonstrate that the physical definition of Eq. (3.24) is equivalent to the operational definition of Eq. (3.25) [12].

Our approach here is to measure $K_u(\omega)$ numerically by performing finite-difference simulations of the above experiment. Details of how the finite-difference algorithm works are given by Masson and Pride [13,14]. The numerical simulations are based on the laws of poroelasticity [15, 16] that provide a continuum description allowing for fluid-pressure changes and fluid flow in addition to the elastic deformation and acceleration of the material. The region Ω occupied by a sample under study is discretized into a cartesian grid at a scale Δx that still implicitly contains within it enough grains ($\Delta x > 3d$) to justify a porous-continuum description of the local physics. The local porous-material properties (elastic moduli of the framework of grains, permeability, density) are distributed over the pixels (2D) or voxels (3D) of size Δx, and the complex bulk modulus of the sample determined by numerically performing the experiment of the previous paragraph.

Let C be an elastic modulus associated with the framework of grains that is specified at each grid point within the sample and that fluctuates locally over the grid. The fluctuations $\Delta C(a\Delta x)$ in C associated with each length scale $a\Delta x$ where $a > 1$ generally vary in real materials as the scale factor a varies. A self-affine fractal means that

$$\Delta C(a\Delta x) \propto a^H \, \Delta C(\Delta x) \tag{3.26}$$

where H is called the Hurst exponent ($H = 1$ corresponds to a self-similar fractal). In practice, since Δx is a finite length ($> 3d$), the fluctuation $\Delta C(\Delta x)$ at the smallest scale $a = 1$ is taken to be the standard of deviation of the probability distribution used to randomly populate the grid with C values.

We generate self-affine fractal structure within our synthetic samples using the following algorithm: (1) Generate a pseudo-random realization $W(\mathbf{x})$ of the white noise associated with the desired statistical distribution of the material property over the grid points $\mathbf{x}$; (2) Calculate a spatial Fourier transform $\tilde{W}(\mathbf{k})$ of this white noise; (3) Multiply the white noise with the spectral filter $\tilde{F}(\mathbf{k}) \propto |\mathbf{k}|^{-E/2-H}$ representing the correlation function of the self-affine fractal where E is the Euclidean-space dimension; (5) Calculate the inverse Fourier transform of the filtered white noise; and (6) Normalize to the desired variance and add the appropriate mean to obtain the final realization of the self-affine fractal material property.

It has been numerically verified that self-affine structure generated in this manner possesses the scaling of Eq. (3.26) in both 2D and 3D.

The compressional attenuation as a function of frequency $Q_{Ku}^{-1}(\omega)$ numerically determined for a material possessing self-affine structure in the bulk modulus of the dry framework of grains is shown in Fig. 3.20. A Gaussian distribution was used to generate the random fractal structure. At low frequencies, there is observed a power-law relation $Q_{Ku}^{-1}(\omega) \propto \omega$ that can be attributed to the finite size of the sample (as will be explained shortly). At high enough frequencies where the fluid-pressure-diffusion penetration length $\delta = \sqrt{D/\omega}$ (D is the fluid-pressure diffusivity) is much smaller than the size of the sample, the finite-size of the sample does not influence the diffusion process and a more interesting power-law relation is observed $Q_{Ku}^{-1}(\omega) \propto \omega^{-H}$. The example given in Fig. 3.20 is a 2D simulation (implicitly, a 3D experiment in which no deformation occurs in the third dimension which necessitates the shear modulus to be measured in order to obtain K_u [14]); however, the same scaling holds for a fully 3D experiment.

Figure 3.21 gives the high-frequency power-law exponent of $Q_{Ku}^{-1}(\omega)$ corresponding to materials covering a range of H values. When the Hurst exponent has a large magnitude compared to one ($|H| \gg 1$), the attenuation exponent tends to either +1 (large negative H) or -1 (large positive H). This suggests the following scaling relation valid for all H

$$Q_{Ku}^{-1}(\omega) \propto \omega^{-\tanh H} \tag{3.27}$$

that, in Fig. 3.21, is seen to do an excellent job of fitting the numerical data. Equation (3.27) and Figs. 3.20 and 3.21 are the main results of this Letter.

We now explain these observations. The rate at which energy is locally being lost per unit volume of porous material is $(k/\eta)|\nabla p_f|^2$ where k is the local fluid-flow permeability, η is the fluid viscosity, and p_f the fluid pressure. If, as in the above examples, the amount of dissipated energy in each cycle is small compared to the amount of stored energy, the average energy reversibly stored per unit volume is half the peak stored energy $K_U\epsilon^2$ where K_U is the local (and real) undrained bulk modulus and ϵ the local volumetric strain. Equation (3.24) then gives

$$Q_{Ku}^{-1} = \frac{1}{\omega\eta}\frac{\int_\Omega k|\nabla p_f|^2\, dV}{\int_\Omega K_U\epsilon^2\, dV}. \tag{3.28}$$

An approximate analysis of this expression is provided that retains the essential elements required to produce the attenuation scaling law of Eq. (3.27).

Each length scale $a\Delta x$ will make its own contribution to Q_{Ku}^{-1}. If the only heterogeneity in the system occured at the length scale $a\Delta x$, the attenuation curve $Q_a^{-1}(\omega)$ associated exclusively with this scale a would rise linearly in ω up to a peak value, then descend as $\omega^{-1/2}$ [6-10]. Peak attenuation at scale a occurs at the frequency ω_a at which the fluid-pressure just has time to diffuse across the distance $a\Delta x$ in a single cycle; i.e., it occurs at the frequency $\omega_a = D/(a\Delta x)^2$. Here, D is the fluid pressure diffusivity that is well approximated as (c.f., Ref. [11]) $D = kK_f/(\eta\phi)$ where K_f is the fluid's bulk modulus and ϕ is porosity.

We will make the approximation that the full attenuation curve $Q_{Ku}^{-1}(\omega)$ in the presence

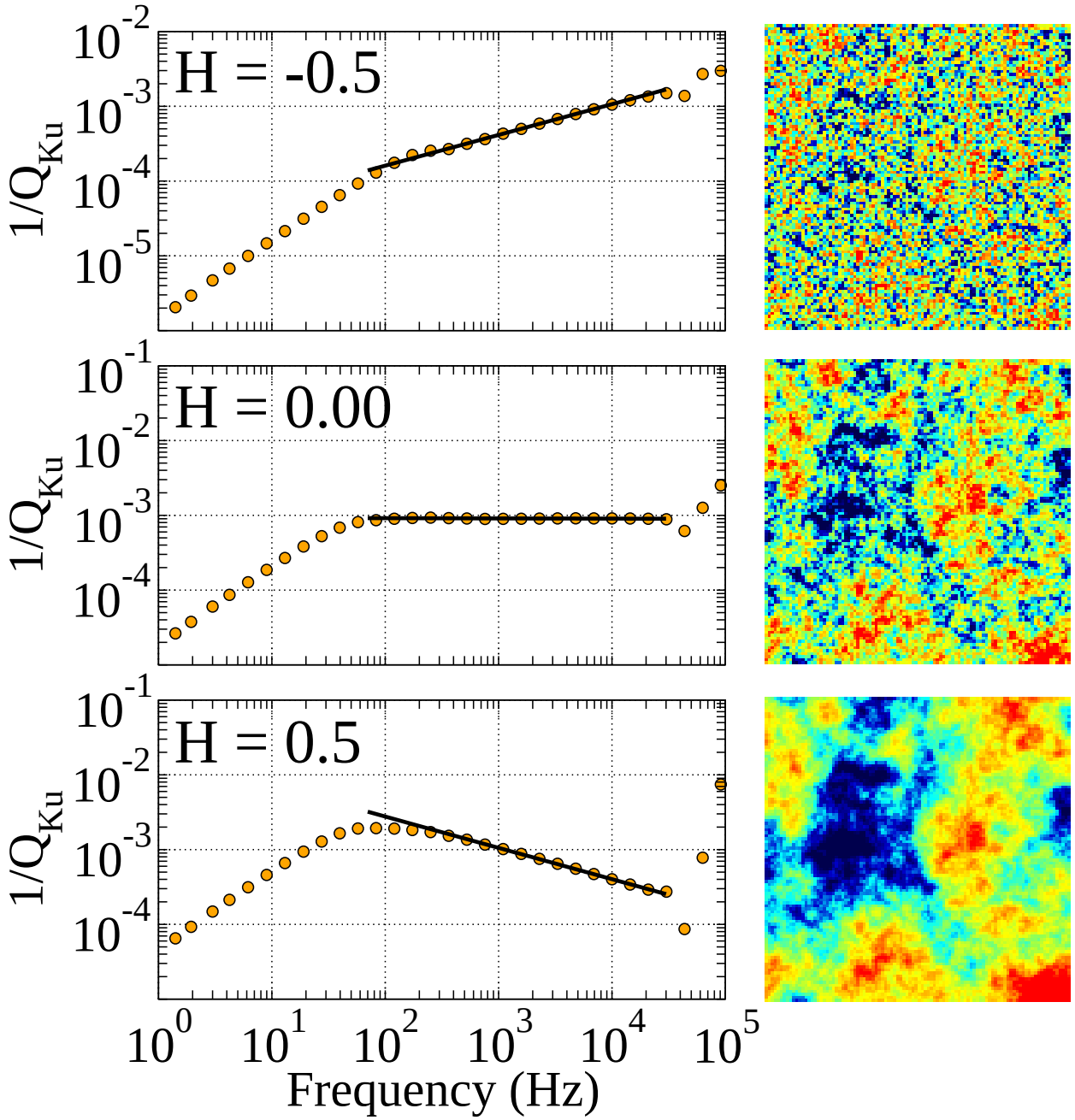

Figure 3.20. Results of 2D numerical simulations of $Q_{Ku}^{-1}(\omega)$ for synthetic samples that have different Hurst exponents. The symbols are numerical data and the solid line corresponds to ω^{-H}. To the right are images of the self-affine structure present in the porous-continuum elastic modulus.

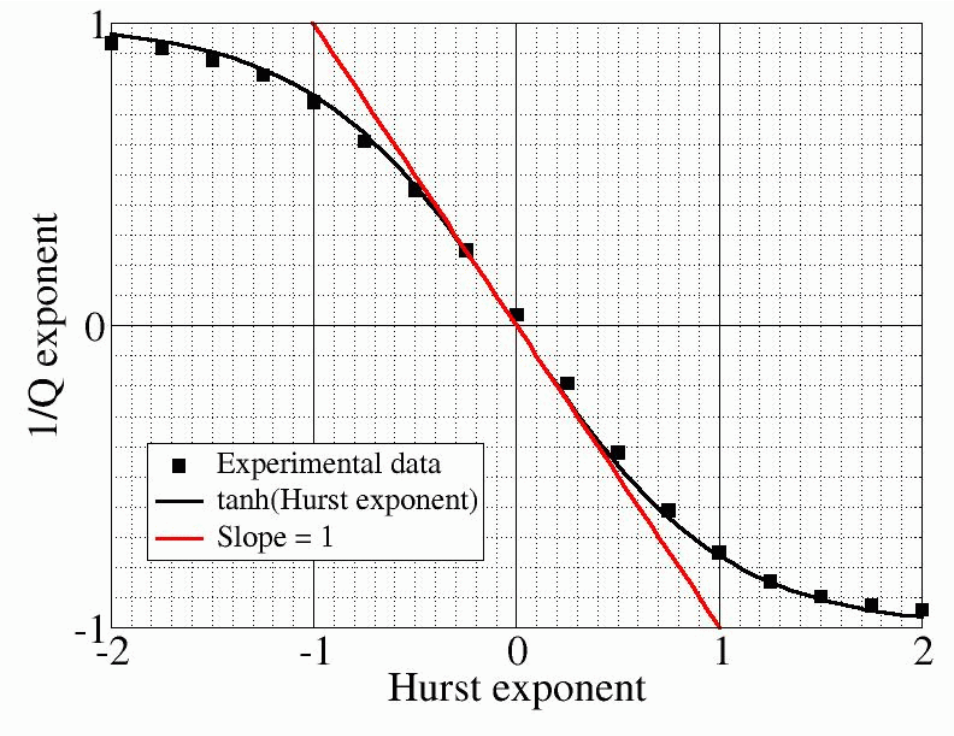

Figure 3.21. Demonstration that $Q_{Ku}^{-1}(\omega) \propto \omega^{-\tanh H}$ does a fine job fitting the numerical data.

of all length scales corresponds to the envelope bounding the sum of the attenuation curves coming from each length scale. In the presence of a continuum of length scales a, this is very well approximated as $Q_{Ku}^{-1}(\omega) = Q_a^{-1}(\omega_a)\ \forall\ a$.

To determine the peak values $Q_a^{-1}(\omega_a)$ of the attenuation associated with each scale a, we return to Eq. (3.28). The local pressure gradient driving the fluid flow is created by the volumetric compression acting on the heterogeneous grain pack and is approximated as $|\nabla p_f| \approx \Delta C(a\Delta x)\epsilon/a\Delta x$ where C is the elastic modulus responsible for creating a fluid-pressure change in the grain pack from the applied volumetric strain; i.e., $C = p_f/\epsilon$ and is, like K_U, defined assuming undrained (sealed sample) conditions. Expressions that detail how C depends on the bulk modulus of the dry framework of grains and on the moduli of the fluid and solid phases can be found in many places including Ref. [11]. Further, in this "order-of-magnitude" analysis, we replace all locally varying fields by their mean values in the system (denoted with $\langle\ \rangle$) to obtain an estimate of the peak attenuation associated with scale a

$$Q_a^{-1}(\omega_a) \approx \frac{\langle k\rangle[\Delta C(a\Delta x)]^2}{\omega_a \eta (a\Delta x)^2 \langle K_U\rangle} = \frac{\langle\phi\rangle[\Delta C(a\Delta x)]^2}{K_f\langle K_U\rangle} \tag{3.29}$$

where

$$\omega_a = \frac{\langle k\rangle K_f}{\eta\langle\phi\rangle(a\Delta x)^2} \tag{3.30}$$

was used for the frequency of peak attenuation at scale a. Equation (3.29) predicts that the peak attenuation associated with a given scale is proportional to the square of the fluctuation at that scale.

To obtain the full curve for the self-affine material, we employ the definition of a self-affine fractal $\Delta C(a\Delta x) = a^H \Delta C(\Delta x)$ and rearrange Eq. (3.30) to give an expression for a in terms of ω_a. Putting this in Eq. (3.29) gives the desired frequency scaling law

$$Q_a^{-1}(\omega_a) = Q_{Ku}^{-1}(\omega) = \frac{\langle\phi\rangle[\Delta C(\Delta x)]^2}{K_f\langle K_U\rangle}\ \left(\frac{\omega}{\omega_1}\right)^{-H} \tag{3.31}$$

where ω_1 is the ω_a of Eq. (3.30) evaluated at $a = 1$. The result of Eq. (3.31) also demonstrates that the attenuation curve is proportional to the variance $[\Delta C(\Delta x)]^2$ of the probability distribution used to randomly distribute the elastic moduli through the sample; a result that has also been numerically confirmed.

In the limits that $|H| \to \infty$, two other scaling rules emerge. As $H \to -\infty$, the only fluctuations present in the sample are those occuring at the smallest scale $a = 1$. Across the finite bandwidth we study, this means we are always in the low-frequency regime where attenuation is increasing linearly with frequency. To explain such linear in ω scaling, we again appeal to Eq. (3.28). At low enough frequencies, the diffusive penetration of the fluid pressure across the low-diffusivity patches of size Δx (the only patches of significance when $H \to -\infty$) occurs rapidly during each stress period, and any remaining pressure gradients are decreasing linearly with decreasing ω not because the diffusion distance is changing, but because the average fluid-pressure difference Δp_f between two local patches is decreasing with ω. Using theoretical results from Ref. [7], one has in this case that $|\nabla p_f| \approx \Delta p_f(\omega)/\Delta x = \alpha(\eta\Delta x\epsilon/k)\omega$ where α is a dimensionless material property bounded as $0 < \alpha < 1$ (c.f., Ref. [7] for the

detailed nature of α). Using this in Eq. (3.28) gives that $\lim_{H\to-\infty} Q_{Ku}^{-1} \propto \omega$ as is numerically observed in the simulations.

As $H \to +\infty$, the dominant fluctuation is that at the scale $a = s$ of the sample itself. In this scenario, over the finite frequency band-width available, we are always in the high-frequency regime where fluid-pressure penetration distances are less than the scale $s\Delta x$ of the sample. The sample-scale fluctuation of the elastic moduli is thus responsible for a sample-scale fluctuation of the fluid pressure so that the fluid-pressure gradient to be used in Eq. (3.28) is independent of frequency and given by $|\nabla p_f| \approx \Delta C(s\Delta x)\epsilon/(s\Delta x)$. Using this in Eq. (3.28) predicts that $\lim_{H\to+\infty} Q_{Ku}^{-1} \propto \omega^{-1}$ as is numerically observed. Combining these results for both the large and small $|H|$ limits yields $Q_{Ku}^{-1} \propto \omega^{-\tanh H}$ which is consistent with the numerical data.

The fact that there exists a simple relation between the frequency exponent for the acoustic attenuation in a self-affine porous material and the Hurst exponent of the structure is the central "interesting" result of this Letter. Many earth scientists (e.g., Klimes 2002 and Pilkington 1990) believe that a reasonable stochastic model for earth materials is self-affine structure in the physical properties with $-1/2 < H < 0$ (property fluctuations decreasing with increasing scale). We encourage laboratory (or field) experimentalists to look for the powerlaw relation $Q_{Ku}^{-1} \propto \omega^{-H}$ that might hold in such heterogeneous earth materials. Unfortunately, this requires performing acoustic (or quasi-elastostatic) measurements on samples much larger than normally considered. To obtain two decades of length-scale variation within a sample, one needs to work with sample sizes on the order of tens of centimeters to a meter. Most laboratory protocols for measuring attenuation employ samples that are several centimeters in size.

The work of S. R. P. was performed under the auspices of the U.S. Department of Energy and supported specifically by both the Geosciences Research Program of the DOE Office of Basic Energy Sciences, Division of Chemical Sciences, Geosciences and Biosciences (BES Contract No. 468115) and by the Fossil Energy Program administered by NETL (Contract No. G32801).

3.3 Can we deduce the shape of heterogeneities in porous rocks from the seismic attenuation ?

(Not yet submitted for publication.)

3.3.1 Introduction

The aim of this paper is to establish a relation between anisotropy in poroelastic attenuation and the aspect ratios of mesoscopic heterogeneities present in porous composites.

Typical heterogeneities encountered in natural rocks include cracks, stratification, and to some extent fluid patches for the case of partial saturation. Many analytical models predict that when such heterogeneity is present within porous rocks, wave-driven fluid flow can produce significant attenuation levels in the seismic band of frequencies. These models include Pride and Berryman (2003a,b) and Pride et al. (2004) for lithological heterogeneities; White (1975), Johnson (2001) and Pride et al. (2004) for fluid patches; White et al. (1975), Norris (1993), and Gurevich and Lopatnikov (1995) for layered media; and Mavko and Nur (1979), Dvorkin et al. (1995), and Pride et al. (2004) for cracks. Unfortunately, none of these models has yet been extended to anisotropic materials and no analytical relation between the attenuation levels of waves propagating in different spatial directions and the geometry of the heterogeneities is currently available. Recently, Tserkovnyak and Johnson (2002) demonstrated that it is possible to use the patchy saturation model to deduce the shape of fluid patches from acoustic attenuation and dispersion measurement. Their method can be used to determine the value of V/A, the ratio of the volume to area of the water patch, and l_f, the Poisson size of the water patch, using the attenuation and dispersion associated with a single elastic modulus. However, the method is limited in the sense that it provides no information on the orientation of fluid patches. As no theory is currently available, we propose to solve the delicate problem of anisotropic attenuation in poroelastic materials numerically. In a recent paper (Masson and Pride 2007), we introduced a computationally-efficient method to determine attenuation and dispersion in porous material that contains an arbitrary amount of mesoscopic-scale heterogeneities. In the first section of the present paper, we show that this method can be used to evaluate the attenuation levels associated with different elastic moduli in the case of an anisotropic porous material. In the second section, we present numerical estimations of the dispersion and attenuation associated with porous materials that are locally isotropic, but where the presence of mesoscale heterogeneity induces anisotropy at the macroscopic scale. Finally, in the last section, an analytical solution for the relative attenuations associated with the different elastic moduli is derived.

3.3.2 Numerical method

For the general case of a fully-anisotropic hookean solid, the stress and strain tensors are related by

$$\sigma_{ij} = C_{ijkl}\epsilon_{kl} \quad (\text{sum over } k \text{ and } l) \tag{3.32}$$

where, σ_{ij} is the stress tensor, ϵ_{kl} is the strain tensor, and C_{ijkl} is the stiffness tensor. Due to the symmetry of the stress, strain, and stiffness tensors, only 21 elastic constants are independent in the general case. For more simplicity, we limit our study to the case of orthotropic materials; i.e., materials for which the elastic properties differ in only the

orthogonal directions of space. In such materials, Equation 3.32 reduces to

$$\begin{bmatrix} \sigma_{xx} \\ \sigma_{yy} \\ \sigma_{zz} \\ \sigma_{yz} \\ \sigma_{zx} \\ \sigma_{xy} \end{bmatrix} = \begin{bmatrix} M_{11} & M_{12} & M_{13} & & & \\ M_{21} & M_{22} & M_{23} & & & \\ M_{31} & M_{32} & M_{33} & & & \\ & & & G_1 & & \\ & & & & G_2 & \\ & & & & & G_3 \end{bmatrix} \begin{bmatrix} \epsilon_{xx} \\ \epsilon_{yy} \\ \epsilon_{zz} \\ \epsilon_{yz} \\ \epsilon_{zx} \\ \epsilon_{xy} \end{bmatrix} \tag{3.33}$$

Where $M_{ii} = C_{iiii}$, $M_{ij} = C_{iijj}$, $G_i = 2C_{jkjk}$ (no sum on i, j, and k, and $i \neq j \neq k$), and there are only 9 elastic constants that are independent because $M_{ij} = M_{ji}$. The linear system in Equations 3.33 has fewer equations than variables; thus, multiple experiments need to be performed in order to compute the M_{ij} and G_i moduli. For a rectangular cuboid sample with faces perpendicular to the x, y, and z directions of space, the moduli M_{11}, M_{21}, and M_{31} can be computed by applying a time-varying strain $\epsilon_{xx}(t)$ on the faces perpendicular to the x axis and imposing a zero strain in the direction perpendicular to the other faces (i.e. $\epsilon_{yy}(t) = 0$ on the faces perpendicular to the y axis, and $\epsilon_{zz}(t) = 0$ on the faces perpendicular to the z axis). The stress fields are zero outside the sample and a sealed boundary condition is applied to all faces of the sample (i.e. no fluid is allowed to escape the sample). The experiments are performed in the time domain and the averaged fields $\langle \epsilon_{xx} \rangle_\Omega (t)$, $\langle \sigma_{xx} \rangle_\Omega (t)$, $\langle \sigma_{yy} \rangle_\Omega (t)$, and $\langle \sigma_{zz} \rangle_\Omega (t)$ are recorded versus time. Here, $\langle x \rangle_\Omega$ denotes the average of the field x over the volume Ω occupied by the sample. Finally, once the experiment is finished, the moduli M_{11}, M_{21}, and M_{31} can be computed versus frequency by taking a Fourier transform FT of the averaged fields recorded and by computing the ratios

$$M_{11}(\omega) = \frac{\mathrm{FT}\left\{\langle \sigma_{xx} \rangle_\Omega (t)\right\}}{\mathrm{FT}\left\{\langle \epsilon_{xx} \rangle_\Omega (t)\right\}} \tag{3.34}$$

$$M_{21}(\omega) = \frac{\mathrm{FT}\left\{\langle \sigma_{yy} \rangle_\Omega (t)\right\}}{\mathrm{FT}\left\{\langle \epsilon_{xx} \rangle_\Omega (t)\right\}} \tag{3.35}$$

$$M_{31}(\omega) = \frac{\mathrm{FT}\left\{\langle \sigma_{zz} \rangle_\Omega (t)\right\}}{\mathrm{FT}\left\{\langle \epsilon_{xx} \rangle_\Omega (t)\right\}}. \tag{3.36}$$

The moduli M_{12}, M_{22}, and M_{32} can be obtained using the same procedure in a second experiment where a time-varying strain $\epsilon_{yy}(t)$ is applied on the faces perpendicular to the y axis. In this case, we have

$$M_{12}(\omega) = \frac{\mathrm{FT}\left\{\langle \sigma_{xx} \rangle_\Omega (t)\right\}}{\mathrm{FT}\left\{\langle \epsilon_{yy} \rangle_\Omega (t)\right\}} \tag{3.37}$$

$$M_{22}(\omega) = \frac{\mathrm{FT}\left\{\langle \sigma_{yy} \rangle_\Omega (t)\right\}}{\mathrm{FT}\left\{\langle \epsilon_{yy} \rangle_\Omega (t)\right\}} \tag{3.38}$$

$$M_{32}(\omega) = \frac{\mathrm{FT}\left\{\langle \sigma_{zz} \rangle_\Omega (t)\right\}}{\mathrm{FT}\left\{\langle \epsilon_{yy} \rangle_\Omega (t)\right\}}. \tag{3.39}$$

Similarly, a third experiment where a time-varying strain $\epsilon_{zz}(t)$ is applied on the faces perpendicular to the z axis gives the moduli

$$M_{13}(\omega) = \frac{\mathrm{FT}\left\{\langle\sigma_{xx}\rangle_\Omega(t)\right\}}{\mathrm{FT}\left\{\langle\epsilon_{zz}\rangle_\Omega(t)\right\}} \tag{3.40}$$

$$M_{23}(\omega) = \frac{\mathrm{FT}\left\{\langle\sigma_{yy}\rangle_\Omega(t)\right\}}{\mathrm{FT}\left\{\langle\epsilon_{zz}\rangle_\Omega(t)\right\}} \tag{3.41}$$

$$M_{33}(\omega) = \frac{\mathrm{FT}\left\{\langle\sigma_{zz}\rangle_\Omega(t)\right\}}{\mathrm{FT}\left\{\langle\epsilon_{zz}\rangle_\Omega(t)\right\}}. \tag{3.42}$$

In order, to compute the remaining moduli G_1, G_2, and G_3, we perform three additional experiments where a time-varying shear stress $\sigma_{ij}(t)$ is applied on the faces of the sample. The stresses normal to the sample's faces are zero outside the sample and a sealed boundary condition is applied on all the faces. In each experiment, the average strain $\langle\epsilon_{ij}\rangle_\Omega(t) = \langle 1/2[\epsilon_{ii}+\epsilon_{jj}]\rangle_\Omega(t)$ induced by the applied stress $\sigma_{ij}(t)$ is recorded versus time and the G_i moduli are

$$G_1(\omega) = \frac{\mathrm{FT}\left\{\langle\sigma_{yz}\rangle_\Omega(t)\right\}}{\mathrm{FT}\left\{\langle\epsilon_{yz}\rangle_\Omega(t)\right\}} \tag{3.43}$$

$$G_2(\omega) = \frac{\mathrm{FT}\left\{\langle\sigma_{zx}\rangle_\Omega(t)\right\}}{\mathrm{FT}\left\{\langle\epsilon_{zx}\rangle_\Omega(t)\right\}} \tag{3.44}$$

$$G_3(\omega) = \frac{\mathrm{FT}\left\{\langle\sigma_{xy}\rangle_\Omega(t)\right\}}{\mathrm{FT}\left\{\langle\epsilon_{xy}\rangle_\Omega(t)\right\}}. \tag{3.45}$$

Last, the attenuation associated with a given elastic modulus C_{ij} can be evaluated by computing the inverse quality factor (Masson and Pride, 2007)

$$Q^{-1}_{C_{ij}}(\omega) = \frac{\mathrm{Im}\{C_{ij}(\omega)\}}{\mathrm{Re}\{C_{ij}(\omega)\}} \tag{3.46}$$

where the subscript on Q^{-1} refers to the modulus from which it has been derived.

3.3.3 Numerical results

In Figure 3.22, we show that the mesoscale fluid-pressure anomalies that drive the fluid flow can be created in two different ways in fluid-saturated porous samples. On the one hand, when the sample is subject to a global volume change, the fluid pressure response is heterogeneous and correlates with the local incompressibilities within the sample. On the other, when the sample is subject to some amount of shear stress, mesoscale heterogeneities can create fluid-pressure anomalies due the local anisotropy associated with their shape. In Figure 3.22 (a), we present the fluid pressure observed during a uniaxial compressional experiment with a sample containing a single ellipsoidal heterogeneity. We see that the pressure increase is more important in the ellipsoid, which is more compressible, than in the

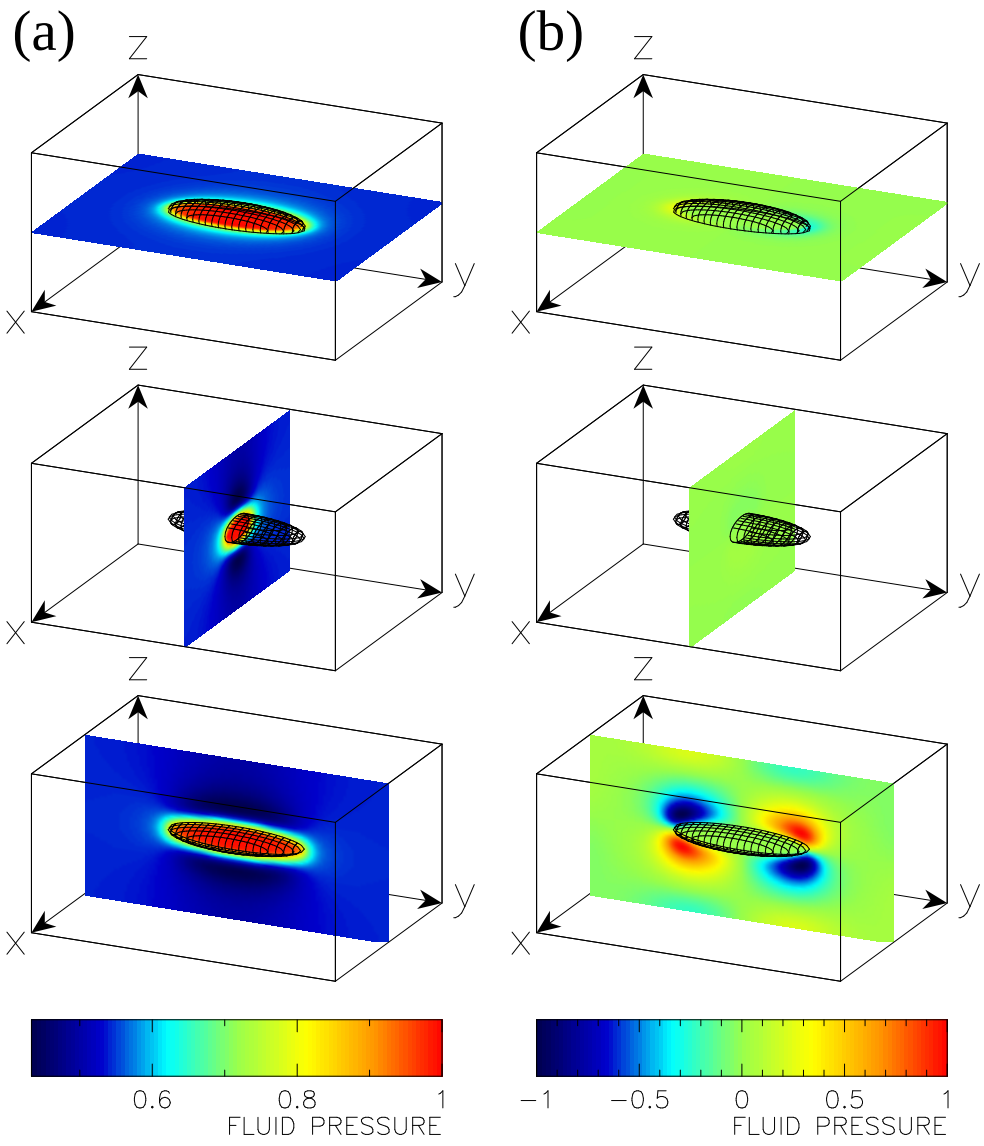

Figure 3.22. Snapshots showing the fluid pressure recorded during a uniaxial compression experiment (a) and a simple shear experiment (b). The sample consists of a homogeneous matrix containing a single ellipsoidal heterogeneity. In (a), most of the fluid equilibration occurs between the inclusion and the matrix. In (b), the fluid pressure equilibrates between the lobes of compression and dilatation induced in the matrix by the heterogeneity.

surrounding matrix, which is stiffer. Even if the sample is homogeneously compressible in the matrix outside the ellipsoid, fluid-pressure anomalies also occur within the matrix due to the presence of heterogeneity. In Figure 3.22 (b), a tangential shear stress is applied to the sample. In this case the volume of the sample, and hence the average fluid pressure, remains constant during the experiments. However, lobes of fluid-pressure anomaly appear in the surrounding material due to the local anisotropy created by the ellipsoid. Figure 3.22 clearly emphasizes the fact that the way the fluid-pressure equilibrates within the sample strongly depends on how the sample is deformed or stressed relative to the orientation of the heterogeneity. Consequently, attenuations associated with the different elastic moduli will not necessarily be equal in anisotropic materials.

Property	**Phase 1**
Matrix	
Grain Bulk modulus (K_s)	36.0 GPa
Grain density (ρ_s)	2650 kg/m^3
Bulk modulus (K_d)	6.21 GPa
Shear modulus (μ)	4.55 GPa
Porosity (ϕ)	0.33
Permeability (k)	310^{-14} m^2
Ellipsoid	
Grain Bulk modulus (K_s)	36.0 GPa
Grain density (ρ_s)	2650 kg/m^3
Bulk modulus (K_d)	62.1 MPa
Shear modulus (μ)	45.5 MPa
Porosity (ϕ)	0.33
Permeability (k)	310^{-14} m^2
Fluid	
Bulk modulus (K_f)	2.25 GPa
Density (ρ_f)	10^3 kg/m^3
Viscosity (η)	10^{-3} N s m^{-2}

In Figure 3.23, we show the real parts of the 9 orthotropic moduli and their associated attenuations measured in a sample consisting of a single ellipsoidal inclusion surrounded by a homogeneous matrix and shown in Figure 3.24 (a). The attenuation curves presented in the three top panels exhibit some similarities: at low enough frequencies, the attenuation increases with increasing frequency; then, a peak of attenuation is observed; and at high enough frequencies, the attenuation decreases with increasing frequency. It is important to note that the shapes of the different attenuation curves are very similar but their amplitudes differ. Many studies (see for example White 1975 and Pride et al. 2004) have shown that, for regularly-spaced heterogeneities of equal sizes, attenuation is maximum when the fluid pressure has just enough time to equilibrate between the heterogeneities and the matrix in each wave period. In this case, the relaxation frequency ω_p at which the attenuation is maximum is

$$\omega_p = \frac{D}{L^2} \propto \frac{k_0}{L^2} \tag{3.47}$$

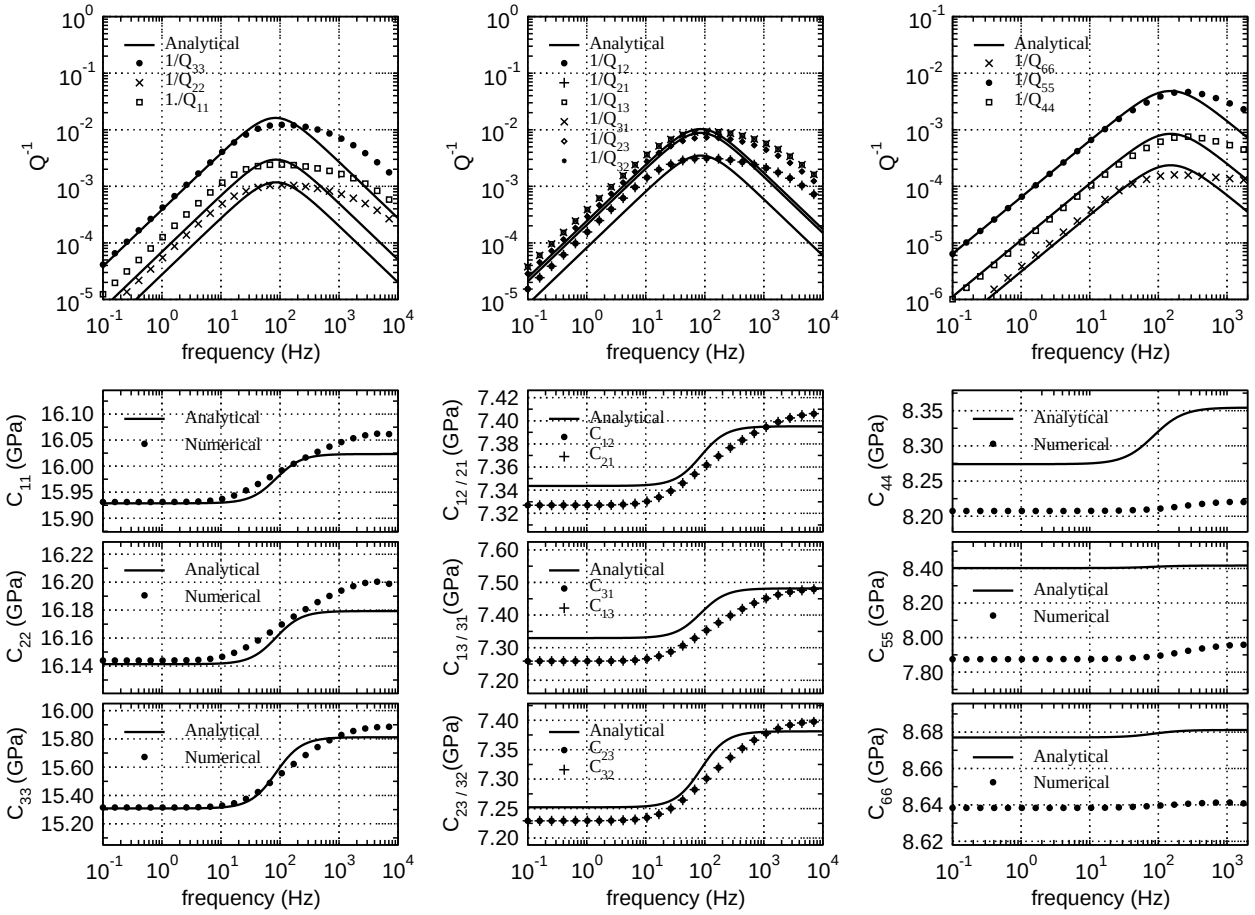

Figure 3.23. Real parts of the 9 orthotropic moduli and their respective attenuations obtained for a single weak ellipsoidal heterogeneity embedded within a stiffer homogeneous matrix. The dimensions of the sample are $L_1 = 31$mm, $L_2 = 41$mm, and $L_3 = 21$mm; the dimensions of the ellipsoid are $l_1 = 10.3$mm, $l_1 = 27.3$mm, and $l_3 = 4.7$mm (see Figure3.24 for a definition of these parameters). The elastic properties of the matrix and the inclusions are given in Table 3.3.3. In all graphs, the points represent numerical results and solid lines represent results obtained using the analytical expression presented in section 3.3.4.

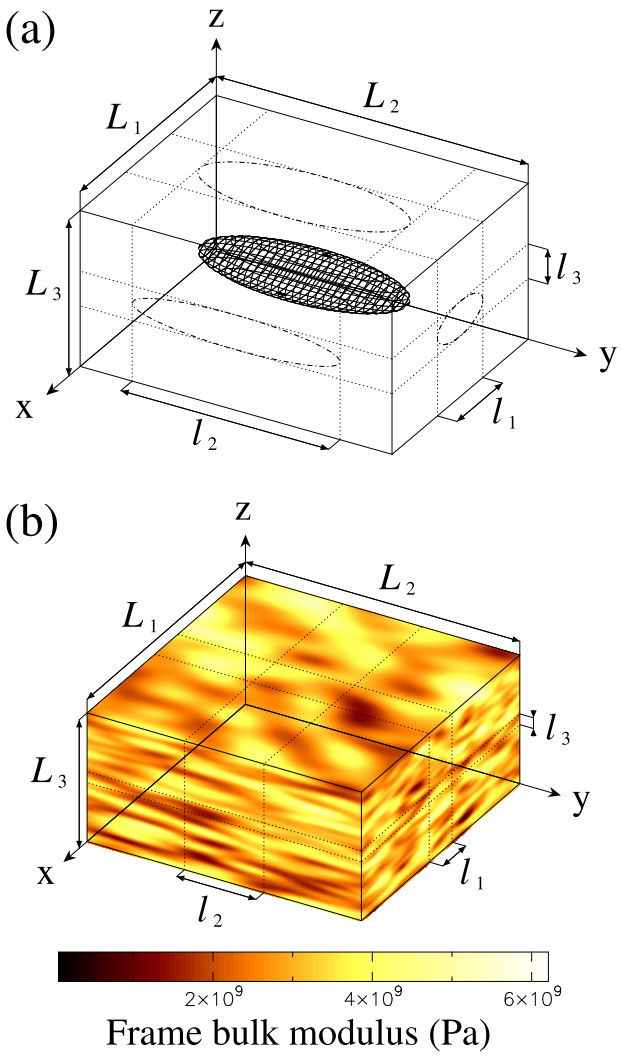

Figure 3.24. An illustration of the two different types of sample geometries used for the numerical experiments. (a) The sample consists of a single ellipsoidal heterogeneity embedded within a homogeneous matrix. (b) The sample is a random material having a different gaussian correlation function in the three orthogonal directions of space. In both (a) and (b), L_1, L_2, and L_3 are the sample dimensions in the x, y, and z directions respectively. In (a), l_1, l_2, and l_3 are the main diameters of the ellipsoid. In (b) l_1, l_2, and l_3 correspond to the correlation lengths in the x, y, and z directions respectively.

where L is the characteristic size of the heterogeneities (a diffusion length)and is explicitly defined in Appendix B, k_0 is the permeability, and D is the fluid pressure diffusivity. A definition of D can be found in Pride et al. (2004). The numerical results show that all the attenuation curves associated with the M_{ij} moduli reach their maximum at the same frequency. As the M_{ij} moduli are obtained using uniaxial compression experiments, pressure equilibration is dominated by the fluid exchange between the heterogeneity and the matrix, and Equation 3.47 gives a good estimate of the frequency at which the maximum attenuation is observed. The situation is different when the fluid-pressure equilibration occurs between the compressional and dilatational lobes induced in the matrix by stress applied tangentially to the cuboid. In this case the position of the attenuation peak depends on the distance between the compressed and the dilated regions and on the permeabilities of both the ellipsoid and the matrix. Thus, the attenuation peaks associated with the G_i will not necessarily be observed at the same frequency depending on the direction of the applied shear stress and on the elongation of the ellipsoid in the different directions. In the rest of this paper, for well-localized inclusions (i.e., inclusions that are not very elongated or flattened), we consider that the differences between the relaxation frequencies associated with the three G_i are small.

When both the matrix and heterogeneities consist of a homogeneous, isotropic, porous material, the only way to induce anisotropy in the macroscopic moduli of the sample is to have some anisotropy in the shape of the heterogeneity. As we have seen in the previous paragraph, when this anisotropy in the shape is small, similar elastic moduli have about the same relaxation frequency. In this case it is relevant to compare their maximum attenuations. In Figure 3.23, we see that the attenuation observed at the attenuation peak varies greatly depending on the elongation of the ellipsoidal inclusion in the different spatial directions. For example, the maximum attenuations $\mathrm{Max}\,[Q_{ii}(\omega)]$ associated with the moduli M_{ii} increase when the ellipsoid's diameter l_i gets smaller.

In order to evaluate how the attenuation levels relate to the aspect ratios of the heterogeneities present within the material, we performed two series of experiments. The results of these experiments are presented in Figure 3.25. The first series has been conducted using samples containing a single ellipsoidal inclusion embedded in a homogeneous matrix as shown in Figure 3.24(a). The hydro-physical properties of the inclusion and the matrix are given in Table 3.3.3. We generated ten different samples with dimensions

$$L1 = L2 = L3 = 4\mathrm{cm} \tag{3.48}$$

for which the values of the principal diameters of the ellipsoid l_1, l_2, and l_3 are chosen randomly under the conditions

$$v_1 = \frac{4}{3}\pi l_1 l_2 l_3 = 837\mathrm{mm}^3 \ \text{(volume of the ellipsoid is constant)} \tag{3.49}$$

$$\max\,[l_1, l_2, l_3] < L_i \ \text{(ellipsoid fits within the sample).} \tag{3.50}$$

For each sample, we computed the 9 orthotropic moduli in Equation 3.33 and their respective attenuations. We then measured the maximum attenuation associated with each modulus

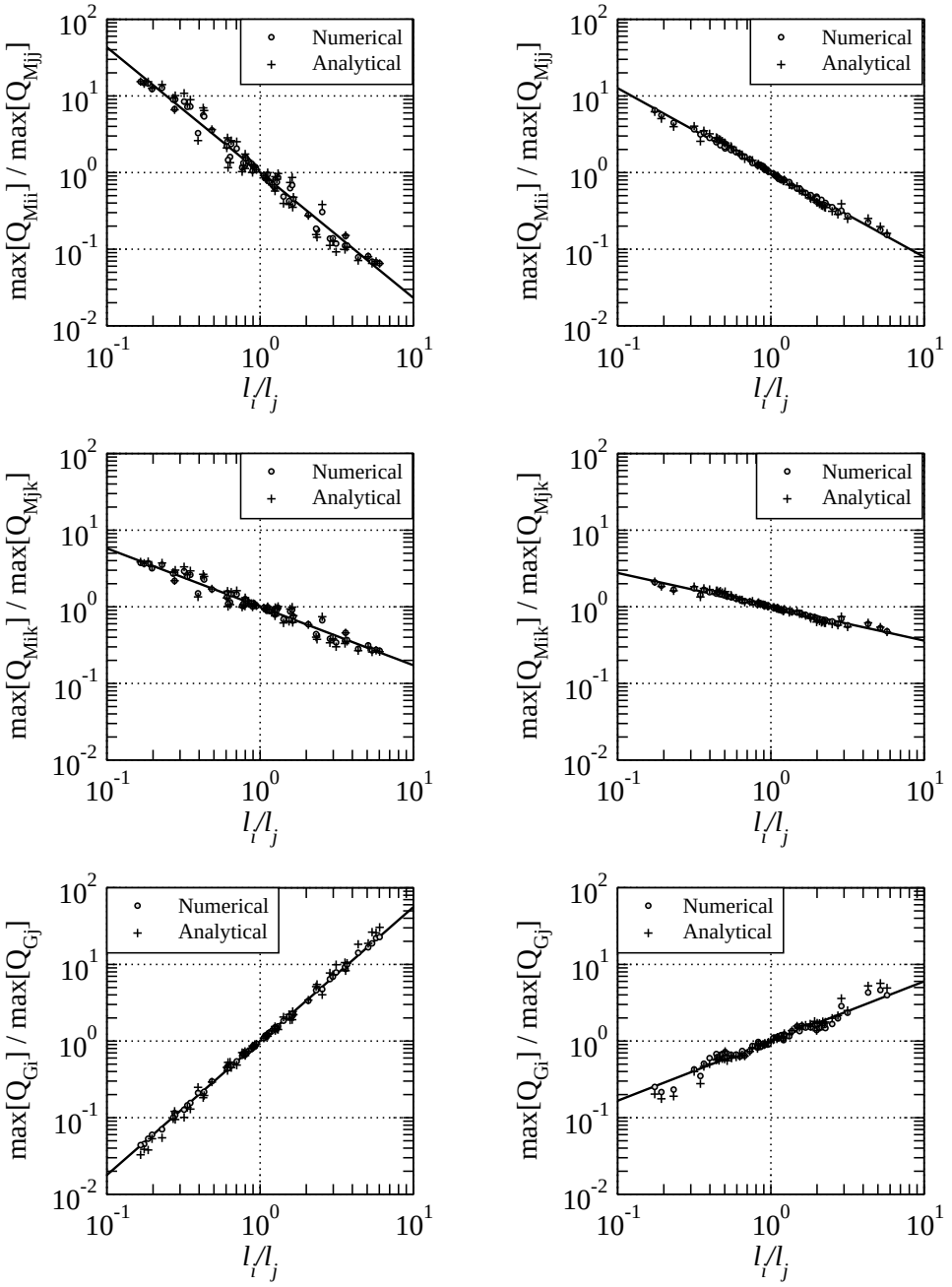

Figure 3.25. Ratios of the maximum attenuations plotted as a function of geometrical aspect ratios. (a1),(a2), and (a3) show the result of a series of ten experiments using samples containing a single ellipsoidal heterogeneity (model (a) in figure3.24). (b1),(b2), and (b3) show the results of a series of ten experiments using the random gaussian model (model (b) in figure3.24). The circles correspond to the numerical measurements, and the pluses are the theoretical estimates.

and computed the following ratios:

$$\frac{\max\left[Q_{M_{ii}^{-1}}(\omega)\right]}{\max\left[Q_{M_{jj}^{-1}}(\omega)\right]} \quad \forall \quad i,j \in [1,2,3] \text{ and } i \neq j \tag{3.51}$$

$$\frac{\max\left[Q_{M_{ik}^{-1}}(\omega)\right]}{\max\left[Q_{M_{jk}^{-1}}(\omega)\right]} \quad \forall \quad i,j,k \in [1,2,3] \text{ and } i \neq j \neq k \tag{3.52}$$

$$\frac{\max\left[Q_{G_i^{-1}}(\omega)\right]}{\max\left[Q_{G_j^{-1}}(\omega)\right]} \quad \forall \quad i,j \in [1,2,3] \text{ and } i \neq j. \tag{3.53}$$

The second series of experiments has been performed in the same way, but using the random property model of Figure 3.24(b). In this case, l_1, l_2, and l_3 denote the correlation length of the materials in the x, y, and z directions respectively. The poroelastic properties used in the samples are similar to those of the matrix in Table 3.3.3 except for the bulk and shear moduli. An example of the bulk modulus distribution is shown in Figure 3.24, and the corresponding distribution for the shear modulus is obtained using $\mu(x,y,z) = \frac{3}{4}K_d(x,y,z)$. For both series of experiments, the numerical results plotted as circles in Figure 3.25 show a strong power-law correlation between the attenuation ratios in Equations 3.51, 3.52 and 3.53 and the aspect ratios l_i/l_j. The simple expressions

$$\frac{\max\left[Q_{M_{ii}^{-1}}(\omega)\right]}{\max\left[Q_{M_{jj}^{-1}}(\omega)\right]} \approx \left(\frac{l_i}{l_j}\right)^{\alpha_1} \tag{3.54}$$

$$\frac{\max\left[Q_{M_{ik}^{-1}}(\omega)\right]}{\max\left[Q_{M_{jk}^{-1}}(\omega)\right]} \approx \left(\frac{l_i}{l_j}\right)^{\alpha_2} \tag{3.55}$$

$$\frac{\max\left[Q_{G_i^{-1}}(\omega)\right]}{\max\left[Q_{G_j^{-1}}(\omega)\right]} \approx \left(\frac{l_i}{l_j}\right)^{\alpha_3} \tag{3.56}$$

plotted as solid lines on Figure 3.25 fit the data quite well. We will show in the next section that the discrepancy between the numerical data and Equations 3.54, 3.55 and 3.56 is not due to measurement errors, and that the exponents α_i depends on many parameters. The fact that the attenuation ratios are correlated to the geometrical aspect ratios has practical implication. For example, by measuring the amplitude ratios of seismic waves such as P-waves or S-waves traveling in different directions, it should be possible to deduce the shape and the orientation of the mesoscale heterogeneities present in the propagation medium.

3.3.4 Analytical solution for peak attenuation ratios

The delicate problem of a mismatched elastic ellipsoid embedded within an infinite elastic medium subject to remote stress was first solved by Eshelby in his famous paper Eshelby (1957). Only recently, his principal result has been extended to the poroelastic case by Berryman (1997). Many authors have used Eshelby's results to derive expressions for the anisotropic elastic moduli in elastic composites [see for example Mori and Tanaka (1973), Benveniste (1987), and Maewal (1987)]. Following the Mori-Tanaka (1973) method, Pan and Weng (1995) derived explicit expressions for the elastic moduli of heterogenous elastic composites containing ellipsoidal inclusions and elliptic cracks. Their result for an elastic composite containing aligned ellipsoidal inclusions can be applied directly to get the elastic moduli of a dry porous material containing ellipsoidal heterogeneities. We have

$$\mathbf{C}_D^{-1} = (\mathbf{I} + v_1 \mathbf{A}_D^*) \left(\mathbf{C}_0^{dry} \right)^{-1} \tag{3.57}$$

where $\mathbf{C}_D$ is the stiffness tensor of the dry porous composite, $\mathbf{C}_0$ is the stiffness tensor of the dry porous matrix surrounding the ellipsoids, $\mathbf{A}_D$ is an eigenstrain concentration tensor introduced by Pan and Weng (1995) , v_1 is the fraction volume occupied by the ellispoid, and $\mathbf{I}$ is the identity tensor. In our case of a dry porous material containing aligned ellipsoidal heterogeneities, $\mathbf{A}_D$ has the expression

$$\mathbf{A}_D^* = \left[\left(\mathbf{C}_1^{dry} - \mathbf{C}_0^{dry} \right) (v_1 \mathbf{I} + v_0 \mathbf{S}) + \mathbf{C}_0^{dry} \right]^{-1} \left(\mathbf{C}_1^{dry} - \mathbf{C}_0^{dry} \right) \tag{3.58}$$

where $\mathbf{C}_1$ is the stiffness tensor of the dry ellipsoids, $\mathbf{S}$ is the Eshelby tensor (the components of the Eshelby tensor for ellipsoidal inclusions can be found in Appendix G), and $v_0 = 1 - v_1$ is the volume fraction occupied by the matrix. In the case where both the ellipsoids and the matrix consist of an isotropic porous material, the tensors $\mathbf{C}_0$, and $\mathbf{C}_1$ can be expressed in the matrix form

$$C_m^{dry} = \begin{pmatrix} K_d^m + \frac{4}{3}\mu^m & K_d^m - \frac{2}{3}\mu^m & K_d^m - \frac{2}{3}\mu^m & 0 & 0 & 0 \\ K_d^m - \frac{2}{3}\mu^m & K_d^m + \frac{4}{3}\mu^m & K_d^m - \frac{2}{3}\mu^m & 0 & 0 & 0 \\ K_d^m - \frac{2}{3}\mu^m & K_d^m - \frac{2}{3}\mu^m & K_d^m + \frac{4}{3}\mu^m & 0 & 0 & 0 \\ 0 & 0 & 0 & 2\mu^m & 0 & 0 \\ 0 & 0 & 0 & 0 & 2\mu^m & 0 \\ 0 & 0 & 0 & 0 & 0 & 2\mu^m \end{pmatrix} \tag{3.59}$$

where K_d^m and μ^m denote the drained bulk moduli and the shear moduli of the porous material composing the ellipsoids ($m = 1$) and the matrix ($m = 0$).

When the porous composite is saturated with a single fluid and no fluid exchange occurs between the ellipsoids and the matrix (which corresponds to the high-frequency response of

the undrained sample), a relation similar to Equation 3.57 can be derived. In this case, we have

$$\mathbf{C}_U^{-1}(\infty) = (\mathbf{I} + v_1 \mathbf{A}_U^*) \left[\mathbf{C}_0^{sat}\right]^{-1} \tag{3.60}$$

where $\mathbf{C}_U(\infty)$ is the high-frequency undrained stiffness tensor of the porous composite, $\mathbf{C}_0^{sat}$ is the undrained stiffness tensor of the matrix, and the undrained eigenstrain concentration tensor $\mathbf{A}_U$ is

$$\mathbf{A}_U^* = \left[\left(\mathbf{C}_1^{sat} - \mathbf{C}_0^{sat}\right)(v_1\mathbf{I} + v_0\mathbf{S}) + \mathbf{C}_0^{sat}\right]^{-1} \left(\mathbf{C}_1^{sat} - \mathbf{C}_0^{sat}\right) \tag{3.61}$$

where $\mathbf{C}_1^{sat}$ is the undrained stiffness tensor of the ellipsoids. The tensors $\mathbf{C}_i^{sat}$ in Equations 3.60 and 3.61 can be written in the matrix form

$$C_m^{sat} = \begin{pmatrix} K_u^m + \frac{4}{3}\mu^m & K_u^m - \frac{2}{3}\mu^m & K_u^m - \frac{2}{3}\mu^m & 0 & 0 & 0 \\ K_u^m - \frac{2}{3}\mu^m & K_u^m + \frac{4}{3}\mu^m & K_u^m - \frac{2}{3}\mu^m & 0 & 0 & 0 \\ K_u^m - \frac{2}{3}\mu^m & K_u^m - \frac{2}{3}\mu^m & K_u^m + \frac{4}{3}\mu^m & 0 & 0 & 0 \\ 0 & 0 & 0 & 2\mu^m & 0 & 0 \\ 0 & 0 & 0 & 0 & 2\mu^m & 0 \\ 0 & 0 & 0 & 0 & 0 & 2\mu^m \end{pmatrix} \tag{3.62}$$

where the k_u^m are the undrained bulk moduli of the ellipsoids ($m = 1$) and the matrix ($m = 0$).

Finally, knowing the stiffness tensor $\mathbf{C}_D$ of the dry sample, the low-frequency undrained moduli of the sample can be derived using Gassman's result

$$S_{ijkl}^{dry} - S_{ijkl}^{sat}(0) = \frac{\left(S_{ij\alpha\alpha}^{dry} - S_{ij\alpha\alpha}^{g}\right)\left(S_{kl\alpha\alpha}^{dry} - S_{kl\alpha\alpha}^{g}\right)}{(M_f - M_\phi)\,\phi + (M_{dry} - M_g)} \tag{3.63}$$

where we have used the notation of Brown and Korringa (1975) in which $\mathbf{S}^{dry} = \mathbf{C}_D^{-1}$ is the compliance tensor of the dry sample; $\mathbf{S}^{sat}(0) = \mathbf{C}_U^{-1}(0)$ is the low-frequency compliance tensor of the undrained sample; $\mathbf{S}^g$ is the compliance tensor of the solid grains; and M_f, M_ϕ, M_{dry}, and M_g are the compressibilities of the fluid, unjacketed pores, dry sample, and solid grain respectively, and can be obtained using

$$M_f = \frac{1}{K_f}, \tag{3.64}$$

$$M_\phi = \frac{1}{K_\phi}, \tag{3.65}$$

$$M_{dry} = \sum_{i=1}^{3}\sum_{j=1}^{3} S_{ij}^{dry}, \tag{3.66}$$

and

$$M_g = \sum_{i=1}^{3} \sum_{j=1}^{3} S_{ij}^g. \tag{3.67}$$

A discussion on the nature of K_ϕ as well as various models can be found in Berryman (1992) . For our computation, the CPA (Berryman, 1992) models have been used. When writing the compliance tensors $\mathbf{S}$ in the matrix form

$$\mathbf{S} = S_{ij} = \begin{pmatrix} S_{11} & S_{12} & S_{13} & 0 & 0 & 0 \\ S_{21} & S_{22} & S_{33} & 0 & 0 & 0 \\ S_{31} & S_{32} & S_{33} & 0 & 0 & 0 \\ 0 & 0 & 0 & S_{44} & 0 & 0 \\ 0 & 0 & 0 & 0 & S_{55} & 0 \\ 0 & 0 & 0 & 0 & 0 & S_{66} \end{pmatrix}, \tag{3.68}$$

Equation 3.63 can be rewritten in the simpler form

$$S_{ij}^{dry} - S_{ij}^{sat}(0) = \frac{\left(V_i^{dry} - V_i^g\right)\left(V_j^{dry} - V_j^g\right)}{\left(M_f - M_\phi\right)\phi + \left(M_{dry} - M_g\right)} \tag{3.69}$$

where

$$V_i = \sum_{j=1}^{3} S_{ij}. \tag{3.70}$$

As mentioned previously, the problem of dynamic fluid transport is difficult for anisotropic materials and will not be treated in this paper. Nonetheless, in the case where the fluid pressure equilibration between the inclusions and the matrix is dominant, it is reasonable to assume that the double porosity theory of Pride et al. (2004) capture much of the frequency dependence in the undrained anisotropic moduli. We propose to force the double porosity theory to match the high $\mathbf{C}_U(\infty)$ and low $\mathbf{C}_U(0)$ frequency limits of the anisotropic moduli previously derived. This can be achieved using the simple formula

$$C_{Uijkl}(\omega) = C_{Uijkl}(0) + \frac{C_{Uijkl}(\infty) - C_{Uijkl}(0)}{K_u(\infty) - K_u(0)} \left[K_U(\omega) - K_u(0)\right] \tag{3.71}$$

where $K_U(\omega)$ is the frequency-dependent undrained modulus of the sample computed using the double porosity theory, and $K_u(\infty)$ and $K_u(0)$ are its high and low frequency limits. Expressions for $K_u(\infty)$, $K_u(0)$, and $K_U(\omega)$ can be found in Appendices A and B.

The estimates of the frequency-dependent undrained elastic moduli $C_{Uijkl}(\omega)$ (using Equation 3.71) are presented as the solid lines in Figure 3.23. We see that this rough derivation of the elastic moduli versus frequency is in good agreement with the numerical data. Note that the fit is better for the M_{ij} moduli, which is due to the fact that the fluid equilibrates mostly between the inclusions and the matrix in this case which is what the double-porosity theory allows for. When looking at the attenuation peaks, we see that the theoretical attenuation levels are in very good agreement with the numerical experiments. The frequency dependence in the attenuation is less accurate due to the assumption that a homogeneous compression is driving the fluid flow.

As Equation 3.71 gives accurate predictions for attenuation levels at attenuation peaks, it could be used to estimate the attenuation ratios in Equations 3.51, 3.52 and 3.53 by simply picking the maximum values of the attenuation curves. The easiest way to compute the attenuation ratios is to use the fact that the maximum attenuation associated with a given elastic modulus C is proportional to the difference between its high $C(\infty)$ and low $C_(0)$ frequency limits; i.e.,

$$\max\left[Q_C^{-1}(\omega)\right] = A\left[C(\infty) - C(0)\right] \tag{3.72}$$

where A is a proportionality constant which depends on how the fluid pressure equilibrates within the sample. If we assume that A is constant for a given group of elastic moduli such as the M_{ii}, the M_{ij}, or the G_i, then the attenuation ratios in Equations 3.51, 3.52 and 3.53 can be computed using

$$\frac{\max\left[Q_{M_{ii}}^{-1}(\omega)\right]}{\max\left[Q_{M_{jj}}^{-1}(\omega)\right]} = \frac{C_{Uiiii}(\infty) - C_{Uiiii}(0)}{C_{Ujjjj}(\infty) - C_{Ujjjj}(0)} \tag{3.73}$$

$$\frac{\max\left[Q_{M_{ik}}^{-1}(\omega)\right]}{\max\left[Q_{M_{jk}}^{-1}(\omega)\right]} = \frac{C_{Uiikk}(\infty) - C_{Uiikk}(0)}{C_{Ujjkk}(\infty) - C_{Ujjkk}(0)} \tag{3.74}$$

$$\frac{\max\left[Q_{G_i}^{-1}(\omega)\right]}{\max\left[Q_{G_j}^{-1}(\omega)\right]} = \frac{C_{Ujkjk}(\infty) - C_{Ujkjk}(0)}{C_{Uikik}(\infty) - C_{Uikik}(0)}. \tag{3.75}$$

In Figure 3.25, the attenuation ratios computed using Equations 3.73, 3.74 and 3.75 are represented by pluses and correlate very well with the ratios estimated numerically. We see that the differences between the computed data and the expression in Equations 3.54, 3.55 and 3.56 are not due to measurement errors and can be predicted. Other series of experiments have shown that Equations 3.54, 3.55 and 3.56 fit the data well only when the anisotropy in the shape of the ellipsoidal inclusion is weak (say, when $0.5 < l_i/l_j < 2$). In Figure 3.26, we see that a perfect bijective relation between the attenuation ratios and the aspect ratios of the inclusions is observed for spheroidal inclusions (i.e. when two of the three ellipsoid radii are equal). When the anisotropy is weak, this relation takes the form of a power law. The exponent of this power law depends on many parameters such as the volume of the ellipsoid (as shown in Figure 3.26) or the elastic properties of the ellipsoid and the matrix. The relations 3.73, 3.74 and 3.75 are the more general and important result of this paper.

3.3.5 Conclusion

For the special class of porous materials consisting of aligned ellipsoidal inclusions within a homogeneous matrix, it is possible to relate the poroelastic attenuation associated with the different anisotropic moduli to the geometry of the heterogeneities responsible for this attenuation. We showed that this can be achieved without solving the difficult problem of dynamic fluid flow induced when the material is subject to a non-homogeneous stress or

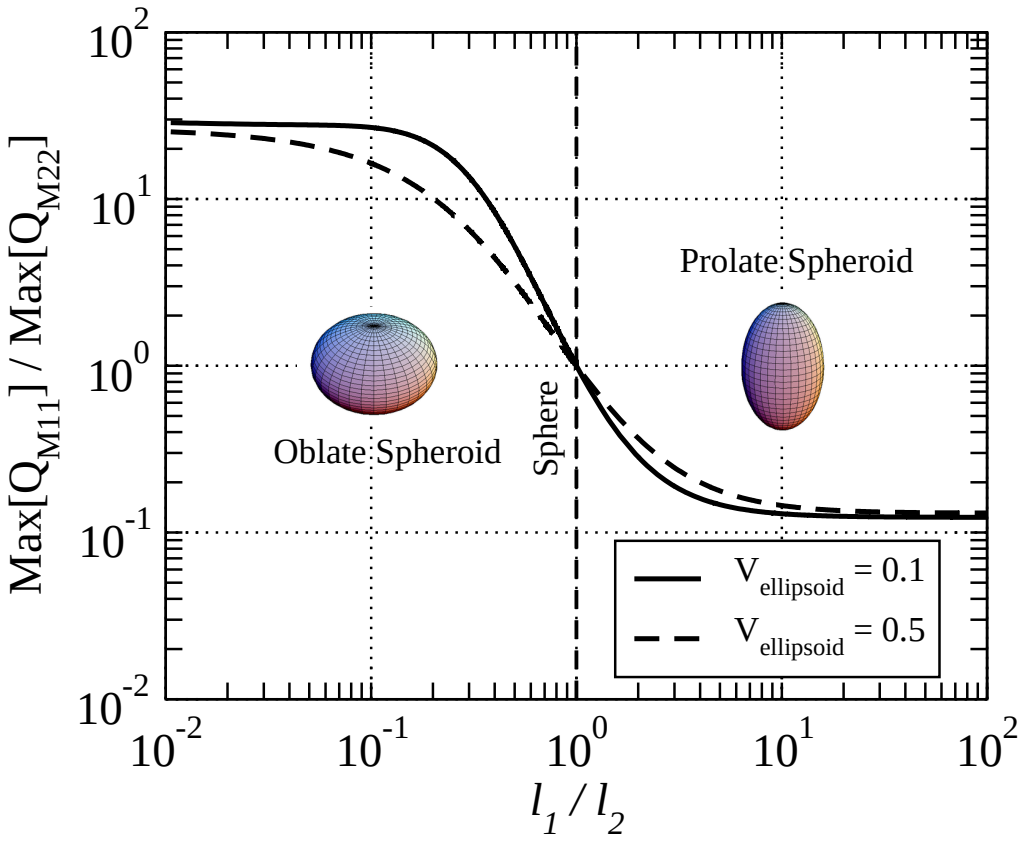

Figure 3.26. Attenuation ratio $\left(\max\left[Q^{-1}_{M_{11}}\right]/\max\left[Q^{-1}_{M_{22}}\right]\right)$ computed using Equation 3.73 and plotted as a function of the aspect ratio l_i/l_j for spheroidal inclusion where $l_1 \neq l_2 = l_3$. The properties of the matrix and the ellipsoid are given in Table 3.3.3; the black curve corresponds to ellipsoids occupying 10% of the sample's volume and the dashed curve corresponds to ellipsoids occupying 50% of the sample's volume. We see that when the shape of the inclusion is close to a sphere, the attenuation ratios can be related to the aspect ratios by a power law. When l_1 becomes large, the attenuation ratio reaches a limit corresponding to an infinite cylinder. When l_1 is small, the attenuation ratio reaches a limit corresponding to an infinite flat slab (penny shape).

strain. The expression in Equations 3.73, 3.74 and 3.75 still needs to be developed to obtain explicit relations between the attenuation ratios and the aspect ratios of the ellipsoidal inclusions. In the special case of weak anisotropy, we have shown that these attenuation ratios are related to the aspect ratios of the ellipsoid by a power law. The exact dependence of the power law exponents on the physical and geometrical parameters of the material still needs to be established.

Chapter 4

Seismic attenuation due to patchy saturation

(Submitted for publication in the JOURNAL OF GEOPHYSICAL RESEARCH.)

4.1 Introduction

Rocks and sediments at or near the Earth's surface are often partially saturated with air and water while at depth rocks can be partially saturated with oil and/or gas in addition to water. Partial water saturation in rocks and sediments is known to create significant amounts of acoustic attenuation and dispersion [e.g., Murphy, 1982; Cadoret et al., 1998]. Understanding how seismic wave amplitudes and velocities are modified by the level of saturation, the fluid properties, and the spatial distribution of fluid patches is important both for developing accurate wave propagation models and for interpreting seismic data. Mechanisms that are able to produce significant levels of attenuation in the seismic band of frequencies (1 Hz to 10^4 Hz) are of particular interest and remain the subject of ongoing research. Patchy saturation provides such a mechanism.

The early work of Biot (1956) shows that when a porous rock is saturated with a single fluid, seismic attenuation occurs due to wave-induced fluid flow caused either by pressure gradients between the peaks and troughs of a compressional wave or by acceleration of the framework of grains which is the frame of reference for the relative flow. These effects are known as the Biot mechanism and the predicted attenuation (as measured by Q^{-1}) is maximum at the Biot relaxation frequency

$$\omega_c = \frac{\eta}{\rho_f F k_0} \tag{4.1}$$

where η denotes the fluid viscosity, k_0 the permeability, ρ_f the fluid density and F the formation factor. However, ω_c is generally too high (typically by a few orders of magnitude) to generate significant attenuation levels in the seismic band of frequencies.

Many models of attenuation in partially-saturated rocks [e.g., White et al., 1975; Norris, 1973; Knight et al., 1998; Johnson, 2001; Pride et al., 2004] suggest that loss in the seismic band can be important. In these models, patches of fluid having a larger bulk modulus respond to a compressional wave with a larger fluid-pressure change compared to patches with a smaller bulk modulus. The pressure gradients so created cause flow and create loss. Such models are called "patchy-saturation" models. For regularly spaced patches having a characteristic size L, the relaxation frequency ω_p at which the attenuation is maximum scales as [c.f., Pride, 2005]

$$\omega_p = \frac{D}{L^2} \propto \frac{k_o}{L^2} \tag{4.2}$$

where

$$D = \frac{k_o B K_u}{\eta \alpha} \left(\frac{K + 4G/3}{K_u + 4G/3} \right) \approx \frac{k_o K_f}{\eta \phi} \tag{4.3}$$

is the fluid-pressure diffusivity. Definitions of the poroelastic moduli α, B, K, and K_u are given in Appendix A, while ϕ is porosity and K_f is the bulk modulus of the slowest moving fluid (typically the fluid having the largest viscosity). From equation (4.2), the frequency ω_p at which the attenuation is maximum depends sensitively on the characteristic size of the patches L. For realistic values of L (say centimeters and larger), patchy saturation models can easily explain the observed levels of attenuation in the seismic band of frequencies.

All the aforementioned patchy-saturation models apply to a regular distribution of fluids such as uniformly spaced patches of arbitrary shape and equal size or a periodic flat slab geometry. In these models, only a single relaxation frequency is present. Significant deviation from these models is expected when the fluid patches have various sizes and/or are unevenly distributed.

Müller and Gurevich (2004) are the first authors to account for randomness in the spatial distribution of the fluids. They do so using a 1D approximation for the coherent wave field in a random porous media and assuming a continuous random media with a distribution of different patch sizes. Randomness in the patch sizes is introduced by means of a correlation function and the authors provide explicit results for the attenuation versus frequency in the case of media containing a mixture of two fluids and having Gaussian or exponential correlation functions. However, the model is general and allows the use of any correlation function for the fluid distribution. This model has been extended to 3D by Toms and Gurevich (2007).

An important question when considering wave-induced flow due to equilibrating patches of fluids is weather or not capillary forces present at the interface between two fluids should be accounted for. This question has been addressed in detail by Tserkovnyak and Johnson (2003), from which Pride et al. (2004) obtain a condition to neglect capillary forces at fluid interfaces

$$\frac{\sigma}{k_0 K}\frac{V}{S} < 1 \tag{4.4}$$

where σ denotes the surface tension, K is the drained bulk modulus, and V/S is a volume-to-surface ratio related to the geometry of fluid patches with S the total surface area of the meniscii within each volume V of porous material. Throughout this paper, we assume that criterion (4.4) is satisfied and that capillary effects (surface tension) do not need to be allowed for in the numerical modeling. Further, we work at frequencies satisfying $\omega \ll \omega_c$ so that the development of viscous boundary layers in the pores can be neglected.

The goal of the present work is to understand attenuation and dispersion in porous rocks having realistic fluid distributions that were created by the slow immiscible invasion of one fluid into a region initially saturated with another fluid. To study this problem, we create fluid distributions numerically using the invasion-percolation algorithm of Wilkinson and Wilemsen (1983) and perform stress-strain numerical experiments at different frequencies of applied stress to determine the attenuation and dispersion. The numerical scheme for performing the stress-strain experiments and for computing attenuation is similar to that of Masson and Pride (2007) and is described in the next section. In the final Section 4.5, we perform the stress-strain experiments on the invasion-percolation samples using different combinations of air, water, and oil as the invading and defending fluids. Rather different frequency dependencies are obtained depending on which fluids are used as the invaders and the defenders. In order to explain these various results, we first study in Section 4.3 the effect of the fluid-compressibility contrast and how that influences equilibration at both small and large scales. We then study in Section 4.4 the particular case of attenuation when the fluid saturation is distributed as a self-affine fractal and when the fluid-compressibility contrast is small. The results from Sections 4.3 and 4.4 allow us to understand and model the numerical results obtained in Section 4.5 for samples having invasion-percolation fluid distributions.

4.2 Numerical method

Following Masson and Pride (2007), we perform quasi-static numerical experiments to compute the time-dependent strain response to a stress applied on the boundaries of a synthetic rock sample. The numerical simulations are performed using a finite-differences scheme that solves the Biot set of equations [Biot, 1962] as given in Appendix A. The samples so studied can be thought of as the voxels used in a seismic forward modeling and their moduli are the macroscopic moduli that control wave propagation. The samples need

to be large enough to contain a sufficient amount of heterogeneity to correctly average the properties of the porous continuum while staying much smaller than the wavelength.

The method consists of three steps: (1) On a three-dimensional grid, numerically generate a synthetic sample of the material to be studied. (2) Apply a time-varying normal stress to each external face of the sample and record both the average stress and strain throughout the sample. (3) Take a temporal Fourier transform of the spatially-average stress and strain and perform a spectral ratio to obtain the complex and frequency-dependent sealed-sample (or "undrained") bulk modulus $K_u(\omega)$ and its respective attenuation $Q^{-1}(\omega)$.

A representation of the experimental setup is presented in Figure 4.2. In this paper, attenuation curves obtained from both 2D and 3D experiments are presented. A detailed description of the method in 2D is provided by Masson et al. (2007). The 3D extension of the method is now briefly detailed.

The 3D finite-differences scheme for solving the Biot set of equations is presented in Appendix F. During the modeling, the following sealed-boundary conditions are imposed on the external faces of a cubic sample

$$\begin{aligned}
\tau_{xx} &= \begin{cases} S(t) & \text{on the left and right faces,} \\ 0 & \text{elswhere;} \end{cases} \\
\tau_{yy} &= \begin{cases} S(t) & \text{on the front and back faces,} \\ 0 & \text{elswhere;} \end{cases} \\
\tau_{zz} &= \begin{cases} S(t) & \text{on the top and bottom faces,} \\ 0 & \text{elswhere;} \end{cases} \\
\tau_{xy} &= \tau_{xz} = \tau_{yz} = q_x = q_y = q_z = 0
\end{aligned} \tag{4.5}$$

where the field components are defined in Appendix A and where $S(t)$ denotes the source time function controlling the stress applied to the faces of the sample. In this work, the following expression is employed

$$S(t) = \int_0^t w(\tau)\mathrm{sinc}[2\pi f_c(\tau - T)]\, d\tau \tag{4.6}$$

where

$$w(t) = \begin{cases} \sin(\frac{\pi}{2}\frac{t}{T}) & \forall \quad t < 2T \\ \\ 0 & \forall \quad t > 2T \end{cases} \tag{4.7}$$

and

$$T = \frac{N_T}{f_c}. \tag{4.8}$$

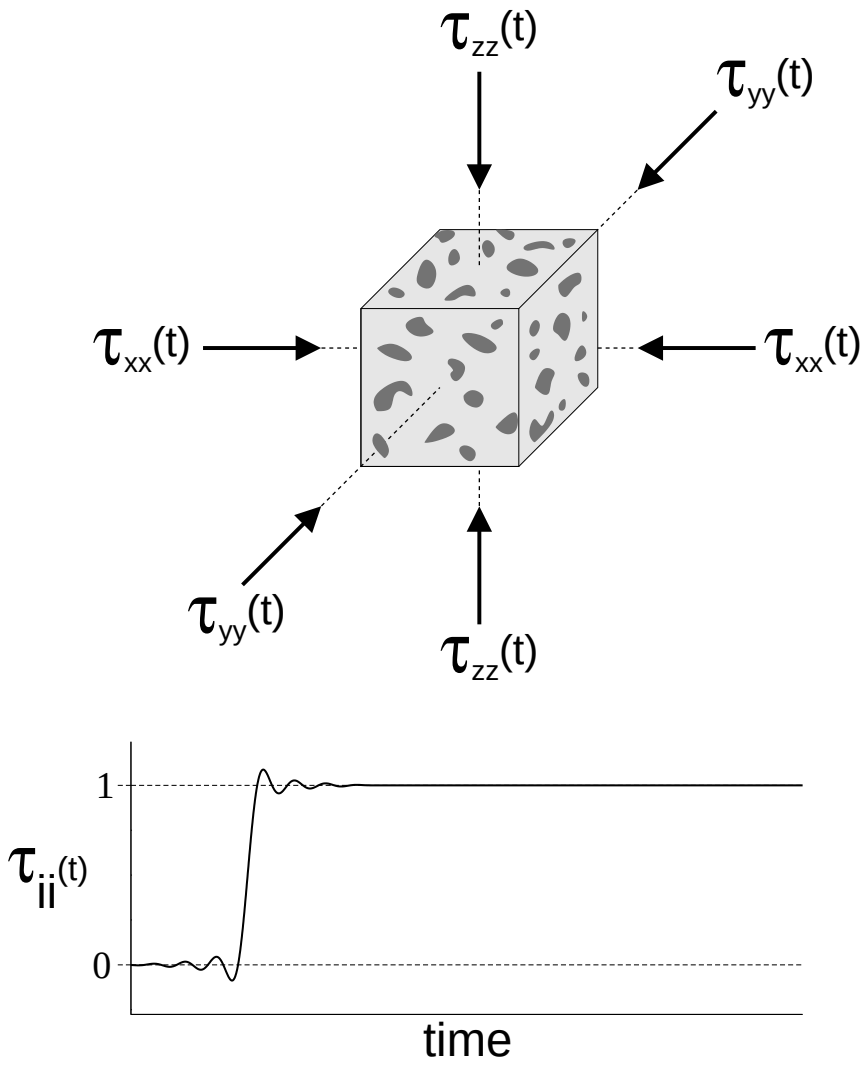

Figure 4.1. A representation of the experimental setup used for the numerical simulations. The bottom graph shows the source time function $S(t)$ of equation 4.6.

Equation 4.6 defines a low-pass filtered step function with a cut frequency f_c and with N_T controling the quality of the filter; i.e., when N_T is large, the expression reduces to the time response of an ideal low-pass filter. The reason for filtering out the high frequencies is to avoid resonances within the sample due to its finite size. In the usual situation where the shear waves have the lowest velocity β, one should use

$$f_c \ll \frac{\beta}{L\Delta x} \tag{4.9}$$

where $L\Delta x$ is the size of the sample.

During the numerical simulation, the following averaged fields are recorded versus time

$$\langle D_i v_i \rangle (k) = \frac{1}{LMN} \sum_{l=1}^{L} \sum_{m=1}^{M} \sum_{n=1}^{N} [D_i v_i]_{l,m,n} \tag{4.10}$$

$$\langle D_t \tau_{ii} \rangle (k) = \frac{1}{LMN} \sum_{l=1}^{L} \sum_{m=1}^{M} \sum_{n=1}^{N} [D_t \tau_{ii}]_{l,m,n} \tag{4.11}$$

where the D_i are the spatial finite-difference operators given in Appendix F and where L, M, and N, are the grid dimensions; l, m, and n are the spatial indexes and k is the time index. Once the simulation is finished, the stress and strain rates are computed in the frequency domain using a fast Fourier transform (FFT)

$$\dot{\epsilon}_{ii}(\omega) = \mathrm{FFT}\left\{\langle D_i v_i \rangle\right\} \tag{4.12}$$

$$\dot{\tau}_{ii}(\omega) = \mathrm{FFT}\left\{\langle D_t \tau_{ii} \rangle\right\}. \tag{4.13}$$

Finally, the complex frequency-dependent bulk modulus of the sample is

$$K_u(\omega) = \frac{1}{3}\left(\frac{\dot{\tau}_{xx} + \dot{\tau}_{yy} + \dot{\tau}_{zz}}{\dot{\epsilon}_{xx} + \dot{\epsilon}_{yy} + \dot{\epsilon}_{zz}}\right), \tag{4.14}$$

and the corresponding attenuation is

$$Q^{-1}(\omega) = \frac{\mathrm{Im}\left\{K_u\right\}}{\mathrm{Re}\left\{K_u\right\}}. \tag{4.15}$$

4.3 Effect of the contrast in fluid incompressibility on the frequency dependence

The principal effect of increasing the contrast in fluid incompressibility between the various fluid patches is to increase the attenuation levels. Masson and Pride (2007) have shown that Q^{-1} increases as the square in the contrast. In this section, we show that the contrast in the fluid incompressibility can also greatly influence how attenuation varies with frequency. This is especially true when the contrast of incompressibility between the fluids is small.

The fluid-pressure differences between patches equilibrate via diffusion with the smaller patches equilibrating first and the larger patches later. Once each patch in the medium has locally equilibrated its fluid pressure with the surrounding fluid, fluid-pressure gradients may still exist if the medium has variations in the fluid saturation at still larger scales. In this case, these larger regions have fluid pressures that are uniform within them but that vary from one such larger volume to the next as a function of the saturation they contain. This can be understood and modeled using Wood's (1941) law to determine a local effective fluid bulk modulus K_W for each of the larger volumes. Wood's law applies to regions having two immiscible fluids that experience the same change in pressure and is given by

$$K_W = [s_1/K_{f1} + s_2/K_{f2}]^{-1} \tag{4.16}$$

where s_1 and s_2 are the volume fractions of fluid 1 and fluid 2 in the region and K_{fi} denotes the bulk modulus of fluid i ($s_1 + s_2 = 1$). Using equation (4.16) for the effective fluid modulusa in the Biot-Gassman laws of Appendix A allows the pressure in the larger-scale volumes to be determined given an applied strain. Such pressure response of the larger-scale regions is thus directly related to the saturation of the region.

To show the effect on the attenuation of having two distinct scales at which fluid-pressure equilibration occurs, we numerically create porous samples having fluids patches at both small and large scales. The properties of the elastic skeleton are taken to be uniform within the samples and the distribution of the two fluids is obtained in the following manner. We first define a background saturation function $f_{sat}(x, y, z)$ which gives the probability that fluid 2 is saturating the medium at a particular location (x, y, z). The sample is then discretized into voxels which will be completely saturated with either of fluid 1 or fluid 2. Each voxel is assigned with a random number $r_{i,j,k}$ in the interval $[0, 1]$. All voxels satisfying

$$r_{i,j,k} > f_{sat}(x_i, y_j, z_k) \tag{4.17}$$

are filled with fluid 1, and the remaining voxels are filled with fluid 2. An example of a 2D fluid distribution is given in Figure 4.3 and was obtained using the periodic background function

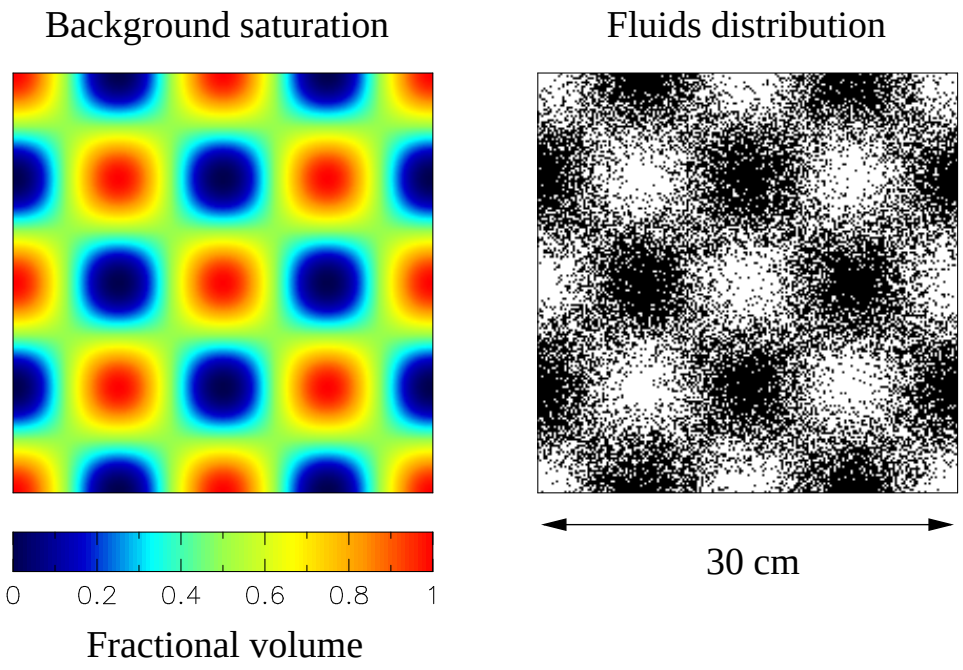

Figure 4.2. An example of a medium having periodic saturation fluctuations. A given realization of the fluid distribution is plotted on the right-hand side. The background saturation function used to generate this fluid distribution is presented on the left-hand side. In this particular example, the saturation varies between 0 and 1.

Table 4.1. Material properties used in the numerical experiments.

Property	Value
Solid Grain Material	
Bulk modulus K_s	36 GPa
Density ρ_s	2650 kg/m^3
Skeletal Framework of Grains	
Bulk modulus K_d	6.21 GPa
Shear modulus μ	4.55 GPa
Porosity ϕ	0.33
Permeability k	10^{-14} m^2
Air	
Bulk modulus K_f	142 kPa
Density ρ_f	1.2 kg/m^3
Viscosity η	18.3×10^{-6} N s m^{-2}
Oil	
Bulk modulus K_f	1.5 GPa
Density ρ_f	800 kg/m^3
Viscosity η	0.1 N s m^{-2}
Water	
Bulk modulus K_f	2.2 GPa
Density ρ_f	1000 kg/m^3
Viscosity η	0.001 N s m^{-2}

$$f_{sat}(x, y) = \cos(2\pi x/L)\cos(2\pi y/L) \tag{4.18}$$

where L defines the length of the large-scale fluctuations in the fluid saturation. Note that the patch sizes are not explicitly defined; the smallest patches have the size of the individual voxels, but larger patches are allowed to form when two or more neighbors voxels are filled with the same fluid. However, all patches are smaller than L. In Figure 4.3, we present results of 2D simulations using a fluid distribution similar to the one shown in Figure 4.3, but with f_{sat} in the interval $[0.1, 0.9]$. The size of the voxels is 1 mm^2, $L = 15$ cm and the material properties are given in Table 4.1. The top panel presents the attenuation measured versus frequency when using oil as fluid 1 and water as fluid 2. The two peaks in the attenuation curve are the direct signature of the fluid pressure equilibrating at two distinct scales. The high-frequency peak is due to fluid-pressure equilibration between the relatively small fluid patches at the scale of the individual voxels, while the low-frequency peak is due to equilibration between larger areas having differing amounts of fluid content (saturation). The bottom panel shows the attenuation obtained using the exact same configuration of fluids but when the oil is replaced with air. The permeability of the medium has been reduced as well so that the frequencies at which both attenuation peaks are observed are similar in both experiments. Here we see that substituting oil with air has had a radical

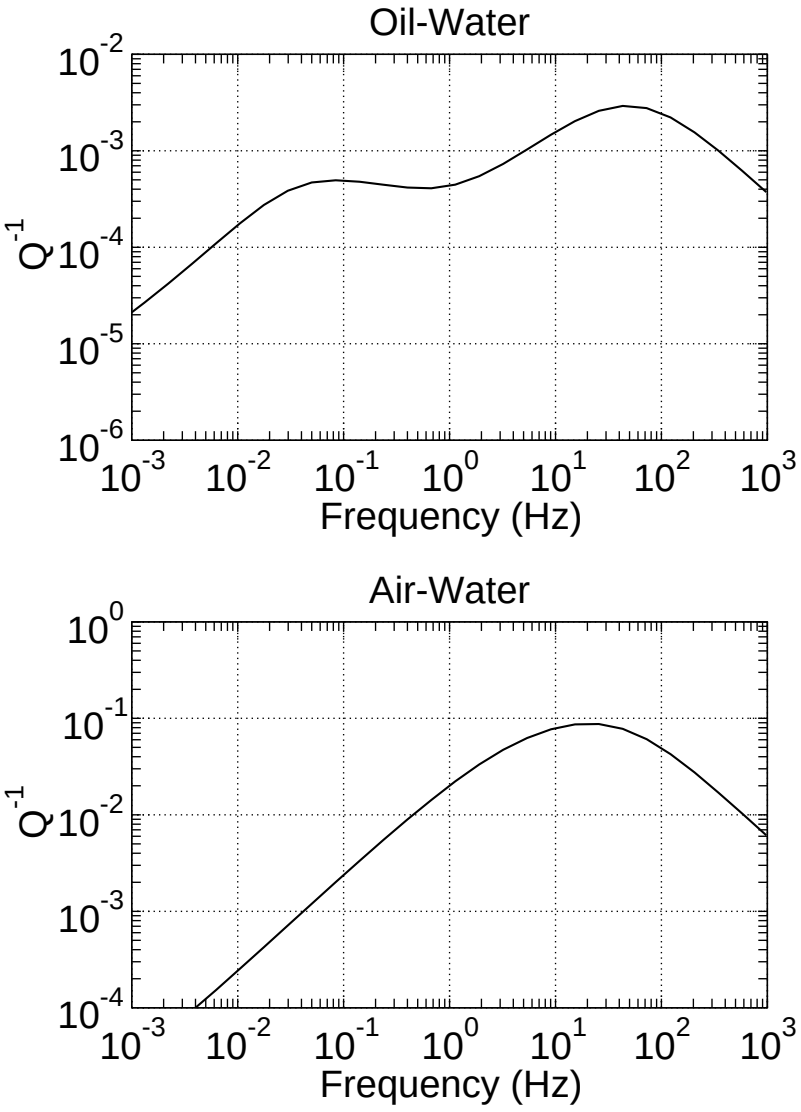

Figure 4.3. Attenuation plotted as a function of frequency obtained using a fluid distribution similar to the one presented in Figure 4.3 and with saturation varying between 0.1 and 0.9. The top graph corresponds to the case where the fluids are oil and water while the bottom graph is for air and water.

effect. Although the attenuation curve still exhibits a peak of attenuation at high frequencies due to equilibration of the voxel scale patches, the low frequency peak is no longer present. This is easily understood because when on of the two fluids is a gas (like air), K_W is much smaller than the drained modulus of the framework of grains and can effectively be put to zero in the Biot-Gassmann formulae. There are therefore no large-scale pressure gradients when one of the two fluids is a gas and this is the reason why no attenuation peak is observed at low frequencies in the bottom panel of Figure 4.3.

For clarity purposes, the two numerical examples presented above were chosen so that both attenuation peaks are well separated in frequency; i.e., the difference between the small-scale and large-scale relaxation frequencies is large. This situation is of course not general and the frequencies at which the attenuation peak are observed can vary greatly. An important parameter that controls the rate at which fluid pressure equilibrates between two regions having different fluid saturations is the hydraulic conductivity $(k_0/\eta)_{eff}$ of the material connecting the regions. It can be defined using Darcy's law

$$q = -\left(\frac{k_0}{\eta}\right)_{eff} \nabla p \tag{4.19}$$

where q denotes the Darcy velocity at which the fluid moves between the two regions and ∇p is the fluid-pressure gradient between the two regions. The effective conductivity $(k_0/\eta)_{eff}$ depends on the permeability of the medium and on the fluid viscosities. However, when the medium is saturated with a mixture of two fluids, $(k_0/\eta)_{eff}$ depends strongly on the way the fluids are distributed within the medium. In our numerical experiments, varying $(k_0/\eta)_{eff}$ can be achieved by varying the volume fraction of fluids in the samples. The reason for this is that we are using a simple percolation process (random placement of fluids) to map the background saturation function into the actual fluid distribution. Indeed, in simple percolation, when the probability p_i of having the fluid i filling one voxel is superior to the so-called percolation-threshold p_c, it can be shown [e.g., Stauffer and Aharony, 1992] that fluid i will percolate through the whole medium; i.e., we can always find a continuous path within fluid i linking one point to another. In this situation, the effective hydraulic conductivity $(k_0/\eta)_{eff}$ is controlled by the viscosity of fluid i and the permeability of the medium. An illustration of this point is presented in Figure 4.3. In Figure 4.3, we present a set of three experiments showing how $(k_0/\eta)_{eff}$ is controlling the frequency at which the attenuation peak associated with the fluid-pressure equilibration occurs. In this set of experiments, we use a background saturation function similar to the one presented in Figure 4.3 but varying between different bounds for each experiment. The solid line in Figure 4.3 represents the attenuation observed when f_{sat} stays in the interval $[p_c, 1]$. In this case, the oil percolates through the whole medium and its viscosity η_{oil} controls the rate at which the fluid pressure equilibrates between areas having different K_W. The dotted-dashed line represents the attenuation observed in the exact opposite case; i.e., when f_{sat} stays in the interval $[0, 1 - p_c]$. In this case, water percolates through the whole medium and its viscosity η_{wat} controls the rate of fluid-pressure equilibration between areas having different K_W. The last attenuation curve represented by a dashed line is obtained with f_{sat} varying in the interval $[1 - p_c, p_c]$. In this case, neither fluid percolates and the effective hydraulic

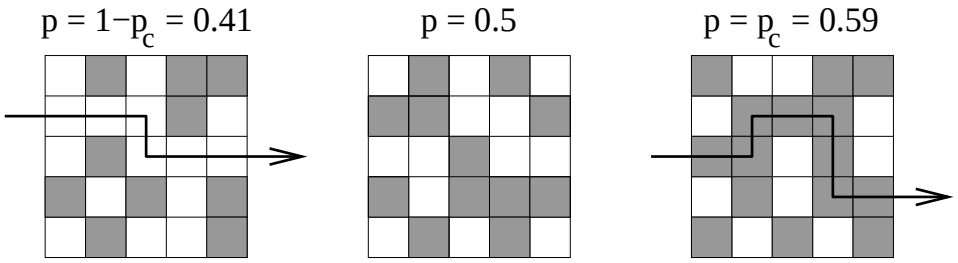

Figure 4.4. Illustration showing the effects of varying the fluid volume fractions on the hydraulic conductivity $(k_0/\eta)_{eff}$. On the left, the probability p of having a site filled with the black fluid is $p = 1-p_c$ and the white fluid percolates; i.e., we can always find a continuous path through the white fluid and $(k_0/eta)_{eff}$ is given by the viscosity of the white fluid. In the m
percol

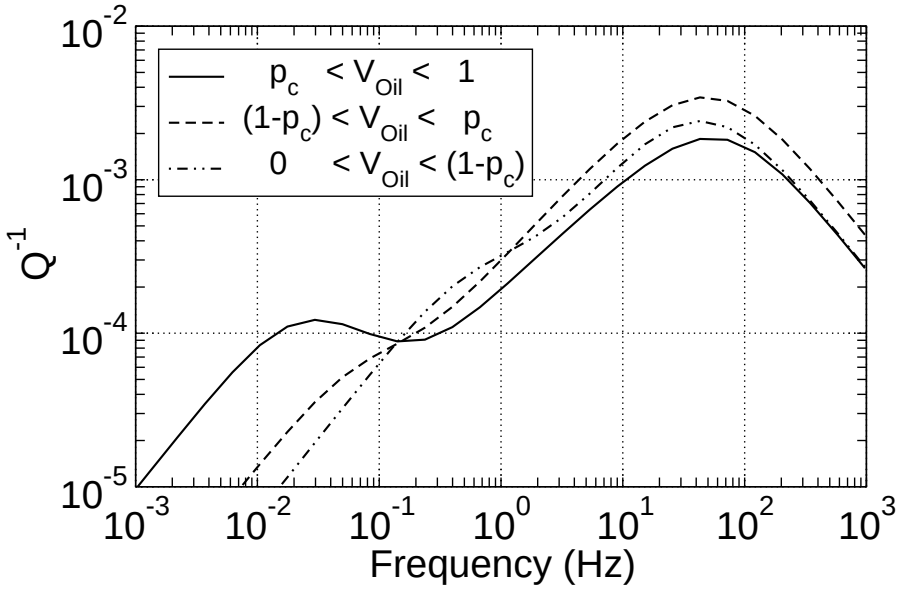

Figure 4.5. Attenuation curves showing the effect of varying the hydraulic conductivity $(k_0/\eta)_{eff}$ via the volume fraction of the oil. All curves have been obtained using a mixture of oil and water and a similar background saturation function f_{sat} but with different volume fractions of fluids.

conductivity $(k_0/\eta)_{eff}$ depends on both η_{oil}, η_{wat}, and the permeability k_0 of the medium. When comparing the three curves, we see that when oil is controlling the rate of equilibration, the attenuation peak is observed at lower frequencies due to oil moving more slowly than water. When water is controlling the rate of equilibration, the attenuation peak is observed at higher frequencies and is partly hidden by the attenuation peak related to fluid-pressure equilibration between local voxel-scale patches. The last case is an intermediate situation.

Note that the aforementioned result should not be interpreted as the consequence of how varying the fluid saturation changes the effective incompressibility contrasts in the sample. Varying the saturation in this case is modifying the nature of the fluid connectivity between the fluid patches and this is what is dominantly responsible for the changes in the $Q^{-1}(\omega)$ curves.

4.4 Attenuation due to spatial fluctuations in the fluid saturation over multiple scales

Pride and Masson (2006) have shown that when the distribution of the local Biot's coupling incompressibility C (defined in the next paragraph) is a self-affine fractal characterized by a Hurst exponent H, the attenuation $Q^{-1}(\omega)$ is related to circular frequency ω by a power law scaling as

$$Q^{-1} \propto \omega^{-\tanh H}. \tag{4.20}$$

A self-affine distribution for the modulus C means that

$$\Delta C(a\Delta x) \propto a^H \Delta C(\Delta x), \tag{4.21}$$

where $\Delta C(\Delta x)$ represents the average amplitude of fluctuation in C at scale Δx and where a is a dimensionless stretch parameter that changes scale. For negative H, the fluctuations in C are decreasing when increasing scale, while when H is positive, the fluctuations are increasing with increasing scale. In the special case where $H = 0$, the fluctuations are the same across all scales. When $H = 1$, the scaling is said to be "self-similar".

The elastic modulus C controls the fluid-pressure change in the grain pack when a volumetric strain ϵ is applied to a sealed sample of porous material (i.e., $C = p_f/\epsilon$ under the condition that the increment in fluid content is zero). The Biot-Gassmann result for this modulus is that in a material with a fluid modulus K_f, a solid modulus K_s, a drained modulus K_d and a porosity ϕ, then [e.g., Biot and Willis, 1957; Pride, 2005]

$$C = \frac{(1 - K_d/K_s)\, K_f/\phi}{1 + \Delta} \tag{4.22}$$

where Δ is a small dimensionless parameter given by

$$\Delta = \frac{1-\phi}{\phi}\frac{K_f}{K_s}\left(1 - \frac{K_d}{(1-\phi)K_s}\right). \tag{4.23}$$

In a partially-saturated region that has had time to locally equilibrate at the smallest scales of saturation, the fluid modulus K_f can be replaced by the Wood modulus K_W of equation (4.16) that depends on the saturation in the region. Thus, in a material having uniform frame properties, fluctuations in saturation are directly proportional to fluctuations in C. So if the saturation is distributed in a self-affine manner, both equations (4.20) and (4.21) should hold. To verify this hypothesis, we generate a series of self-affine fluid-saturation distributions at different Hurst exponents H. To do so, we define a self-affine background saturation function which is then mapped to create the actual fluid distribution as explained in the previous section [i.e., based on equation (4.17)]. Some fluid distributions so obtained are presented in Figure 4.4 and the algorithm used to generate a self-affine background saturation function for use in equation (4.17) is presented in Appendix E. In Figure 4.4, we present the attenuation curves obtained in a series of 5 experiments using a mixture of oil and water, with geometries similar to those presented in Figure 4.4. In this series of experiments, we modified the viscosity of water so that the fluid-pressure diffusivities [see equation (4.3)] are equal in both fluids. Thus, there is no scale dependence to the fluid-pressure diffusivity. In this case, equation (4.20) should apply at least to a part of the frequency range. There are three frequency ranges seen in the results. At high enough frequencies, all realizations at different H (the various solid lines) have roughly the same frequency dependence that is dominated by a relaxation at the frequency corresponding to the equilibration time of a single voxel. Next, at intermediate frequencies, we are in the regime where the self-affine structure is being probed and equation (4.20) holds. The dashed lines represent the power law fits of the solid curves in this intermediate range. Finally, at low-enough frequencies, there is a transition to a $Q^{-1} \propto \omega$ dependence. This effect was explained in detail by Pride and Masson (2006) and is due to the diffusion skin depth at low-enough frequencies being larger than the finite size of the sample. The measured values of the power-law exponents in the intermediate frequency range are plotted in Figure 4.4 as a function of the Hurst exponents. We see that equation 4.20, represented by a solid line, is in good agreement with the observations in the frequency band of interest. The small misfit between the data and equation (4.20) is mainly due to the attenuation peak observed at high frequencies also contributing to the total attenuation in the intermediate frequency range in which the power law fits have been performed.

In Figure 4.4, we present the attenuation curves obtained using the exact same experimental setting, but where the viscosities of the fluids have been changed to their actual values given in Table 4.1. In this situation, the effective hydraulic conductivity is varying spatially within the medium and also depends on the scale at which we look at the medium. For a material containing mesoscopic heterogeneities or fluid patches having a unique size, varying the viscosity of the fluids results in a frequency shift of the attenuations curves [e.g., Masson and Pride, 2007]. Thus, in self-affine materials, where heterogeneities are present at all scales, we would expect some deviation from equation (4.20) if the hydraulic conductivity

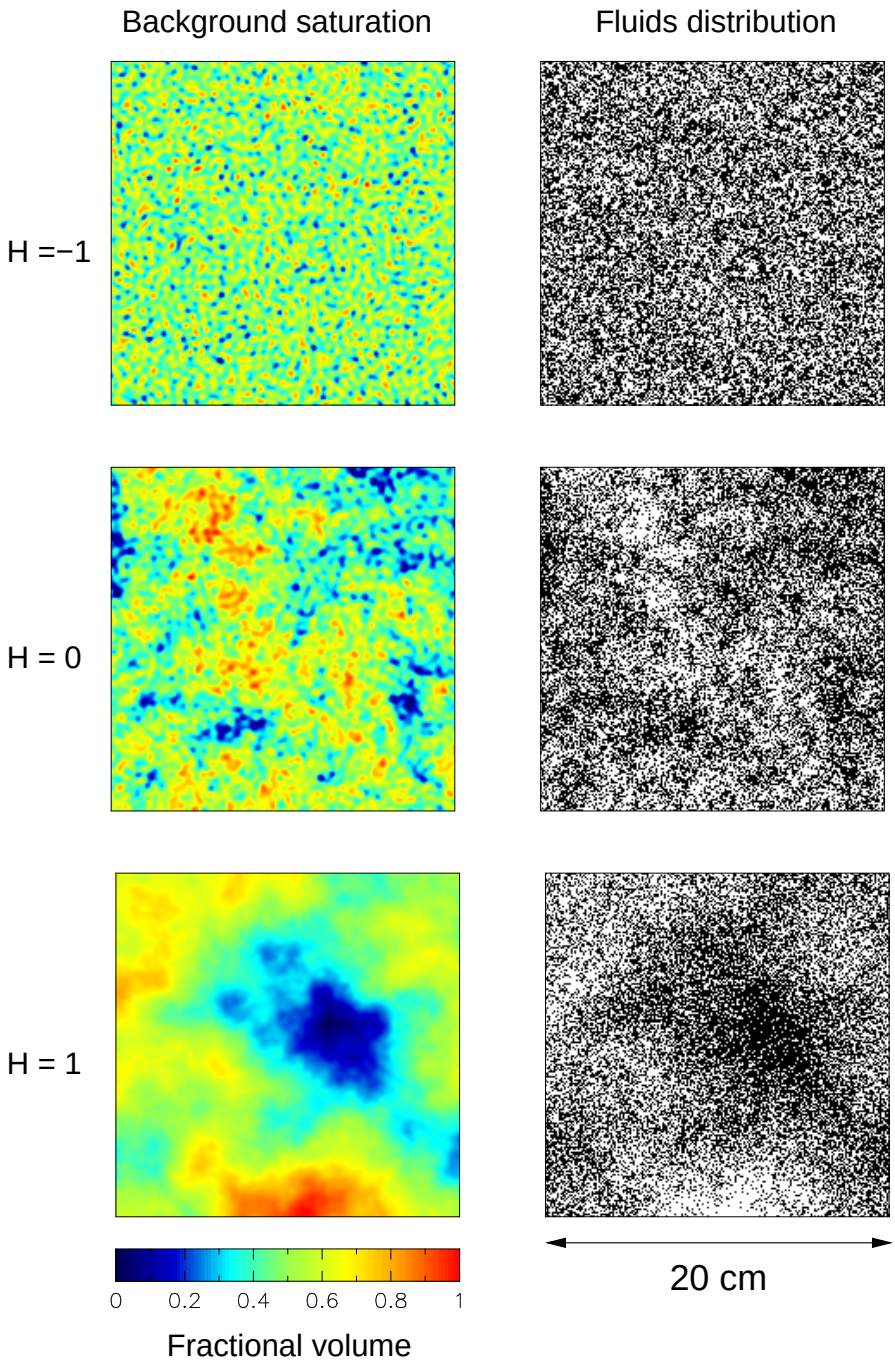

Figure 4.6. An example of fluid distributions obtained when the fluctuations in the background saturation are self affine.

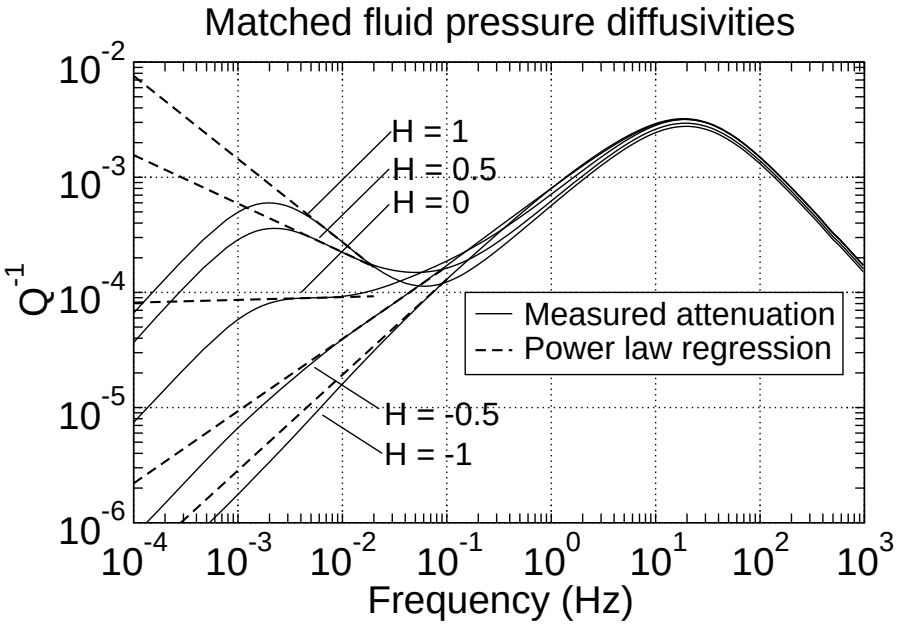

Figure 4.7. Attenuation curves obtained for a mixture of oil and water and where the background saturation function is self affine, as presented in Figure 4.4. Each curve has been obtained using a different Hurst exponent. The dashed lines corresponds to power law fits of the different attenuation curves within a given frequency band. In this example, the viscosity of water has been changed so that the fluid-pressure diffusivities D_i of both fluids are equal.

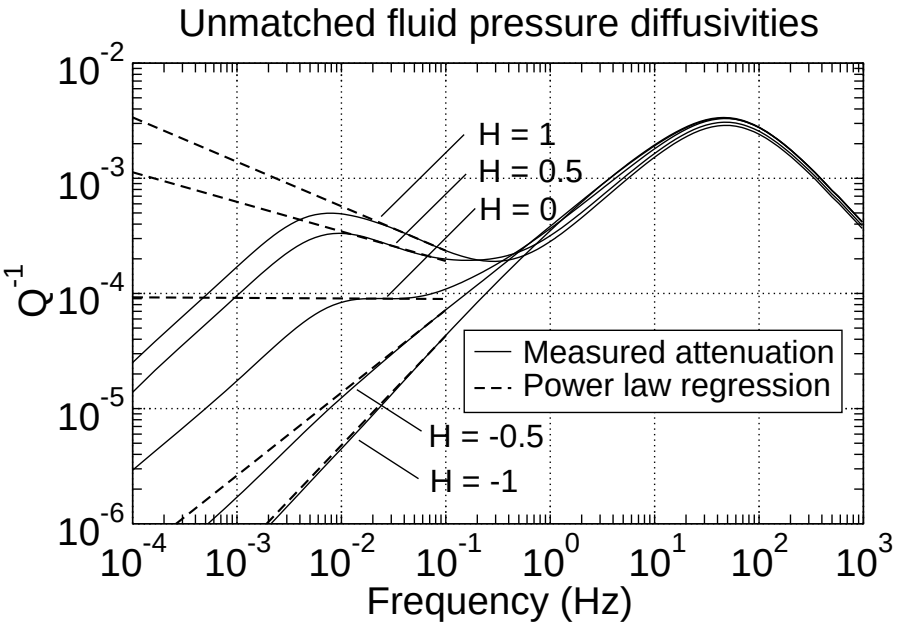

Figure 4.8. Similar to Figure 4.4 but when the physically correct viscosity of water η_{wat} has been used so that the fluid-pressure diffusivities D_i of both fluids are not equal.

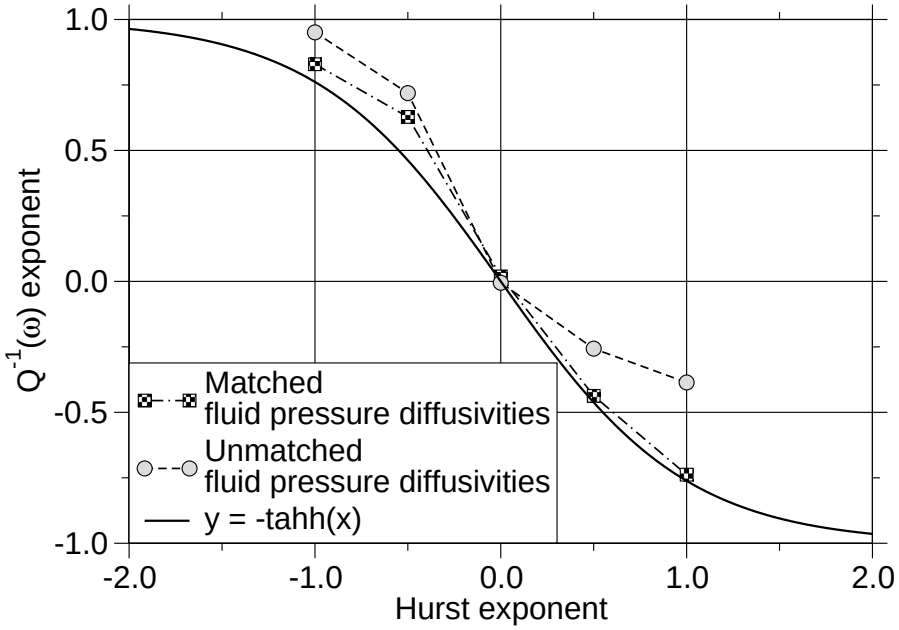

Figure 4.9. Measured exponent describing the variation in the attenuation versus frequency. The measured values corresspond to the curves presented in Figures 4.4 and 4.4 and are plotted as a function of the Hurst exponent of the background saturation function.

$(k_0/\eta)_{eff}$ is a function of scale. In the special case where $(k_0/\eta)_{eff}$ is correlated to the fluctuation in the elastic modulus C, this would result in a stretching of the attenuation curves versus frequency. Thus attenuation would still be related to the frequency via a similar power law but with a different exponent which should be a function of both the Hurst exponent of the background saturation function and of $(k_0/\eta)_{eff}$. Looking at Figure 4.4, we see that in this situation where $(k_0/\eta)_{eff}$ is varying within the material, the observed exponent differs indeed from the values predicted by equation (4.20). For the special case where $H = 0$, the data are similar in both series of experiments because there is no scale dependence of the fluctuations.

The main result of this section is the observation that in the special case where the fluid saturation is self affine, the attenuation is given approximately by the frequency power law of equation (4.20). This result will be used in the next section to explain the attenuation observed when the fluid distribution is generated using an invasion-percolation process.

4.5 Attenuation due to fluid distributions created via invasion percolation.

4.5.1 Invasion percolation

Invasion percolation is a dynamic process introduced by Wilkinson and Willemsen (1983) to study the slow immiscible invasion of one fluid into a porous region orginally occupied by another fluid. Experimental studies [e.g., Lenormand et al., 1988] have shown that the theory accurately reproduces the fluid distribution observed in the laboratory when capillary forces dominate viscous forces during the invasion; i.e., when the capillary number is small.

The theory considers an idealized porous medium consisting of a regular lattice for which the sites and bonds correspond to the pores and throats respectively. Randomness is introduced in the medium by assigning each pore or throat with a random value corresponding to its radius. For scenarios in which a non-wetting fluid invades and a wetting fluid defends (drainage), it is the bonds (pore throats) that represent the capillary barriers to invasion. When a wetting fluid invades and a non-wetting fluid defends (drainage), it is the sites (pores) that represent the capillary barriers. For a given pair of immiscible fluids, the threshold pressure p_c (defined as the minimum pressure difference between the two fluids needed to advance the fluid interface through a capillary barrier) is a function of the radius r of the capillary barrier and given by

$$p_c = |p_{fluid1} - p_{fluid2}| = \frac{2\sigma \cos\theta}{r}, \tag{4.24}$$

where σ is the interfacial tension between the two fluids and θ the contact angle between

the fluid interface and the pore or throat wall. A simulation starts with all the sites and bonds saturated by the defending fluid. The invading fluid is then injected into the medium and advances one pore at a time. At each step of drainage, the next pore to be invaded is the one that has the smallest threshold pressure on the bond linking it to the previously invaded pores. To describe imbibition, one need only exchange the words sites and bonds (or pores and throats).

The invasion-percolation algorithm of Wilkenson and Willemson (1983) is a simplified version of the above invasion process that consists of the following steps and is assumed to apply equally to drainage and imbibition alike:

1. Assign random numbers r in the range $[0, 1]$ to the sites of an $L \times L \times L$ lattice.
2. Select the source sites where the invading fluid is injected and the exit sites where the defending fluid is allowed to escape.
3. List all the sites belonging to the defending fluid and that are immediately adjacent to the invading fluid.
4. Pick from the list the site that has the lowest random number r and fill that site with the invading fluid.
5. Repeat steps 2,3 and 4 until the invading fluid reaches an exit site.

An example of a fluid distribution generated by the invasion-percolation algorithm is presented in Figure 4.5.1. In the example, a grid of size $L \times L \times 2L$ is used, the invading fluid is injected on the bottom face, the defending fluid escapes through the top face and periodic boundaries conditions have been applied on the front/back and left/right faces. The invasion-percolation algorithm produces complex tree-like fluid distributions with branches spanning a large range of scales. By varying the size L of the grid, Wilkinson (1983) show that the mass of invading fluid $M(L)$ present in the central volume $L \times L \times L$ at percolation (i.e. when the invading fluid first reaches the top face) obeys the scaling

$$M(L) \propto L^D \tag{4.25}$$

where D is the fractal dimension of the cluster formed by the invading fluid. Wilkinson (1983) establish that $D = 2.52$ in 3 dimensions.

Last, for the fluid distributions produced by invasion percolation, global connectivity is ensured within the invading cluster due to the invasive nature of the process. This is not the case for the defending fluid that can become trapped in places by the invading fluid to form isolated clusters that are not connected to each other. However, Wilkinson (1983) have shown that trapping of the defending fluid is marginal in three dimensions and doesn't need to be accounted for (trapping is a 2D problem). In the next sections, global connectivity will be assumed in both the invading and the defending fluids.

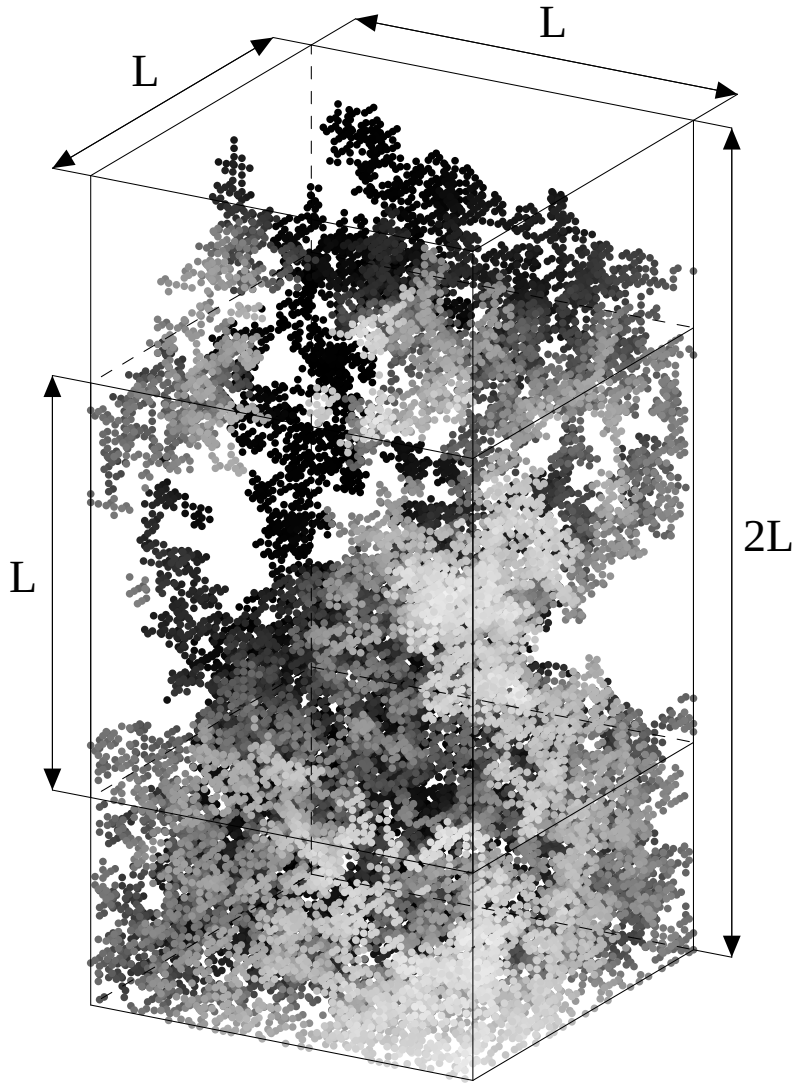

Figure 4.10. An example of the spatial distribution of fluids obtained using the invasion-percolation process. The invading fluid is injected at the bottom face of the domain and is represented by the dark grey cluster. The invasion-percolation process stops when the invading fluid reaches the top face of the domain. Periodic boundaries have been used on the front-back and left-right faces of the domain. For the poroelastic simulations, only the central volume $L \times L \times L$ is used.

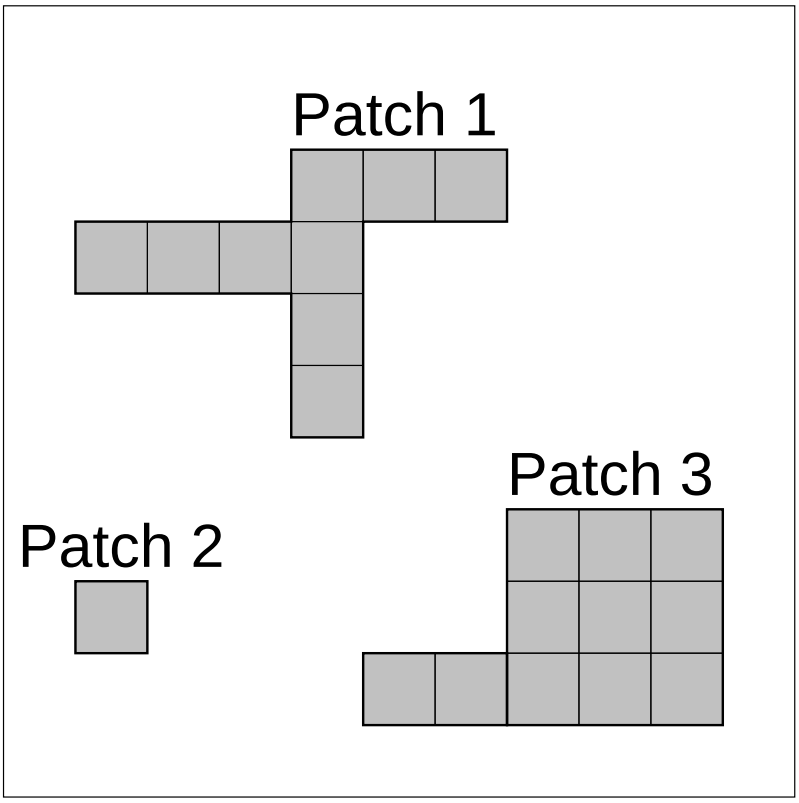

Figure 4.11. Example showing different patch geometries.

4.5.2 Estimating the patch size distribution in materials having complex geometries

In the previous section, equation (4.25) contains information on how the fluid mass of the invader is distributed as a function of scale. This information alone is not sufficient to model the seismic attenuation using existing models of patchy saturation [e.g., Pride et al., 2004]. Indeed, these analytical models require information about the geometries and sizes of the fluid patches. We now present an algorithm designed to estimate the distribution of patch sizes within fluid clusters of arbitrary geometries. In the next sections, this algorithm will be used as a base to build an average patchy-saturation model that can predict the attenuation results obtained using the finite-difference code for fluid distributions of arbitrary geometries. For a given fluid, and for a simple patch geometry like a sphere, the relaxation frequency ω_c associated with the diffusive equilibration of the patch is proportional to the square of the diffusion length L_1 of the patch [e.g., Pride et al., 2004]. Thus, for modeling purposes, we need to estimate what fraction of the volume occupied by the patches is associated with a given diffusion length L_1. Note that the actual dimension of the patches is not of any

interest here since patches having different dimensions can be considered to have the same diffusion length. For example, patches 1 and 2 in Figure 4.5.2 have very different shapes and dimensions but their width never exceeds the size of a pixel. Consequently, the fluid pressure equilibrates in roughly the same time within both patches. The situation is different in patch 3 which consist of a large square of size 3×3 touching a rectangle of size 1×2. For patch 3, the fluid pressure will take less time to equilibrate in the small rectangular area than in the large square area. In this case, it is better to model patch 3 as two different patches, one of size 1 and one of size 3 even though fluid exchange takes place between the two areas. We define the "patch-size distribution" to be the fraction of the total volume occupied by patches of size a.

The simple algorithm used to compute the patch-size distribution is based on a multi-scale analysis using boxes of varying sizes a_i and is described as follows:

1. Define a box shape. Simple choices include circular or square boxes in 2D and cubic or spherical boxes in 3D. In this case a can be taken as the radius of the circle/sphere, or as the side length of the square/cube.

2. Initialize $a = a_0$ so that the box size is equal to the size of the smallest patch present (typically a pixel/voxel).

3. Scan the volume by moving the box to every possible position. For each box position:

   (a) check if the box is totally filled with the fluid of interest.

   (b) If yes, assign the current value a_i of a to all points within the box.

4. Increase the size of the box: $a_i = a_{i-1} + \Delta a$

5. Go back to step 3 and continue until the box's size becomes larger than the volume being studied.

6. Finally, the fraction of the total fluid volume occupied by patches of size a_i is computed for each i.

A schematic example showing how the algorithm applies to a 2D fluid distribution is presented in Figure 4.5.2. In this example, we use square boxes with sizes $a = k\Delta x$ where $k = 1, 2, 3, ...$ and $\Delta x = 1$ is the grid spacing. The goal is to find the patch-size distribution of the black clusters. The top panel presents the values assigned to the black sites after the domain has been scanned with a box of size $a_0 = \Delta x$. Since all the sites belong to patches having a size greater than or equal to the grid spacing, all the points take the value 1 after this first pass. The middle panel shows the result after a second scan using a box of size $a_1 = 2\Delta x$. Here, all the sites that belong to a patch having a size greater than or equal to $2\Delta x$ take the value 2. Note that on the side of the domain, we assume that the fluid pattern is symmetrically mirrored across the boundary. This is motivated by the fact that when computing the attenuation, no fluid flow is allowed through the boundaries of the sample. Thus, patches placed on the boundaries of the domain take more time to equilibrate than

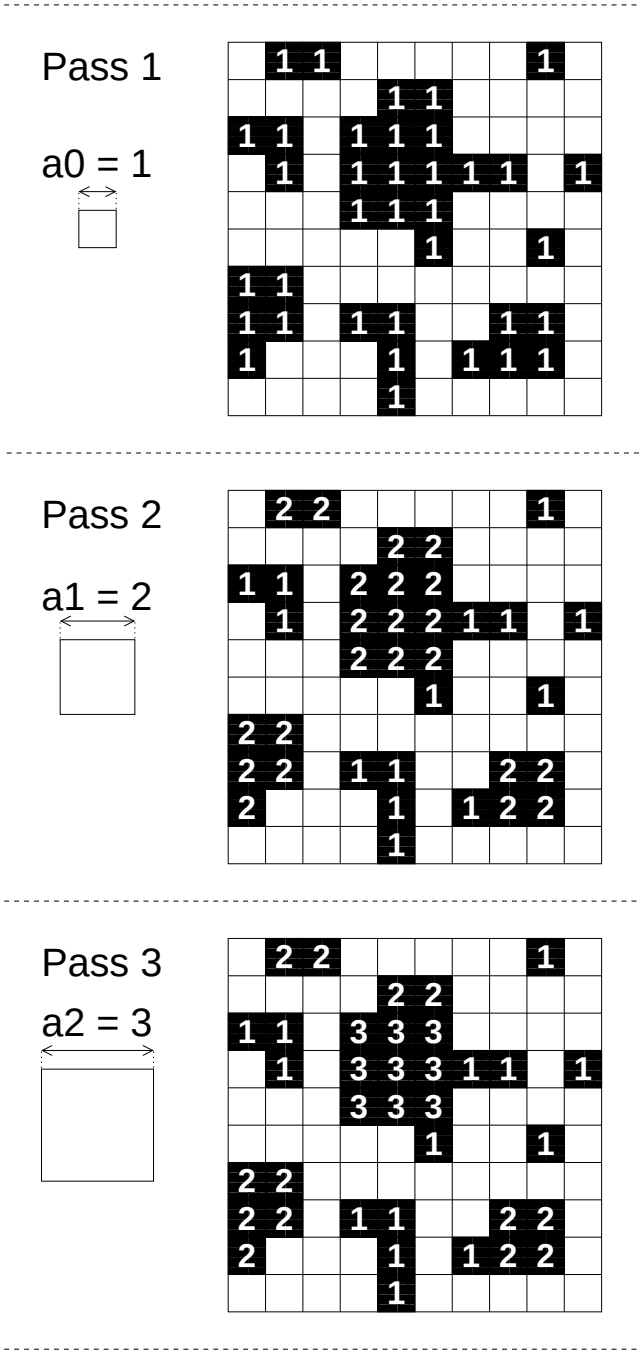

Figure 4.12. Example showing how the patches are identified by size at different passes corresponding to using larger measurement boxes.

Table 4.2. Fluid combinations used in the numerical experiments. The star indicates which fluid is controlling the timing of diffusion.

Experiment	Invading fluid	Defending fluid	Permeability
1	Oil*	Water	10^{-12} m^2
2	Water	Oil*	10^{-12} m^2
3	Air	Water*	10^{-15} m^2
4	Water*	Air	10^{-15} m^2

patches away from the boundaries. For example, a patch of size one placed in a corner of the domain will take as much time to equilibrate its fluid pressure as a patch of size 2 placed in the center of the domain. Finally, the bottom panel shows the result obtained after the third pass using a box of size $a_2 = 3\Delta x$. Here all the sites belonging to a patch of size greater or equal to 3 now have the value 3. In this schematic, the value of the sites remains unchanged for additional passes (i.e. when $k > 3$) because no patches having a size greater than 3 are present in the domain. Finally counting the sites sharing the same value gives the following result for this example: 39% of the black cluster volume is occupied by patches of size 1, 36% by patches of size 2 and 25% by patches of size 3.

Figure 4.5.2 shows the result obtained when the algorithm is applied to a three dimensional fluid cluster generated using the invasion-percolation result of Figure 4.5.1. In Figure 4.5.2, we present the patch-size distribution for the invading cluster (top panel) and the defending cluster (lower panel). The invading fluid is not forming patches of size greater than 2 grid spaces and almost all the patches have a size equal to the grid spacing. The situation is very different for the defending fluid which forms patches spanning a large range of sizes.

Last, the algorithm as presented in this section is not computationally efficient. However, if one needs to use it intensively, it can and should be implemented efficiently.

4.5.3 Attenuation associated with invasion percolation

We now present attenuation curves obtained when the fluid distribution is created using the invasion-percolation algorithm. The cental volume $L \times L \times L$ of the invasion-percolation cluster shown in Figure 4.5.1 is removed and used for the quasi-static poroelastic finite-difference simulations. For a given percolation cluster, we perform four different stress-strain numerical experiments using the fluid substitutions presented in Table 4.2. In all experiments, the properties of the solid skeleton are taken as uniform within the sample and

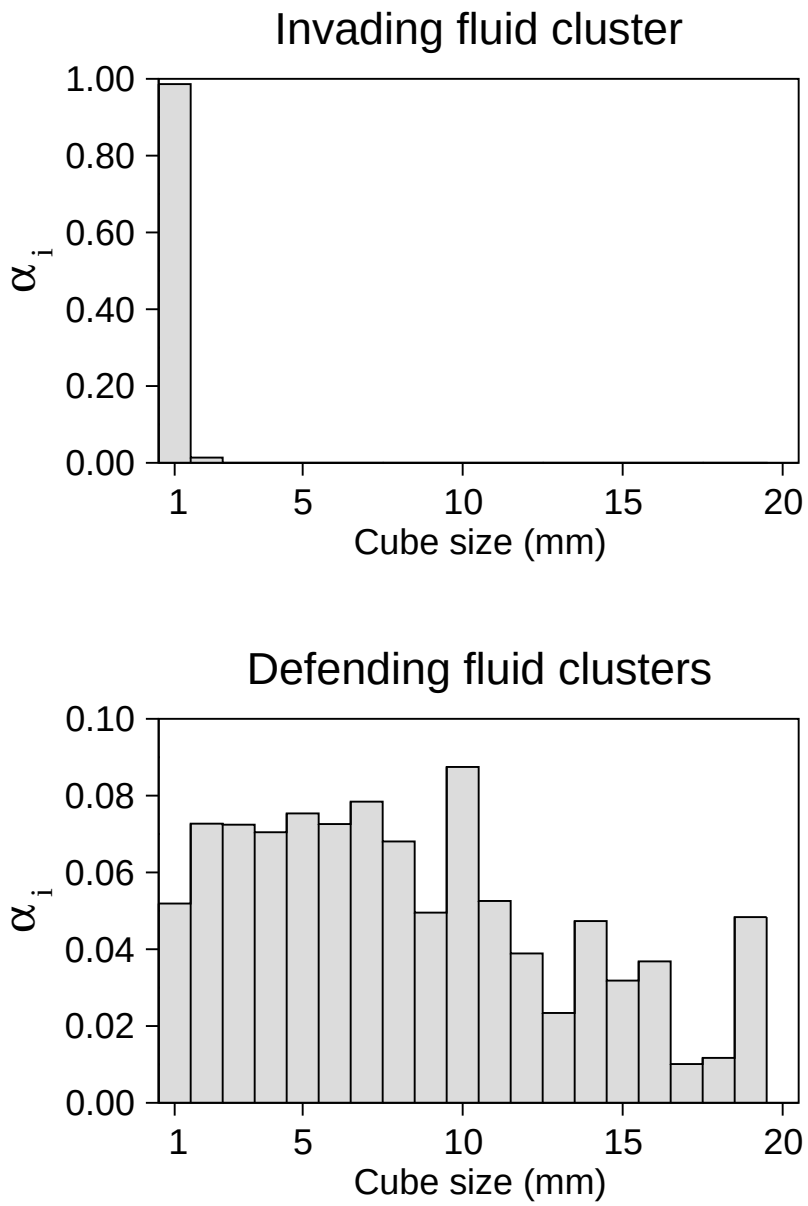

Figure 4.13. Distribution of the cube sizes computed using the cube counting algorithm for both the invading and defending fluid clusters created using invasion percolation. Here, α_i is the volume fraction of the defending fluid occupied by voxels belonging to a cube of size ia where a is the size of the voxels.

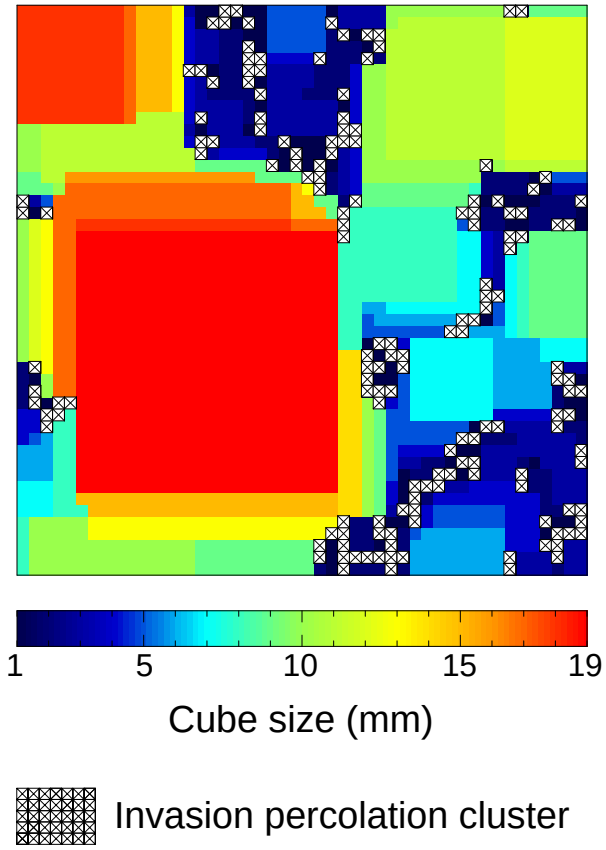

Figure 4.14. Result obtained when applying the cube counting algorithm to the cluster formed by the defending fluid. Here, the algorithm has been applied to the central region of the fluid distribution presented in Figure 4.5.1. A slice through the 3D matrix obtained once the algorithm has been applied is presented. Each voxel has the value corresponding to the size of the largest cube fully saturated by the defending fluid and containing the voxel.

are given in Table 4.1. To ensure that patches of similar sizes have a comparable relaxation frequency in all experiments, the permeability within the sample has been modified so that η^*/k_0 is the same for all experiments. Here η^* denotes the viscosity of the fluid in which the fluid-pressure diffusion dominantly occurs; i.e., the liquid if the patchy mix is liquid and gas, or the higher-viscosity liquid if both fluids are liquids.

A final point needs to be discussed before presenting the attenuation results. The invasion-percolation algorithm provides a fluid distribution at the pore scale while the poroelastic laws apply to the macroscopic porous-continuum scale. Thus, there is the question of how to input the invasion-percolation results into the poroelastic finite-difference code. One approach is to first compute locally averaged poroelastic properties from the invasion-percolation distribution, and then use these fluid-dependent properties in the finite-difference code. However, in this case, the results depend on the way the averaging is performed. Since the fluids are not all experiencing the same induced pressure or strain change, it is unclear what average to apply across all frequencies. And different averaging schemes, for example arithmetic versus harmonic means, give completely different results. For that reason we think it is more accurate to use the invasion-percolation result directly in the finite-difference code; i.e., take the voxels to be the same in both models. Two different arguments justify this choice. First, the fractal nature of the fluid distribution created using invasion percolation suggests that the scale at which we look at the problem is not critical. Second, many studies [e.g., Maloy et al., 1992] have shown that in real invasion-percolation experiments at low capillary numbers, fluid bursts are observed and the fluid is not invading one pore at a time but many pores. Thus, locally we have groups of pores saturated by the invading fluid. Thus, the smallest voxel of an invasion-percolation scheme might more correctly be thought of as containing several grains to the side and thus be directly equivalent to a porous-continuum voxeled in the stress-strain experiments.

The attenuation curves obtained using the invasion-percolation cluster of Figure 4.5.1 and the four fluid substitutions given in Table 4.2 are presented in Figure 4.5.3. We see that the shape and amplitude of the attenuation curves varies greatly depending on the pair of fluids present in the sample as well as on which fluid is the invader or defender. The top left and bottom right graphs correspond to when fluid pressure equilibrates within the cluster formed by the invading fluid. In this case, we see that a narrow attenuation peak is observed in the high-frequency range and the attenuation is decreasing with decreasing frequency toward low frequencies. The top right and bottom left graphs correspond to the opposite situation where the fluid pressure equilibrates outside the invading cluster. In this case, we see that when the sample is saturated with a mixture of oil and water (top right panel), the attenuation can be related to frequency as a power low. When the fluid mixture consists of air and water (bottom left), no simple relation relates the attenuation to frequency and high levels of attenuation are observed over a large range of frequencies. This last case will be the most challenging to model.

Figure 4.5.2 clarifies why the frequency dependence of the attenuation is different when the fluid pressure equilibrates inside or outside the invading fluid. The size of patches formed by the invading cluster never exceeds twice the grid spacing with the vast majority of patches being at the grid dimension. Thus all the patches have about the same relaxation frequency

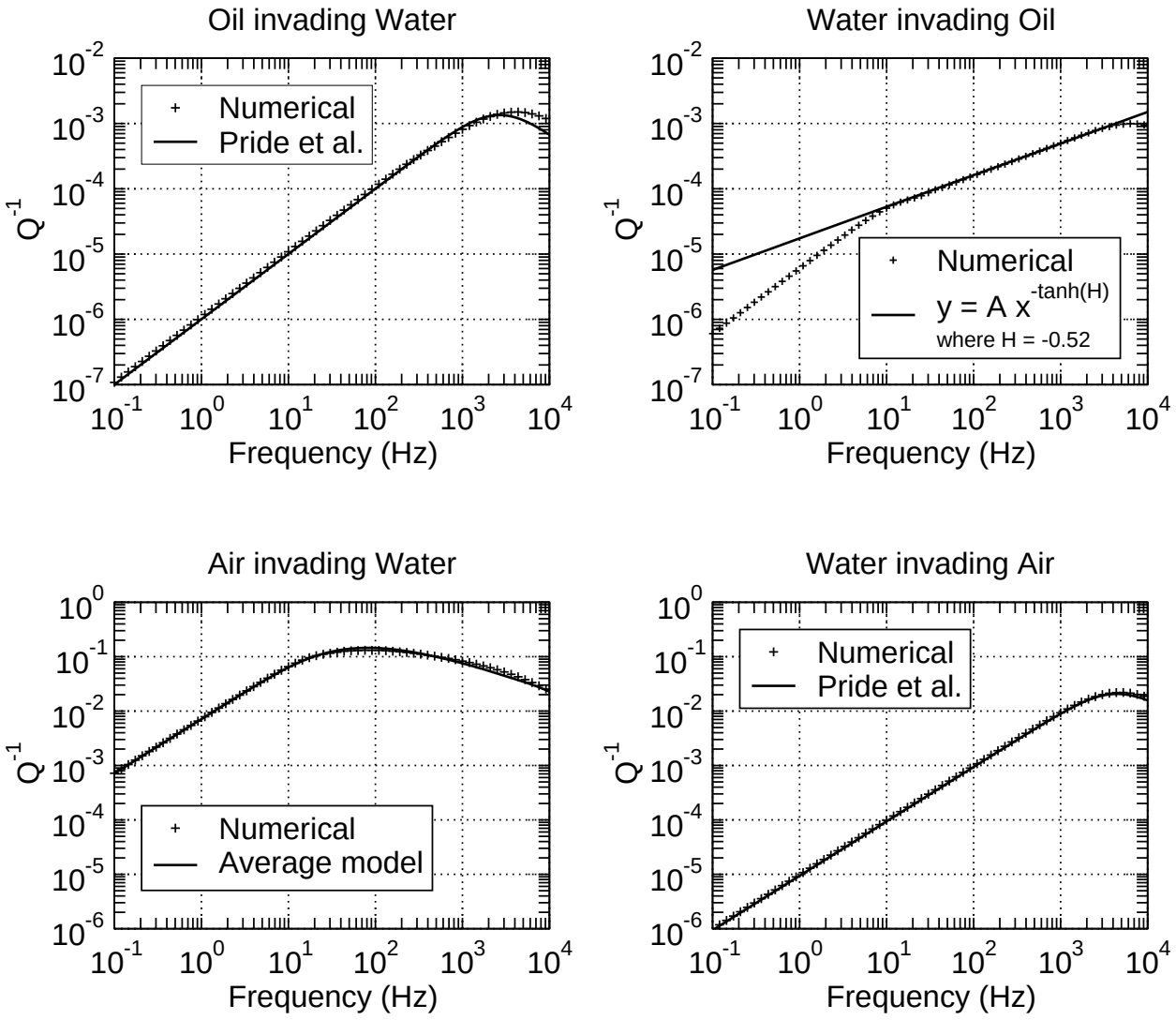

Figure 4.15. Attenuation curves obtained when an invasion-percolation algorithm is used to generate the fluid distribution. All curves have been obtained using the same realization of an invasion-percolation process. Results using the following fluid substitutions are presented: air invading water, water invading air, oil invading water, water invading oil.

and a single attenuation is observed at high frequencies due to the small size of the patches. The situation is very different in the clusters formed by the defending fluid. Here the patches exhibit a large range of sizes. Consequently, the patches will have a large range of different relaxation frequencies.

4.5.4 Modeling choices

In this section, we detail different approaches that can be used to model the numerical attenuation data presented in Figure 4.5.3. The different attenuation curves are explained separately.

4.5.4.1 Oil invading water

In this scenario, the timing of the fluid-pressure diffusion is controlled by the invading oil which has the highest viscosity. Since trapping of the defending fluid is marginal in 3D, and because the viscosity of water is much smaller than oil, the induced fluid pressure can be taken as uniform throughout the water-filled areas. This, along with the fact that the thickness of the patches forming the invading cluster is roughly constant (see Figure 4.5.2), allows the patchy-saturation model of Pride et al. (2004) to be used to fit the numerical data without any free fit parameters. The attenuation predicted using the analytical expression presented in Appendix C is represented by the solid line in the top left panel of Figure 4.5.3. The ratio V/S and the length L_1 required by the patchy-saturation model have been computed numerically for the invading cluster using the expressions in Appendix C.

4.5.4.2 Water invading oil

Here, the timing of the diffusion is controlled by the higher-viscosity defending fluid (oil). The invasion percolation ensures connectivity in the invading fluid and the fluid pressure within the water can again be considered constant due to its relatively low viscosity. As shown in Figure 4.5.2, the size distribution of the oil patches spans a large range of scales. Thus, during the simulation, the small oil patches will equilibrate first and the larger patches will take more time. Because of the small contrast in the fluid incompressibilities, it is judicious to adopt the approach presented in Section 4.4 to model the attenuation.

A first step consists of estimating the fluctuation of the fluid saturation as a function of scale. This is achieved by taking a 3D Fourier transform of the fluid's spatial distribution; i.e., the invasion-percolation matrix which takes the value 1 at nodes filled with the invading fluid and the value 0 at nodes filled with the defending fluid. The resulting spectrum is presented in Figure 4.5.4.2. We then perform a least-squares fit of the spectrum assuming the spatial fluid distribution is self affine (a power law). The result of the fit is represented as the dashed line in Figure 4.5.4.2 and the estimated value for the Hurst exponent is H

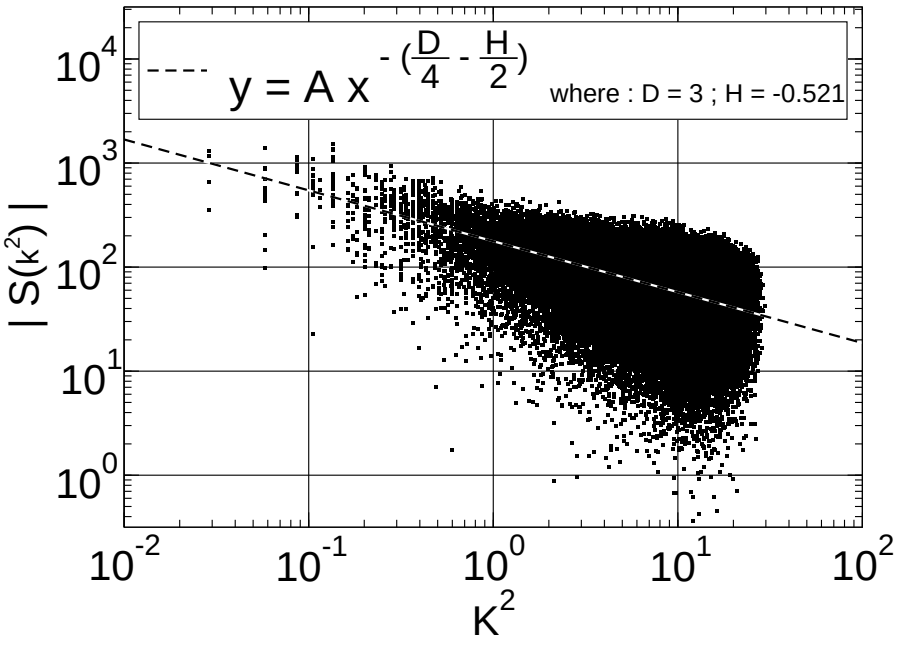

Figure 4.16. Spectrum obtained by taking the 3D Fourier transform of the fluid saturation. Here, $k^2 = k_x^2 + k_y^2 + k_z^2$ is the spatial wave number. The data have been fit as a power law assuming a spectrum corresponding to a self-affine function. The value for the Hurst exponent so obtained is $H = -0.52$ which, as anticipated, provides a good power-law fit to the attenuation results in Figure 4.5.3.

= -0.521. We then use this exponent in equation(4.20) to fit the high-frequency power law observed in Figure 4.5.3. The fit is excellent thus confirming the arguments of Section 4.4.

4.5.4.3 Air invading water

In this case, the fluid-pressure equilibrates within the regions filled with the defending water. Due to the large fluid incompressibility contrast as discussed in Section 4.3, equilibration between larger scale regions of air and water is not important and we need only focus on the equilibration between a patch of water of size i and the air it immediately surrounds.

The first step in modeling the numerical result of Figure 4.5.3 is to compute the patch-size distribution α_i of water patches as discussed in Section 4.5.2 (α_i is the volume fraction of the water associated with patches of size i). For each water-patch size i, we then determine the associated patchy-saturation attenuation $Q_i^{-1}(\omega)$ using the analytical theory presented in Appendix C. The overall attenuation is obtained as a volumetrically-weighted sum of the

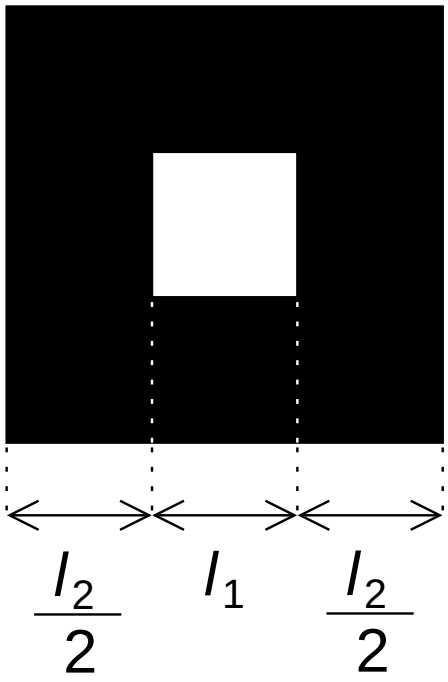

Figure 4.17. The model of an inner cube of air (white) surrounded by an outer layer of water (black) used in determining the patchy-saturation geometric properties. For each size of water patch l_2 present in the defending water, this domain model is used to calculate the patchy-saturation diffusion length L_1 using the approach outlined in Appendix C. See Figure 4.5.1 for why this particular domain geometry was chosen for the case of air invading water.

attenuation associated with each patch size and given by

$$Q_{\rm av}^{-1}(\omega) = \sum_i \alpha_i Q_i^{-1}(\omega). \tag{4.26}$$

A similar average was used by Pride and Masson (2006) in the derivation of equation (4.20). To determine Q_i^{-1} using the patchy-saturation model of Appendix C, a geometry must be assumed for both the air and water at each size i. A look at Figure 4.5.1 suggests that an appropriate domain model is to embed a small cube of air within a larger cube of water. The cube of air has an edge length l_1 and is surrounded by water in a composite cube having an edge length $l_1 + l_2$ (see Figure 4.5.4.3 for the domain model). We take l_2 as the length a_i associated with patch size i. To determine the length l_1 of the inner cube of air, we assume the volume fraction of air and water in each such modeling domain is the same as the overall volume fraction of air v_1 and water v_2 in the entire system (where $v_1 + v_2 = 1$). This ensures that the ensemble of domains corresponding to all patch sizes i preserves the proper volume of air and water in the system. The length l_1 is thus obtained from the simple geometrical result

$$l_1 = l_2/(v_1^{-\frac{1}{3}} - 1), \tag{4.27}$$

where v_1 is the overall volume fraction of air in the system. The diffusion length L_1 is evaluated numerically for each patch size $l_2 = a_i$ by numerically solving the boundary-value problem defined in Appendix C for the domain of Figure 4.5.4.3. The ratio V/S required by the patchy saturation model for this particular geometry is

$$\frac{V}{S} = \frac{(l_1 + l_2)^3}{6\, l_1^2}. \tag{4.28}$$

Without any free parameters, this scheme provides a nice fit to the numerical attenuation data as shown in Figure 4.5.3.

4.5.4.4 Water invading air

This situation is similar to the case where oil is invading water and the patchy-saturation model can be applied directly to the invading cluster. The estimated attenuation is plotted as the solid line in the upper left graph of Figure 4.5.3 and fits the numerical data very well.

4.6 Other invasion scenarios

Most scenarios for how partial-saturation distributions are created in the Earth involve the slow invasion of one fluid into a region intially occupied by another fluid. In this case, the invasion-percolation scheme provides realistic fluid distributions and is why we used it in the present paper. However, when the invasion occurs at faster rates, which is typically defined when the capillary number Ca is greater than roughly 10^{-6} [e.g., Lenormand et al., 1988], other distributions are created that are distinct from the invasion-percolation clusters. The capillary number is the dimensionless ratio of viscous shear stress to capillary pressure and is given by $\text{Ca} = \eta q/\sigma$ where q is the Darcy velocity of the invading fluid, η the viscosity of the invader, and σ the surface tension.

In particular, when the viscosity of the invading fluid is significantly less than the defender (e.g., a gas invading liquid) and when $\text{Ca} > 10^{-6}$, the viscous-fingering instablity occurs. Though the viscosity ratio (invader viscosity divided by defender viscosity) at which viscous fingering in porous media begins to occur has never been analytically determined, there is experimental evidence [e.g., Lenormand et al., 1988 and Stokes et al., 1986] that it needs to be 10^{-2} or smaller. For the case of drainage (e.g., water the defender and air the invader), the invasion cluster for viscous fingers resembles a diffusion-limited aggregation (DLA) and has a fractal dimension and structure quite distinct from invasion percolation [e.g., Lenormand et al., 1988]. The width of the individual fingers are quite thin (no more than a few pore widths) and the cluster overall is more ramified and sparse than in invasion percolation

(which is also called capillary fingering). For the case of imbibition, the viscous fingers are much broader than in invasion percolation and scale as $\mathrm{Ca}^{-1/2}$ [e.g., Stokes et al, 1986].

We have not attempted to simulate viscous-fingering structure in our numerical experiments, but expect the effect of such structure on the seismic attenuation to be distinct from invasion percolation due to the different geometries involved even if the modeling principles are the same. In particular, since the defender is always controlling the induced fluid-pressure equilibration for a viscous-fingering cluster (since the defender by definition has the largest viscosity), the analysis of the present paper used to model the air invading water (drainage) and water invading oil (imbibition) scenarios above should be directly applicable to the viscous-fingering clusters. In the case of viscous fingering in drainage, we would expect even more intense levels of attenuation at low frequencies compared to the invasion-percolation clusters because the patches of defending fluid will be wider in viscous fingering (the invading viscous fingers are narrower). For viscous fingering in imbibition (e.g., water invading oil), we expect a power law to emerge for $Q(\omega)$ with an exponent again given by the Hurst exponent of the saturation of the defender. However, this exponent will be different than for invasion percolation and is not currently known.

4.7 Conclusions

In this paper, we have shown that the contrast in the fluid incompressibility in patchy fluid distributions greatly influences how attenuation depends on frequency. On the one hand, when the contrast in the fluid incompressibility is large (e.g., gas and liquid), no fluid-pressure equilibration occurs at scales larger than the patch size and one only needs to consider fluid-pressure equilibration between adjacent patches. On the other hand, when the contrast in the fluid incompressibility is small (e.g., oil and water), fluid-pressure equilibration can occur at scales larger than the patches. In this case, fluid pressure can equilibrate between distant areas if the fluid saturation is varying spatially.

We computed seismic attenuation for homogeneous porous samples saturated with a mixture of two fluids and for which the spatial distribution of fluids was obtained using an invasion-percolation process. We showed that when the fluid-pressure diffusion takes place within the invading cluster, like when water is invading air or when oil is invading water, a single attenuation peak is observed at high frequencies. In this case, we expect no significant attenuation levels in the seismic band of frequencies. When the fluid-pressure diffusion takes place within the clusters formed by the defending fluid, significant attenuation levels are observed over a much wider frequency range. This is because the defending cluster forms patches of various sizes spanning a large range of scales. When the invading fluid is water and the defending fluid oil, the attenuation is related to frequency as a power law for which the exponent is a function of the Hurst exponent associated with the defending cluster. While this result is interesting, because the fluid incompressibility contrast is small in this case, the overall level of attenuation is not very high. The most interesting situation is when air is invading water. In this case, high levels of attenuation can be observed even at

very low frequencies. No simple relation has been determined between the attenuation and frequency. However, we developed a method to estimate an average attenuation based on applying a patchy-saturation analytical model to each size patch in the system. We showed that this method performs very well in fitting the numerical data. Also, this method can be applied to fluid distributions of arbitrarily complex geometries when the contrast in the fluid incompressibility is large.

Chapter 5

Measuring the spatial fluctuations in the elastic properties of natural rocks at the mesoscale

(Not yet submitted for publication.)

5.1 Introduction

Recent analytical and numerical studies have shown that fluctuations in the mechanical properties of porous rocks at the mesoscopic scale (say, from a millimeter up to a few centimeters) can explain the significant attenuation levels observed in the seismic frequency band (10 Hz-10000 Hz). Generally speaking, the stronger these fluctuations in the mechanical properties are, the stronger the attenuation is. Masson and Pride showed that, if a given elastic modulus M is expressed as $\langle M \rangle + \Delta M$, where $\langle M \rangle$ represents its average value inside an earth sample and ΔM denotes the fluctuations around its mean value, the attenuation scales as

$$Q^{-1} \propto (\Delta M)^2 , \tag{5.1}$$

where Q^{-1} is the inverse quality factor. This fact raises the question: *How much heterogeneity in the elastic moduli of real rocks and sediments is typically present at the mesoscale ?*

Answering this question requires experimental measurement of the spatial fluctuations of the elastic properties within real rock samples. Micro-indentation and nano-indentation techniques are widely used and are efficient for measuring the elastic modulus of different

material types. Recent studies have shown that the micro-indenatation technique can be used to measure the elastic modulus of natural rocks [see for example Wang et al. (2009) , or Leite and Ferland (2001) for the special case of porous rocks]. We have found no reports of studies showing the spatial distribution of elastic moduli within sedimentary rocks at the mesoscopic scale. Zhu et al. (2007) showed that nano-indentation mapping of the Young's modulus is feasible in cement pastes and natural rocks; however, the dimensions of their experimental maps don't exceed the size of a few grains, which is too small to answer our question about fluctuations in the frame moduli of porous rocks. In this paper, we present experimental equipment that allows us to perform a micro-indentation mapping of the Young's modulus in natural rock samples with millimetric resolution. Then, we show that these maps can be used as an input for the numerical computation of seismic attenuation.

5.2 Materials and experimental method

5.2.1 Rock samples

Preliminary tests have been conducted using natural stone flooring tiles, which are an easy supply of clean cut rock samples. Results obtained using two different samples are presented in this study. The first sample is a clean, well-consolidated sandstone exhibiting stratification. The second sample is a travertine limestone which is highly heterogeneous and contains holes and shells. Both samples are pictured in the top row of Figure 5.7.

5.2.2 The micro indentation scanner

The MIScan (Micro-Indentation Scanner) consists of an indentation probe mounted on an industrial x-y-z motion system. The schematic of this device is given in Figure 5.2 and photographs in Figure 5.2. The device performs multiple automated indentation tests at different locations on the surface of a flat rock sample. The heavy-duty motion system is stiff enough to minimize frame deformation when performing the indentations. It is also sufficiently fast to perform high-resolution mapping in a reasonable amount of time (say, a few hours). The indentation probe of the MIScan schematized in Figure 5.1 consists of an indenter mounted on a rigid rod. The force transmitted to the sample through the rod is monitored using a piezoelectric load cell, and the indentation depth (i.e., the distance between the sample's surface and the indenter's tip) is monitored using three displacement sensors (LVDT). The piezoelectric transducer used to monitor the applied load has been chosen because it offers a faster response than the more classical load cells based on strain gages. The linear variable differential transformers (LVDTs) have been selected for their high reliability and accuracy that offer sub-micron resolution. As shown in Figure 5.2, three LVDTs positioned at equal angular intervals around the main rod are used to monitor the indentation depth. This reduces noise level and prevents measurement error due to an eventual

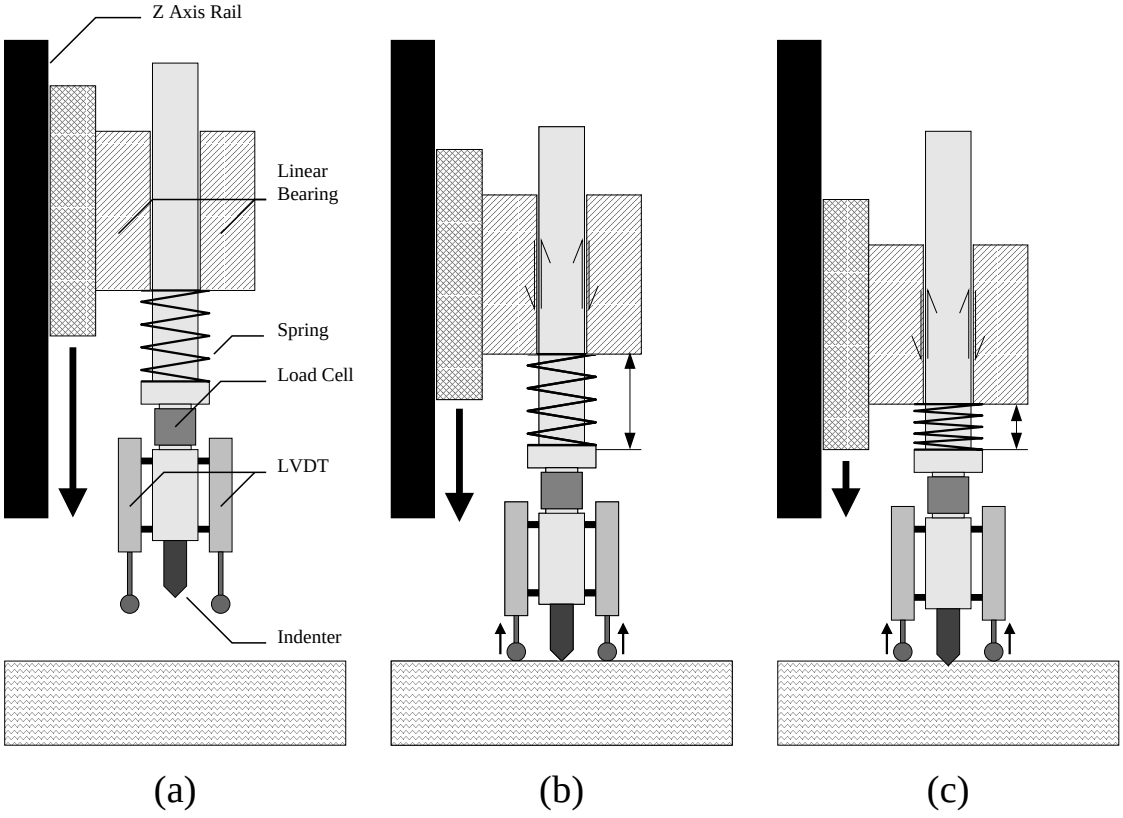

Figure 5.1. Mechanical Principle of the micro-indenter. The indenting probe is mounted on a rod fixed to the z-axis rail of the motorized frame. (a) When the indenter tip is away from the surface of the rock sample, the probe is at rest and no force or displacement is recorded. The indenting probe is lowered until the indenter tip first touches the surface of the rock sample (b). The applied load is increased by lowering the indenting probe until it reaches its maximum value (c). These operations are then reproduced in reverse.

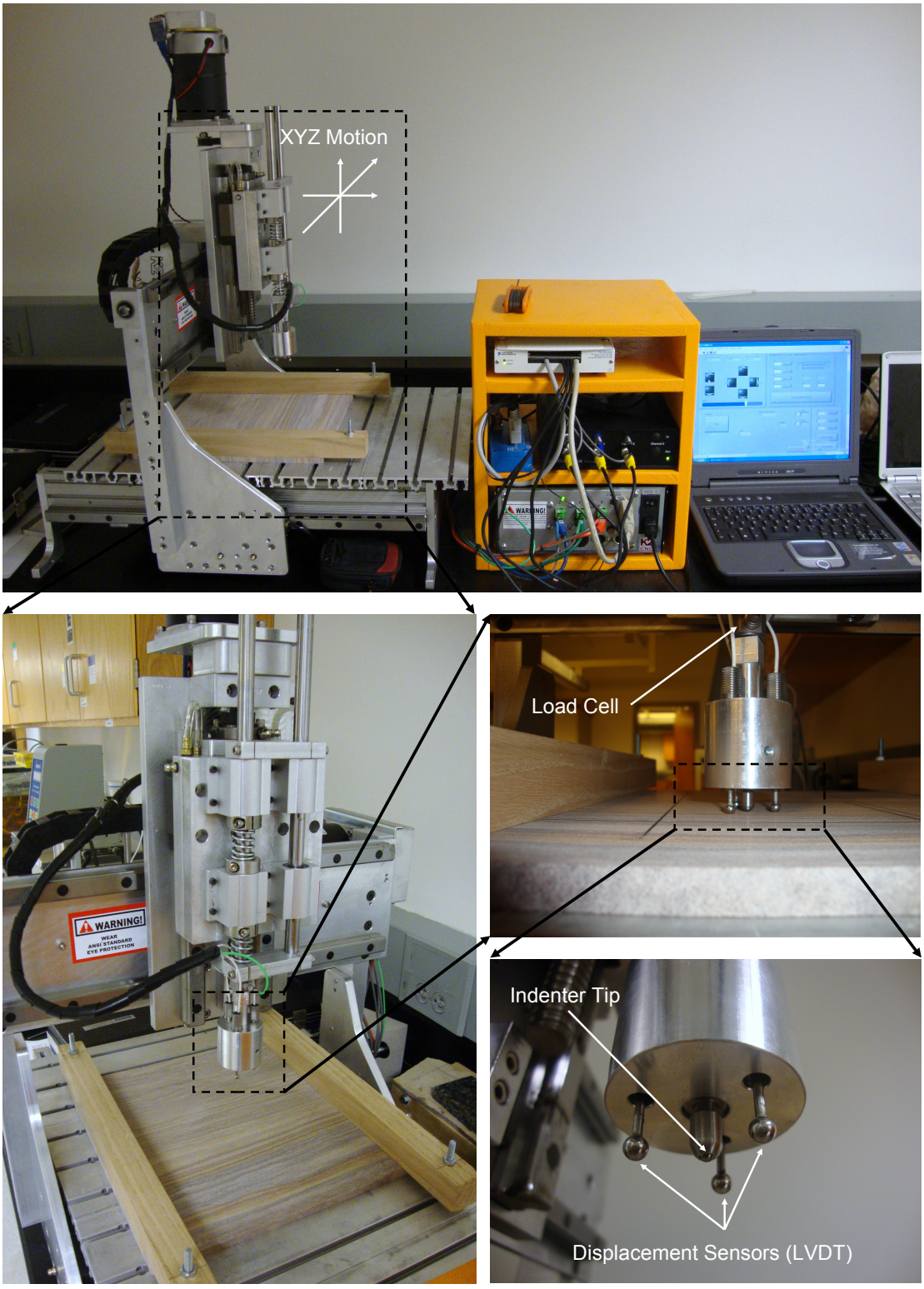

Figure 5.2. Various views of the micro indentation scanner

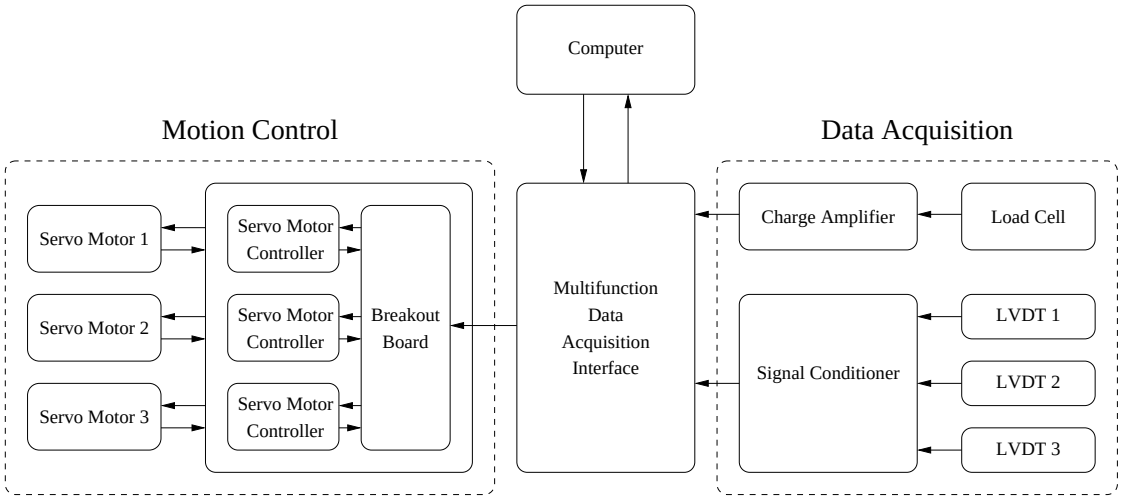

Figure 5.3. Simplified circuit diagram of the micro-indenter. The arrows symbolize the direction of the data flow.

angle between the indenter and the sample's surface. The indentation probe is maintained by a spring and mounted on a linear ball-bearing attached to the vertical axis of the motorized frame as schematized in Figure 5.1. The advantage of this setup is that the servo motor driving the vertical axis can be used both to raise and to lower the indentation probe, and to control the force applied on the rock sample's surface by the indenter. When the indenter is in contact with the sample's surface, the force applied is directly proportional to the length of the compressed spring. The motion system can theoretically achieve positioning with an accuracy of about a micron; thus, the force applied on the rock sample can be controlled with a very high precision as it is proportional the spring's rigidity. Finally, all the operations performed during the micro-indentation scanning are automated and controlled by a computer. The software driving the MIScan was developed using the graphical programming environment LabVIEW, which is highly efficient in simultaneously interfacing and controlling the hardware used for motion and data acquisition. A simplified circuit diagram of the MIScan is drawn in Figure 5.3.

5.2.3 Indentation cycle

The micro-indentation tests are performed using a loading, relaxation, unloading sequence. For each test, the indentation probe is first lowered until the indenter establishes contact with the sample's surface. Then, the force applied on the sample's surface by the indenter is progressively increased until it reaches its maximum desired value. Once the applied force reaches the maximum value, the indentation probe is maintained in place for a certain period allowing for eventual viscoelastic relaxation. Finally, the force applied is released slowly until contact between the sample's surface and the indenter is broken. Generally, during the loading stage, most materials exhibit a non-linear elasto-plastic behavior.

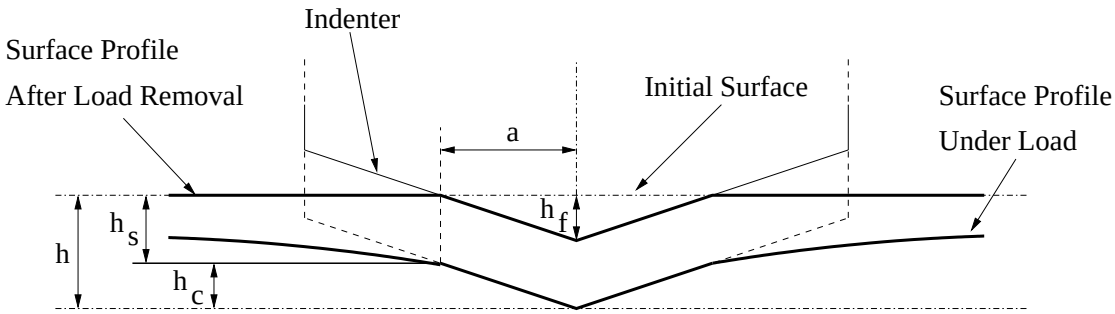

Figure 5.4. Adapted from Oliver and Pharr (1992): A schematic representation of a section through an indentation showing various quantities used in the analysis.

The relaxation stage can eliminate the viscosity impact and thereby make sure that the unloading data used for analytical purposes are almost elastic. During each test, the indentation depth and applied force are recorded continuously. Once the test is done, the results can be plotted as a load-displacement curve similar to the one shown in Figure 5.6. These curves are then numerically analyzed to compute an indentation modulus.

5.2.4 Data analysis

On the assumption that the indentation data arise from a purely elastic contact (Hertzian contact), numerous models have been proposed for indentation data analysis (see for example Sneddon, 1965; Doerner and Nix, 1986; and Oliver and Pharr, 1992). The form most often used is the one presented by Oliver and Pharr, and is known as the Oliver and Pharr method. In this method, load-displacement curves are analyzed using the analytical model

$$S = \frac{\partial P}{\partial h} = \frac{2}{\sqrt{\pi}} E_r \sqrt{A} \tag{5.2}$$

which was first introduced by Sneddon for contact between a rigid indenter of defined shape and a homogeneous isotropic elastic half space. Later, Pharr, Oliver, and Brotzen (1992) were able to show that this equation is robust and applies to tips with a wide range of shapes. In Equation 5.2, the contact stiffness $S = \partial P/\partial h$ is the slope of the tangent to the unloading part of the load displacement curve at the maximum load, as illustrated in Figure 5.5. The reduced indentation modulus E_r is an averaged modulus that accounts for the effects of using a non-rigid indenter. We have

$$\frac{1}{E_r} = \frac{1-\nu^2}{E} + \frac{1-\nu_i^2}{E_i} \tag{5.3}$$

where ν and E are the Poisson's ratio and the Young's modulus of the rock sample, and ν_i and E_i are the Poisson's ratio and the Young's modulus of the indenter. Sneddon's contact solution predicts that the unloading data for an elastic contact for many simple

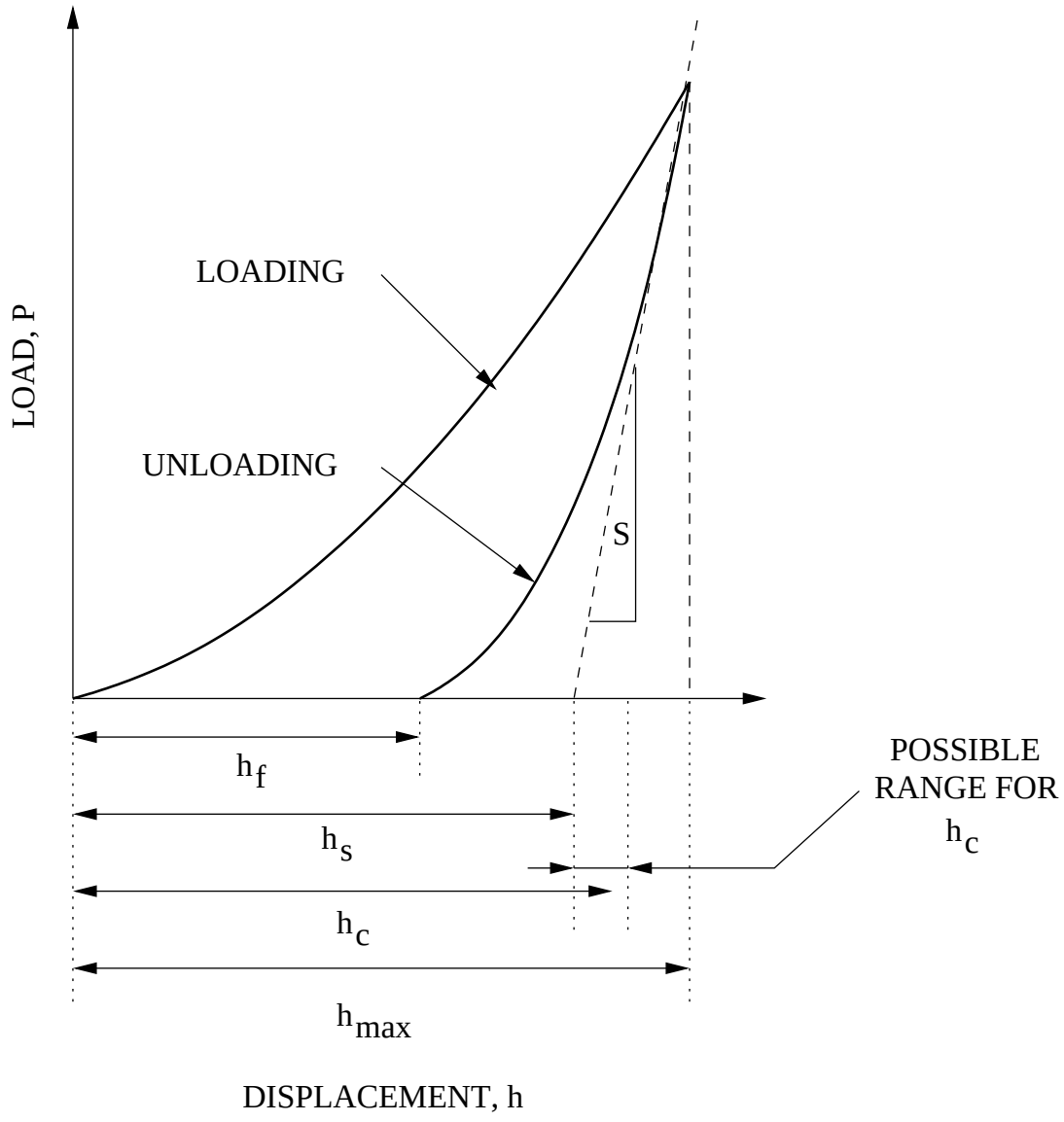

Figure 5.5. Adapted from Oliver and Pharr (1992): A schematic representation of load versus indenter displacement data for an indentation experiment. The quantities shown are : h_{max}, the indenter displacement at peak load; h_s, the projected indentation depth; h_f, the final depth of the contact impression after unloading; and S, the initial unloading stiffness. A graphical interpretation of the contact depth is presented as well.

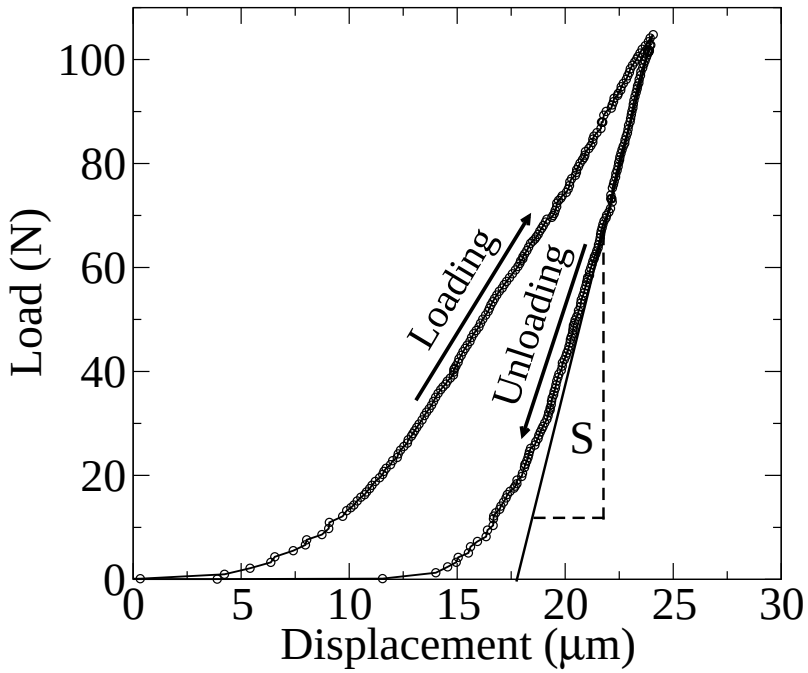

Figure 5.6. An example of an actual force-displacement curve obtained using a well-consolidated sandstone sample.

axi-symmetric indenter geometries (sphere, cone, flat punch and paraboloids of revolution) follow the power law

$$P(h) = \alpha\,(h - h_{\max})^m \tag{5.4}$$

where P is the applied load, h is the elastic displacement of the indenter, and α and m are constants. Oliver and Pharr use this model to fit the unloading part of the load displacement curve and to obtain the indentation stiffness

$$S = \alpha\, m\, [h - h_{\max}]^{m-1}\,. \tag{5.5}$$

To estimate the projected contact area A, the tip shape of the indenter must be known accurately so A can be expressed as a function of the indentation depth h_c

$$A_c = f(h_c) \tag{5.6}$$

Oliver and Pharr derive the following relationship for the contact depth h_c from Sneddon's solutions

$$h_c = h_{\max} - h_{\mathrm{s}} = h_{\max} - \epsilon\frac{P_{\max}}{S} \tag{5.7}$$

where $\epsilon = 0.72$, 0.75 and 1, for cone-, sphere- and flat-punch geometry respectively.

In summary, the Oliver and Pharr method consists of first fitting a power law function to the unloading segment of the load displacement curve. Taking the slope of this function at maximum load yields the contact stiffness E_r. This contact stiffness in addition to the appropriate value of ϵ is used in order to determine the actual contact depth h_c so that it is

finally possible to derive the modulus E. Figure 5.4 and Figure 5.5 show a schematic sketch of such an analysis.

5.2.5 Calibration

Calibration of the indenter is achieved by measuring the reduced modulus E_r for a material with a known Young's modulus E. Knowing E_r, the Young's modulus of the indenter E_i is obtained directly from Equation 5.3. Even thought E_i can be estimated using a single test, it is better to perform multiple estimates using different materials to ensure the consistency of the results.

5.3 Preliminary results

5.3.1 Spatial distribution

In order to test the ability of the Micro-Indenter Scanner to accurately map the mechanical properties of natural rocks, various samples have been scanned. Indenters with different shapes and made of different materials have been tested: conical (diamond), spherical (carbide), and flat (steel). In the final setup, a flat indenter was selected because it induces less damage to the sample's surface. It also offers the advantage of not having to determine the contact area from the load displacement curve, which reduces error in the estimated indentation modulus. In the central row of Figure 5.7, two different maps showing the measured spatial distribution of the Young's modulus for a sandstone sample and a travertine sample are presented. Both maps have been obtained using a flat indenter; the spatial sampling interval is 1mm in both space directions and the sample's size is 10 cm $\times$ 10 cm. The total time needed to complete each map was approximately 10 hours. When comparing the spatial distribution of the Young's modulus to the actual photographs of the samples (presented in the top row of Figure 5.7), we note a very good correlation between the mechanical properties measured locally and the small-scale structure of the rock in both samples. This excellent correlation shows that the experimental setup is able to quantify the spatial distribution of the mechanical properties within the samples.

For a fine analysis of the data, the average value of the measurement error should be quantified. As the indentation produces some damage within the samples during the loading/unloading cycles, the repeatability of the measurement cannot be estimated by performing multiple measurements at a given location. Under the weak assumption that measurement error is independent of the material, it can been estimated by performing measurements at different locations on a homogeneous sample (for example, a glass). Such tests have been performed, and showed that the amplitude of the measurement error is significantly smaller than the spatial fluctuations measured for the sample presented in Figure 5.7. Spectral

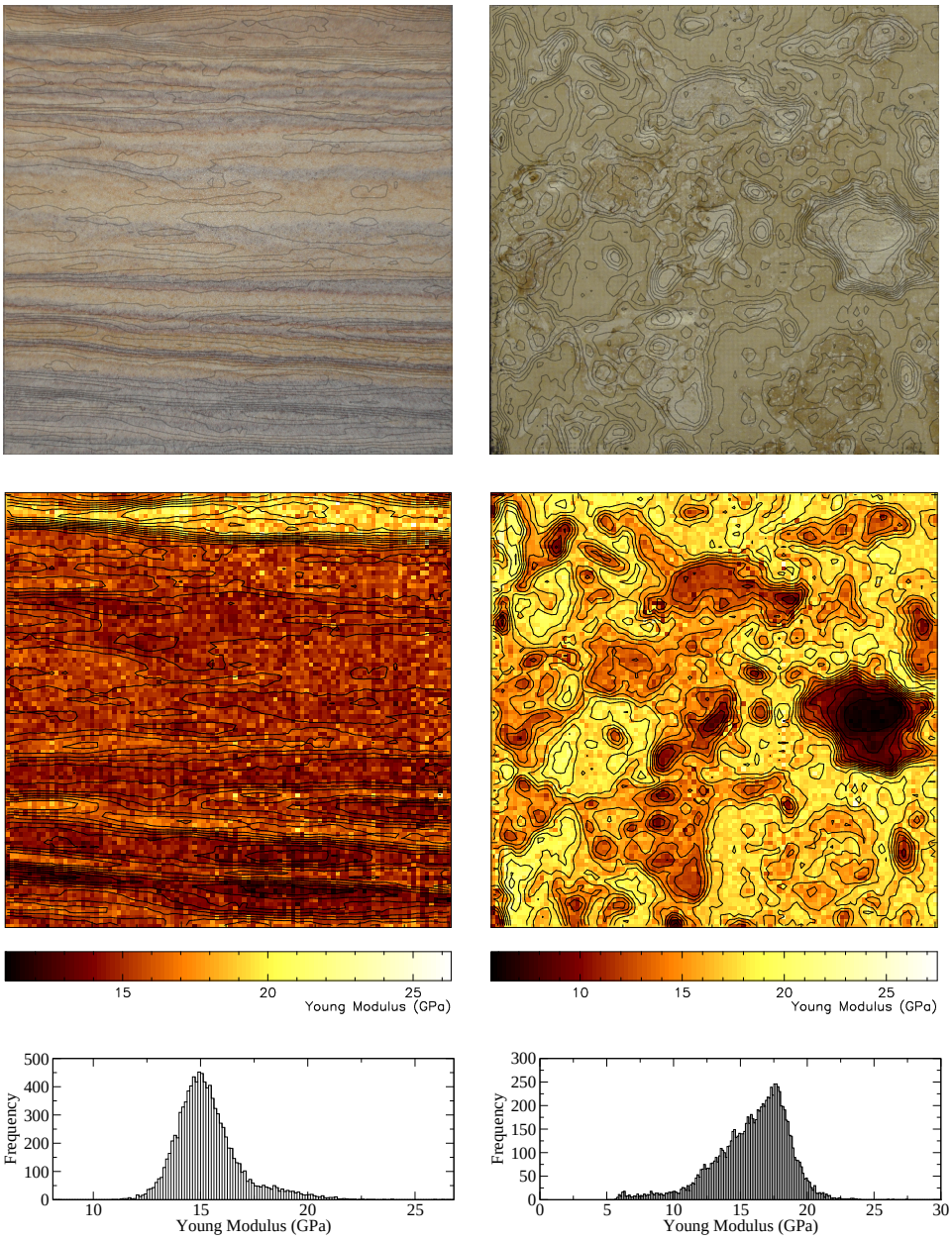

Figure 5.7. Presentation of the Young's modulus spatial distribution measured for two different samples. The graphs on the left show the results obtained for a clean consolidated sandstone sample, and the right graphs show the results obtained with a travertine sample. Pictures of the actual samples are presented in the top row, the color maps in the central row show the spatial distribution of the Young's modulus within the samples, and the histograms on the bottom are the probability density functions of both distributions. The size of both samples is 10cm $\times$ 10cm and the spatial sampling interval is 1mm in both directions (i.e. both maps consists of 10,000 measurements)

.

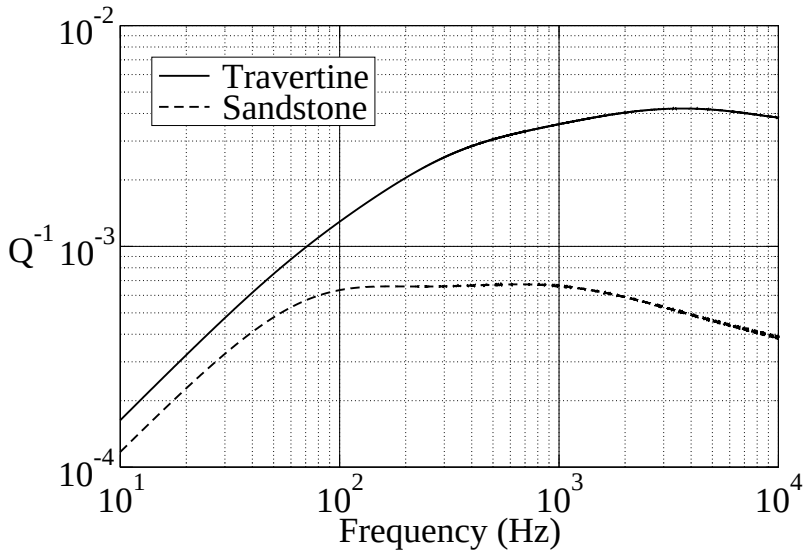

Figure 5.8. Attenuation versus frequency computed using the Young's modulus distributions shown in Figure 5.7. The dashed line corresponds to the attenuation obtained for the sandstone sample and the solid line is the attenuation computed for the travertine sample.

methods such as wavelet or curvelet could also be used to extract the measurement error by directly analyzing the spatial correlation of the noise in the indentation maps. Such methods haven't been implemented yet, and developing a robust method to properly estimate the measurement error is still part of ongoing research. Due to the damage produced within the samples by successive indentation tests, the noise present in the data might also vary when using indenters of different sizes and shapes, or when varying the spatial sampling interval. Further tests will be performed in the near future to quantify these effects.

5.3.2 Attenuation

In addition to the fluctuations of the mechanical properties, the spatial distribution of other hydro-physical parameters (essentially the permeability and porosity) must be known in order to estimate seismic attenuation numerically. Such data can be collected using existing equipment, such as an X-ray scanner for the porosity, and a micro-permeameter for the permeability. These data are not yet available and will be integrated later to improve the attenuation estimates. For the preliminary test, both the porosity and the permeability have been taken to be constant within the samples. In Figure 5.8 the attenuation curves versus frequency computed using the quasi-static method introduced by Masson and Pride (2007) for the maps given in Figure 5.7 are presented. For the numerical simulation, the grid spacing has been taken to be equal to the spatial resolution of the experimental maps (i.e., $\Delta x = 1$mm), and only the values of the bulk modulus and the shear modulus are varying spatially. Both the bulk modulus and the shear modulus have been computed from a single indentation modulus assuming a constant Poisson's ratio throughout the samples. The values

Table 5.1. Material properties assumed when computing attenuation

Solid grain material	
Bulk modulus (K_s)	36.0 GPa
Density (ρ)	2650 kg/m^3
Skeletal framework of grains	
Porosity (ϕ)	0.3
Permeability (k)	10^{-12} m^2
Fluid	
Bulk modulus (K_f)	2.25 GPa
Density (ρ_f)	1000 kg/m^3
Viscosity (η)	10^{-3} N s m^{-2}

of the remaining parameters required for the numerical simulations have been taken to be constant within the sample and are given in Table 5.1. The attenuation curve obtained from the sandstone sample is plotted as the dashed line in Figure 5.8 and the solid line corresponds to the travertine sample. As predicted theoretically, the attenuation decreases toward high and low frequencies, as the samples contain a distribution of heterogeneities with finite sizes. Interestingly, the attenuation levels stay almost constant within a wide frequency band around the attenuation peaks. Masson and Pride (2007) showed that such flat attenuation curves are typical of materials containing an equal amount of mesoscopic heterogeneities with different sizes. This observation suggests that the attenuation data can practically be used to deduce the structure of the propagating medium at the mesoscopic scale. Last, the two samples studied produced low attenuation levels compared to what is observed in field data in the shallow subsurface. This is because both rocks are well-consolidated and exhibit small fluctuations in their elastic properties. Still, we note that the attenuation levels computed for the travertine sample are a lot higher than the ones computed with the sandstone. This is due to the fact that the Young's modulus distribution in the travertine sample exhibits a larger spread of values as shown in Figure 5.7.

5.4 Conclusion

We introduced a micro-indentation scanner that is able to measure the spatial distribution of Young's modulus within natural rocks at the mesoscopic scale. Preliminary results show that mapping the mechanical properties of rocks with a fine resolution (say, one millimeter) is feasible using automated micro-indentation tests. Further effort needs to be conducted to accurately estimate the measurement error due to the experimental process. The effects of the indenter shape and size, and of the sampling spacing, should be estimated as well. We showed that the indentation data can be used along with numerical experiments to compute realistic estimates of the attenuation versus frequency. First results shows that

well-consolidated rocks do not produce much attenuation. Further measurements will be conducted on damaged rocks and lightly consolidated rocks, which should produce significantly higher attenuation levels. This innovative approach combining experimental data with numerical experiments is a major improvement to existing methods used to measure or estimate poroelastic attenuation. The results obtained with this combined approach should be compared with attenuation estimates obtained in the laboratory using the resonant bar technique. It will help to separate poroelastic attenuation from possible anelastic losses that are often subject to debate. In the future, the spatial distribution of permeability and porosity should be measured in addition to the spatial distribution of the mechanical properties. This will make the combined method even more efficient in predicting precisely the frequency dependence in the poroelastic attenuation.

Chapter 6

Conclusion

I hope that after reading this manuscript the reader will have a clearer view of how the different hydro-physical and geometrical parameters influence the frequency dependence in seismic attenuation due to wave-induced flow. Even though numerous results have been presented in detail that can be used for a finer analysis of the seismic data, I really think the strength of the present work lies in the fact that the reader, once through the numerous examples presented, should get a good idea what type of materials may be responsible for the attenuation in the data. Indeed, even if geophysics resides on a strong physical and mathematical basis, the depth of the final interpretation (even after intense rigorous processing) greatly depends on human imagination, and new discoveries are often the result of an innovative view of the data. I modestly hope that the present thesis will help whoever is collecting or interpreting seismic data to better understand what kind of mechanism may be responsible for the observed attenuation. As mentioned in the introduction, solving the inverse problem is not the focus of this work; however, we show that a link can be established between the properties of certain classes of materials and the attenuation of seismic waves. For example, we demonstrate that attenuation versus frequency scales differently in fractal materials, and that anisotropy in seismic attenuation relates to the geometrical aspect of the heterogeneities present in the medium. Among others, these results can be used to get partial information on the propagating medium, and should help in the formulation and parametrization of the inverse problem.

We also introduced new numerical tools that compute seismic attenuation in poroelastic media of arbitrary complexity, which, I hope, will help to answer future problems and questions. In the last section of this manuscript, we propose to use these numerical methods along with experimental data collected in the laboratory. I think that once the development of this new combined approach is achieved, it will allow estimation of attenuation versus frequency associated with real rock samples with previously-unachieved accuracy. It should also help with the interpretation of laboratory data where the relative importance of poroelastic attenuation and other possible losses mechanism is still a matter of debate.

Bibliography

[1] M. Abramowitz and I. A. Stegun, Eds., *Handbook of Mathematical Functions.* New York: Dover, 1965.

[2] L. Adam, M. Batzle, K. T. Lewallen, and K. van Wijk, "Seismic wave attenuation in carbonates," *Journal of Geophysical Research-Solid Earth*, vol. 114, Jun 25 2009.

[3] K. Aki and P. Richards, *Quantitative Seismology, Theory and Methods, Volume II.* San Francisco: Freeman, 1980.

[4] G. E. Archie, "The electrical resistivity log as an aid in determining some reservoir characteristics," *Trans. AIME*, vol. 146, pp. 54–62, 1942.

[5] M. L. Batzle, D.-H. Han, and R. Hofmann, "Fluid mobility and frequency-dependent seismic velocity — direct measurements," *Geophysics*, vol. 71, no. 1, pp. N1–N9, 2006.

[6] Y. Benveniste, "A new approach to the application of Mori-Tanaka theory in composite-materials," *Mechanics of materials*, vol. 6, no. 2, pp. 147–157, Jun 1987.

[7] J. Berryman, "Single-scattering approximations for coefficients in Biot equations of poroelasticity," *Journal of the acoustical society of America*, vol. 91, no. 2, pp. 551–571, Feb 1992.

[8] J. Berryman, "Generalization of Eshelby's formula for a single ellipsoidal elastic inclusion to poroelasticity and thermoelasticity," *Physical review letters*, vol. 79, no. 6, pp. 1142–1145, Aug 11 1997.

[9] M. A. Biot, "Theory of propagation of elastic waves in a fluid-saturated porous solid. I. Low-frequency range," *J. Acoust. Soc. Am.*, vol. 28, pp. 168–178, 1956.

[10] M. A. Biot, "Theory of propagation of elastic waves in a fluid-saturated porous solid. II. Higher frequency range," *J. Acoust. Soc. Am.*, vol. 28, pp. 179–191, 1956.

[11] M. A. Biot, "Mechanics of deformation and acoustic propagation in porous media," *J. Appl. Phys.*, vol. 33, pp. 1482–1498, 1962.

[12] M. A. Biot and D. G. Willis, "The elastic coefficients of the theory of consolidation," *J. Appl. Mech.*, vol. 24, pp. 594–601, 1957.

[13] F. Birch and D. Bancroft, "The effect of pressure on the rigidity of rocks. ii," *The Journal of Geology*, vol. 46, no. 2, pp. pp. 113–141, 1938.

[14] R. J. S. Brown and J. Korringa, "On the dependence of the elastic properties of a porous rock on the compressiblity of the pore fluid," *Geophysics*, vol. 40, pp. 608–616, 1975.

[15] B. Budiansky and R. J. O'Connell, "Elastic moduli of a cracked solid," *Int. J. Solids Struct.*, vol. 12, pp. 81–97, 1976.

[16] R. Burridge and J. B. Keller, "Poroelasticity equations derived from microstructure," *J. Acoust. Soc. Am.*, vol. 70, pp. 1140–1146, 1981.

[17] T. Cadoret, "Effet de la saturation eau/gaz sur les propriétés acoustiques des roches. étude aux fréquences sonores et ultrasonores." Ph.D. dissertation, Université de Paris VII, Paris, France, 1993.

[18] T. Cadoret, G. Mavko, and B. Zinszner, "Fluid distribution effect on sonic attenuation in partially saturated limestones," *Geophysics*, vol. 63, pp. 154–160, 1998.

[19] J. M. Carcione and G. Q. Goode, "Some aspects of the physics and numerical modeling Biot compressional waves," *J. Comput. Acoustics*, vol. 3, pp. 261–272, 1995.

[20] J. M. Carcione, H. B. Helle, and N. H. Pham, "White's model for wave propagation in partially saturated rocks: Comparison with poroelastic numerical experiments," *Geophysics*, vol. 68, pp. 1389–1398, 1995.

[21] J. M. Carcione, "Wave propagation in anisotropic, saturated porous media: Plane-wave theory and numerical simulation," *The Journal of the Acoustical Society of America*, vol. 99, no. 5, pp. 2655–2666, 1996.

[22] J. M. Carcione and H. B. Helle, "Numerical solution of the poroviscoelastic wave equation on a staggered mesh," *J. Comput. Phys.*, vol. 154, no. 2, pp. 520–527, 1999.

[23] M. Doerner and W. Nix, "A method for interpreting the data from depth-sensing indentation instruments," *Journal of Materials Research*, vol. 1, no. 4, pp. 601–9, July-August 1986.

[24] N. C. Dutta and H. Odé, "Attenuation and dispersion of compressional waves in fluid-filled porous rocks with partial gas saturation (White model)— Part I: Biot theory," *Geophysics*, vol. 44, pp. 1777–1788, 1979.

[25] N. C. Dutta and H. Odé, "Attenuation and dispersion of compressional waves in fluid-filled porous rocks with partial gas saturation (White model)— Part II: Results," *Geophysics*, vol. 44, pp. 1789–1805, 1979.

[26] N. C. Dutta and A. J. Seriff, "On White's model of attenuation in rocks with partial gas saturation," *Geophysics*, vol. 44, pp. 1806–1812, 1979.

[27] J. Dvorkin, G. Mavko, and A. Nur, "Squirt flow in fully saturated rocks," *Geophysics*, vol. 60, pp. 97–107, 1995.

[28] J. Eshelby, "The determination of the elastic field of an ellipsoidal inclusion, and related problems," *Proceedings of the royal society of london series A-mathematical and physical sciences*, vol. 241, no. 1226, pp. 376–396, 1957.

[29] S. Flatte and R. Wu, "Small-scale structure in the lithosphere and asthenosphere deduced from arrival time and amplitude fluctuations at norsar," *Journal of geophysical research-solid earth and planets*, vol. 93, no. B6, pp. 6601–6614, Jun 10 1988.

[30] J. Frenkel, "On the theory of seismic and seismoelectric phenomena in a moist soil," *J. Physics (Soviet)*, vol. 8, pp. 230–241, 1944.

[31] S. Garg, A. Nayfeh, and A. Good, "Compressional waves in fluid-saturated elastic porous-media," *Journal of Applied Physics*, vol. 45, no. 5, pp. 1968–1974, 1974.

[32] F. Gassmann, "Über die Elastizität poröser Medien," *Vierteljahrsschrift der Naturforschenden Gesellschaft in Zürich*, vol. 96, pp. 1–23, 1951.

[33] S. Gelinsky and S. A. Shapiro, "Dynamic-equivalent medium approach for thinly layered saturated sediments," *Geophys. J. Internat.*, vol. 128, pp. F1–F4, 1997.

[34] B. Gurevich and S. L. Lopatnikov, "Velocity and attenuation of elastic waves in finely layered porous rocks," *Geophys. J. Internat.*, vol. 121, pp. 933–947, 1995.

[35] A. Hanyga and J.-F. Lu, "Wave field simulation for heterogeneous transversely isotropic porous media with the jkd dynamic permeability," *Computational Mechanics*, vol. 36, pp. 196–208, 2005.

[36] B. T. Hefner and K. L. Williams, "Sound speed and attenuation measurements in unconsolidated glass-bead sediments saturated with viscous pore fluids," *The Journal of the Acoustical Society of America*, vol. 120, no. 5, pp. 2538–2549, 2006.

[37] W. F. M. III, "Effects of partial water saturation on attenuation in massilon sandstone and vycor porous glass," *The Journal of the Acoustical Society of America*, vol. 71, no. 6, pp. 1458–1468, 1982.

[38] T. M. M. J. Toms and B. Gurevich, "Seismic attenuation in porous rocks with random patchy saturation," *Geophysical Prospecting*, vol. 55, pp. 671–678, 2007.

[39] D. L. Johnson, "Theory of frequency dependent acoustics in patchy-saturated porous media," *J. Acoust. Soc. Am.*, vol. 110, pp. 682–694, 2001.

[40] D. L. Johnson, J. Koplik, and R. Dashen, "Theory of dynamic permeability and tortuosity in fluid-saturated porous media," *J. Fluid Mech.*, vol. 176, pp. 379–402, 1987.

[41] L. Klimes, "Correlation functions of random media," *Pure and applied geophysics*, vol. 159, no. 7-8, pp. 1811–1831, Jul 2002.

[42] R. Knight, J. Dvorkin, and A. Nur, "Acoustic signatures of partial saturation," *Geophysics*, vol. 63, pp. 132–138, 1998.

[43] M. Leite and F. Ferland, "Determination of unconfined compressive strength and Young's modulus of porous materials by indentation tests," *Engineering geology*, vol. 59, no. 3-4, pp. 267–280, Apr 2001.

[44] A. R. Levander, "Fourth-order finite-difference P-SV seismograms," *Geophysics*, vol. 53, pp. 1425–1436, 1988.

[45] T. Levy, "Propagation of waves in a fluid-saturated porous elastic solid," *Int. J. Engng. Sci.*, vol. 17, pp. 1005–1014, 1979.

[46] N. Lucet, P. N. J. Rasolofosaon, and B. Zinszner, "Sonic properties of rocks under confining pressure using the resonant bar technique," *The Journal of the Acoustical Society of America*, vol. 89, no. 3, pp. 980–990, 1991.

[47] R. Madariaga, "Dynamics of an expanding circular fault," *Bull. Seism. Soc. Am.*, vol. 66, pp. 163–182, 1976.

[48] A. Maewal and D. Dandekar, "Effective thermoelastic properties of short-fiber composites," *Acta mechanica*, vol. 66, no. 1-4, pp. 191–204, Apr 1987.

[49] K. J. Malloy, L. Furuberg, J. Feder, and T. Jossang, "Dynamics of slow drainage in porous media," *Phys. Rev. Lett.*, vol. 68, pp. 2161–2164, 1992.

[50] Y. J. Masson and S. R. Pride, "Poroelastic finite difference modeling of seismic attenuation and dispersion due to mesoscopic-scale heterogeneity," *Journal of geophysical research*, vol. 112, p. B03204, 2007.

[51] Y. J. Masson, S. R. Pride, and K. T. Nihei, "Finite-difference modeling of biot's poroelastic equations at seismic frequencies," *J. Geophys. Res.*, vol. submitted, 2006.

[52] G. Mavko and A. Nur, "Wave attenuation in partially saturated rocks," *Geophysics*, vol. 44, pp. 161–178, 1979.

[53] T. M. Mller and B. Gurevich, "One-dimensional random patchy saturation model for velocity and attenuation in porous rocks," *Geophysics*, vol. 69, p. 11661172, 2004.

[54] C. Morency and J. Tromp, "Spectral-element simulations of wave propagation in porous media," *Geophysical Journal International*, vol. 175, no. 1, pp. 301–345, Oct 2008.

[55] T. Mori and K. Tanaka, "Average stress in matrix and average elastic energy of materials with misfitting inclusions," *Acta metallurgica*, vol. 21, no. 5, pp. 571–574, 1973.

[56] I. B. Morozov, "Thirty Years of Confusion around "Scattering Q"?" *Seismological research letters*, vol. 80, no. 1, pp. 5–7, Jan-Feb 2009.

[57] T. Mura, *Micromechanics of defects in solids*. The Hague, Netherlands: Martinus Nijhoff Publishers, 1982 1982.

[58] W. F. Murphy III, "Effects of partial water saturation on attenuation in Massilon sandstone and Vycor porous-glass," *J. Acoust. Soc. Am.*, vol. 71, pp. 1458–1468, 1982.

[59] A. N. Norris, "Low-frequency dispersion and attenuation in partially saturated rocks," *J. Acoust. Soc. Am.*, vol. 94, pp. 359–370, 1993.

[60] R. J. O'Connell and B. Budiansky, "Viscoelastic properties of fluid-saturated cracked solids," *J. Geophys. Res.*, vol. 82, pp. 5719–5735, 1977.

[61] R. J. O'Connell and B. Budiansky, "Measures of dissipation in viscoelastic media," *Geophys. Res. Lett.*, vol. 5, pp. 5–8, 1978.

[62] W. Oliver and G. Pharr, "An improved technique for determining hardness and elastic-modulus using load and displacement sensing indentation experiments," *Journal of materials research*, vol. 7, no. 6, pp. 1564–1583, Jun 1992.

[63] T. Ozdenvar and G. A. McMechan, "Algorithms for staggered-grid computations for poroelastic, elastic, acoustic, and scalar wave equations," *Geophys. Prospect.*, vol. 45, pp. 403–420, 1997.

[64] H. Pan and G. Weng, "Elastic-moduli of heterogeneous solids with ellipsoidal inclusions and elliptic cracks," *Acta mechanica*, vol. 110, no. 1-4, pp. 73–94, 1995.

[65] G. Pharr, W. Oliver, and F. Brotzen, "On the generality of the relationship among contact stiffness, contact area, and elastic-modulus during indentation," *Journal of materials research*, vol. 7, no. 3, pp. 613–617, Mar 1992.

[66] M. Pilkington and J. Todoeschuck, "Stochastic inversion for scaling geology," *Geophysical journal international*, vol. 102, no. 1, pp. 205–217, Jul 1990.

[67] B. Plyushchenkov and V. Turchaninov, "Acoustic logging modeling by refined Biot's equations," *International journal of modern physics C*, vol. 11, no. 2, pp. 365–396, Mar 2000.

[68] S. R. Pride, "Governing equations for the coupled electromagnetics and acoustics of porous media," *Phys. Rev. B*, vol. 50, pp. 15 678–15 696, 1994.

[69] S. R. Pride, "Relationships between seismic and hydrological properties," in *Hydrogeophysics*, Y. Rubin and S. Hubbard, Eds. The Netherlands: Springer, 2005, pp. 253–291.

[70] S. R. Pride and J. G. Berryman, "Connecting theory to experiment in poroelasticity," *J. Mech. Phys. Solids*, vol. 46, pp. 719–747, 1998.

[71] S. R. Pride and J. G. Berryman, "Linear dynamics of double-porosity and dual-permeability materials. I. Governing equations and acoustic attenuation," *Phys. Rev. E*, vol. 68, p. 036603, 2003.

[72] S. R. Pride and J. G. Berryman, "Linear dynamics of double-porosity and dual-permeability materials. II. Fluid transport equations," *Phys. Rev. E*, vol. 68, p. 036604, 2003.

[73] S. R. Pride, J. G. Berryman, and J. M. Harris, "Seismic attenuation due to wave-induced flow," *J. Geophys. Res.*, vol. 109, 2004.

[74] S. R. Pride, A. F. Gangi, and F. D. Morgan, "Deriving the equations of motion for porous isotropic media," *J. Acoust. Soc. Am.*, vol. 92, pp. 3278–3290, 1992.

[75] S. R. Pride, J. M. Harris, D. L. Johnson, A. Mateeva, K. T. Nihei, R. L. Nowack, J. W. Rector, H. Spetzler, R. Wu, T. Yamomoto, J. G. Berryman, and M. Fehler, "Permeability dependence of seismic amplitudes," *The Leading Edge*, vol. 22, pp. 518–525, 2003.

[76] S. R. Pride and Y. J. Masson, "Acoustic attenuation in self-affine porous structures," *Phys. Rev. Lett.*, vol. 97, no. 18, p. 184301, Oct 2006.

[77] E. T. R. Lenormand and C. Zarcone, "Numerical models and experiments on immiscible displacements in porous media," *J. Fluid Mech.*, vol. 189, pp. 165–187, 1988.

[78] M. S. Sams, J. P. Neep, M. H. Worthington, and M. S. King, "The measurement of velocity dispersion and frequency-dependent intrinsic attenuation in sedimentary rocks," *Geophysics*, vol. 62, pp. 1456–1464, 1997.

[79] A. W. Skempton, "The pore-pressure coefficients A and B," *Geotechnique*, vol. 4, pp. 143–147, 1954.

[80] I. N. Sneddon, "The relation between load and penetration in the axisymmetric boussinesq problem for a punch of arbitrary profile," *International Journal of Engineering Science*, vol. 3, no. 1, pp. 47 – 57, 1965.

[81] J. Spencer, "Stress relaxations at low-frequencies in fluid-saturated rocks - attenuation and modulus dispersion," *Journal of Geophysical Research*, vol. 86, pp. 1803–1812, 1981.

[82] D. Stauffer and A. Aharony, *Introduction to Percolation Theory*. London: Taylor and Francis, 1992.

[83] J. P. Stokes, D. A. Weitz, J. P. Gollub, A. Dougherty, M. O. Robbins, P. M. Chaikin, and H. M. Lindsay, "Interfacial stability of immiscible displacement in a porous medium," *Phys. Rev. Lett.*, vol. 57, pp. 1718–1721, 1986.

[84] Y. Tserkovnyak and D. L. Johnson, "Capillary forces in the acoustics of patchy-saturated porous media," *J. Acoust. Soc. Am.*, vol. 114, pp. 2596–2606, 2003.

[85] Y. Tserkovnyak and D. Johnson, "Can one hear the shape of a saturation patch?" *Geophysical Research Letters*, vol. 29, no. 7, pp. 12–1–4, 1 April 2002.

[86] J. Virieux, "P-SV wave propagation in heterogeneous media: Velocity-stress finite-difference method," *Geophysics*, vol. 51, pp. 889–901, 1986.

[87] J. Virieux and R. Madariaga, "Dynamic faulting studied by a finite difference method," *Bulletin of the Seismological Society of America*, vol. 72, no. 2, pp. 345–369, 1982.

[88] W. Wang, S. Corn, and P. Ienny, "Characterization of mechanical properties of geomaterials by microindentation test. Calibration and applications," *European journal of environmental and civil engineering*, vol. 13, no. 3, pp. 305–328, 2009.

[89] J. E. White, "Computed seismic speeds and attenuation in rocks with partial gas saturation," *Geophysics*, vol. 40, pp. 224–232, 1975.

[90] J. E. White, N. G. Mikhaylova, and F. M. Lyakhovitsky, "Low-frequency seismic waves in fluid-saturated layered rocks," *Izvestija Academy of Sciences USSR, Phys. Solid Earth*, vol. 11, pp. 654–659, 1975.

[91] D. Wilkinson and J. F. Willemsen, "Invasion percolation: a new form of percolation theory," *Journal of Physics A: Mathematical and General*, vol. 16, p. 3365, 1983.

[92] K. L. Williams, D. R. Jackson, E. I. Thorsos, D. Tang, and S. G. Schock, "Comparison of sound speed and attenuation measured in a sandy sediment to predictions based on the Biot theory of porous media," *IEEE J. Ocean. Eng.*, vol. 27, pp. 413–428, 2002.

[93] K. W. Winkler and A. Nur, "Seismic attenuation: Effects of pore fluids and frictional-sliding," *Geophysics*, vol. 47, no. 1, pp. 1–15, 1982.

[94] A. Wood, *A Textbook of Sound*. London: G. Bell and Sons, 1941.

[95] K. S. Yee, "Numerical solution of initial boundary value problems involving Maxwell's equations in isotropic media," *IEEE Trans. Antennas Propag.*, vol. 14, pp. 302–312, 1966.

[96] J. Zhang, "Quadrangle-grid velocity-stress finite difference method for poroelastic wave equations," *Geophys. J. Int.*, vol. 139, pp. 171–182, 1999.

[97] W. Zhu, J. J. Hughes, N. Bicanic, and C. J. Pearce, "Nanoindentation mapping of mechanical properties of cement paste and natural rocks," *Materials characterization*, vol. 58, no. 11-12, pp. 1189–1198, Nov-Dec 2007.

[98] X. Zhu and G. A. McMechan, "Numerical simulation of seismic responses of poroelastic reservoirs using biot theory," *Geophysics*, vol. 56, pp. 328–339, 1991.

Appendix A

The local poroelastic equations

Biot's (1962) equations are used to model the local response within a heterogeneous porous sample that is being stressed in a time-varying manner. As demonstrated by Masson et al. (2006), at low enough applied frequencies where $\omega \ll \eta/(\rho_f F k)$ so that viscous boundary layers do not develop in the pores, Biot's (1962) equations in the time domain may be written

$$\rho \frac{\partial \mathbf{v}}{\partial t} = \nabla \cdot \tau - \rho_f \frac{\partial \mathbf{q}}{\partial t} \tag{A.1}$$

$$\rho_f (1+\Phi) F \frac{\partial \mathbf{q}}{\partial t} + \frac{\eta}{k_0} \mathbf{q} = -\nabla p - \rho_f \frac{\partial \mathbf{v}}{\partial t}. \tag{A.2}$$

$$\frac{\partial \tau}{\partial t} = (\lambda_U \nabla \cdot \mathbf{v} + \alpha M \nabla \cdot \mathbf{q})\, \mathbf{I} + \mu \left[\nabla \mathbf{v} + (\nabla \mathbf{v})^{\mathbf{T}} \right] \tag{A.3}$$

$$-\frac{\partial p}{\partial t} = M \left(\alpha \nabla \cdot \mathbf{v} + \nabla \cdot \mathbf{q} \right). \tag{A.4}$$

In sedimentary rocks, these equations can be considered as valid across the seismic band (1 to 10^4 Hz). The various coefficients are all real. Here, ρ is the local bulk density of the material, ρ_f is the fluid density which is taken to be spatially uniform throughout each sample, and F is the electrical formation factor that is modeled here using the Archie (1942) law $\phi^{-1.75}$ where ϕ is local porosity, and Φ is a dimensionless pore-topology parameter defined and discussed by Masson et al. (2006) that is bounded as $\Phi > 1/4$ and will simply be set to 1 in the present article. Over the seismic band of frequencies, the inertial term in the generalized Darcy law of Equation (A.2) has a magnitude $|\rho_f(1+\Phi)F\partial\mathbf{q}/\partial t|$ that is always negligible in amplitude relative to the viscous resistance $|(\eta/k_o)\mathbf{q}|$; however, the inertial term is entirely responsible for the finite-difference scheme to be stable (c.f., Masson et al., 2006) and thus cannot be discarded.

The local poroelastic constants used here are the undrained Lamé modulus λ_U, the shear modulus μ (the same for both drained and undrained conditions), the so-called Biot-Willis (1957) constant α, and the fluid-storage coefficient M. For any porous material, these constants are related to the undrained bulk modulus K_U, the drained bulk modulus K, and

Skempton's (1954) undrained fluid-pressure to confining-pressure ratio B as

$$\begin{aligned} \lambda_U &= K_U - 2\mu/3 = K + \alpha^2 M - 2\mu/3 && \text{(A.5)} \\ \alpha &= (1 - K/K_U)/B && \text{(A.6)} \\ M &= BK_U/\alpha. && \text{(A.7)} \end{aligned}$$

In the special case considered by Gassmann (1951), in which the solid frame is composed of a single isotropic mineral characterized by a bulk modulus K_s, we have as well the so-called "fluid-substitution" relations given by

$$\begin{aligned} B &= \frac{1/K - 1/K_s}{1/K - 1/K_s + \phi(1/K_f - 1/K_s)} && \text{(A.8)} \\ K_U &= \frac{K}{1 - B(1 - K/K_s)} && \text{(A.9)} \end{aligned}$$

where K_f is the fluid bulk modulus and ϕ is the porosity. From these, one further obtains $\alpha = 1 - K/K_s$. We use the Gassmann expressions to model the local poroelastic constants in all the numerical experiments.

Appendix B

The double-porosity theory

In the special case where the sample is a composite of two distinct porous materials saturated by a single fluid and when the heterogeneity has a single dominant lengthscale, the double porosity theory of Pride and Berryman (2003a,b) is applicable and predicts that the undrained bulk modulus $K_u(\omega)$ of the porous composite is complex (due to the mesoscale fluid equilibration) and given by

$$\frac{1}{K_d(\omega)} = a_{11} - \frac{a_{13}^2}{a_{33} - \gamma/i\omega}, \tag{B.1}$$

$$B(\omega) = \frac{-a_{12}(a_{33} - \gamma/i\omega) + a_{13}(a_{23} + \gamma/i\omega)}{(a_{22} - \gamma/i\omega)(a_{33} - \gamma/i\omega) - (a_{23} + \gamma/i\omega)^2}, \tag{B.2}$$

$$\frac{1}{K_u(\omega)} = \frac{1}{K_d(\omega)} + B(\omega)\left(a_{12} - \frac{a_{13}(a_{23} + \gamma/i\omega)}{a_{33} - \gamma/i\omega}\right). \tag{B.3}$$

Here, $K_d(\omega)$ is the complex drained bulk modulus of the composite (drained in this context means that the average fluid pressure in a sample does not change, which in no way prevents mesoflow from occuring), and $B(\omega)$ is the complex Skempton's coefficient. The a_{ij} are real elastic compliances that depend on the elastic moduli of the two porous consituents, while γ is a complex function of frequency given by

$$\gamma(\omega) = \gamma_o\sqrt{1 - i\frac{\omega}{\omega_o}} \tag{B.4}$$

that controls the degree of mesoflow between the two phases. Expressions for the real parameters γ_o and ω_o, as well as for the high-frequency elastic compliances a_{ij} have been derived by Pride and Berryman (2003a,b) and are also given by Pride et al. (2004).

The a_{ij} are given by

$$a_{11} = 1/K_d(0) \tag{B.5}$$

$$a_{22} = \frac{v_1\alpha_1}{K_1}\left(\frac{1}{B_1} - \frac{\alpha_1(1-Q_1)}{1-K_1/K_2}\right) \tag{B.6}$$

$$a_{33} = \frac{v_2\alpha_2}{K_2}\left(\frac{1}{B_2} - \frac{\alpha_2(1-Q_2)}{1-K_2/K_1}\right) \tag{B.7}$$

$$a_{12} = -v_1Q_1\alpha_1/K_1 \tag{B.8}$$

$$a_{13} = -v_2Q_2\alpha_2/K_2 \tag{B.9}$$

$$a_{23} = -\frac{\alpha_1\alpha_2K_1/K_2}{(1-K_1/K_2)^2}\left(\frac{1}{K_d(0)} - \frac{v_1}{K_1} - \frac{v_2}{K_2}\right) \tag{B.10}$$

where

$$v_1Q_1 = \frac{1-K_2/K_d(0)}{1-K_2/K_1} \quad \text{and} \quad v_2Q_2 = \frac{1-K_1/K_d(0)}{1-K_1/K_2}. \tag{B.11}$$

Here, v_i is the volume-fraction of phase i in each sample ($v_1 + v_2 = 1$), K_i is the drained frame modulus of phase i, B_i is the Skempton's coefficient of phase i, α_i is the Biot-Willis constant of phase i.

The one parameter in these a_{ij} that has not yet been modeled is the overall static drained modulus $K_d(0) = 1/a_{11}$ of the two-phase composite. It is through $K_d(0)$ that all dependence on the mesoscopic geometry of the two phases occurs. Although many mixture models for $K_d(0)$ exist, none are exact for arbitrary geometry of the inclusions. In the present paper, we numerically calculate $K_d(0)$ using our finite-difference scheme in the long-time limit and use this measured drained bulk modulus in the above double-porosity expressions for all "theoretical" predictions.

The low-frequency and high-frequency limits of $K_u(\omega)$ are determined from Equation (B.4) to be

$$K_u(0) = a_{11} - \frac{(a_{12}+a_{13})^2}{a_{22}+2a_{23}+a_{33}} \tag{B.12}$$

$$K_u(\infty) = a_{11} - \frac{a_{13}^2}{a_{33}} - \frac{(a_{12}a_{33}-a_{13}a_{23})^2}{a_{33}(a_{22}a_{33}-a_{23}^2)}. \tag{B.13}$$

At peak attenuation defined when $\omega = \omega_p$ one can approximte that $K_u(\omega_p) \approx [K_u(0) + K_u(\infty)]/2$.

If phase 2 is defined to be more permeable than phase 1, the low-frequency limit of the internal transport coefficient γ_o is given by

$$\gamma_o = -\frac{k_1K_1^d}{\eta L_1^2}\left(\frac{a_{12}+B_o(a_{22}+a_{33})}{R_1 - B_o/B_1}\right)[1 + O(k_1/k_2)]\,. \tag{B.14}$$

where the parameters B_o, R_1, and L_1 are now defined. The dimensionless number $B_o = B(0)$ is the static Skempton's coefficient for the composite and is exactly

$$B_o = -\frac{(a_{12}+a_{13})}{a_{22}+2a_{23}+a_{33}}. \tag{B.15}$$

The dimensionless number R_1 is the ratio of the average static confining pressure in the host phase 1 of a sealed sample divided by the confining pressure applied to the sample and is exactly

$$R_1 = Q_1 + \frac{\alpha_1(1-Q_1)B_o}{1-K_1^d/K_2^d} - \frac{v_2}{v_1}\frac{\alpha_2(1-Q_2)B_o}{1-K_2^d/K_1^d} \tag{B.16}$$

where the Q_i are given by Equation (B.11). Last, the length L_1 is the distance over which the fluid-pressure gradient still exists in phase 1 in the final approach to fluid-pressure equilibrium and is formally defined as

$$L_1^2 = \frac{1}{V_1}\int_{\Omega_1} \Phi_1 \, dV \tag{B.17}$$

where Ω_1 is the region of an averaging volume occupied by phase 1 and having a volume measure V_1. The potential Φ_1 has units of length squared and is a solution of an elliptic boundary-value problem that under conditions where the permeability ratio k_1/k_2 can be considered small, reduces to

$$\nabla^2\Phi_1 = -1 \text{ in } \Omega_1, \tag{B.18}$$

$$\mathbf{n}\cdot\nabla\Phi_1 = 0 \text{ on } \partial E_1, \tag{B.19}$$

$$\Phi_1 = 0 \text{ on } \partial\Omega_{12} \tag{B.20}$$

where $\partial\Omega_{12}$ is the surface separating the two phases within a sample of composite and ∂E_1 is the external surface of the sample that is coincident with phase 1.

In all the examples of the present paper, the boundary-value problem for Φ_1 is solved numerically by finite-differences. To do so, we add a diffusion term $-\partial\Phi_1/\partial t$ to the left-hand side of Equation (B.18) and replace 1 by a step function on the right-hand side, then solve the resulting diffusion equation using explicit time-stepping. The long-time steady-state response to the imposed step-function source term is the solution of Equation (B.18). We then determine numerically the length L_1 using Equation (B.17).

Last, the transition frequency ω_o corresponds to the onset of a high-frequency regime in which the fluid-pressure-diffusion penetration distance becomes small relative to the scale of the mesoscopic heterogeneity, and is given by

$$\omega_o = \frac{\eta B_1 K_1}{k_1\alpha_1}\left(\gamma_o\frac{V}{S}\right)^2\left(1+\sqrt{\frac{k_1 B_2 K_2 \alpha_1}{k_2 B_1 K_1 \alpha_2}}\right)^2 \tag{B.21}$$

where S is the surface area of the interface between the two phases in each volume V of composite.

Appendix C

The patchy-saturation theory

In the special case where the sample consists of porous material with a homogeneous solid skeleton saturated by a mixture of two fluids and when the fluid patches have a single dominant lengthscale, the theory of *Pride et al.* [2004] is applicable and predicts that the undrained bulk modulus $K_u(\omega)$ of the porous composite is complex (due to the mesoscale fluid equilibration) and given by

$$\frac{1}{K_d(\omega)} = a_{11} - \frac{a_{13}^2}{a_{33} - \gamma/i\omega}, \tag{C.1}$$

$$B(\omega) = \frac{-a_{12}(a_{33} - \gamma/i\omega) + a_{13}(a_{23} + \gamma/i\omega)}{(a_{22} - \gamma/i\omega)(a_{33} - \gamma/i\omega) - (a_{23} + \gamma/i\omega)^2}, \tag{C.2}$$

$$\frac{1}{K_u(\omega)} = \frac{1}{K_d(\omega)} + B(\omega)\left(a_{12} - \frac{a_{13}(a_{23} + \gamma/i\omega)}{a_{33} - \gamma/i\omega}\right). \tag{C.3}$$

Here, $K_d(\omega)$ is the complex drained bulk modulus of the composite (drained in this context means that the average fluid pressure in a sample does not change, which in no way prevents mesoflow from occuring), and $B(\omega)$ is the complex Skempton's coefficient. The a_{ij} are real elastic compliances that depend on the elastic moduli of the two fluids, while γ is a complex function of frequency given by

$$\gamma(\omega) = \gamma_p \sqrt{1 - i\frac{\omega}{\omega_p}} \tag{C.4}$$

that controls the degree of mesoflow between the fluids. The low-frequency limit of γ is given by

$$\gamma_p = \frac{v_1 k_0}{\eta_1 L_1^2}. \tag{C.5}$$

The parameter L_1 is the distance over which the fluid-pressure gradient still exists in phase 1 (which is the homogeneous porous material saturated with fluid 1) in the final approach to fluid-pressure equilibrium and is formally defined as

$$L_1^2 = \frac{1}{V_1} \int_{\Omega_1} \Phi_1 \, dV \tag{C.6}$$

where Ω_1 is the region of an averaging volume saturated by fluid 1 and having a volume measure V_1. The potential Φ_1 has units of length squared and is a solution of an elliptic boundary-value problem that under conditions where the viscosity ratio η_2/η_1 can be considered small, reduces to

$$\begin{aligned} \nabla^2 \Phi_1 &= -1 \text{ in } \Omega_1, & \text{(C.7)} \\ \mathbf{n} \cdot \nabla \Phi_1 &= 0 \text{ on } \partial E_1, & \text{(C.8)} \\ \Phi_1 &= 0 \text{ on } \partial \Omega_{12} & \text{(C.9)} \end{aligned}$$

where $\partial \Omega_{12}$ is the surface separating the volumes occupied by the two fluids within in the sample and ∂E_1 is the external surface of the sample that is coincident with phase 1.

In all the examples of the present paper, the boundary-value problem for Φ_1 is solved numerically by finite-differences. To do so, we add a diffusion term $-\partial \Phi_1/\partial t$ to the left-hand side of equation (C.7) and replace 1 by a step function on the right-hand side, then solve the resulting diffusion equation using explicit time-stepping. The long-time steady-state response to the imposed step-function source term is the solution of equation (C.7). We then determine numerically the length L_1 using equation (C.6).

The transition frequency ω_p corresponds to the onset of a high-frequency regime in which the fluid-pressure-diffusion penetration distance becomes small relative to the scale of the fluid patch, and is given by

$$\omega_p = \frac{B_1 K}{\eta_1 \alpha} \frac{k_0 \left(v_1 V/S \right)^2}{L_1^4} \left(1 + \sqrt{\frac{\eta_2 B_2}{\eta_1 B_1}} \right)^2 , \tag{C.10}$$

where S is the surface area of the interface between the two phases in each volume V of composite.

Last, the a_{ij} are given by

$$a_{11} = 1/K \tag{C.11}$$
$$a_{22} = (-\beta + v_1/B_1)\,\alpha/K \tag{C.12}$$
$$a_{33} = (-\beta + v_2/B_2)\,\alpha/K \tag{C.13}$$
$$a_{12} = -v_1\alpha/K \tag{C.14}$$
$$a_{13} = -v_2\alpha/K \tag{C.15}$$
$$a_{23} = \beta\alpha/K \tag{C.16}$$

where

$$\beta = v_1 v_2 \left(\frac{v_1}{B_2} + \frac{v_2}{B_1}\right)\left[\frac{\alpha - (1 - K/K_H)\,/\,(v_1 B_1 + v_2 B_2)}{\alpha - (1 - K/K_H)\,(v_1/B_1 + v_2/B_2)}\right] \tag{C.17}$$

Here, v_1 is the volume-fraction of the fluid having the highest viscosity, v_2 is the volume-fraction of the fluid having the lowest viscosity, in each sample $v_1 + v_2 = 1$, B_i is the Skempton's coefficient of the homogeneous porous material saturated with fluid i, K is the drained modulus of the solid grain skeleton, K_H is called the Hill modulus, and α_i is the Biot-Willis constant. In the present situation (elasticity of an isotropic composite having uniform G and all heterogeneity confined to the bulk moduli K_i^u) Hill's theorem applies and K_H is defined as

$$\frac{1}{K_H + 4G/3} = \frac{v_1}{K/(1 - \alpha\beta_1) + 4G/3} + \frac{v_2}{K/(1 - \alpha\beta_2) + 4G/3}. \tag{C.18}$$

The low-frequency and high-frequency limits of $K_u(\omega)$ are determined from equation (C.4) to be

$$K_u(0) = a_{11} - \frac{(a_{12} + a_{13})^2}{a_{22} + 2a_{23} + a_{33}} \tag{C.19}$$
$$K_u(\infty) = a_{11} - \frac{a_{13}^2}{a_{33}} - \frac{(a_{12}a_{33} - a_{13}a_{23})^2}{a_{33}(a_{22}a_{33} - a_{23}^2)}. \tag{C.20}$$

At peak attenuation, defined when $\omega = \omega_p$, one can approximate that $K_u(\omega_p) \approx [K_u(0) + K_u(\infty)]/2$.

Appendix D

Syntethic realization of an isotropic, correlated, gaussian random medium

The algorithm used to generate our random correlated materials (as shown, for example, in Figure 3.13) is now presented:

(a). At each point x on a 2D square grid, we generate a pseudo-random realization $W(x)$ of the white noise of the desired statistical distribution for a given material property having unit standard deviation.

(b). Calculate the 2D Fourier transform $\hat{W}(\mathbf{k})$ of the white noise.

(c). Multiply the Fourier Transform with the spectral filter $\hat{F}(\mathbf{k})$ that represents the correlation function,

$$\hat{U}(\mathbf{k}) = \hat{F}(\mathbf{k})\hat{W}(\mathbf{k}). \tag{D.1}$$

For an isotropic Gaussian medium, the correlation function is

$$\hat{F}(\mathbf{k}) = \hat{F}_G(\mathbf{k}) = \exp\left(-\frac{a_G^2\mathbf{k}^2}{8}\right) \tag{D.2}$$

where a_G is the Gaussian correlation length.

(d). Calculate the 2D inverse Fourier Transform $U(x)$ of the product $\hat{U}(\mathbf{k})$.

(e). Normalize the appropriate variance and add the appropriate mean to obtain the desired random realization $c_g(x)$ of the material properties possessing a Gaussian correlation function.

(f). The random medium with a bimodal distribution can be obtained from a Gaussian random medium having unit standard of deviation (e.g., Yamazaki and Shinozuka, 1988) using the mapping

$$H_b[c_b(x)] = H_g[c_g(x)]. \tag{D.3}$$

Here, $c_g(x)$ and $c_b(x)$ are the field variables in the case of a unimodal Gaussian and bimodal Gaussian realization. The functional maps H_g and H_b are the cumulative PDF of the unimodal Gaussian and bimodal Gaussian distribution and are thus given by

$$2H_g[c_g(x)] = 1 + \text{erf}\left(\frac{c_g(x)}{\sqrt{2}}\right) \tag{D.4}$$

$$2H_b[c_b(x)] = 1 + \text{erf}\left(\frac{c_b(x) - \mu_1}{\sigma_1 2\sqrt{2}} + \frac{c_b(x) - \mu_2}{\sigma_2 2\sqrt{2}}\right) \tag{D.5}$$

where erf denotes the error function. By substituting Equations (D.4) and (D.5) into (D.3), and finding the root $c_b(x)$ for each grid point x, we obtain the desired bimodal medium with the imposed Gaussian correlation function.

Appendix E

Synthetic realization of a self affine random medium

The algorithm used to generate the self-affine background-saturation function $f_{\text{sat}}^{SA}(x, y)$ for use in equation (4.17) is now presented:

(a). At each point x, y on a 2D square grid, we generate a pseudo-random realization $W(x, y)$ of the white noise of the desired statistical distribution for a given material property having unit standard deviation.

(b). Calculate the 2D Fourier transform $\hat{W}(\mathbf{k})$ of the white noise.

(c). Multiply the Fourier transform with the spectral filter $\hat{F}(\mathbf{k})$ that represents the correlation function,

$$\hat{U}(\mathbf{k}) = \hat{F}(\mathbf{k})\hat{W}(\mathbf{k}). \tag{E.1}$$

For a self affine medium, the correlation function is

$$\hat{F}(\mathbf{k}) = \hat{F}_{SA}(\mathbf{k}) = k^{-(E/2-H)} \tag{E.2}$$

where E is the Euclidian dimension of space (i.e. E = 2 in two dimension) and H is the Hurst exponent.

(d). Calculate the 2D inverse Fourier Transform $U(x)$ of the product $\hat{U}(\mathbf{k})$.

(e). Normalize the appropriate variance and add the appropriate mean to obtain the desired self-affine background saturation function $f_{sat}^{SA}(x, y)$.

Appendix F

3D finite differencing scheme

First, all the poroelastic fields and the properties of the materials are discretized on staggered regular cubic lattices. The material properties and the stress component τ_{xx}, τ_{yy}, τ_{zz} and p are assigned to the grid points $[x = l\Delta x,\ y = m\Delta y,\ z = n\Delta z]$, where l, m and n are integers; the velocities v_x and q_x to the points $[x = (l + 1/2)\Delta x,\ y = m\Delta y,\ z = n\Delta z]$; the velocities v_y and q_y to the points $[x = l\Delta x,\ y = (m + 1/2)\Delta y,\ z = n\Delta z]$; the velocities v_z and q_z to the points $[x = l\Delta x,\ y = m\Delta y,\ z = (n + 1/2)\Delta z]$; the shear stress τ_{xy} to the points $[x = (l + 1/2)\Delta x,\ y = (m + 1/2)\Delta y,\ z = n\Delta z]$; the shear stress τ_{xz} to the points $[x = (l + 1/2)\Delta x,\ y = m\Delta y,\ z = (n + 1/2)\Delta z]$; the shear stress τ_{yz} to the points $[x = l\Delta x,\ y = (m + 1/2)\Delta y,\ z = (n + 1/2)\Delta z]$. Further, the fluid and solid velocity fields are temporally discretized and evaluated at instants $[t = k\Delta t]$, while the stresses and fluid-pressure fields are evaluated at instants $[t = (k + 1/2)\Delta t]$.

Once the poroelastic fields has been discretized, knowing v_x, v_y, v_z, q_x, q_y and q_z at instants $t = k\Delta t$, the fields τ_{xx}, τ_{yy}, τ_{zz}, τ_{xy}, τ_{xz}, τ_{yz}, and p can be evaluated at instants $t = (k + 1/2)\Delta t$ using

$$\begin{aligned} D_t\tau_{xx} &= (\lambda_u + 2\mu)D_x v_x + \lambda_u(D_y v_y + D_z v_z) \\ &\quad + \alpha M(D_x q_x + D_y q_y + D_z q_z)\Big|_{l,m,n,k} \end{aligned} \tag{F.1}$$

$$\begin{aligned} D_t\tau_{yy} &= (\lambda_u + 2\mu)D_y v_y + \lambda_u(D_x v_x + D_z v_z) \\ &\quad + \alpha M(D_x q_x + D_y q_y + D_z q_z)\Big|_{l,m,n,k} \end{aligned} \tag{F.2}$$

$$\begin{aligned} D_t\tau_{zz} &= (\lambda_u + 2\mu)D_z v_z + \lambda_u(D_x v_x + D_y v_y) \\ &\quad + \alpha M(D_x q_x + D_y q_y + D_z q_z)\Big|_{l,m,n,k} \end{aligned} \tag{F.3}$$

$$D_t\tau_{xy} = \langle\mu\rangle_{lm}\left(D_x v_y + D_y v_x\right)\Big|_{l+\frac{1}{2},m+\frac{1}{2},n,k} \tag{F.4}$$

$$D_t\tau_{xz} = \langle\mu\rangle_{ln}\left(D_x v_z + D_z v_x\right)\Big|_{l+\frac{1}{2},m,n+\frac{1}{2},k} \tag{F.5}$$

$$D_t\tau_{yz} = \langle\mu\rangle_{mn}\left(D_y v_z + D_z v_y\right)\Big|_{l,m+\frac{1}{2},n+\frac{1}{2},k} \tag{F.6}$$

and

$$\begin{aligned} D_t p &= -\alpha M(D_x v_x + D_y v_y + D_z v_z) \\ &\quad + M(D_x q_x + D_y q_y + D_z q_z)\Big|_{l,m,n,k} \end{aligned} \tag{F.7}$$

where

$$\begin{aligned} \frac{1}{\langle\mu\rangle_{lm}}\Big|_{l+\frac{1}{2},m+\frac{1}{2},n} &= \frac{1}{4}\left[\frac{1}{\mu_{(l,m,n)}} + \frac{1}{\mu_{(l+1,m+1,n)}}\right. \\ &\quad \left. + \frac{1}{\mu_{(l+1,m,n)}} + \frac{1}{\mu_{(l,m+1,n)}}\right] \end{aligned} \tag{F.8}$$

$$\begin{aligned} \frac{1}{\langle\mu\rangle_{ln}}\Big|_{l+\frac{1}{2},m,n+\frac{1}{2}} &= \frac{1}{4}\left[\frac{1}{\mu_{(l,m,n)}} + \frac{1}{\mu_{(l+1,m,n+1)}}\right. \\ &\quad \left. + \frac{1}{\mu_{(l+1,m,n)}} + \frac{1}{\mu_{(l,m,n+1)}}\right] \end{aligned} \tag{F.9}$$

$$\begin{aligned} \frac{1}{\langle\mu\rangle_{mn}}\Big|_{l,m+\frac{1}{2},n+\frac{1}{2}} &= \frac{1}{4}\left[\frac{1}{\mu_{(l,m,n)}} + \frac{1}{\mu_{(l,m+1,n+1)}}\right. \\ &\quad \left. + \frac{1}{\mu_{(l,m+1,n)}} + \frac{1}{\mu_{(l,m,n+1)}}\right]. \end{aligned} \tag{F.10}$$

Then, knowing the stress fields τ_{ij} and p at instants $t = (k+1/2)\Delta t$ and the velocity fields q_i and v_i at $t = k\Delta t$, the velocity fields can then be determined at instants $t = (k+1)\Delta t$ using

$$\psi_l \langle \rho_f \rangle_l D_t q_x + \left\langle \frac{\eta}{k_0} \right\rangle_l \langle q_x \rangle_k =$$
$$-D_x p - \frac{\langle \rho_f \rangle_l}{\langle \rho \rangle_l} (D_x \tau_{xx} + D_y \tau_{xy} + D_z \tau_{xz}) \Big|_{l+\frac{1}{2},m,n,k+\frac{1}{2}} \tag{F.11}$$

$$\psi_m \langle \rho_f \rangle_m D_t q_y + \left\langle \frac{\eta}{k_0} \right\rangle_m \langle q_y \rangle_k =$$
$$-D_y p - \frac{\langle \rho_f \rangle_m}{\langle \rho \rangle_m} (D_x \tau_{xy} + D_y \tau_{yy} + D_z \tau_{yz}) \Big|_{l,m+\frac{1}{2},n,k+\frac{1}{2}} \tag{F.12}$$

$$\psi_n \langle \rho_f \rangle_n D_t q_z + \left\langle \frac{\eta}{k_0} \right\rangle_n \langle q_z \rangle_k =$$
$$-D_z p - \frac{\langle \rho_f \rangle_n}{\langle \rho \rangle_n} (D_x \tau_{xz} + D_y \tau_{yz} + D_z \tau_{zz}) \Big|_{l,m,n+\frac{1}{2},k+\frac{1}{2}} \tag{F.13}$$

and

$$\begin{aligned} \langle \rho \rangle_l D_t v_x &= \\ &\left(1 + \frac{1}{\psi_l} \frac{\langle \rho_f \rangle_l}{\langle \rho \rangle_l}\right) (D_x \tau_{xx} + D_y \tau_{xy} + D_z \tau_{xz}) \\ &+ \frac{1}{\psi_l} \left(D_x p + \left\langle \frac{\eta}{k_0} \right\rangle_l \langle q_x \rangle_k\right) \Big|_{l+\frac{1}{2},m,n,k+\frac{1}{2}} \end{aligned} \tag{F.14}$$

$$\begin{aligned} \langle \rho \rangle_m D_t v_y &= \\ &\left(1 + \frac{1}{\psi_m} \frac{\langle \rho_f \rangle_m}{\langle \rho \rangle_m}\right) (D_x \tau_{xy} + D_y \tau_{yy} + D_z \tau_{yz}) \\ &+ \frac{1}{\psi_m} \left(D_y p + \left\langle \frac{\eta}{k_0} \right\rangle_m \langle q_y \rangle_k\right) \Big|_{l,m+\frac{1}{2},n,k+\frac{1}{2}} \end{aligned} \tag{F.15}$$

$$\begin{aligned} \langle \rho \rangle_n D_t v_z &= \\ &\left(1 + \frac{1}{\psi_n} \frac{\langle \rho_f \rangle_n}{\langle \rho \rangle_n}\right) (D_x \tau_{xz} + D_y \tau_{yz} + D_z \tau_{zz}) \\ &+ \frac{1}{\psi_n} \left(D_z p + \left\langle \frac{\eta}{k_0} \right\rangle_n \langle q_z \rangle_k\right) \Big|_{l,m,n+\frac{1}{2},k+\frac{1}{2}} \end{aligned} \tag{F.16}$$

where

$$\langle q_x \rangle_k \Big|_{k+\frac{1}{2}} = \frac{q_x(k+1) + q_x(k)}{2} \tag{F.17}$$

$$\langle \rho \rangle_l \Big|_{l+\frac{1}{2},m,n} = \frac{\rho(l+1,m,n) + \rho(l,m,n)}{2} \tag{F.18}$$

$$\langle \rho \rangle_m \Big|_{l,m+\frac{1}{2},n} = \frac{\rho(l,m+1,n) + \rho(l,m,n)}{2} \tag{F.19}$$

$$\langle \rho \rangle_n \Big|_{l,m,n+\frac{1}{2}} = \frac{\rho(l,m,n+1) + \rho(l,m,n)}{2} \tag{F.20}$$

and where

$$\psi_m = \langle (1+\Phi)F \rangle_m - \frac{\langle \rho_f \rangle_m}{\langle \rho \rangle_m} \tag{F.21}$$

with the bracket averages defined as in equations (55)-(57). The first spatial derivatives in equations (F.1)-(F.16) can be evaluated using the fourth order finite difference operator

$$D_x v_x \Big|_{l,m,n} = \frac{1}{\Delta_x} \left\{ c_1 \left[v_{x(l+\frac{1}{2},m,n)} - v_{x(l-\frac{1}{2},m,n)} \right] - c_2 \left[v_{x(l-\frac{3}{2},m,n)} - v_{x(l+\frac{3}{2},m,n)} \right] \right\}$$

where $c_1 = 9/8$ and $c_2 = 1/24$. The first order time derivatives can be evaluated using the second-order time operator

$$D_t v_x \Big|_{l,m,n,k+\frac{1}{2}} = \frac{1}{\Delta_t} \left[v_{x(l,m,n,k+1)} - v_{x(l,m,n,k-1)} \right]. \tag{F.22}$$

Last, the time spacing Δt must satisfy the classic Courant condition

$$\Delta_t \leq \frac{\Delta_x}{\sqrt{3}\,(c_1 + c_2)\,v_p} \tag{F.23}$$

where v_p denotes the velocity of the fast p-wave.

Appendix G

Eshelby's tensor

The derivation of the Eshelby tensor in isotropic materials can be found in Eshelby (1957) and Mura (1982). For isotropic medium, the Eshelbys tensor can be expressed in terms of elliptic integrals. Assuming that $a_1 > a_2 > a_3$ and that the semi axis a_1, a_2 and a_3 aligns

with the coordinate x, y, and z, respectively, then

$$S_{1111} = \frac{3a_1^2}{8\pi(1-\nu)}I_{11} + \frac{1-2\nu}{8\pi(1-\nu)}I_1 \quad \text{(G.1)}$$

$$S_{1122} = \frac{3a_2^2}{8\pi(1-\nu)}I_{12} - \frac{1-2\nu}{8\pi(1-\nu)}I_1 \quad \text{(G.2)}$$

$$S_{1133} = \frac{3a_3^2}{8\pi(1-\nu)}I_{13} - \frac{1-2\nu}{8\pi(1-\nu)}I_1 \quad \text{(G.3)}$$

$$S_{1212} = \frac{3(a_1^2+a_2^2)}{16\pi(1-\nu)}I_{12} + \frac{1-2\nu}{16\pi(1-\nu)}(I_1+I_2) \quad \text{(G.4)}$$

$$S_{3333} = \frac{3a_3^2}{8\pi(1-\nu)}I_{33} + \frac{1-2\nu}{8\pi(1-\nu)}I_3 \quad \text{(G.5)}$$

$$S_{3311} = \frac{3a_1^2}{8\pi(1-\nu)}I_{31} - \frac{1-2\nu}{8\pi(1-\nu)}I_3 \quad \text{(G.6)}$$

$$S_{3322} = \frac{3a_2^2}{8\pi(1-\nu)}I_{32} - \frac{1-2\nu}{8\pi(1-\nu)}I_3 \quad \text{(G.7)}$$

$$S_{3131} = \frac{3(a_3^2+a_1^2)}{16\pi(1-\nu)}I_{31} + \frac{1-2\nu}{16\pi(1-\nu)}(I_3+I_1) \quad \text{(G.8)}$$

$$S_{2222} = \frac{3a_2^2}{8\pi(1-\nu)}I_{22} + \frac{1-2\nu}{8\pi(1-\nu)}I_2 \quad \text{(G.9)}$$

$$S_{2233} = \frac{3a_3^2}{8\pi(1-\nu)}I_{23} - \frac{1-2\nu}{8\pi(1-\nu)}I_2 \quad \text{(G.10)}$$

$$S_{2211} = \frac{3a_1^2}{8\pi(1-\nu)}I_{21} - \frac{1-2\nu}{8\pi(1-\nu)}I_2 \quad \text{(G.11)}$$

$$S_{2323} = \frac{3(a_2^2+a_3^2)}{16\pi(1-\nu)}I_{23} + \frac{1-2\nu}{16\pi(1-\nu)}(I_2+I_3) \quad \text{(G.12)}$$

The rest of the terms are equal to zero. The I_i terms are defined in terms of standard elliptic integrals,

$$I_1 = \frac{4\pi a_1 a_2 a_3}{(a_1^2-a_2^2)\sqrt{a_1^2-a_3^2}}(F-E) \quad \text{(G.13)}$$

$$I_3 = \frac{4\pi a_1 a_2 a_3}{(a_2^2-a_3^2)\sqrt{a_1^2-a_3^2}}\left(\frac{a_2\sqrt{a_1^2-a_3^2}}{a_1 a_3} - E\right) \quad \text{(G.14)}$$

$$I_2 = 4\pi - I_1 - I_3 \quad \text{(G.15)}$$

where the I_{ij} terms are

$$I_{12} = \frac{I_2 - I_1}{3(a_1^2 - a_2^2)} \tag{G.16}$$

$$I_{21} = \frac{I_1 - I_2}{3(a_2^2 - a_1^2)} \tag{G.17}$$

$$I_{13} = \frac{I_3 - I_1}{3(a_1^2 - a_3^2)} \tag{G.18}$$

$$I_{31} = \frac{I_1 - I_3}{3(a_3^2 - a_1^2)} \tag{G.19}$$

$$I_{23} = \frac{I_3 - I_2}{3(a_2^2 - a_3^2)} \tag{G.20}$$

$$I_{32} = \frac{I_2 - I_3}{3(a_3^2 - a_2^2)} \tag{G.21}$$

$$I_{11} = \frac{4\pi}{3a_1^2} - I_{12} - I_{13} \tag{G.22}$$

$$I_{22} = \frac{4\pi}{3a_2^2} - I_{23} - I_{21} \tag{G.23}$$

$$I_{33} = \frac{4\pi}{3a_3^2} - I_{31} - I_{32} \tag{G.24}$$

and the standard elliptic integrals $F(\theta, k)$ and $E(\theta, k)$ have the following definition

$$E(\theta, k) = \int_0^\theta (1 - k^2 sin^2 w)^{\frac{1}{2}} dw \tag{G.25}$$

$$F(\theta, k) = \int_0^\theta \frac{dw}{(1 - k^2 sin^2 w)^{\frac{1}{2}}} \tag{G.26}$$

where

$$\theta = \sin^{-1}\left(\sqrt{1 - \frac{a_3^2}{a_1^2}}\right) \tag{G.27}$$

$$k = \sqrt{\frac{a_1^2 - a_2^2}{a_1^2 - a_3^2}}. \tag{G.28}$$

In the special case of an oblate spheroid ($a_1 = a_2 > a_3$) the I_i terms reduce to

$$I_1 = \frac{2\pi a_1 a_2 a_3}{(a_1^2 - a_3^2)^{\frac{3}{2}}} \left[\cos^{-1}\left(\frac{a_3}{a_1}\right) - \frac{a_3}{a_1}\sqrt{1 - \frac{a_3^2}{a_1^2}}\right] \tag{G.29}$$

$$I_2 = I_1 \tag{G.30}$$

$$I_3 = \frac{4\pi a_1 a_2 a_3}{(a_2^2 - a_3^2)\sqrt{a_1^2 - a_3^2}} \left(\frac{a_2\sqrt{a_1^2 - a_3^2}}{a_1 a_3} - E\right) \tag{G.31}$$

where

$$I_{13} = \frac{I_3 - I_1}{3(a_1^2 - a_3^2)} \tag{G.32}$$

$$I_{31} = \frac{I_1 - I_3}{3(a_3^2 - a_1^2)} \tag{G.33}$$

$$I_{23} = \frac{I_3 - I_2}{3(a_2^2 - a_3^2)} \tag{G.34}$$

$$I_{32} = \frac{I_2 - I_3}{3(a_3^2 - a_2^2)} \tag{G.35}$$

$$I_{12} = \frac{\pi}{3a_1^2} - \frac{I_{13}}{4} \tag{G.36}$$

$$I_{21} = I_{12} \tag{G.37}$$

$$I_{11} = \frac{4\pi}{3a_1^2} - I_{12} - I_{13} \tag{G.38}$$

$$I_{22} = \frac{4\pi}{3a_2^2} - I_{23} - I_{21} \tag{G.39}$$

$$I_{33} = \frac{4\pi}{3a_3^2} - I_{31} - I_{32}. \tag{G.40}$$

And for a prolate spheroid ($a_1 > a_2 = a_3$) the I_i terms reduce to

$$I_1 = \frac{4\pi a_1 a_2 a_3}{(a_1^2 - a_2^2)\sqrt{a_1^2 - a_3^2}}(F - E) \tag{G.41}$$

$$I_2 = \frac{2\pi a_1 a_2 a_3}{(a_1^2 - a_3^2)^{\frac{3}{2}}}\left[\frac{a_1}{a_3}\sqrt{\left(\frac{a_1^2}{a_3^2} - 1\right)} - \cosh^{-1}\left(\frac{a_1}{a_3}\right)\right] \tag{G.42}$$

$$I_3 = I_2 \tag{G.43}$$

where

$$I_{12} = \frac{I_2 - I_1}{3(a_1^2 - a_2^2)} \tag{G.44}$$

$$I_{21} = \frac{I_1 - I_2}{3(a_2^2 - a_1^2)} \tag{G.45}$$

$$I_{13} = \frac{I_3 - I_1}{3(a_1^2 - a_3^2)} \tag{G.46}$$

$$I_{31} = \frac{I_1 - I_3}{3(a_3^2 - a_1^2)} \tag{G.47}$$

$$I_{23} = \frac{\pi}{3a_2^2} - \frac{I_{21}}{4} \tag{G.48}$$

$$I_{32} = I_{23} \tag{G.49}$$

$$I_{11} = \frac{4\pi}{3a_1^2} - I_{12} - I_{13} \tag{G.50}$$

$$I_{22} = \frac{4\pi}{3a_2^2} - I_{23} - I_{21} \tag{G.51}$$

$$I_{33} = \frac{4\pi}{3a_3^2} - I_{31} - I_{32}. \tag{G.52}$$

For a spherical inclusion, the Eshelby tensor has the simple form

$$S_{1111} = \frac{7 - 5\nu}{15(1 - \nu)} \tag{G.53}$$

$$S_{2222} = S_{1111} \tag{G.54}$$

$$S_{3333} = S_{1111} \tag{G.55}$$

$$S_{1212} = \frac{4 - 5\nu}{15(1 - \nu)} \tag{G.56}$$

$$S_{2323} = S_{1212} \tag{G.57}$$

$$S_{3131} = S_{1212} \tag{G.58}$$

$$S_{1122} = \frac{5\nu - 1}{15(1 - \nu)} \tag{G.59}$$

$$S_{2233} = S_{1122} \tag{G.60}$$

$$S_{3311} = S_{1122} \tag{G.61}$$

$$S_{1133} = S_{1122} \tag{G.62}$$

$$S_{2211} = S_{1122} \tag{G.63}$$

$$S_{3322} = S_{1122} \tag{G.64}$$

$$\tag{G.65}$$

And for an infinite cylinder ($a_3 \to \infty$) we have

$$
\begin{aligned}
S_{1111} &= \frac{1}{2(1-\nu)}\left(\frac{a_2^2+2a_1a_2}{(a_1+a_2)^2}+(1-2\nu)\frac{a_2}{a_1+a_2}\right) && \text{(G.66)}\\
S_{2222} &= \frac{1}{2(1-\nu)}\left(\frac{a_1^2+2a_1a_2}{(a_1+a_2)^2}+(1-2\nu)\frac{a_1}{a_1+a_2}\right) && \text{(G.67)}\\
S_{3333} &= 0 && \text{(G.68)}\\
S_{1122} &= \frac{1}{2(1-\nu)}\left(\frac{a_2^2}{(a_1+a_2)^2}-(1-2\nu)\frac{a_2}{a_1+a_2}\right) && \text{(G.69)}\\
S_{2233} &= \frac{1}{2(1-\nu)}\frac{2\nu a_1}{a_1+a_2} && \text{(G.70)}\\
S_{2211} &= \frac{1}{2(1-\nu)}\left(\frac{a_1^2}{(a_1+a_2)^2}-(1-2\nu)\frac{a_1}{a_1+a_2}\right) && \text{(G.71)}\\
S_{3311} &= 0 && \text{(G.72)}\\
S_{3322} &= 0 && \text{(G.73)}\\
S_{1212} &= \frac{1}{2(1-\nu)}\left(\frac{a_1^2+a_2^2}{2(a_1+a_2)^2}+\frac{1-2\nu}{2}\right) && \text{(G.74)}\\
S_{1133} &= \frac{1}{2(1-\nu)}\frac{2\nu a_2}{a_1+a_2} && \text{(G.75)}\\
S_{2323} &= \frac{a_1}{2(a_1+a_2)} && \text{(G.76)}\\
S_{3131} &= \frac{a_2}{2(a_1+a_2)}. && \text{(G.77)}
\end{aligned}
$$

Finally, the simplified form S_{ij} of the Eshelby tensor S_{ijkl} is

$$
S_{ij} = \begin{pmatrix}
S_{1111} & S_{1122} & S_{1133} & 0 & 0 & 0\\
S_{2211} & S_{2222} & S_{2233} & 0 & 0 & 0\\
S_{3311} & S_{3322} & S_{3333} & 0 & 0 & 0\\
0 & 0 & 0 & 2S_{1212} & 0 & 0\\
0 & 0 & 0 & 0 & 2S_{3131} & 0\\
0 & 0 & 0 & 0 & 0 & 2S_{2323}
\end{pmatrix}. \qquad \text{(G.78)}
$$